Fluorine Partitioning Between Nominally Anhydrous Minerals (Olivine, Clinopyroxene, and Plagioclase) and Silicate Melt using Secondary Ion Mass Spectrometry and Newly Synthesized Basaltic Fluorine Microanalytical Glass Standards

by

Steve Guggino

A Dissertation Presented in Partial Fulfillment
of the Requirements for the Degree
Doctor of Philosophy

Approved May 2012 by the
Graduate Supervisory Committee:

Richard Hervig, Chair
Donald Burt
Amanda Clarke
Lynda Williams
Stanley Williams

ARIZONA STATE UNIVERSITY

August 2012

ABSTRACT

Fluorine (F) is a volatile constituent of magmas and hydrous mantle minerals. Compared to other volatile species, F is highly soluble in silicate melts, allowing F to remain in the melt during magma differentiation and rendering F less subject to disturbance during degassing upon magma ascent. Hence, the association between fluorine in basalts and fluorine in the mantle source region is more robust than for other volatile species. The ionic radius of F^- is similar to that of OH^- and O^{2-}, and F may substitute for hydroxyl and oxygen in silicate minerals and melt. Fluorine is also incorporated at trace levels within nominally anhydrous minerals (NAMs) such as olivine, clinopyroxene, and plagioclase. Investigating the geochemical behavior of F in NAMs provides a means to estimate the pre-eruptive F contents of degassed magmas and to better understand the degassing behavior of H.

The partition coefficients of F were determined for clinopyroxene, olivine, plagioclase, and hornblende within melts of olivine-minette, augite-minette, basaltic andesite, and latite compositions. The samples analyzed were run products from previously-published phase-equilibria experiments. Fluorine was measured by secondary ion mass spectrometry (SIMS) using an $^{16}O^-$ primary beam and detection of negative secondary ions ($^{19}F^-$, $^{18}O^-$, $^{28}Si^-$). SIMS ion intensities are converted to concentrations by analyzing matrix-matched microanalytical reference materials and constructing calibration curves. For robust F calibration standards, five basaltic glasses (termed Fba glasses) were synthesized in-house using a natural tholeiite mixed with variable amounts of CaF_2. The Fba glasses were characterized for F content and homogeneity using both SIMS and electron-probe microanalysis (EPMA) and used as F standards.

The partition coefficients for clinopyroxene (0.04-028) and olivine (0.01-0.16) varied with melt composition such that D_F (olivine-minette) < D_F (augite-minette) < D_F (basaltic andesite) < D_F (latite). Crystal chemical controls strongly influence the incorporation of F into clinopyroxene, but none were found that affected olivine. Fluorine

substitution into olivine is dominantly controlled by melt viscosity and degree of melt polymerization. Fluorine partitioning was compared with that of OH within clinopyroxenes, and the alumina content of clinopyroxene was shown to be a strong influence on the incorporation of both anions.

DEDICATION

This work is the culmination of a lifetime of influences and personal choices that have steered me toward this endeavor. From my early childhood ensconced in the religion of my parents when I would pray for the “knowledge of the universe”; to my initiation into research with my Masters advisor Peter Harries and our knee-slapping discoveries of ancient climates hidden within shells; to the honing of my research skills and scientific acumen with my Ph.D. advisor Rick Hervig, whose words always motivated me and encouraged me to pursue my curiosities; and to all within the last four decades who have impressed me, instructed me, worked with me, laughed with me, listened to me, loved me, and frankly put up with me; I dedicate this dissertation to all of you.

ACKNOWLEDGMENTS

The presentation of my research in this dissertation embodies an endeavor that spanned over five years of my life, and would not have been possible without the tutelage, support, and patience of many faculty, researchers, post-docs, graduate students and other collaborators, as well as my family and friends. First, I want to thank my advisor, Richard Hervig, who provided the guidance I needed throughout the years, and whose words always encouraged me and whose professional expertise set an example for me to emulate. I want to also thank my committee members, Lynda Williams, Stanley Williams, Amanda Clarke, and Donald Burt, who were always ready to assist me in any way possible. Lynda Williams' expertise on the secondary ion mass spectrometer (SIMS) and dedication to its users saved many analysis sessions that were on the brink of disaster. Stanley Williams' professional knowledge and good cheer helped me maintain a positive outlook on research and life in academia in general. Amanda Clarke, along with Stanley Williams, impressed upon me the beauty and physical nature of igneous and volcanological processes, as well as the subtleties and details of performing volcanological work out in the field. Donald Burt provided me with fluorine standards (fluor-topaz) which allowed me to perform key analyses on the proton-beam accelerator. I would also like to acknowledge the sources of funding for my research, which was awarded to Richard Hervig and David Bell through the National Science Foundation.

The most important aspect of my research, without which my research would not have reached a satisfactory conclusion, was the synthesis of apt fluorine glass standards in a basaltic matrix. I want to thank Gordon Moore for graciously allowing me the use of the experimental lab at Arizona State University (ASU) to synthesize the basalt fluorine standard glasses that will ultimately be distributed throughout the microanalytical community. Gordon Moore's assistance and patience was extraordinary, and his staff of undergraduates, especially Amber Gullickson, was instrumental in my success in the experimental lab. I want to thank Kenneth Domanik at the University of Arizona electron-

probe microanalysis (EPMA) lab who worked hard to help me analyze my fluorine glass standards on the electron microprobe. Kenneth taught me much about the difficulties and nuances of measuring fluorine with the EPMA. I also want to thank Keith Morrison, one of the most intelligent people I know and admire, who not only gave me moral support, but who also assisted me in performing baseline corrections on the results from proton-induced gamma-ray emission (PIGE) analysis of fluorine on glass standards.

I would like to thank my parents, Nelson and Fina Guggino, for their unfailing encouragement and support throughout my education, and my daughters, Danielle and Ariel, of whom I am so proud and who have given me the personal drive to fulfill my educational and professional edification. I want to thank two of my best friends, Kim Genareau and Ada Pabon, who have had the wherewithal to endure my ups and downs and who have given me the professional and personal reality checks needed to make it through. Finally, I would like to thank Beth Townsend who came into my life at just the right time. Her experience in academia, her drive to get me finished, and her superb cooking were just what I needed during this denouement.

TABLE OF CONTENTS

Page

LIST OF TABLES xi

LIST OF FIGURES xiii

PREFACE xvi

CHAPTER

1. INTRODUCTION 1

1. Motivation 1

2. Summary of Chapters 2-5 6

3. References 8

2. FLUORINE CONTENT OF THE MICROANALYTICAL GLASS STANDARDS BHVO-2G, GSE-1G, NIST-610, AND UTR-2 USING PROTON-INDUCED GAMMA-RAY EMISSION (PIGE) ANALYSIS 12

ABSTRACT 12

1. Introduction 13

2. Methods 16

2.1. Sample Preparation 16

2.2. PIGE Analysis 17

2.2.1. Calibration Standards for PIGE Analysis 18

2.3. SIMS Analysis 18

3. Results and Discussion 19

3.1. PIGE Basics 19

3.2. PIGE Results 25

3.3. SIMS Analysis 29

4. Conclusions 32

5. References 33

6. Figure Captions 38

CHAPTER Page

3. SYNTHESIS AND CHARACTERIZATION OF FIVE NEW FLUORINE -BEARING BASALT REFERENCE MATERIALS AND THEIR USE IN QUANTIFYING THE FLUORINE CONTENT OF THE BASALT GLASS STANDARDS BCR-2G, BHVO-2G, GSA-1G, GSC-1G, GSD-1G, ML3B-G, KL2-G, AND ALV-519-4 48

ABSTRACT 48

1. Introduction 49

2. Experimental Methods 55

3. Analytical Methods and Instrumentation 56

3.1. EPMA Analysis 56

3.1.1. EPMA at Arizona State University (ASU) 56

3.1.2. EPMA at University of Arizona (UofA) 57

3.2. SIMS Analysis 59

4. Results 59

4.1. Homogeneity of the Fba Glasses 59

4.1.1. Homogeneity Determination using SIMS 60

4.1.2. SIMS Output, Homogeneity, and the limit on Quantitation 61

4.2 EPMA Analysis 61

4.2.1. EPMA: Peak-Count Method 61

4.2.2. EPMA: Peak Integration Method 63

4.2.3. EPMA: Peak-count Versus Peak Integration Methods 64

4.2.4. Homogeneity with EPMA 64

4.3 Fluorine Loss during Synthesis of the Fba Glasses 65

4.3.1. Open-system Fluorine Partitioning between CO_2 Gas and Basaltic Melt 65

CHAPTER Page

5. Application of New Fba Fluorine Standards for SIMS Calibration 67

5.1. Matrix Effects 67

5.2. Calibration Curves 67

5.3. Comparison of Ion Yields for F^- and F^+ Secondary Ions 69

5.4. Fluorine Content of USGS, MPI-DING, and ALV-519 Basalt Reference Glasses using SIMS 70

6. Conclusions 72

7. References 73

8. Figure Captions 80

4. FLUORINE IN OLIVINE: DEVELOPMENT OF A TECHNIQUE TO MEASURE FLUORINE IN NOMINALLY ANHYDROUS MINERALS USING SIMS 106

ABSTRACT 106

1. Introduction 107

2. Methods 109

2.1. Samples 109

2.2. SIMS Measurements 109

2.2.1. Primary Beams 109

2.2.2. Analytical Parameters 112

2.2.3. Quantifying SIMS Measurements 113

3. Results and Discussion 115

3.1. Fluorine Secondary Ion Yields under Cs^+ and O^- Primary Beam Bombardment 115

3.2. Comparing $^{19}F/^{18}O$ Ion Ratios between Cs^+ and O^- Primary Beams 117

3.3 Matrix Effects and the Use of the Fba Standards 118

CHAPTER Page

3.4 Fluorine Content of the Olivine Samples 119

3.4.1 Fluorine Content of Kimberlitic Olivine..... 120

3.4.2 Fluorine Content of Extrusive and Hypabyssal Rocks.... 120

3.4.3 Fluorine Content of Plutonic Rocks 121

3.4.4 Fluorine Content of Olivines from the Kiglapait Layered Intrusion 122

4. Summary and Conclusions 123

5. References 124

6. Figure Captions 128

5. FLUORINE PARTITIONING BETWEEN NOMINALLY ANHYDROUS MINERALS (CLINOPYROXENE, OLIVINE, AND PLAGIOCLASE) AND SILICATE MELT .. 151

ABSTRACT 151

1. Introduction 152

2. Samples Suites 155

2.1 Chemical Equilibrium of Sample Suites 156

2.2 Criteria for Selection of Crystals and Glass for Analysis 158

3. Analytical Methods 159

3.1 SIMS Analysis 159

3.2 EPMA Analysis 159

3.3 Fluorine Standards for SIMS Analysis (Fba Glasses) 160

3.3.1 EPMA on Fluorine Standards (Fba Glasses) 160

3.3.2 SIMS Analysis of Fluorine Standards (Fba Glasses) 161

4. Analytical Results 161

4.1 Major and Trace Element Composition 161

4.2 Partition Coefficients 162

CHAPTER Page

4.3 Clinopyroxene Partition Coefficients 163

4.4 Olivine Partition Coefficients 163

4.5 Plagioclase and Hornblende Partition Coefficients 163

5. Discussion 164

5.1 Crystal Chemical Controls on the Incorporation of F in NAMs 164

5.2 Fluorine in Olivine 165

5.3 Fluorine in Pyroxene 168

5.3.1 Elastic Strain Model 168

5.3.2 Fluorine in Pyroxene: End-Member Components 169

5.3.3 Total Iron Content of Cpx and Fe^{2+} - F Avoidance in Silicate Minerals 172

5.3.4 Fluorine in Pyroxene: Fe^{3+} Substitutions 173

5.3.5 Fluorine in Pyroxene: Al^{3+} Substitution and Comparison to H^{+} in Pyroxene 176

5.4 Melt Viscosity and Fluorine Partition Coefficients 179

6. Conclusion 182

7. References 184

8. Figure Captions 192

6. SYNTHESIS 228

ABSTRACT 228

1. Major Contributions: Basaltic Microanalytical Glass Standards for Fluorine 228

2. Major Contributions: Fluorine Partitioning 230

3. Future Work 231

4. References 233

REFERENCES 239

LIST OF TABLES

Table Page

2.1. Major Element and Density Data for Mineral Standards, Basaltic Glasses, and High-silica Glasses. 39

2.2. PIGE Analysis of Fluor-topaz, Durango Apatite, and Basaltic and Rhyolitic Glasses. 40

2.3. Results of SIMS and PIGE Analyses of the F Content of Select Basaltic and Rhyolitic Glasses..... 41

2.4. Fluorine Concentration Values of ALV-519, USGS Basaltic and MPI-DING Basaltic Glass Reference Materials, and NIST-620 using SIMS Calibration Curves. 42

3.1. Masses of EPR-2001 and CaF_2 (96 % pure) Powders to Achieve Desired F Concentrations in Final Powder Mixtures..... 83

3.2. Analytical Instruments, Operating Conditions, and Fluorine Standards for Analysis of the Fba Glasses 84

3.3. Average SIMS Values and % RSD of the Homogeneous F Standard Glasses, the Fba Glasses, and Mica Standards 85

3.4 Electron Probe Microanalysis of the Major, Trace, and Fluorine Abundances of the Fba Glasses, Bt-3, and F-phlogopite. 86-87

3.5 Results of the Peak-count and Peak-integration Methods on the Fba Glasses and Mica Standards. 88

3.6 Mass Loss of F during Fusing 89

3.7 Results of SIMS, EPMA, and Literature F Concentration Values of the Fba Glasses, High-silica Glass Standards, and Mica Standards 90

3.8 Nominal F Concentrations for the Fba Glasses, the Average SIMS Intensities of the F Signal from the Fba Glasses for both the F^- and F^+ Analyses, the Average Primary Current, and the Calculated Ion Yields..... 91

Table Page

3.9 Fluorine Concentration Values of ALV-519, USGS, and MPI-DING Basaltic Glass Reference Materials using Calibration Curves 92

4.1 Average SIMS Measurements and Secondary Ion Yields of F on the High-silica Glass Standards using both Cs^+ and O^- Primary Beams 131

4.2 List of Olivine Samples from Extrusive Suites Showing Collection Location, Description of Host Rock, Major Element, and F Data 132

4.3 List of Olivine Samples from Xenoliths Showing Collection Location, Description of Host Rock, Major Element, and F Data 133

4.4 List of Olivine Samples from Hypabyssal Suites Showing Collection Location, Description of Host Rock, and Major Element Data 134

4.5 List of Olivine Samples from Plutonic Suites Showing Collection Location, Description of Host Rock, and Major Element Data 135

5.1 Major Element Compositions of the Starting Materials for the Experimental Samples Analyzed in this Study 196

5.2 Experimental Run Conditions of the Samples used in this Study 197

5.3 SIMS Results ($^{19}F/^{18}O$) of the Glass Phases from the Experimental Sample Suites of this Study 198

5.4 Experimental Conditions during Synthesis of the Fba Glasses, Their $^{19}F^-/^{18}O^-$ Ratios from SIMS, and Their F Concentration Values from EPMA..... 199

5.5 Average of SIMS and EPMA Data from this Study and the Literature.....200-201

6.1 Comparison of the F Content of Selected Reference Glasses Based on Two Methods: PIGE and SIMS Fba Glasses Calibration Curves 236

LIST OF FIGURES

Figure		Page
2.1	Gamma-ray Energy Spectrum for ^{60}Co	43
2.2	SIMS High-resolution Mass Spectrum of NIST-610	44
2.3	PIGE Energy Spectrum of Natural Fluor-topaz, Topaz Mountain, Utah (20.3 wt.% F)	45
2.4	Gamma-ray Energy Spectrum Showing Low-energy Interfering Resonances	46
2.5	SIMS results ($^{19}F/^{18}O$) for the basaltic and High-silica Glasses Versus Their Fluorine Concentration Values Based on PIGE Analysis	47
3.1	Wavelength Scans of Biotite-3 and Synthetic Fluor-phlogopite Using the Cameca SX-100 Electron Microprobe at the University of Arizona EPMA Lab	93
3.2	SIMS High-resolution Mass Spectrum of NIST-610	94
3.3	SIMS 6f Determination of Homogeneity of the Fba Glasses and Mica F Standards	95
3.4	Precision of Both the Peak-count and Peak Integration Methods between Various F Calibration Standards Expressed as Percent Difference	96
3.5	EPMA (Peak Integration Method) Determination of Homogeneity of the Fba Glasses with Respect to F	97
3.6	Fluorine Concentration (wt.%) of Pre-fusing Initial Powder Aliquots Versus the Mass Loss of Fluorine (wt.%) after Fusing	98
3.7	Fluorine Content of the Fba Glasses Versus the Apparent Partition Coefficient (APC) of F between CO_2 Gas and the Basaltic Melt	99-100
3.8	SIMS Calibration Curves Generated from the Data in Table 3.7 Showing the Variability in Fluorine Measurements Due to Matrix Effects	101-105

Figure Page

4.1 Selected Olivine Grain Mounts from the Original Study by Simkin and Smith (1970) 136

4.2 Plan View of the Cameca Ims 6f Secondary Ion Mass Spectrometer 137

4.3 SIMS High Resolution Mass Spectrum of F from an Analysis of NIST-610 138

4.4 Ratio of the $^{19}F^-$ Secondary Ion Yields Generated by Both the Cs^+ and O^- Primary Beams for the Glass Standards Used in this Study 139

4.5 The $^{19}F/^{18}O$ Ratios for the Low- and High-silica Glasses Generated from the O^- Primary Beam Versus those Generated from the Cs^+ Primary Beam 140

4.6 SIMS Calibration Curves for the Low- and High-silica Glass Standards Based on the SIMS Cs^+ Primary-beam Method 141-142

4.7 Histograms Showing the F Content of the Olivine Samples from this Study 143-145

4.8 Forsterite Content of the Olivines from Extrusive Suites Versus their F Content 146-147

4.9 Forsterite Content of the Olivine Samples from the Plutonic Suites Versus their F Content 148

4.10 Mg/Fe Ratio of the Olivine Grains from the Kiglapait Layered Intrusion Versus their F Content 149

4.11 The F Content of Olivine Grains from the Kiglapait Layered Intrusion Versus the Percent Solidified (PCS) Within the Intrusion during its Cooling History . 150

5.1 SIMS High Resolution Mass Spectrum of F from an Analysis of NIST-610 202

5.2 Sample MOA-2 Showing SIMS Craters in a Euhedral Cpx Crystal and Adjacent Glass 203

5.3 SIMS F Calibration Curve Generated from the Data in Table 5.4 using the synthetic Fba Glasses, Biotite-3, and a Silica Blank 204

Figure Page

5.4 Range of F Partition Coefficients for the Mineral Phases Cpx, Olivine, and Plagioclase within Melts of Different Chemistries and $D_F^{\min / melt}$ Versus Silica Content 205-206

5.5 Semi-log Plots of OH and F Concentrations in Olivine as a Function of Mole Fraction of Fayalite Content..... 207-208

5.6 $D_F^{Oliv / melt}$ Plotted Against the Magnesium Number (Mg#) of the Olivine Crystals from the Current Study..... 209

5.7 Generalized Model of Enstatite Cut Perpendicular to the C-axis [001]..... 210

5.8 Possible Mechanism for F Replacing Oxygen in the O3 Site where Charge Balance is Maintained by a Coupled Substitutions..... 211-213

5.9 Variation in F Partitioning with Different Pyroxene End-member Compositions..... 214-216

5.10 Ferrosilite Content and Fe/Mg Ratio Versus $D_F^{Cpx / melt}$ 217-218

5.11 Magnesium and Iron Crystal Chemistry of Cpx Phases from EPMA Analysis..... 219

5.12 Plot of Log fO_2 Versus $D_F^{Cpx / melt}$ for the Sample Suites of this Study 220

5.13 Literature Data of $D_H^{Cpx / melt}$ vs. the Al Content of Pyroxenes..... 221-222

5.14 Current Data of $D_F^{Cpx / melt}$ vs. the Al Content of Pyroxenes 223-224

5.15 Variations in Melt Viscosity with D_F, Including Both Cpx and Olivine Samples from this Study 225

5.16 Plots of NBO/T Versus $D_F^{Cpx / melt}$ and $D_F^{Oliv / melt}$ 226-227

PREFACE

“This is geology, not malevolence. These planets live fast and die hard.

The question is, why?” — William T. Riker

CHAPTER 1

INTRODUCTION

1. Motivation

The study of the volatile content (H_2O, CO_2, S, Cl, and F) within the various constituents of igneous systems (e.g. volcanic gas emissions, igneous rocks, minerals, melt inclusions, and glass) expands our understanding of the behavior and effects of volatiles within magmas, including the generation of magmas at subduction zones, mid-ocean ridges, and hotspots, as well as fluid-flux melting, magma rheology, eruption dynamics, and volatile storage in magmas, the crust, and the mantle (e.g. Smith 1981, Smith et al. 1981, London et al. 1988, Micheal 1988, Symonds et al. 1994, Carroll and Webster 1994, Johnson et al. 1994, Watson 1994, Hirschmann et al. 2005, Alletti et al. 2007, Chevychelov et al. 2008, Aiuppa et al. 2009, Dalou et al. 2011). Although the most abundant volatile species include H_2O, CO_2, and SO_2, the role of halogens (F, Cl, Br, I) in geological processes has been undergoing increasing attention over the past decade (for example, a special issue of Chemical Geology was devoted to halogens; Aiuppa et al., 2009) because they can substantially affect the chemical and physical properties of magmas, can be useful geochemical tracers in establishing the constraints on the genesis and fluid evolution of magmatic systems within various tectonic environments, and may constrain the volatile budgets of the lithosphere and lower mantle (Dingwell 1985, Sigvaldason, G.E and Oskarsson, N. 1986, Symonds et al. 1994, Carroll and Webster 1994, Johnson et al. 1994, Watson 1994, Hauri 2002, Straub and Layne 2003, Aiuppa et al. 2009, Köhler et al. 2009).

Fluorine is the most reactive of the halogens, possessing the highest electronegativity of all the elements in general and allowing it to readily ionize and induce ionization, pulling electrons strongly away from its bonded cation creating a dipole moment, (Sawyer and Oppenheimer 2006). Fluorine forms many complexes within fluids

and melt, preferentially bonding with the alkaline earth metals, Al, Na, and Si, as well as metal complexes that play a role in the transport of ore-forming metals, rare earth elements (REE's), and high field strength elements (HFSE's) in volatile-rich systems (Carroll and Webster 1994, Pan and Fleet 1996, Williams-Jones et al. 2000, Tagirov et al. 2002, Köhler et al. 2009, Aiuppa et al. 2009). Fluorine complexes to form the volcanic gas species HF, SiF_4, $SiOF_2$, $ClSiF_3$, AlF_2O (Sawyer and Oppenheimer 2006, Aiuppa 2009), yet fluorine is the last volatile element to be exsolved from ascending magma and does so at pressures much lower than those for carbon, water, sulfur, and chlorine (e.g. S: ~140 MPa, Cl: ~100 MPa, F: <10 MPa) (Spilliaert et al 2006). Fluorine's capacity to form complexes renders fluorine highly soluble in silicate melts compared to other magmatic volatile species, allowing F to behave as an incompatible element through the general retention of F in silicate melts during differentiation and degassing upon magma ascent (Dingwell et al. 1985, Carroll and Webster 1994; Stecher 1998, Mysen et al. 2004, Scaillet and MacDonald 2004, Aiuppa et al. 2009). This implies that the association between fluorine in basalts and fluorine in the mantle source region is more robust than for many other volatile species, and measurements of fluorine in glasses quenched at depth, such as melt inclusions and pillow lavas, may provide important information regarding the pre-eruptive and source-region volatile dynamics at depths where other more insoluble volatile species are lost to degassing (Carroll and Webster 1994, Roggensack et al. 1997).

Compared to oxygen and other halogens, the ionic radius of fluorine is relatively small, and its small ionic radius allows it to fit within the structure of silicate melts and mineral phases. The ionic radius of F^- (1.33 Å, octahedral coordination) is similar to that of OH^- and O^{2-} (1.40 Å) (Shannon 1976), allowing F to substitute for hydroxyl and oxygen in silicate minerals and melt (Stolper 1982, Stecher 1998). Fluorine substitution for hydroxyl routinely occurs in micas, amphiboles, apatites, humite group minerals, and in accessory minerals of the crust such as fluorite and topaz (e.g. Smith 1981, Smith et al.

1981, Robert et al. 1993), and these nominally hydrous minerals are thought to be the main reservoir for storage of fluorine in the Earth's lithosphere. Likewise, fluorine storage in the mantle occurs in nominally-hydrous mantle-derived accessory phases such as primary apatites, amphiboles, and phlogopite (Delaney et al. 1980, Smith 1981, Smith et al. 1981, Matson et al. 1986, O'Reilly and Griffin 2000, Aiuppa et al. 2009), although these fluoridated phases are thermally more stable in much of the convecting mantle than the OH end members. Nevertheless, Straub and Layne (2003) show that within subduction zones fluorine within oceanic lithosphere remains relatively fixed to the subducting slab, a major portion of fluorine returning to the deep mantle, while H and Cl are separated out during decomposition of hydrous phases at lower pressures. Hence, there is an inference that a stable mineralogical repository for fluorine exists under the temperature and pressure conditions of the mantle, and that the F/H ratio should increase within recycled materials.

It has been shown that fluorine is incorporated at trace levels within nominally anhydrous minerals (NAMs) of the upper mantle such as olivine and clinopyroxene (Hervig et al. 1988, Hervig and Bell 2005, Guggino et al. 2007, O'Leary et al. 2010), and the range of F incorporation is similar to that for H_2O on a molar basis. Hoskin (1999) suggests, because clinopyroxene contains a major fraction of the mantle's water budget (Bell and Rossman 1992), that F and OH may substitute within this phase as well as within olivine (Sykes et al. 1994). At pressures and temperatures that approximate the conditions within the transition zone of the mantle, Gasparik (1990, 1993) experimentally created a new hydrous phase with the formula $Mg_{10}Si_3O_{14}(OH,F)_4$ that is stable with stishovite and which he called superfluorous or superhydrous phase B, showing that F and OH can substitute at these pressures and temperatures (Hazen 1997) and implicating olivine and pyroxene as the major mantle fluorine reservoir (Hazen et al 1997, Hoskin 1999).

Few investigations have been conducted to determine the geochemical behavior of fluorine in igneous systems, and quantifying the behavior of fluorine in NAMs has been attempted in only a handful of studies and is not well understood. Reconnaissance studies have been performed to determine the abundance and geochemical significance of fluorine in olivine and clinopyroxene megacrysts from South African kimberlites and olivine phenocrysts from intrusive, extrusive, and hypabyssal suites from various tectonic environments, showing that fluorine fractionates within magmas as an incompatible element and the partitioning of fluorine within these mineral phases may be related to increasing iron content within the minerals (Stecher 1998, Hervig and Bell 2005, Guggino et al. 2007). Bromiley and Kohn (2007) experimentally determined the solubility of fluorine in forsterite using a variety of fluorine molecular species (e.g. MgF_2, CaF_2, NaF), and found that up to 0.45 wt.% fluorine can be incorporated into forsterite from MgF_2, but more work needs to be performed to rule out clinohumite lamellae. A more comprehensive study of fluorine, chlorine, and trace element partitioning between basaltic melt and NAMs, namely olivine, orthopyroxene, clinopyroxene, plagioclase, and garnet, was performed by Dalou et al. (2011) under conditions of 8-25 kbars and 1265-1430°C and found that fluorine partitioning within these phases is globally ordered as $D^{Cpx/melt} > D^{Opx/melt} > D^{Grt/melt} > D^{Ol/melt} > D^{Plag/melt}$.

Microbeam methods, particularly electron probe microanalysis (EPMA) and secondary ion mass spectrometry (SIMS), have proven to be powerful approaches in the investigation and measurement F at the scale and resolution necessary to measure trace amounts of F at both high sensitivity and high spatial resolution in glasses and crystals. However, SIMS is an attractive alternative over EPMA for microanalyses of F because of the much higher sensitivity compared to EPMA. For example, Hauri et al. (2002) analyzed San Carlos olivine, using literature values for baseline volatile concentrations, and were able to report detection limits of < 1 part per million (ppm) for F when counting negative secondary ions and using a Cs^+ primary beam and normal incidence electron

gun for charge balance. These low detection limits were achieved because of the high useful yield of F^- ions when using a Cs^+ primary beam. Guggino et al. (2007), analyzing an aliquot of F-free silica glass as the control blank, were able to measure F concentrations below 1 ppm in olivine crystals from various tectonic suites. The primary beam diameter using SIMS is often tens of microns (as small as 5 microns using a Cs^+ primary source or 10 microns using an O^- primary source), but the area from which secondary ions are detected can be manipulated electronically and with field apertures to be substantially smaller than with EPMA. Because of the ability of SIMS to analyze small areas (a few to tens of microns in diameter), SIMS has chiefly dominated the study of F and other volatiles in trapped melt inclusions, small mineral grains, and high-pressure experimental run products (Hauri 2002, Hervig et al. 2003).

In this study, I used SIMS to determine the Nernst partition coefficients of F between the nominally anhydrous minerals olivine, clinopyroxene, and plagioclase and melts of olivine-minette, augite-minette, basaltic andesite, and latite compositions. The objectives of this study are three-fold: 1) to quantify the partitioning behavior of F in these mineral phases, 2) to compare the partitioning of fluoride with that of hydroxide to assess the chemical controls on these anionic species and 3) to address any geochemical similarities that may exist due to the similarities in the fluoride and hydroxide ionic radii and charge. The mineral and glass samples of this study were selected from previously-published phase equilibria experiments and graciously provided by their respective authors.

A brief summary of each subsequent chapter is provided. Chapters 2-5 were prepared for publication in peer-reviewed journals, and as such, there is overlap in the background material.

2. Summary of Chapters 2-5

The output of SIMS is in counts per second of the ions of interest. To convert the secondary ion intensity to a concentration value, a calibration curve must be constructed from a series of standard glasses for which SIMS measurements of the elements of interest have been performed (Kane 2001, Straub and Layne 2003, Hervig et al. 2003). However, SIMS measurements of crystals and glasses are susceptible to matrix effects, defined as a variation in the ion yield of an element due to its occurrence within different matrixes of distinct major and minor element composition (Deline et al. 1978, Ottolini et al. 2000, 2002). To minimize matrix effects and to increase the accuracy of SIMS analyses, appropriate standards must be used that are closely matrix-matched to the unknown samples undergoing analysis. In Chapters 2 and 3, I attempted to establish a set of microanalytical glass standards of a low-silica basaltic matrix that are appropriately matrix-matched to our unknown samples. In Chapter 2, we used proton-induced gamma-ray emission (PIGE) spectrometry to determine the F concentrations of five natural and synthetic basaltic (BHVO-2G, GSE-1G) and high-silica (NIST-610, NIST-620, UTR-2) glasses. The method of PIGE analysis for F requires the use of a calibration standard of sufficiently high concentrations of F (1000's of ppm) to establish the gamma-ray yield per concentration of F per incident proton. Determination of fluorine concentration *C* in an unknown homogeneous medium requires knowledge of the number of detected gamma rays per incident proton, the reaction cross section as a function of energy, and the areal stopping power of the material being measured. Stopping power is defined as the rate that a charged particle with initial energy, upon penetrating the target, readily loses energy per unit of path length divided by the total target density. Therefore, the calibration standard must have a similar density (i.e. stopping power) as the unknown samples in order to compare the gamma-ray yields among similar volumes of material analyzed (Volume = Beam Spot Size $\times$ Stopping Distance). The calibration standards used in our

study were Durango apatite and Topaz Mountain topaz, both of whose densities were much greater than the glasses analyzed.

In Chapter 3, I embarked on a study to synthesize a set of in-house F standards in a basaltic matrix. A natural tholeiite from the East Pacific Rise was mixed with variable amounts of CaF_2 to create five glasses (termed Fba glasses) with F contents ranging from 0.13 wt.% to 2.24 wt.%. Fluorine concentrations and homogeneity of the Fba glasses were established by both SIMS and EPMA, and these glasses were used to construct a SIMS calibration curve to further determine the F contents of six U.S. Geological Survey basaltic glass standards BCR-2G, BHVO-2G, GSA-1G, GSC-1G, GSD-1G, and GSE-1G, two MPI-DING basaltic glass standards ML3B-G and KL2-G, and the commonly used ALV-519-4.

In Chapter 4, I performed SIMS analysis on a suite of olivine grains from the classic paper by Simkin and Smith (1970). The original Simkin and Smith (1970) olivine grain mounts were analyzed for F on the SIMS. The olivine samples represent a variety of igneous, petrologic, and tectonic environments, reflecting different source rocks, cooling histories, and fractionation trends. The majority of the crystals lacked geologic context. However, samples from the genetically related Hawaiian basalts and andesites and olivine grains from the Kiglapait Layered Intrusion showed that F behaves as an incompatible element and displays robust fractionation trends as a volatile constituent of magmas.

In Chapter 5, I report fluorine partition coefficients for clinopyroxene, olivine, plagioclase, and hornblende within melts of olivine-minette, augite-minette, basaltic andesite, and latite compositions. The samples used were run products from previously-published experiments (see Chapter 5 for references) at *P-T* conditions ranging from 0.607 to 20 kbars and 1,000 to 1,175°C. The partition coefficients of fluorine (D_F) for olivine and clinopyroxene showed variations among the different melt compositions, and possible crystal chemical and melt structural controls on the F partitioning were

investigated. Fluorine mainly substitutes for oxygen, and a number of different coupled substitutions among monovalent and trivalent cations can be charge-balanced by F incorporation. Melt structure was found to have a strong influence on D_F for both clinopyroxene and olivine, and a strong positive correlation emerged between melt polymerization and D_F.

3. References

Aiuppa, A., Baker, D. and Webster, J. (2009) Halogens in volcanic systems. Chemical Geology, 263, 1-18.

Alletti, M., Baker, D.R. and Freda, C. (2007) Halogen diffusion in a basaltic melt. Geochimica et Cosmochimica Acta, 71, 3570-3580.

Bell,D.R. and Rossman, G.R. (1992) Water in Earth's mantle: The role of nominally anhydrous minerals. Science, 255, 1391-1397.

Bromiley, D.W. and Kohn, S.C. (2007) Comparisons between fluoride and hydroxide incorporation in nominally anhydrous and fluorine-free mantle minerals. Goldschmidt conference abstracts.

Carroll, M.R. and Webster, J.D. (1994) Solubilities of sulfur, noble gases, nitrogen, chlorine, and fluorine in magmas. In: Carroll, M.R. and Holloway, J.R. (eds), Volatiles in Magmas. Reviews in Mineralogy Volume 30. Mineralogical Society of America (Washington, D.C.), 231-279.

Chevychelov, V.Y., Botcharnokov, R.E., and Holtz, F. (2008) Partitioning of Cl and F between fluid and hydrous phonolitic melt of Mt. Vesuvius at ~850-1000 C and 200 Mpa. Chemical Geology, doi:10.1016/j.chemgeo.2008.06.025.

Dalou, C., Koga, K.T., Shimizu, N., Boulon, J. and Devidal, J.L. (2011) Experimental determination of F and Cl partitioning between lherzolite and basaltic melt. Contributions to Mineralogy and Petrology, 1-19.

Delaney, J., Smith, J., Carswell, D. and Dawson, J. (1980) Chemistry of micas from kimberlites and xenoliths--II. Primary-and secondary-textured micas from peridotite xenoliths. Geochimica et Cosmochimica Acta, 44, 857-872.

Deline, V., Katz, W., Evans, C. and Williams, P. (1978) Mechanism of the SIMS matrix effect. Applied Physics Letters, 33, 832-835.

Dingwell, D.B. (1985) The structures and properties of fluorine-rich magmas: A review of experimental studies. In: Taylor, R.P. and Strong, D.F. (eds), Recent Advances in the Geology of Granite-Related Mineral Deposits. Canadian Institute of Mining and Metallurgy (Montreal), 1-12.

Dingwell, D.B., Scarfe, C.M., and Cronin, D.J. (1985) The effect of fluorine on viscosities in the system Na_2O-Al_2O_3-SiO_2: implications for phonolites, trachytes, and rhyolites. American Mineralogist, 70, 80-87.

Gasparik, T. (1993) The role of volatiles in the transition zone. Journal of Geophysical Research, 98, 4287-4299.

Gasparik, T. (1990) Phase relations in the transition zone. Journal of Geophysical Research, 5, 15751-15769.

Guggino, S., Hervig, R. and Bell, D. (2007) Fluorine in olivines from plutonic, extrusive, and hypabyssal suites. AGU Fall Meeting Abstract.

Hauri, E., Wang, J., Dixon, J.E., King, P.L., Mandeville, C. and Newman, S. (2002) SIMS analysis of volatiles in silicate glasses 1: Calibration, matrix effects and comparisons with FTIR. Chemical Geology, 183, 99-114.

Hauri, E. (2002) SIMS analysis of volatiles in silicate glasses, 2: Isotopes and abundances in Hawaiian melt inclusions. Chemical Geology, 183, 115-141.

Hazen, R.M., Yang, H., Prewitt, C.T., Gasparik, T. (1997) Crystal chemistry of superfluorous phase B ($Mg_{10}Si_3O_{14}F_4$): Implications for the role of fluorine in the mantle. American Mineralogist, 82, 647-650.

Hervig, R. and Bell, D. (2005) Fluorine and hydrogen in mantle megacrysts. AGU Fall Meeting Abstract.

Hervig, R.L., Mazdab, K., Moore, G., McMillan, P.F. (2003) Analysing hydrogen (H_2O) in silicate glass by secondary ion mass spectrometry and relfectance Fourier transform infrared spectroscopy. In: De Vivo, B. and Bodnar, R.J. (eds), Melt Inclusions in Volcanic Systems: Methods Applications and Problems. Developments in Volcanology 5. Elsevier, 83-103.

Hervig, R.L., Smith, J.V. and Rivers, M.L. (1988) Fluorine content of upper mantle minerals. EOS, Transactions of the American Geophysical Union, 69, 502.

Hirschmann, M.M., Aubaud, C. and Withers, A.C. (2005) Storage capacity of H_2O in nominally anhydrous minerals in the upper mantle. Earth and Planetary Science Letters, 236, 167-181.

Hoskin, P.W.O. (1999) SIMS Determination of μg g^{-1} - level fluorine in geological samples and its concentration in NIST SRM 610. Geostandards Newsletter, 23, 69-76.

Johnson, M.C., Anderson, A.T., and Rutherford, M.J. (1994) Pre-eruptive volatile contents of magmas. In: Carroll, M.R. and Holloway, J.R. (eds), Volatiles in Magmas. Reviews in Mineralogy Volume 30. Mineralogical Society of America (Washington, D.C.), 281-330

Kane, J.S. (2001) The use of Reference Materials: A tutorial. Geostandards Newsletter, 25, 7-22.

Köhler, J., Schönenberger, J., Upton, B. and Markl, G. (2009) Halogen and trace-element chemistry in the Gardar Province, South Greenland: Subduction-related mantle metasomatism and fluid exsolution from alkalic melts. Lithos, 113, 731-747.

London, D., Hervig, R.L. and Morgan, G.B. (1988) Melt-vapor solubilities and elemental partitioning in peraluminous granite-pegmatite systems: Experimental results with Macusani glass at 200 MPa. Contributions to Mineralogy and Petrology, 99, 360-373.

Matson, D.W., Muenow, D.W. and Garcia, M.O. (1986) Volatile contents of phlogopite micas from South African kimberlite. Contributions to Mineralogy and Petrology, 93, 399-408.

Michael, P.J. (1988) The concentration, behavior and storage of H_2O in the suboceanic upper mantle: Implications for mantle metasomatism. Geochimica et Cosmochimica Acta, 52, 555-566.

Mysen, B.O., Cody, G.D. and Smith, A. (2004) Solubility mechanisms of fluorine in peralkaline and meta-aluminous silicate glasses and in melts to magmatic temperatures. Geochimica et Cosmochimica Acta, 68, 2745-2769.

O'Leary, J.A., Gaetani, G.A., Hauri, E.H. (2010) The effect of tetrahedral Al^{3+} on the partitioning of water between clinopyroxene and silicate melt. Earth and Planetary Science Letters, 297, 111-120

O'Reilly, S.Y. and Griffin, W. (2000) Apatite in the mantle: Implications for metasomatic processes and high heat production in Phanerozoic mantle. Lithos, 53, 217-232.

Ottolini, L., Cámara, F., Hawthorne, F.C. and Stirling, J. (2002) SIMS matrix effects in the analysis of light elements in silicate minerals: Comparison with SREF and EMPA data. American Mineralogist, 87, 1477-1485.

Ottolini, L., Cámara, F. and Bigi, S. (2000) An investigation of matrix effects in the analysis of fluorine in humite-group minerals by EMPA, SIMS, and SREF. American Mineralogist, 85, 89-102.

Pan, Y. and Fleet, M.E. (1996) Rare earth element mobility during prograde granulite facies metamorphism: Significance of fluorine. Contributions to Mineralogy and Petrology, 123, 251-262.

Robert, J.L., Bény, J.M., Della Ventura, G. and Hardy, M. (1993) Fluorine in micas: crystal-chemical control of the OH-F distribution between trioctahedral and dioctahedral sites. European Journal of Mineralogy, 5, 7-18.

Roggensack, K., Hervig, R.L., McKnight, S.B. and Williams, S.N. (1997) Explosive basaltic volcanism from Cerro Negro volcano: Influence of volatiles on eruptive style. Science, 277, 1639-1642.

Sawyer, G.M. and Oppenheimer, C. (2006) Volcanic Fluorine Emissions: Observations by Fourier Transform Infrared Spectroscopy. In: Tressaud, A. (eds), Fluorine and the Environment: Atmospheric Chemistry, Emissions, & Lithosphere. Elsevier (San Francisco), 165-185.

Scaillet, B. and Macdonald, R. (2004) Fluorite stability in silicic magmas. Contributions to Mineralogy and Petrology, 147, 319-329.

Shannon, R. (1976) Revised effective ionic radii and systematic studies of interatomic distances in halides and chalcogenides. Acta Crystallographica Section A: Crystal Physics, Diffraction, Theoretical and General Crystallography, 32, 751-767.

Sigvaldason, G.E. and Óskarsson, N. (1986) Fluorine in basalts from Iceland. Contributions to Mineralogy and Petrology, 94, 263-271.

Simkin, T. and Smith, J. (1970) Minor-element distribution in olivine. The Journal of Geology, 304-325.

Smith, J.V. (1981) Halogen and Phosphorous Storage in the Earth. Nature, 289, 762-765.

Smith, J., Delaney, J., Hervig, R. and Dawson, J. (1981) Storage of F and Cl in the upper mantle: Geochemical implications. Lithos, 14, 133-147.

Spilliaert, N., Métrich, N. and Allard, P. (2006) S–Cl–F degassing pattern of water-rich alkali basalt: Modelling and relationship with eruption styles on Mount Etna volcano. Earth and Planetary Science Letters, 248, 772-786.

Stecher, O. (1998) Fluorine geochemistry in volcanic rock series: Examples from Iceland and Jan Mayen. Geochimica et Cosmochimica Acta, 62, 3117-3130.

Stolper, E. (1982) The speciation of water in silicate melts. Geochimica et Cosmochimica Acta, 46, 2609-2620.

Straub, S.M. and Layne, G.D. (2003) The systematics of chlorine, fluorine, and water in Izu arc front volcanic rocks: Implications for volatile recycling in subduction zones. Geochimica et Cosmochimica Acta, 67, 4179-4203.

Sykes, D., Rossman, G.R., Veblen, D.R. and Grew, E.S. (1994) Enhanced H and F incorporation in borian olivine. American Mineralogist, 79, 904-908.

Symonds, R.B., Rose, W.I., Bluth, G.S.J., and Gerlach, T.M. (1994) Volcanic-gas studies: Methods, results, and applications. In: Carroll, M.R. and Holloway, J.R. (eds), Volatiles in Magmas. Reviews in Mineralogy Volume 30. Mineralogical Society of America (Washington, D.C.), 1-66.

Tagirov, B., Schott, J., Harrichourry, J.C. and Salvi, S. (2002) Experimental study of aluminum speciation in fluoride-rich supercritical fluids. Geochimica et Cosmochimica Acta, 66, 2013-2024.

Watson, E.B. (1994) Diffusion in volatile-bearing magmas. In: Carroll, M.R. and Holloway, J.R. (eds), Volatiles in Magmas. Reviews in Mineralogy Volume 30. Mineralogical Society of America (Washington, D.C.), 371-411.

Williams-Jones, A.E., Samson, I.M. and Olivo, G.R. (2000) The genesis of hydrothermal fluorite-REE deposits in the Gallinas Mountains. New Mexico Economic Geology, 95, 327-341.

CHAPTER 2

FLUORINE CONTENT OF THE MICROANALYTICAL GLASS STANDARDS BHVO-2G, GSE-1G, NIST-610, AND UTR-2 USING PROTON-INDUCED GAMMA-RAY EMISSION (PIGE) ANALYSIS

ABSTRACT

Proton-induced gamma-ray emission (PIGE) spectrometry was utilized to measure the fluorine content of five natural and synthetic basaltic and high-silica glasses that are commonly used as geologic microanalytical reference materials. PIGE analysis was conducted using a 1.7 MeV Tandetron Cockroft-Walton, gas-insulated, high frequency tandem accelerator. The nuclear reaction measured was the non-destructive resonant reaction $^{19}F(p,\alpha\gamma)^{16}O$. PIGE analyses for fluorine were calibrated using two well-established mineral standards: a natural fluor-topaz from Topaz Mountain, Utah (20.3 wt.% F) and Durango Apatite, a natural fluor-apatite from Cerro de Mercado, Durango, Mexico (3.53 wt.% F). The calculated fluorine values differ by about 17 % between the two mineral standards, with the fluor-topaz standard underestimating the fluorine content of Durango apatite and the Durango apatite standard overestimating the fluorine content of the Topaz Mountain fluor-topaz. Utilizing the Durango Apatite standard, the average fluorine concentrations of the standard glasses were calculated to be as follows: BHVO-2G (301±22 ppm), GSE-1G (140±8 ppm), NIST 610 (180±8 ppm), UTR-2 (1048±21 ppm). SIMS analyses were conducted on the above reference glasses, and calibration curves were constructed based on the SIMS output ($^{19}F/^{18}O$) and PIGE fluorine analysis. Two calibration curves were observed that showed the occurrence of SIMS matrix effects of about 52 % between the low-silica and high-silica glasses. SIMS calibration factors were calculated for the basaltic and high-silica curves to be 96.6 and 165.6, respectively. SIMS analyses were performed on eight other commonly used microanalytical glass standards of basaltic and high-silica compositions, and based on the above calibration

factors, their fluorine contents are as follows: ALV-519-4-1 (76±8 ppm); BCR-2G (319±32 ppm); GSA-1G (7±1 ppm); GSC-1G (9±1 ppm); GSD-1G (18±2 ppm); ML3B-G (47±5 ppm); KL2-G (81±8 ppm); NIST-620 (23±2 ppm).

1. Introduction

Fluorine is the most abundant halogen in most rocks, and within the past several decades researchers have shown considerable interest concerning the distribution of fluorine within geologic materials. Fluorine research within igneous rocks, minerals, and magmas has demonstrated that F can effect the chemical and physical properties of magmas, can be useful geochemical tracers in establishing the constraints on the genesis and fluid evolution of magmatic systems within various tectonic environments, and may constrain the volatile budgets of the lithosphere and lower mantle (Dingwell 1985, Roelandts et al. 1986, Sigvaldason and Oskarsson 1986, Symonds et al. 1994, Carroll and Webster 1994, Johnson et al. 1994, Watson 1994, Hauri 2002, Straub and Layne 2003, Aiuppa et al. 2009, Köhler et al. 2009). Fluorine is the most reactive of the halogens and has the highest electronegativity of all the elements. Fluorine readily ionizes and induces ionization and can fit within the structure of silicate melts and mineral phases, particularly in hydrous phases such as micas and amphiboles, but also in nominally anhydrous minerals (NAMs) such as olivine and pyroxene (Hervig and Bell 2005, Sawyer and Oppenheimer 2006, Guggino et al. 2007, Aiuppa 2009, O'leary et al. 2010), implicating olivine and pyroxene as the major mantle fluorine reservoir (Hazen et al 1997, Hoskin 1999). Fluorine forms many complexes within fluids and melt, such as with ore-forming elements (Li, Be, Sn, Al, Ca), rare-Earth elements (REEs), high field strength elements (HFSEs) (Pan and Fleet 1996, Williams-Jones et al. 2000, Tagirov et al. 2002, Köhler et al. 2009, Aiuppa et al. 2009), and the volcanic gas species HF, SiF_4, $SiOF_2$, $ClSiF_3$, AlF_2O (Sawyer and Oppenheimer 2006). Fluorine is highly soluble in silicate melts compared to other magmatic volatile species, which results in F exhibiting

the behavior of an incompatible element, remaining in the silicate melt during differentiation and degassing upon magma ascent (Dingwell et al. 1985, Carroll and Webster 1994; Stecher 1998, Mysen et al. 2004, Scaillet and MacDonald 2004, Aiuppa et al. 2009).

Measurements of fluorine in rocks and minerals have historically relied on bulk extraction techniques and wet chemical analysis, such as pyrohydrolysis, ion chromatography, and ion-specific electrode, which requires destruction of the sample and large powder aliquots, eliminating the ability for investigations of F at the micro-scale (e.g. Boyle 1981, Nicholson 1983, Stecher 1998, Wang et al. 2010). Microbeam methods, such as electron probe microanalysis (EPMA), secondary ion mass spectrometry (SIMS), and nuclear reaction methods such as proton-induced gamma-ray emission (PIGE) analysis, are routinely used to measure trace amounts of F at both high sensitivity and high spatial resolution in glasses and crystals, such as trapped melt inclusions, small mineral grains in terrestrial rocks and meteorites, and high-pressure experimental run products (eg. Allen and Clark 1977, Coote and Sparks 1982, Przybylowicz et al. 1986, Mosbah et al. 1991, 1995, Noll et al. 1998, Hauri 2002, Hervig et al. 2003, Noll et al. 2003, Witter and Kuehner (2004). SIMS, however, has become the method of choice for many researchers who study F at the micro-scale. SIMS is capable of measuring F at levels from parts per million (ppm) to several weight percent (wt.%), and SIMS detection limits for F can be as low as <1 ppm when detecting negative secondary ions (Ihinger et al. 1994). The SIMS primary beam diameter is routinely operated in the tens of microns, but it can be manipulated electronically, optically, and with field apertures to sample substantially smaller areas. SIMS also has the ability to reduce background signals when analyzing F and other volatiles by utilizing a high vacuum and by the ability of SIMS to raster the primary ion beam over a small area (e.g. 50 x 50 μm) for a few minutes to eliminate adsorbed surface contamination (Ihinger et al. 1994).

Fluorine measurements with SIMS are strongly sensitive to matrix effects. As a consequence, SIMS is a technique that relies on the use of standards that are appropriately matrix-matched to the unknown samples to be analyzed. However, there are few well-established F concentration values for the glass standards routinely used in microanalytical laboratories, particularly standards of low silica (basaltic) composition. Some workers have attempted to quantify the F content of some microanalytical glass and mineral standards of basaltic, intermediate, and rhyolitic composition to varying degrees of uncertainty (e.g. Smith et al. 1981, Hervig et al. 1989, Hinton, 1995, Hoskin, 1999, Jochum et al, 2005, 2006), but the concentration values for the basaltic reference glasses are unreliable and are annotated as “information values”. There are, however, some microanalytical fluorine standards that are in widespread use that have been characterized for their fluorine content over the years: Durango apatite (3.53 wt.% F; Young et al. 1969); natural fluor-topaz from Topaz Mountain, Utah (20.3 wt.% F; Barton et al. 1982), a few F-rich peralkaline (KE-12 pantellerite; 4000 ppm; Mosbah et al. 1991) and peralkaline (KN-18; comendite; 6400 ppm; Mosbah et al. 1991) glasses; and synthetic silica-rich glasses, namely the National Institute of Standards and Technology (NIST SRM) 600 series (Hinton et al. 1995, 1999; Hoskin, 1999).

Proton-induced gamma-ray emission (PIGE) analysis is a well-established technique for the non-destructive analysis of fluorine within various types of materials (Dobeli et al. 2006). Coote (1992) presents a comprehensive review of PIGE analysis of fluorine and the nuclear reactions that are suitable for the various applications and materials of interest to researchers, including geologic materials. Ever since Bewers and Flack (1969) used PIGE to measure F in the diabase reference powder W1, ion beam analysis of fluorine in geologic materials has developed into a routine procedure. There are two nuclear reactions that are most commonly used on geologic materials. One reaction involves inelastic proton scattering with subsequent γ-ray emission $^{19}F(p,p'\gamma)^{19}F$,

and the other reaction involves proton absorption followed by emission of an alpha particle plus a γ-ray $^{19}F(p,\alpha\gamma)^{16}O$ (Clark et al. 1975).

In this study, we used PIGE analysis to quantify the F contents of the United States Geological Survey (USGS) microanalytical basaltic reference glasses BHVO-2G and GSE-1G, the National Institute of Standards (NIST) microanalytical high-silica reference glass NIST 610, and the natural pantellerite glass UTR-2. The nuclear reaction used in PIGE analysis is the non-destructive resonant reaction $^{19}F(p,\alpha\gamma)^{16}O$. We constructed calibration curves from the PIGE analyses of the above reference glasses to illustrate and quantify the extent of SIMS matrix effects of fluorine for geologic materials of varying matrix chemistries, and we used the calibration curves to determine the fluorine content of eight other microanalytical glass reference materials of basaltic and high-silica compositions.

2. Methods

2.1 Sample Preparation

One of the main advantages of utilizing PIGE spectrometry is the ease and rapidity of sample preparation. When using whole samples, as opposed to making pressed pellets from a 9:1 mixture of sample powder and powder graphite binder (e.g. Clark et al. 1975, Allen and Clark 1977, Roelandts et al. 1985, 1986, Przybylowicz et al. 1986), the preparation requires simply that the surface be polished flat with an area large enough to accommodate the beam size, which in our study was 2 mm^2. The initial stock of the USGS and pantellerite glasses were amorphous in shape, and thick portions of appropriate size for PIGE analysis were chipped off from the original material by hand or with a mini rock saw. The aliquots were then hand polished with 3 micron alumina polishing paper. The NIST glasses were in their original form as flat, polished wafers, and no polishing was required. NIST-620 was rectangular, and NIST-610 was a flattened disc. Nevertheless, a light polishing of the NIST glasses was performed with the 3 micron

alumina paper in an attempt to minimize F contamination from normal handling. All glasses were sonicated in isopropanol and de-ionized water prior to analysis.

2.2 PIGE Analysis

The PIGE experimental procedure employed in this study was performed at the Leroy Eyring Center for Solid State Science at Arizona State University utilizing a 1.7 MV Tandetron Cockroft-Walton, gas-insulated, high frequency tandem accelerator. The nuclear reaction measured was the non-destructive resonant reaction $^{19}F(p,\alpha\gamma)^{16}O$, where a ^{19}F atom in the sample is bombarded and implanted by an incident proton, expelling an alpha particle and a gamma-ray photon, producing a ^{16}O atom. The source of protons consisted of a beam of H ions produced in a duoplasmatron and propelled through a lithium charge-exchange canal containing lithium vapor. The valence electrons of lithium are weakly bound and are efficiently exchanged with colliding positive ions. A portion of the H ions become negatively charged and are separated by a low-energy switching magnet, producing an ion beam with a constant mass/charge ratio. Negative H ions are accelerated to the high-voltage terminus where a gas stripper removes electrons, creating positive ions. These positive ions are then accelerated to ground and selected for H^+ (protons) by the high-energy swiching magnet to bombard the target along the target beamline with a 20-30 nA, 1.5 MeV incident proton beam. The beam spot area was ~2 mm^2. The vacuum inside the sample chamber was maintained at $<10^{-6}$ torr. As the focussed proton beam exited the quadropoles, the number of incident protons (about 10 %) was monitored with a beam chopper located in front of the quadrupoles. The beam chopper counts proton pulses using a charge digitizer, where 1 pulse (count) equals 10^{-11} coulomb (C) and the charge on a proton equals 1.6×10^{-19} C. Samples were counted for an accumulated charge of 1 milli coulomb (mC), noting that small changes in the proton beam intensity does not effect this charge integration (Roelants et al. 1996, Mosbah et al. 1991). The gamma rays were detected using a high-purity 5-inch (12.7 cm) diameter NaI detector (resolution $\Delta E/E$ = 20 % full width half maximum (FWHM)) set at

90° to the ion beam at a distance of 5 cm. All replicate measurements of F on each sample and standard were conducted at the same spot, and the low uncertainties between measurements indicated the absence of F migration during analysis. The energy calibration was made with a ^{60}Co source. Cobalt-60 naturally undergoes beta (β) decay, simultaneously emitting gamma ray lines at two distinctive energies of 1.17 MeV and 1.33 MeV. The ^{60}Co gamma rays were detected on a multichannel analyzer, and the energy spectrum was calibrated to the respective channels (Fig. 2.1). The fluorine gamma-ray intensities of the targets (samples and standards) were determined based on the integrated counts from channels 270 to 360 (4.8 MeV to 6.4 MeV). Background and blank corrections were applied throughout.

2.2.1 Calibration Standards for PIGE Analysis

PIGE analyses for fluorine were calibrated using two well-established mineral standards: a natural fluor-topaz from Topaz Mountain, Utah (F = 20.3 wt.%; Barton et al. 1982) and Durango Apatite, a natural fluor-apatite from Cerro de Mercado, Durango, Mexico (F = 3.53 wt.%; Young et al. 1969). A crystal of Topaz Mountain topaz was selected whose crystal faces were large enough to accommodate the proton beam surface area (~ 2 mm^2). The crystal face was polished with 3 μm alumina polishing paper to remove any surface contaminants. The Durango apatite consisted of a doubly polished thick section, approximately 4 mm^2 in surface area and was also polished with 3 μm alumina polishing paper. Both mineral standards were sonicated in isopropanol and de-ionized water prior to analysis.

2.3 SIMS Analysis

SIMS analysis was performed at Arizona State University (ASU) using the Cameca ims 6f. A primary beam of $^{16}O^-$ ions was obtained from a duoplasmatron at -12.5 kV and focused to a diameter of 20-30 μm on the sample held at -5kV. Using a current of 3.5 nA, negative secondary ion intensities for $^{18}O^-$, $^{19}F^-$, and $^{28}Si^-$ (wide open energy window: 0 ± 60 eV excess kinetic energy) were recorded. The mass spectrometer was

operated at a mass resolving power (MRP) sufficient to separate $^{19}F^-$ from $^{18}OH^-$ (M/ΔM ~2500) (Fig. 2.2). SIMS analysis was conducted on the USGS glasses BHVO-2G, GSA-1G, GSC-1G, GSD-1G, GSE-1G, the NIST glasses NIST-610 and NIST-620, the natural pantellerite UTR-2, and the MP-DING basaltic glass standards ML3B-G and KL2-G. All ion intensities were normalized to that of $^{18}O^-$. Session-to-session precision was monitored by analyzing NIST-610 and UTR-2. Intersession values of $^{19}F/^{18}O$ for NIST-610 ranges from 0.95 to 1.0, and the range for UTR-2 is 6.75 to 6.9.

3. Results and Discussion

3.1 PIGE Basics

The reaction $^{19}F(p,\alpha\gamma)^{16}O$ (Q-value = 8.114 MeV, where the Q value for a reaction is the amount of energy released during that reaction) using the 1375 keV resonance was chosen for its high cross section of 300 millibarns (mb; where 1 barn = 1 x 10^{-24} cm^2), although the reaction results in a large Compton contribution along the low energy portion of the spectra (Mateus et al. 2007) (Note: in nuclear and particle physics, the reaction cross section is a concept used to describe the likelihood of an interaction occurring between particles. When particles in a beam are thrown against a foil made of a certain substance, the cross section is a measure of the hypothetical area around the target particles of the substance (usually its atoms) that represents a surface. If particles from the beam cross this surface, there will be some kind of interaction). The reaction involves proton absorption followed by emission of alpha particles from the groups α_1, α_2, α_3 whose annihilation gamma photons are expelled with three distinct main gamma-ray total-absorption energy peaks (full energy peaks) at 6.13 MeV, 6.92 MeV, and 7.12 MeV, respectively (Dieumegard et al. 1980, Clark et al. 1975, Coote 1992). However, the 6.92 MeV and 7.12 MeV lines are produced from levels in ^{16}O with similar lifetimes (6.8 x 10^{-15} s and 10.6 x 10^{-15} s, respectively), resulting in the two peaks undergoing Doppler broadening to approximately 140 keV (Kenny, 1981). At the energies required for

gamma-ray production from fluorine analysis using the above reaction, the electron/positron pair production phenomenon occurs, which results in six gamma peaks: two full energy peaks at 6.12 MeV and 7.12 MeV; the 6.12 MeV single escape and double escape peaks; and the 7.12 MeV single and double escape peaks where the 7.12 MeV double escape peak overlaps the 6.12 MeV full energy peak (Kenny 1981, Roelandts et al. 1986; Coote 1992, Dobeli et al. 2006). A typical gamma-ray spectrum for fluorine from a proton-irradiated fluor-topaz (20.3 wt.% F; Barton et al. 1982) is depicted in Figure 2.3.

For accurate fluorine analysis, the identification of interfering resonances and gamma-ray background contributions need to be known and corrected. At proton energies less than 3 MeV, no interfering resonances are known for the range of gamma-ray energies characterized for fluorine. The background signal of each measured gamma-ray yield is due primarily to two sources: 1) External sources: Bremsstrahlung from the accelerator and the Compton interaction in the detector of radiation lines produced by natural radioactivity and the interaction of the proton beam with items in its path such as magnets and slits; and 2) major element composition of the target (Coote 1992, Noll et al. 1998, Mateus et al. 2007) Background signals from external sources are determined by analyzing a blank, such as a silicon wafer, whereby sample chemistry is eliminated as a background source. The blank intensities are then subtracted from the intensities of the standards and unknown samples.

Background contributions due the composition of the target involve interfering elements such as Na, Al, Mg, Si, Fe, Cu, Zn, B, and Ta whose low-energy gamma-ray signals are produced via the (p,p'γ) reactions. For example: $^{23}Na(p,p'\gamma)^{23}Na$ (440 keV); $^{25}Mg(p,p'\gamma)^{25}Mg$ (585 keV); $^{27}Al(p,p'\gamma)^{27}Al$ (1014 keV); $^{23}Na(p,p'\gamma)^{23}Na$ (1635 keV) (see Figure 2.4) (Bird and Clayton 1983, Noll et al. 1998). Because of their high yield and common occurrence at percent levels in geologic materials, Na and Al are the most significant contributors to the background signal in the fluorine region (Bird and Clayton

1983, Coote 1992). Background signals from the Si content of the target make only a small contribution in the fluorine region, hence the usefulness of using a silicon wafer as a blank when analyzing samples whose matrix is devoid of the interfering elements listed above. Elements such as Fe, Cu, Zn, B, and Ta are significant only when they are at percent levels in the target. The intensities from these low-energy resonances can be used to estimate the contributions from these elements to the background signal of the higher-energy fluorine integrated intensities. Bird and Clayton (1983) developed a model to calculate background corrections for sample intensities based on the content of the interfering elements in the sample matrix:

$$N_{corr} = N_0 - \sum_i R_i N_{2i} \quad (1)$$

where N_{corr} is the corrected integrated fluorine intensity from the target, N_0 is the initial integrated fluorine intensity from the target, R_i is the ratio between the integrated fluorine intensity from the target and the low-energy interfering peak intensities measured on pure element i or on an appropriate compound, and N_{2i} is the intensity in a low-energy peak which is characteristic of interfering element i.

An alternative method to determine background contributions in the fluorine region from interfering elements is to analyze blanks that are composed of similar matrix chemistries (with respect to the interfering elements) as the samples and standards. The fluorine integrated intensities of the matrix-matched blanks can then be subtracted from the fluorine integrated intensities of the samples and standards. The alternative background correction method is the method we chose for our analyses. The fluorine "blanks" we used are a suite of USGS basaltic glass standards and 1 NIST high-silica glass standard whose fluorine contents are well below the detection limit of PIGE

measurements based on our analytical parameters (GSA-1G : F = 7±1 ppm; GSC-1G: F = 9±1 ppm; GSD-1G: F = 18±1 ppm; NIST-620: F = < 20 ppm; see Chapter 3).

The determination of the fluorine concentration *C* in a homogeneous medium requires knowledge of the number of detected gamma rays per incident proton, N_γ, the reaction cross section as a function of energy, $\sigma(E)$, and the areal stopping power of the material being measured, $S(E)$. The reaction cross-section $\sigma(E)$ is defined as the probability that the incident proton will strike the target element and initiate the intended reaction. Even though the cross-section for the reaction $^{19}F(p,\alpha\gamma)^{16}O$ can be as high as 300 mb, integrating over a gamma-ray energy spectrum may pose severe limits on precision due to complications with escape peaks, tails, and the large Compton Effect that occurs within the low energy region of the spectrum (see Figure 2.4).

The areal stopping power, *S(E)*, is defined as the rate that a charged particle with initial energy E_0, upon penetrating the target, readily loses energy per unit of path length divided by the total target density, ending with a final energy E_f. When the target is thick enough for the particle to come to a complete stop, $E_f = 0$ (Clark et al. 1975). Mosbah et al. (1991) determined that the most reliable and reproducible target thicknesses for fluorine measurements using PIGE are thicknesses greater than 50 μm. The areal stopping power is expressed as

$$S(E) = \frac{1}{\rho_T}\frac{dE}{dx} \tag{2}$$

For complex matrixes such as geologic samples, the stopping power can be derived from summing the elemental stopping powers of their major components:

$$S(E) = \sum_i \; c_i \, S_i(E) \tag{3}$$

where c_i is the elemental concentration in weight percent and $S_i(E)$ is the stopping power of element i (Clark et al. 1975). As described in equations (2) and (3), knowing the major element composition and the density of the target are essential to calculating the stopping power. Table 2.1 lists the major element composition and density of the standards and samples used for PIGE analysis. Major element compositions were obtained from the literature. Density values were experimentally determined in the present study using the wet pycnometer method. Stopping powers were calculated for standards and samples using the software SRIM-2011 (Ziegler 2011).

The above values are related by the following integral:

$$N_\gamma = AC \int_0^{E_f} \frac{\sigma(E)}{S(E)} dE \quad (4)$$

where *A* is a coefficient that represents the solid angle and efficiency of the detector. However, the values of *A*, and *σ(E)* cannot be known to the necessary precision for accurate fluorine concentration calculations, and the calculation of *S*(*E*) may introduce systematic errors, even though the accuracy of calculated stopping powers for protons in the low MeV energy range is approximately 5 %. As a result, the use of well-characterized standards for the calibration of the fluorine yield has become a routine practice.

The expression for the gamma yield with a standard (*St*) is very similar to equation (4).

$$N_{\gamma,St} = AC_{St} \int_0^{E_0} \frac{\sigma(E)}{S_{St}(E)} dE \quad (5)$$

When making use of standards, the major element compositions and densities of the standards and the unknowns should be similar in order to minimize differences in

stopping powers. The total stopping powers for both the standards and the unknowns should be comparable within error limits (Clark et al. 1975, Dobeli et al. 2006). Clark et al. (1975) and Allen and Clark (1977) show that experiments of stopping powers on a wide range of geologic materials reveal that these stopping powers do not generally vary by more than 5%. However, these estimates were based on measurements of whole rock and meteorite powders that had been pressed into pellets using a 10 % graphite binder. The standards used in the present study consist of oriented crystals whose major element compositions and densities differ significantly from the compositions, densities, and amorphic structures of the sample glasses.

It has been shown that a ratio of the average cross section and representative stopping powers (both for standards and unknowns) can replace the integrals in equation (4) and (5) while maintaining sufficient accuracy (Dobeli et al. 2006) to give the following two expressions:

$$N_\gamma = AC\frac{\overline{\sigma}}{\overline{S}} \quad and \quad N_{\gamma,St} = AC_{St}\frac{\overline{\sigma}}{\overline{S}_{St}} \tag{6}$$

which can be re-arranged to give an expression for the fluorine concentration, *C*, of an unknown sample:

$$C = C_{St}\frac{N_\gamma}{N_{\gamma,St}}\frac{\overline{S}}{\overline{S}_{St}}\frac{Q_{St}}{Q} \tag{7}$$

In equation (7), Q and Q_{St} represent the integrated beam currents supplied to the sample and the standard material. In our experiments, all samples and standards were measured under identical conditions, making this ratio unity (Bird and Clayton 1983, Mosbah et al. 1991, Dobeli et al, 2006, Salah and Arab 2007). The expression for stopping power in

Equation (7) is a ratio of the stopping power of the sample ($\overline{S}$) divided by the stopping power of the standard ($\overline{S}_{St}$), canceling out most systematic errors that may have been introduced during analysis (Dobeli et al. 2006). As stated above, the stopping powers for both the standards and the unknown samples should ideally be similar in order to bring the expression as close to unity as possible.

The lower limit of detection with PIGE depends on a number of factors, including the proton energy, the efficiency of the gamma-ray detector, and the degree of background interference from major and minor elements (Coote et al. 1982). In practice, the detection limit is defined as three times the counting error of the background intensity, or $3\sqrt{N_{bkgd}}$, where *N* represents the integrated counts as pulses measured in the background (e.g. Roelandts et al. 1986, Roelandts et al. 1987, Noll et al. 2003). The fluorine detection limit was calculated based on the average gamma-ray integrated counts from GSA-1G, GSC-1G, GSD-1G, and NIST-620 and was calculated to be 30±2 ppm.

3.2 PIGE Results

Table 2.2 lists the results of the PIGE analyses for fluorine, including the raw and background-corrected gamma-ray counts for each standard, sample, and blank. Table 2.2 also lists the stopping powers and projected range (distance the protons penetrated into a thick sample until they come to a complete stop, $E_f = 0$) for each target as calculated from the SRIM-2011 program. Hence, the greater the stopping power, the smaller the projected range. Given the size of the proton beam as it strikes the target (2 mm^2 in our study) and the range of the proton beam into the target, the active volume of material analyzed can be calculated (see Table 2.2). The sensitivity of the gamma-ray yield, the detection limits, and the amount of sample-induced background depends on the stopping cross sections, and hence the volume of material sampled (Mateus et al. 2007). When utilizing standards for PIGE analysis, it is important that the analytical conditions for the standards, samples, and blanks be identical, including the active volume of

material being analyzed (Clark et al. 1975, Allen and Clark 1977). The stopping powers and active volumes for the glass samples and blanks are similar (about 5 % variation). However, the stopping powers and active volumes between the two mineral standards differ by about 11 % and 9 %, respectively. Comparisons between each standard and the samples show that both the stopping powers and the active volumes between F-topaz and the samples differ by about 30 % and between Durango apatite and the samples differ by about 20 %. These discrepancies can significantly affect the accuracy of the calculated fluorine concentration of the samples. The major element compositions and the densities between the standards and glasses were significantly dissimilar, and consequently the active volume of material sampled from each target was not equal, which may explain qualitatively the disparity in the fluorine values between the two standards.

After background and blank corrections, the fluorine concentrations for both the mineral standards and the basaltic and high-silica glasses were calculated using equation (7) (Table 2.2). Four sets of fluorine values for the targets were obtained using both the F-topaz and Durango apatite standards: two sets using the calculated stopping powers from the SRIM-2011 program and two sets assigning the stopping powers to be unity. When using the calculated stopping powers, the fluorine concentrations for all targets differ by about 17 % between the two mineral standards. Between the mineral standards themselves, the F-topaz standard demonstrably underestimates the fluorine content of Durango apatite and the Durango apatite standard overestimates the fluorine content of the F-topaz. The disparity in the fluorine concentrations between the fluor-topaz and fluor-apatite standards is expected due to their differences in stopping powers and active volumes (see equation 7). When the stopping powers of the samples and the standards are at or near unity, equation (7) becomes a function solely of the corrected gamma-ray counts:

$$C = C_{St} \frac{N_{\gamma}}{N_{\gamma,St}} \tag{8}$$

and it can be assumed that the corrected gamma-ray counts from equation (8) were obtained from similar volumes of sampled material. However, a higher $\overline{S}_{St}$ in equation (7) means the value of the stopping expression is less than 1, and the active volume of the standard is smaller relative to the unknown sample. The smaller active volume keeps the relative counts of $N_{\gamma,St}$ lower than they would be if the sample-standard active volumes were the same. As a result, the overall value of equation (7) is lowered and the fluorine concentration of the sample is underestimated. The above model can be tested by analyzing samples of well characterized and similar fluorine concentrations but with a range of stopping powers.

To test the effect of stopping power, we calculated fluorine concentrations on the mineral standards and sample glasses assuming the stopping powers are unity (Table 2.2). The precision between the fluorine values generated from the two mineral standards increased greatly (percent difference = 6 %), suggesting that precision can be increased and fluorine values deemed more reliable when the stopping powers between the standards and samples are similar. However, this test is complicated by the fact that assuming identical stopping powers implies identical active volumes of material analyzed from each target. As such, the raw gamma-ray counts for all targets, including blanks, would necessarily be different from what is currently reported in Table 2.2. In the present study, the stopping powers of both mineral standards are larger than those of the samples and blanks. From inspection of equation (7), to bring the stopping expression toward unity $\overline{S}_{St}$ must decrease, which would necessitate an increase of $N_{\gamma,St}$ due to the increased in the active volume that would be sampled. Equation (7) is empirical, and we have no way of estimating what those new raw counts would be.

The set of fluorine values generated from the Durango apatite standard (Table 2.2, column 4) was deemed most reliable, and these fluorine values were compared with the literature (Table 2.2). The USGS basalt glass GSE-1G has no reference for fluorine in the literature, however we compare its fluorine content from PIGE with its fluorine content from Chapter 3 of this work. PIGE analysis determined the fluorine content of GSE-1G to be 140±8 ppm, and in Chapter 3 the fluorine content determined by SIMS is 153±5 ppm, within error of each other. The USGS basaltic glass BHVO-2G was synthesized from kilogram aliquots of the USGS reference powder BVHO-2 (Basalt Hawaiian Volcano Observatory) at 1540°C under a nitrogen atmosphere (Jochum et al. 2005). No previous analysis for fluorine had been performed on BHVO-2G glass, so we compared the PIGE fluorine content of the glass with literature fluorine values of BHVO-2 powder and with the fluorine content of the glass from Chapter 3 of this work. BHVO-2G was measured by PIGE to have an average fluorine content of 301±22 ppm, 19 % lower than the lowest powder fluorine value of BHVO-2 powder (370 ppm) and 23 % lower than the average powder fluorine value (390 ppm). Because BHVO-2 powder was not fused in sealed capsules, loss of fluorine and other volatile components is expected. The fluorine content of BHVO-2G from SIMS measurements in Chapter 3 was determined to be 295±14 ppm, also within error of the PIGE value. The high-silica, soda-lime glass NIST-610 was measured by PIGE to have an average fluorine concentration of 180±8 ppm. NIST-610 has been analyzed for fluorine extensively in the literature and it has been shown that individual wafers of NIST-610 contain variable concentrations of fluorine. The nominal fluorine concentration of NIST-610 from the National Institute of Standards and Technology (NIST) is ~500 ppm. Straub and Layne (2003) measured fluorine in NIST-610 using SIMS and a calibration curve, and they calculated a fluorine concentration of 611±101 ppm. Hoskin (1999) used SIMS to measure fluorine in NIST-610 and determined an average fluorine content of 295±16 ppm. Wang et al. (2010), using pyrohydrolysis, measured fluorine in NIST-610 to be 205±6 ppm. The natural pantellerite

glass UTR-2 was analyzed for fluorine by John Stix of McGill University (unpublished data) using ion electrode, ion chromatography, and EPMA, and determined an average fluorine content of 1143±110 ppm. Our PIGE analysis for fluorine of UTR-2 showed it to have an average fluorine concentration of 1048±21 ppm, well within error of previous analyses.

3.3 SIMS Analysis

SIMS analyses were conducted on the basaltic glass ALV-519-4, the USGS basaltic glasses BHVO-2G, BCR-2G, GSA-1G, GSC-1G, GSD-1G, and GSE-1G, The MPI-DING basaltic glasses ML3B-G and KL2-G, and the high silica glasses NIST-610, NIST-620, and UTR-2. The output from SIMS analysis is in counts/second (cps), and the cps of the elemental species of interest is typically normalized to the cps of some ubiquitous isotope within the sample matrix to obtain an elemental ratio; in our case, ^{19}F is normalized to ^{18}O. We chose ^{18}O because 1) the variation in the oxygen contents of the samples is small (the vast majority of silicates contain 62±5 mol % oxygen), and 2) matrix dependence of the $^{18}O^-$ ion yield is also small. Because there are no matrix-correction models for SIMS analysis, elemental concentration values require appropriate matrix-matched standards to build a calibration curve to convert the elemental ratios into a concentration value. SIMS analysis of volatile elements, fluorine in our case, must overcome the influence of matrix effects on the SIMS ion yield. The SIMS matrix effect is characterized as the variation in ion yield of a given element within different matrixes of distinct major and minor element composition, and is a complex function not only of the chemical composition of the matrix, but also crystal structure and the orientation of the matrix to the incident primary ion beam (Deline et al. 1978, Ottolini et al. 2000, 2002). So far, there is no theory of matrix-effect corrections applicable for SIMS analysis. To minimize matrix effects and to increase the accuracy of SIMS analyses, appropriate standards must be used that are closely matrix-matched to the unknown samples undergoing analysis. To convert the secondary ion intensity to a concentration value, a

calibration curve must be constructed from a series of SIMS measurements of the elements of interest from as many matrix-matched standard glasses as possible (Kane 2001, Straub and Layne 2003, Hervig et al. 2003).

SIMS calibration curves were constructed using the basaltic and high-silica glasses analyzed for fluorine by PIGE in the present study. Table 2.3 lists the SIMS $^{19}F/^{18}O$ ion ratios and the fluorine content from PIGE analysis for BHVO-2G, GSE-1G, NIST-610, UTR-2, and a silica blank. Figure 2.3 shows a plot of the SIMS output ($^{19}F/^{18}O$) for the basaltic glasses (BHVO-2G and GSE-1G) and the high-silica glasses (NIST-610, UTR-2, and a silica blank) versus their fluorine concentration values based on our PIGE analysis. Two distinct regression lines can be drawn, one through the basaltic glasses and one through the high-silica glasses, and forced through the origin. The regression lines combine samples with similar matrix composition and demonstrate the effect of matrix composition on the accuracy of calibrations. Curve 1 connects the two basaltic glasses to the origin and shows R^2 = 0.995±3 % RSD. Curve 2 connects the high-silica glasses to the origin and shows R^2 = 0.999±3 % RSD. In Figure 2.3, each calibration curve generates a calibration factor (CF) which allows a fluorine concentration value to be determined by SIMS on an unknown sample with a matrix chemistry matching that of the standards composing the calibration curve. Because our calibration lines are forced through the origin, the CF is simply the reciprocal of the slope. The CF is then multiplied by the SIMS output ($^{19}F/^{18}O$) of the unknown sample to get the fluorine concentration of the unknown sample. The CF for Curve 1 is 96.6±10 % RSD, and for Curve 2 the CF is 165.6±9 % RSD. The two CFs are different by about 52 %, demonstrating that with SIMS analysis significant errors in fluorine concentrations can occur if the standards and unknowns do not share similar matrix chemistries.

Table 2.4 shows the SIMS results and the calculated fluorine concentration for the basaltic glasses ALV-519-4, GSA-1G, GSC-1G, GSD-1G, ML3B-G, KL2-G, and the high-silica glass NIST-620. Fluorine concentration values were calculated using both

Curves 1 and Curves 2 from Figure 3 above to demonstrate the differences in calculated fluorine concentrations due to matrix effects. Compared to literature values, the fluorine values calculated from Curve 2 overestimate the amount of fluorine in the glasses compared to the fluorine values calculated from Curve 1. The natural basaltic glass ALV-519-4 shows a range of literature values for fluorine, from a high of 113 ppm F to a low of 90 ppm. For ALV-519-4, Curve 2 gives a fluorine value of 130 ppm, 14 % higher than the highest literature value, whereas Curve 1 gives a fluorine value of 76 ppm, 17 % lower than the lowest literature value. The literature value for fluorine in BCR-2G has not been previously analyzed, but the fluorine content of BCR-2 powder has been extensively studied, and it has been shown to be about 448 ppm (Michel and Villemant 2003). The fluorine content of BCR-2G is expected to be lower than the fluorine content of BCR-2 powder due to its creation in an open system with a nitrogen atmosphere. Curve 2 depicts the fluorine content of BCR-2G as being 548±49 ppm, about 20 % *higher* than that measured in the powder, which would be unlikely due to the volatilization of F at fusion temperatures. Curve 1 shows the fluorine content of BCR-2G to be 319±32 ppm, about 34 % lower than the fluorine content of the powder. The MPI-DING basaltic glasses ML3B-G and KL2-G had been analyzed for fluorine in the study by Jochum et al. (2006). However, the fluorine values are unreliable because they were obtained by SIMS with only one analysis for each glass, and the authors labeled the fluorine content as “information value”. Both Curves 1 and 2 show fluorine values for the MPI-DING glasses significantly lower than the information values from Jochum et al. (2006). The USGS glasses GSA-1G, GSC-1G, and GSD-1G and the high-silica glass NIST-620 have not been previously analyzed for fluorine, and we show their fluorine contents are low, ranging from 7 to 20 ppm. .

4. Conclusions

Proton induced gamma-ray emission spectroscopy is a common method to measure fluorine in geologic materials, and we utilized this method to measure fluorine content of four natural and synthetic basaltic and high-silica glasses commonly used as geologic microanalytical reference materials. PIGE analyses for fluorine were calibrated using two different mineral standards: a natural fluor-topaz from Topaz Mountain, Utah (20.3 wt.% F) and Durango Apatite, a natural fluor-apatite from Cerro de Mercado, Durango, Mexico (3.53 wt.% F). The results obtained from the two different mineral standards were compared. Our results indicate that using two different calibration standards yielded results on the unknowns that differ by 17 %, with the fluor-topaz standard underestimating the fluorine content of Durango apatite and the Durango apatite standard overestimating the fluorine content of the Topaz Mountain fluor-topaz. The discrepancy of the F values between the calibration standards can be attributed to the difference in stopping powers of the materials being analyzed. A caveat for using PIGE is that the major element compositions and densities of the calibration standards and the unknowns must be similar within one standard deviation to ensure similar stopping powers. The average fluorine contents (± 1 σ) of the analyzed glasses based on PIGE analysis from both calibration standards are as follows: BHVO-2G (301±22 ppm), GSE-1G (140±8 ppm), NIST-610 (180±8 ppm), and UTR-2 (1048±21 ppm), and these values compare within error to their respective fluorine values from the literature.

SIMS analysis was conducted on the above reference glasses, and calibration curves were constructed based on the SIMS output ($^{19}F/^{18}O$) and PIGE fluorine concentration values. Two calibration curves were observed, one connecting the basaltic glasses to the origin and the other connecting the high-silica glasses to the origin. The two calibration curves show that matrix effects occur for fluorine within SIMS analysis with a difference in slopes of the curves of about 52 %. Calibration factors were calculated for the basaltic and high-silica curves, and they were determined to be 96.6

and 165.6, respectively. SIMS analysis was performed on nine other commonly used microanalytical glass standards, and the appropriate calibration factor was used to calculate their fluorine content based on sample matrix chemistry: ALV 519-4 (76±8 ppm F); BCR-2G (319±32 ppm F); GSA-1G (7±1 ppm F); GSC-1G (9±1 ppm F); GSD-1G (18±2 ppm F); ML3B-G (47±5 ppm F); KL2-G (81±8 ppm F); and NIST-620 (23±2 ppm F).

5. References

Aiuppa, A., Baker, D. and Webster, J. (2009) Halogens in volcanic systems. Chemical Geology, 263, 1-18.

Allen, R.O. and Clark, P.J. (1977) Fluorine in meteorites. Geochimica et Cosmochimica Acta, 41, 581-585.

Barton, M., Haselton, H., Hemingway, B., Kleppa, O. and Robie, R. (1982) The thermodynamic properties of fluor-topaz. American Mineralogist, 67, 350-355.

Bewers, J.M. and Flack, F.C. (1969) Determination of fluorine by prompt γ-radiation from proton bombardment. Analyst, 94, 7-14.

Bird, J.R. and Clayton, E. (1983) The PIGME method for fluorine determination. In: Lanford W.A., Tsong I.S.T. and Williams P. (eds), Proceedings of the Sixth International Conference on Ion Beam Analysis, Nuclear Instruments and Methods in Physics Research, Ion Beam Analysis 6, 525-528.

Boyle, D. (1981) The analysis of fluorine in geochemical exploration. Journal of Geochemical Exploration, 14, 175-197.

Carroll, M.R. and Webster, J.D. (1994) Solubilities of sulfur, noble gases, nitrogen, chlorine, and fluorine in magmas. In: Carroll, M.R. and Holloway, J.R. (eds), Volatiles in Magmas. Reviews in Mineralogy Volume 30. Mineralogical Society of America (Washington, D.C.), 231-279.

Clark, P.J., Neal, G.F. and Allen, R.O. (1975) Quantitative multi-element analysis using high energy particle bombardment. Analytical Chemistry, 47, 650-658.

Coote, G. (1992) Ion beam analysis of fluorine: Its principles and applications. Nuclear Instruments and Methods in Physics Research Section B: Beam Interactions with Materials and Atoms, 66, 191-204.

Coote, G., Sparks, R. and Blattner, P. (1982) Nuclear microprobe measurement of fluorine concentration profiles, with application in archaeology and geology. Nuclear Instruments and Methods in Physics Research, 197, 213-221.

Deline, V., Katz, W., Evans, C. and Williams, P. (1978) Mechanism of the SIMS matrix effect. Applied Physics Letters, 33, 832-835.

Dieumegard, D., Maurel, B., Amsel, G. (1980) Microanalysis of fluorine by nuclear reactions 1: $^{19}F(p,\alpha)^{16}O$ and $^{19}F(p,\alpha\gamma)^{16}O$ reactions. Nuclear Instruments and Methods, 168, 93-103.

Dingwell, D.B. (1985) The structures and properties of fluorine-rich magmas: A review of experimental studies. In: Taylor, R.P. and Strong, D.F. (eds), Recent Advances in the Geology of Granite-Related Mineral Deposits. Canadian Institute of Mining and Metallurgy (Montreal), 1-12.

Dingwell, D.B., Scarfe, C.M. and Cronin, D.J. (1985) The effect of fluorine on viscosities in the system Na_2O-Al_2O_3-SiO_2: implications for phonolites, trachytes and rhyolites. American Mineralogist, 70, 80-87.

Döbeli, M., Gaschen, A.A.M. and Krähenbühl, U. (2006) Fluorine analysis by ion beam techniques for dating applications. Advances in Fluorine Science, 2, 215-252.

Guggino, S., Hervig, R. and Bell, D. (2007) Fluorine in olivines from plutonic, extrusive, and hypabyssal suites. Abstract. AGU Fall Meeting.

Hazen, R.M., Yang, H., Prewitt, C.T., Gasparik, T. (1997) Crystal chemistry of superfluorous phase B ($Mg_{10}Si_3O_{14}F_4$): Implications for the role of fluorine in the mantle. American Mineralogist, 82, 647-650.

Hauri, E. (2002) SIMS analysis of volatiles in silicate glasses, 2: Isotopes and abundances in Hawaiian melt inclusions. Chemical Geology, 183, 115-141.

Hervig, R. and Bell, D. (2005) Fluorine and hydrogen in mantle megacrysts. Abstract. AGU Fall Meeting.

Hervig, R.L., Mazdab, F.K., Moore, G. and McMillan, P.F. (2003) Analyzing hydrogen (H_2O) in silicate glass by secondary ion mass spectrometry and reflectance Fourier transform infrared spectroscopy. Developments in Volcanology, 5, 83-103.

Hervig, R.L., Dunbar, N., Westrich, H.R. and Kyle, P.R. (1989) Pre-eruptive water content of rhyolitic magmas as determined by ion microprobe analyses of melt inclusions in phenocrysts. Journal of Volcanology and Geothermal Research, 36, 293-302.

Hinton, R., Harte, B. and Witt-Eickschen, G. (1995) Ion probe measurements of National Institute of Standards and Technology standard reference material SRM 610 glass, trace elements. Analyst, 120, 1315-1319.

Hinton, R.W. (1999) NIST SRM 610, 611 and SRM 612, 613 Multi - element glasses: Constraints from element abundance ratios measured by microprobe techniques. Geostandards Newsletter, 23, 197-207.

Hoskin, P.W.O. (1999) SIMS Determination of μg g^{-1} - level fluorine in geological samples and its concentration in NIST SRM 610. Geostandards Newsletter, 23, 69-76.

Ihinger, P.D., Hervig, R.L., McMillan, P.F. (1994) Analytical methods for volatiles in glasses. In: Carroll, M.R. and Holloway, J.R. (eds), Volatiles in Magmas. Reviews in Mineralogy Volume 30. Mineralogical Society of America (Washington, D.C.), 67-121.

Jochum, K.P., Weis, U., Stoll, B., Kuzmin, D., Yang, Q., Raczek, I., Jacob, D.E., Stracke, A., Birbaum, K. and Frick, D.A. (2011) Determination of reference values for NIST SRM 610–617 glasses following ISO guidelines. Geostandards and Geoanalytical Research.

Jochum, K.P.,et al. (2006) MPI-DING reference glasses for in situ microanalysis: New reference values for element concentrations and isotope ratios. Geochemistry, Geophysics, Geosystems, Technical Brief, 7, 44 p.

Jochum, K.P., Willbold, M., Raczek, I., Stoll, B., Herwig, K. (2005) Chemical Characterization of the USGS Reference Glasses GSA-1G, GSC-1G, GSD-1G, GSE-1G, BCR-2G, BHVO-2G and BIR-1G Using EPMA, ID-TIMS, ID-ICP-MS, and LA-ICP-MS. Geostandards and Geoanalytical Research, 29, 285-302.

Johnson, M.C., Anderson, A.T., and Rutherford, M.J. (1994) Pre-eruptive volatile contents of magmas. In: Carroll, M.R. and Holloway, J.R. (eds), Volatiles in Magmas. Reviews in Mineralogy Volume 30. Mineralogical Society of America (Washington, D.C.), 281-330.

Kane, J.S. (2001) The use of reference materials: A tutorial. Geostandards Newsletter, 25, 7-22.

Kenny, M. (1981) Thick target gamma yields from fluorine. Australian Journal of Physics, 34, 35-41

Köhler, J., Schönenberger, J., Upton, B. and Markl, G. (2009) Halogen and trace-element chemistry in the Gardar Province, South Greenland: Subduction-related mantle metasomatism and fluid exsolution from alkalic melts. Lithos, 113, 731-747.

Lange, R.A. (1994) The effect of H_2O, CO_2 and F on the density and viscosity of silicate melts. In: Carroll, M.R. and Holloway, J.R. (eds), Volatiles in Magmas. Reviews in Mineralogy Volume 30. Mineralogical Society of America (Washington, D.C.), 331-369.

Mateus, R., Jesus, A., Fonseca, M., Luís, H. and Ribeiro, J. (2007) The sensitivity of the PIGE analytical technique. Nuclear Instruments and Methods in Physics Research Section B: Beam Interactions with Materials and Atoms, 264, 340-344.

Michel, A. and Villemant, B. (2003) Determination of halogens (F, Cl, Br, I), sulfur and water in seventeen geological reference materials. Geostandards Newsletter, 27, 163-171.

Mosbah, M., Clocchiatti, R., Métrich, N., Piccot, D., Rio, S. and Tirira, J. (1995) The characterization of glass inclusions through nuclear microprobe. Nuclear Instruments and Methods in Physics Research Section B: Beam Interactions with Materials and Atoms, 104, 271-275.

Mosbah, M., Metrich, N. and Massiot, P. (1991) PIGME fluorine determination using a nuclear microprobe with application to glass inclusions. Nuclear Instruments and Methods in Physics Research Section B: Beam Interactions with Materials and Atoms, 58, 227-231.

Mysen, B.O., Cody, G.D. and Smith, A. (2004) Solubility mechanisms of fluorine in peralkaline and meta-aluminous silicate glasses and in melts to magmatic temperatures. Geochimica et Cosmochimica Acta, 68, 2745-2769.

Nicholson, K. (1983) Fluorine determination in geochemistry: Errors in the electrode method of analysis. Chemical Geology, 38, 1-22.

Noll K., Döbeli M., Krähenbühl U., Grambole D., Herrmann F. and Koeberl C. (2003) Detection of terrestrial fluorine by proton induced gamma emission (PIGE): A rapid quantification for Antarctic meteorites. Meteoritics & Planetary Science, 38, 759-765.

Noll K., Döbeli M. and Krähenbühl U. (1998) Fluorine profiles in Antarctic meteorites by nuclear reaction analysis (NRA). Fresenius' Journal of Analytical Chemistry, 361, 713-715.

O'Leary, J.A., Gaetani, G.A. and Hauri, E.H. (2010) The effect of tetrahedral Al^{3+} on the partitioning of water between clinopyroxene and silicate melt. Earth and Planetary Science Letters, 297, 111-120.

Ottolini, L., Cámara, F., Hawthorne, F.C. and Stirling, J. (2002) SIMS matrix effects in the analysis of light elements in silicate minerals: Comparison with SREF and EMPA data. American Mineralogist, 87, 1477-1485.

Ottolini, L., Cámara, F. and Bigi, S. (2000) An investigation of matrix effects in the analysis of fluorine in humite-group minerals by EMPA, SIMS, and SREF. American Mineralogist, 85, 89-102.

Pan, Y. and Fleet, M.E. (1996) Rare earth element mobility during prograde granulite facies metamorphism: significance of fluorine. Contributions to Mineralogy and Petrology, 123, 251-262.

Przybyłowicz, W., Szymczyk, S. and Kajfosz, J. (1986) Fluorine analysis in serpentinite rocks by proton induced gamma-ray emission. Nuclear Instruments and Methods in Physics Research Section B: Beam Interactions with Materials and Atoms, 15, 573-575.

Roelandts, I., Robaye, G., Weber, G. and Delbrouck-Habaru, J. (1986) The application of proton-induced gamma-ray emission (PIGE) analysis to the rapid determination of fluorine in geological materials. Chemical Geology, 54, 35-42.

Roelandts, I., Robaye, G., Weber, G. and Delbrouck, J.M. (1985) Determination of fluorine in eighty international geochemical reference samples by proton induced gamma ray emission spectrometry (PIGE). Geostandards Newsletter, 9, 191-192.

Salah, H. and Arab, N. (2007) Application of PIGE to determine fluorine concentration in human teeth: Contribution to fluorosis study. Journal of Nuclear and Radiochemical Sciences, 8, 31-34.

Sawyer, G.M. and Oppenheimer, C. (2006) Volcanic fluorine emissions: Observations by Fourier transform infrared spectroscopy. In: Tressaud, A. (eds), Fluorine and the Environment: Atmospheric Chemistry, Emissions, & Lithosphere. Elsevier (San Francisco), 165-185.

Scaillet, B. and Macdonald, R. (2004) Fluorite stability in silicic magmas. Contributions to Mineralogy and Petrology, 147, 319-329.

Sigvaldason, G.E. and Óskarsson, N. (1986) Fluorine in basalts from Iceland. Contributions to Mineralogy and Petrology, 94, 263-271.

Smith, J., Delaney, J., Hervig, R. and Dawson, J. (1981) Storage of F and Cl in the upper mantle: Geochemical implications. Lithos, 14, 133-147.

Stecher, O. (1998) Fluorine geochemistry in volcanic rock series: Examples from Iceland and Jan Mayen. Geochimica et Cosmochimica Acta, 62, 3117-3130.

Straub, S.M. and Layne, G.D. (2003) The systematics of chlorine, fluorine, and water in Izu arc front volcanic rocks: Implications for volatile recycling in subduction zones. Geochimica et Cosmochimica Acta, 67, 4179-4203.

Symonds, R.B., Rose, W.I., Bluth, G.S.J., and Gerlach, T.M. (1994) Volcanic-gas studies: Methods, results, and applications. In: Carroll, M.R. and Holloway, J.R. (eds), Volatiles in Magmas. Reviews in Mineralogy Volume 30. Mineralogical Society of America (Washington, D.C.), 1-66..

Tagirov, B., Schott, J., Harrichourry, and J.C., Salvi, S. (2002) Experimental study of aluminum speciation in fluoride-rich supercritical fluids. Geochimica et Cosmochimica Acta, 66, 2013-2024.

Wang, Q., Makishima, A. and Nakamura, E. (2010) Determination of fluorine and chlorine by pyrohydrolysis and ion chromatography: Comparison with alkaline fusion digestion and ion chromatography. Geostandards and Geoanalytical Research, 34, 175-183.

Watson, E.B. (1994) Diffusion in volatile-bearing magmas. In: Carroll, M.R. and Holloway, J.R. (eds), Volatiles in Magmas. Reviews in Mineralogy Volume 30. Mineralogical Society of America (Washington, D.C.), 371-411.

Williams-Jones, A.E., Samson ,I.M. and Olivo, G.R. (2000) The genesis of hydrothermal fluorite-REE deposits in the Gallinas Mountains, New Mexico. Economic Geology, 95, 327-341.

Witter, J.B. and Kuehner, S.M. (2004) A simple empirical method for high-quality electron microprobe analysis of fluorine at trace levels in Fe-bearing minerals and glasses. American Mineralogist, 89, 57-63.

Young, E., Myers, A., Munson, E. and Conklin, N. (1969) Mineralogy and geochemistry of fluorapatite from Cerro de Mercado, Durango, Mexico. US .Geological Survey Professional Paper, 650, D84-D93.

Zeigler, J. (2011) http://www.srim.org/.

6. Figure Captions

Figure 2.1. Gamma-ray energy spectrum for ^{60}Co. The two distinctive energy lines at 1.17 MeV and 1.33 MeV are used to calibrate the gamma-ray energy values for the channels on the spectrum. Also shown is the Compton Plateau and Compton Edge which denote the energy distribution of the Compton scattering phenomenon in which gamma-rays of lower partial energies are produced when incident gamma rays enter the NaI crystal and collide with "free" electrons, imparting a portion of their energy to the electron.

Figure 2.2. SIMS high-resolution mass spectrum of NIST-610. Notice the separation between the ^{19}F and ^{18}OH peaks. Mass resolving power is 2500.

Figure 2.3. PIGE energy spectrum of natural fluor-topaz, Topaz Mountain, Utah (20.3 wt.% F). *a* = 6.12 MeV double escape peak. *b* = 6.12 single escape peak. *c* = 6.12 MeV total absorption peak (full energy peak). *d* = 7.12 MeV single escape peak. *e* = 7.12 MeV total absorption peak. The 6.13 Mev peaks (*a*, *b*, *c*) were preferred for integration for fluorine analysis.

Figure 2.4. Gamma-ray energy spectrum showing low-energy interfering resonances. The spectrum was generated utilizing a high-purity germanium detector. The high-energy part of the spectrum is the reaction $^{19}F(p,\alpha\gamma)^{16}O$, but the low-energy interfering lines are generated by the elements Na, Mg, and Al undergoing the (p,p'γ) reactions. Modified from Dobeli et al. (2006).

Figure 2.5. SIMS results ($^{19}F/^{18}O$) for the basaltic and high-silica glasses versus their fluorine concentration values based on PIGE analysis. Regression lines drawn separately through the basaltic and high-silica glasses demonstrate the matrix effects. See text for explanation.

Table 2.1. Major element and density data for mineral standards, basaltic glasses, and high-silica glasses.

Sample	SiO_2	TiO_2	Al_2O_3	FeO	MnO	MgO	CaO	Na_2O	K_2O	P_2O_5	F	Density (g/cc)	References
Fluor-topaz	32.7	0.0	56.1	0.0	0.0	0.0	0.0	0.0	0.0	0.0	20.3	3.4	Barton et al. 1982
Durango Apatite	0.3	0.0	0.1	0.0	0.0	0.0	54.0	0.2	0.0	40.8	3.5	3.2	Young et al. 1969
BHVO-2G	49.3	2.8	13.6	11.3	0.2	7.1	11.4	2.4	0.5	0.3	tr	2.9	Jochum et al. 2005
GSE-1G	52.9	0.1	13.4	12.7	0.07	3.5	7.3	4.1	2.7	0.0	tr	2.7	Jochum et al. 2005
GSA-1G	51.5	1.6	14.3	14.2	0.03	3.5	7.8	3.9	2.8	0.0	tr	2.7	Jochum et al. 2006
GSC-1G	53.0	1.4	13.9	13.7	0.03	3.6	7.1	3.8	3.1	0.3	tr	2.7	Jochum et al. 2007
GSD-1G	52.5	1.3	13.7	13.3	0.02	3.6	7.2	3.8	3.0	0.3	tr	2.7	Jochum et al. 2008
NIST 610	69.7	0.1	2.0	0.1	0.1	0.1	11.4	13.4	0.1	0.0	tr	2.5	Jochum et al. 2011
NIST 620	78.3	0.0	1.8	0.0	na	3.7	6.0	14.4	0.4	na	tr	2.5	GeoReM Website
UTR-2	74.2	0.2	10.4	4.8	0.1	0.1	0.2	5.5	4.4	na	tr	2.4	Stix unpub. data

tr = trace amount

Table 2.2. PIGE analysis of fluor-topaz, Durango apatite, and basaltic and rhyolitic glasses.

(1) Samples		(2)			Data				(3) F Conc. F-Topaz Calib. $S(E)$ = Table			(4) F Conc. Durango Ap Calib. $S(E)$ = Table			(5)	(6) F Conc. F-Topaz Calib. $S(E)$ = 1			(7) F Conc. Durango Ap Calib. $S(E)$ = 1			(8)	(9) Literature Values
Name	n	Mean cts	1 σ	Mean cts minus bkgrd	1 σ	$S(E)$ (keV/μm)	Range (μm)	Active Volume (cm^3)	F Conc. (ppm)	1 σ	% RSD	F Conc. (ppm)	1 σ	% RSD	% diff.	F Conc. (ppm)	1 σ	% RSD	F Conc. (ppm)	1 σ	% RSD	% diff.	F Conc. (ppm)
Fluorine Standards																							
F-Topaz	3	448252	1730	447805	1730	50.1	19.4	7.8E-05	203000	783	0.4	240640	930	0.4	17	203000	783	0	215151	830	0.4	6	203000[1]
Durango Apatite	3	73687	2800	73472	2800	44.8	21.3	8.5E-05	29778	1135	4	35300	1345	4	17	33306	1270	4	35300	1345	4	6	35300[2]
Sample Unknowns																							
BHVO-2G	5	1168	50	721	50	38.9	24.7	9.9E-05	254	18	7	301	22	7	17	327	24	7	346	25	7	6	†295±14; 370-409[3,4,5,6]
GSE-1G	4	800	20	353	20	37.0	26.0	1.0E-04	118	6	5	140	8	6	17	160	9	5	169	9	5	6	†153±5
NIST 610	4	823	20	462	20	36.3	26.4	1.1E-04	152	6	4	180	8	4	17	210	9	4	222	9	4	6	205-611[7,8,9,10]
UTR-2	4	3328	60	2881	60	33.9	28.3	1.1E-04	884	18	2	1048	21	2	17	1306	27	2	1384	29	2	6	1000-1450[11]
Fluorine Blanks																							
NIST 620	4	361	16	--	--	35.6	26.9	1.1E-04	bdl	--	--	bdl	--	--	--	bdl	--	--	bdl	--	--	--	--
GSA-1G	4	459	38	--	--	37.0	26.0	1.0E-04	bdl	--	--	bdl	--	--	--	bdl	--	--	bdl	--	--	--	†7±1
GSC-1G	4	435	14	--	--	37.0	26.0	1.0E-04	bdl	--	--	bdl	--	--	--	bdl	--	--	bdl	--	--	--	†9±1
GSD-1G	4	447	23	--	--	37.0	26.0	1.0E-04	bdl	--	--	bdl	--	--	--	bdl	--	--	bdl	--	--	--	†18±2
Si Blank	4	216	13	--	--	34.9	27.7	1.1E-04	0	0	0	0	0	0	--	0	0	0	0	0	0	--	0

1. Barton et al. 1982
2. Young et al. 1969
3. As BHVO-2 powder, 370ppm, USGS Certificate of Analysis 1998, http://minerals.cr.usgs.gov/geo_chem_stand/
4. As BHVO-2 powder, 376 ppm, Balcone-Boissard et al. 2009
5. As BHVO-2 powder, 402 ppm, Michel and Villemont 2003
6. As BHVO-2 powder, 409 ppm, Wang et al. 2010
7. 205 ppm, Wang et al. 2010
8. 295 ppm, Hoskin 1999
9. 413 ppm, Jochum et al. 2006
10. 611 ppm, Straub and Layne 2003
11. Stix, John, unpublished data

† = F values from Chapter 3 of this work.

Table 2.3. Results of SIMS and PIGE analyses of the F content of select basaltic and rhyolitic glasses.

Samples	SIMS			PIGE		
Name	$^{19}F/^{18}O$	1 σ	% RSD	F (ppm)	1 σ	% RSD
BHVO-2G	3.05	0.097	3	301	22	7
GSE-1G	1.59	0.025	2	140	8	6
NIST-610	0.95	0.01	1	180	8	4
UTR-2	6.35	0.09	1	1048	21	2
Si Bank	0.01	2.3E-04	3	0	--	--

Table 2.4. Fluorine concentration values of ALV-519, USGS basaltic and MPI-DING basaltic glass reference materials, and NIST-620 using SIMS calibration curves

Samples	Fluorine Content: Literature Values			SIMS			Calib. Curve 1		Calib. Curve 2	
							CF: 96.6	%RSD: 10	CF: 165.6	%RSD: 9
Name	F (ppm)	1σ	n	n	$^{19}F/^{18}O$	1σ	F (ppm)	1σ	F (ppm)	1σ
ALV-519-4	113[a]	2	14	4	0.783	0.010	76	8	130	12
	95[b]	5	na							
	90[c]	na	na							
USGS basaltic microanalytical reference glasses										
BCR-2G	448[d]	13	3	4	3.307	0.111	319	32	548	49
GSA-1G	na	na	na	3	0.070	0.003	7	1	12	1
GSC-1G	na	na	na	3	0.089	0.001	9	1	15	1
GSD-1G	na	na	na	3	0.185	0.008	18	2	31	3
MPI-DING basaltic microanalytical reference glasses										
ML3B-G	70[e]	na	1	7	0.488	0.085	47	5	81	7
KL2-G	177[e]	na	1	4	0.839	0.020	81	8	139	12
NIST high-silica microanalytical reference glass										
NIST-620	na	na	na	4	0.140	0.020	14	1	23	2

a. Jochum et al. (2006)
b. Hauri et al. (2011)
c. Monteleone, B. (personal communication) WHOI calibration standard
d. Michel and Villemant (2003) as BCR-2 powder
e. Jochum et al. (2006) information value
na: not analysed
CF: calibration factor
% RSD is that of the calibration factor

Figure 2.1

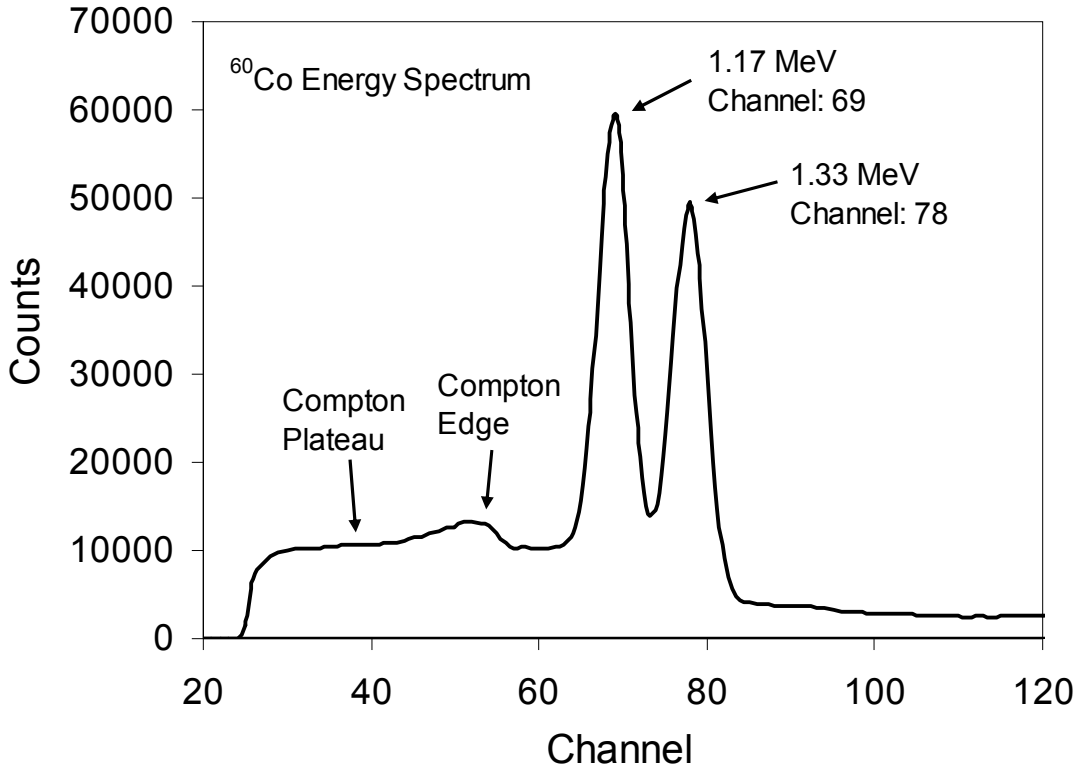
70000
60000
50000
40000
30000
20000
10000
0
Counts
^{60}Co Energy Spectrum
1.17 MeV
Channel: 69
1.33 MeV
Channel: 78
Compton
Plateau
Compton
Edge
20
40
60
80
100
120
Channel

Figure 2.2

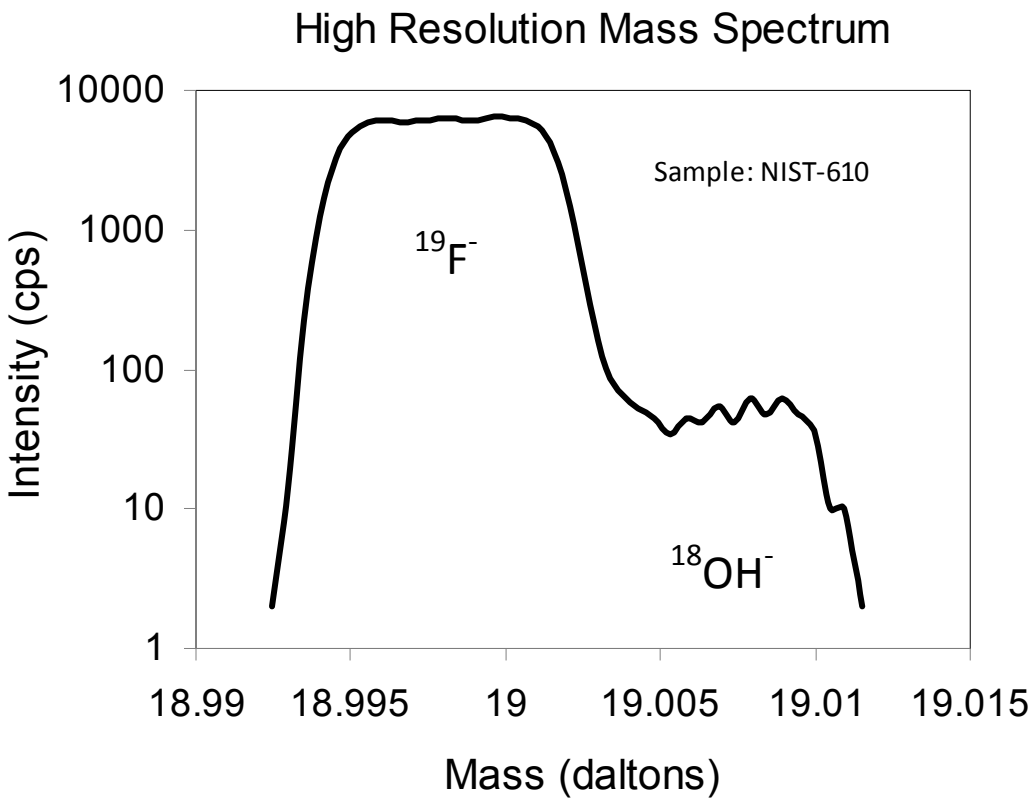
High Resolution Mass Spectrum
Sample: NIST-610
$^{19}F^-$
$^{18}OH^-$
Intensity (cps)
10000
1000
100
10
1
18.99
18.995
19
19.005
19.01
19.015
Mass (daltons)

Figure 2.3

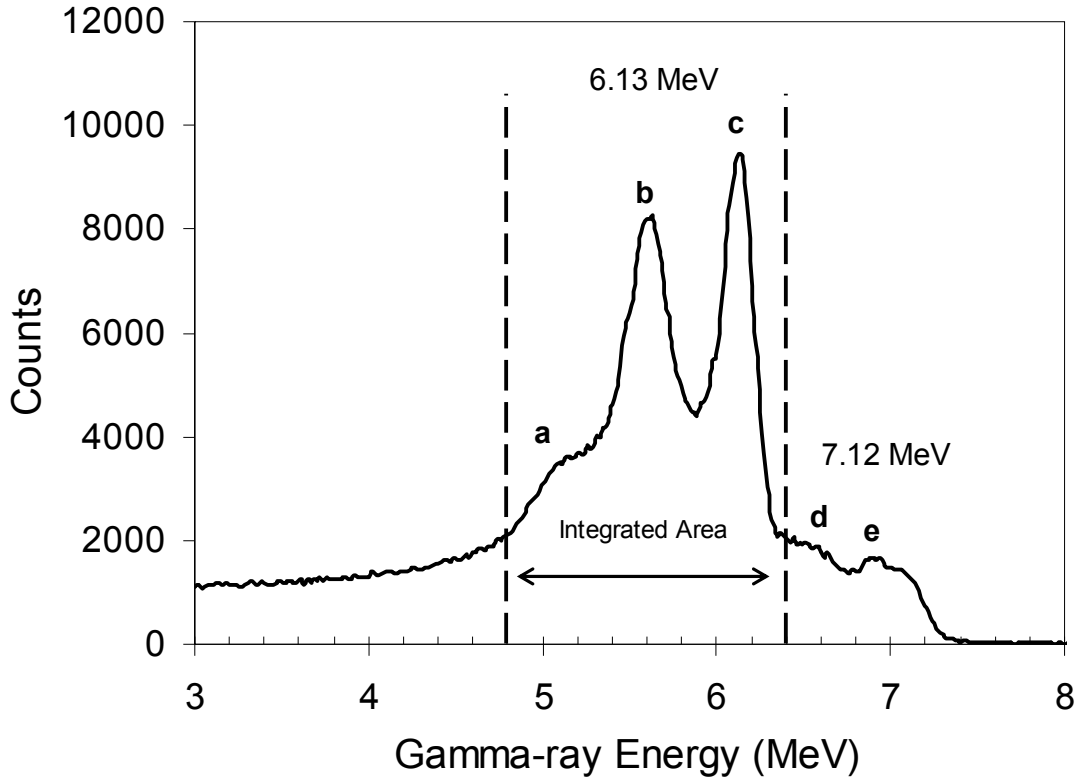
12000
10000
8000
6000
4000
2000
0
Counts
6.13 MeV
a
b
c
d
e
7.12 MeV
Integrated Area
3
4
5
6
7
8
Gamma-ray Energy (MeV)

Figure 2.4

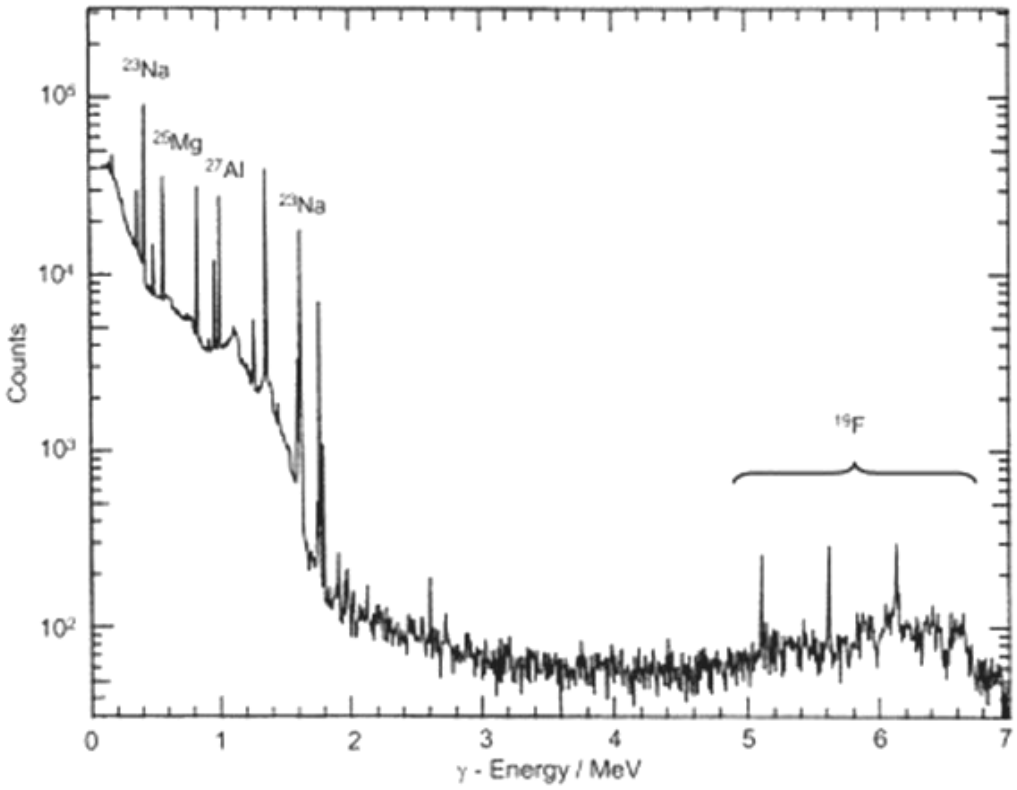
^{23}Na
^{25}Mg
^{27}Al
^{23}Na
^{19}F
Counts
10^5
10^4
10^3
10^2
0
1
2
3
4
5
6
7
γ - Energy / MeV

Figure 2.5

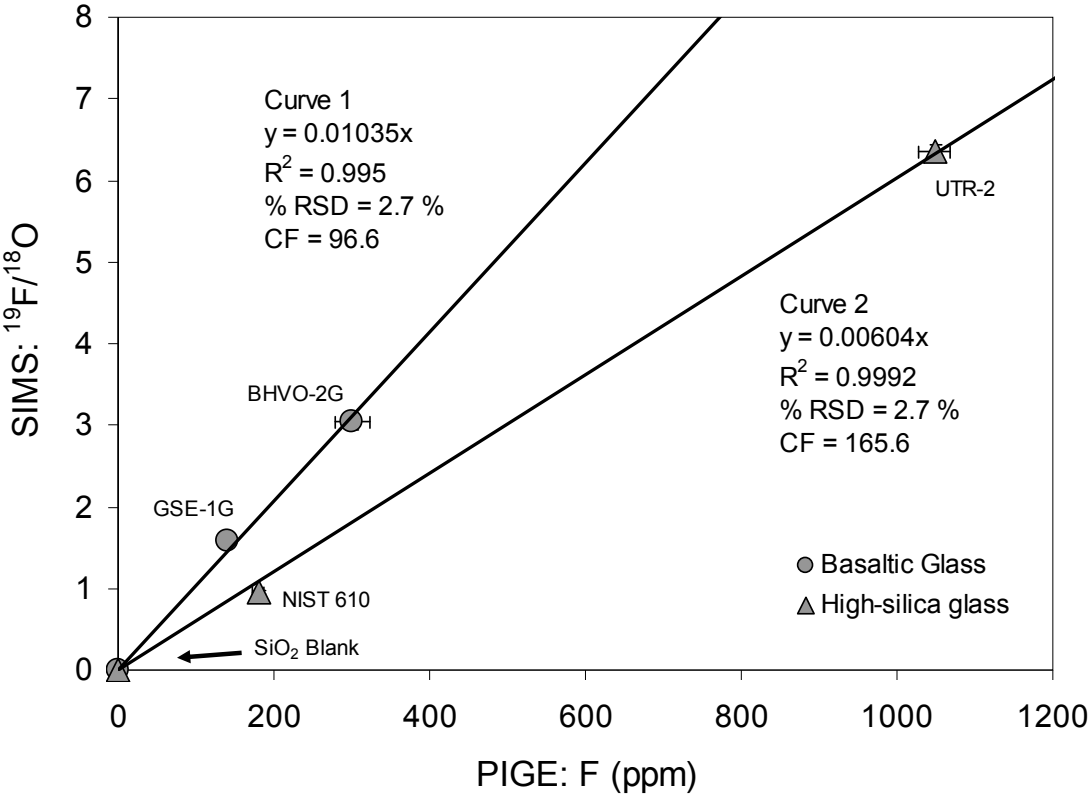
Curve 1
y = 0.01035x
R2 = 0.995
% RSD = 2.7 %
CF = 96.6
Curve 2
y = 0.00604x
R2 = 0.9992
% RSD = 2.7 %
CF = 165.6
BHVO-2G
GSE-1G
NIST 610
SiO2 Blank
UTR-2
Basaltic Glass
High-silica glass
SIMS: 19F/18O
PIGE: F (ppm)
0
1
2
3
4
5
6
7
8
0
200
400
600
800
1000
1200

CHAPTER 3

SYNTHESIS AND CHARACTERIZATION OF FIVE NEW FLUORINE-BEARING BASALT REFERENCE MATERIALS AND THEIR USE IN QUANTIFYING THE FLUORINE CONTENT OF THE BASALT GLASS STANDARDS BCR-2G, BHVO-2G, GSA-1G, GSC-1G, GSD-1G, ML3B-G, KL2-G, AND ALV-519-4

ABSTRACT

A natural tholeiite from the East Pacific Rise was mixed with variable amounts of CaF_2 to create five glasses with the following F content (wt.% ± 1σ): Fba-1 (0.13 ± 0.05); Fba-2 (0.53 ± 0.11); Fba-3 (0.87 ± 0.10); Fba-4 (1.41 ± 0.11); Fba-5 (2.24 ± 0.12). Portions of the Fba glasses were studied by EPMA and SIMS. EPMA used Biotite-3 (Bt-3: 3.3 wt.% F) and synthetic fluorphlogopite (F-phlog: 9.02 wt.% F) as F calibration standards. Wavelength scans of the F Kα line on Bt-3 and F-phlog showed asymmetric peaks, requiring the use of peak-integration analysis of the Kα signal. Results showed < 6% difference in the F content of the Fba glasses between the Bt-3 and F-phlog standards. Homogeneity of the Fba glasses was established by both SIMS and EPMA. Glasses labeled Fba-2, -3, -4, and -5 pass statistical tests for homogeneity and may be used as EPMA or SIMS standards. SIMS calibration curves were constructed using the Fba glasses, Bt-3, and F-phlog, and these curves were used to determine the F contents (ppm ±1σ) of the following nine commonly used basaltic glass standards: BCR-2G (321±15), BHVO-2G (295±14), GSA-1G (7±1), GSC-1G (9 ±1), GSD-1G (18±2), GSE-1G (153±7), ML3B-G (47±2), KL2-G (81±4), ALV-519-4 (76±4). SIMS analyses of silica-rich, iron-poor materials showed a difference in calibration by a factor of ~1.5 to 3, demonstrating large matrix effects for the analysis of F by this technique.

1. Introduction

The study of volatiles (H_2O, CO_2, S, Cl, and F) in volcanic gases and igneous rocks expands our understanding of the diffusion, partitioning, and release of volatiles from magmas as well as volatile storage in the crust and mantle (e.g. Smith 1981, Smith et al. 1981, London et al. 1988, Michael 1988, Symonds et al. 1994, Carroll and Webster 1994, Johnson et al. 1994, Watson 1994, Hirschmann et al. 2005, Alletti et al. 2007, Chevychelov et al. 2008, Aiuppa et al. 2009). The role of halogens (F, Cl, Br, I) in geological processes has received increasing attention over the past decade (for example, a special issue of Chemical Geology was devoted to halogens; Aiuppa et al., 2009) because they can substantially affect the chemical and physical properties of magmas, can be useful geochemical tracers in establishing the constraints on the genesis and fluid evolution of magmatic systems within various tectonic environments, and may constrain the volatile budgets of the lithosphere and lower mantle (Dingwell 1985, Sigvaldason, G.E and Oskarsson, N. 1986, Symonds et al. 1994, Carroll and Webster 1994, Johnson et al. 1994, Watson 1994, Hauri 2002, Straub and Layne 2003, Aiuppa et al. 2009, Köhler et al. 2009). Fluorine is the most reactive of the halogens, and forms many complexes within fluids and melt (Pan and Fleet 1996, Williams-Jones et al. 2000, Tagirov et al. 2002, Köhler et al. 2009, Aiuppa et al. 2009), including the volcanic gas species HF, SiF_4, $SiOF_2$, $ClSiF_3$, AlF_2O (Carroll and Webster 1994, Sawyer and Oppenheimer 2006). Fluorine is also highly soluble in silicate melts compared to other magmatic volatile species, allowing F to behave as an incompatible element through the general retention of F in silicate melts during differentiation and degassing upon magma ascent and storage (Dingwell et al. 1985, Carroll and Webster 1994; Stecher 1998, Mysen et al. 2004, Scaillet and MacDonald 2004, Aiuppa et al. 2009). The ionic radius of F^- in both two-fold and octahedral coordination (1.285 Å and 1.33 Å, respectively) is similar to that of OH^- (1.32 Å and 1.37 Å) and O^{2-} (1.35 Å and 1.40 Å) (Shannon, 1976), allowing F to substitute for hydroxyl and oxygen in silicate minerals and melts (Stolper

1982, Stecher 1998), including the common hydroxyl substitutions within micas (e.g. Robert et al. 1993) and other hydrous phases. At pressures and temperatures that approximate the conditions within the transition zone of the mantle, Gasparik (1990, 1993) experimentally created a new hydrous phase with the formula $Mg_{10}Si_3O_{14}(OH,F)_4$ that is stable with stishovite and which he called superfluorous or superhydrous phase B, showing that F and OH can substitute at these pressures and temperatures (Hazen 1997). It has also been shown that fluorine is incorporated at trace levels within nominally anhydrous minerals (NAMs) such as olivine and clinopyroxene (Hervig et al. 1988, Hervig and Bell 2005, Guggino et al. 2007, O'leary et al. 2010). Based on the observation that clinopyroxene represents a major host of H_2O in the mantle (Bell and Rossman 1992), Hoskin (1999) suggested, that F and OH may substitute within this phase as well as within olivine (Sykes et al. 1994), implicating the Earth's mantle as a major reservoir for fluorine.

Measurements of F in rocks and minerals have historically relied on bulk extraction techniques and wet chemical analyses, such as pyrohydrolysis, ion chromatography, and ion-specific electrode, which offer relatively simple preparation procedures, high sensitivity, and low detection limits (e.g. Boyle 1981, Nicholson 1983, Stecher 1998, Michel and Villemant 2003, Wang et al. 2010 and references therein). Notwithstanding the low detection limits and high sensitivities of bulk extraction methods, a number of problems and limitations accompany these techniques, such as 1) the large amount of sample material needed (up to a few hundred milligrams) which may introduce contaminants associated with adsorbed volatiles and minute amounts of altered material and 2) sample size limitations which may preclude the analysis of micro-scale samples such as melt inclusions, lamellae, the detection of micro-heterogeneities in glasses, and the measurement of elemental gradients over small scales in glasses and crystals (Hauri et al. 2002).

Microbeam methods, particularly EPMA and SIMS, have proven to be a powerful approach in the investigation and measurement of F at a lateral resolution precluded by bulk extraction techniques, and these methods are routinely used to measure trace amounts of F at both high sensitivity and high spatial resolution in glasses and crystals. Witter and Kuehner (2004; and references therein) document the historical use of the electron microprobe for measurements of F in minerals and glasses. Although the spatial resolution and non-destructive nature of EPMA has a distinct advantage over bulk methods, some problems exist that can render measurements of F by EPMA suspect, including 1) low count rates for these easily-absorbed, soft x-rays when single-crystal reflectors such as TAP in wavelength dispersive spectrometry (WDS) are used; 2) interferences from higher-order lines of heavier elements, particularly the Fe Lα line; 3) the occurrence of matrix effects related to high x-ray absorption in the specimen; 4) the unavailability of suitable standards that are sufficiently matrix-matched to the unknown specimens (Ottolini et al. 2000, Kane 2001); 5) the occurrence of peak shifts and peak-shape alterations between specimens with chemical and structural differences; and 6) detection limits too high (hundreds of ppm) and beam diameters too large (> 20 μm to minimize any F migration) for certain applications, such as melt inclusion studies and the determination of partition coefficients between glass and the edge of a mineral phase (Ottolini et al. 2000, Hauri et al. 2002, Witter and Kuehner 2004). Over the past 30 years, researchers have developed techniques to ameliorate some of the aforementioned problems with F measurements using EPMA, such as: 1) development of new layered synthetic microstructure (LSM) reflectors, which have improved count rates (McGee and Keil 2001); 2) the development of Φ(ρz) computational methods that have improved corrections for matrix effects on light elements (Bastin and Heijligers 1991, Ottolini et al. 2000); and 3) techniques for integrating the peak area to accommodate peak shifts and changes in peak shape (Bastin and Heijligers 1991, Ottolini et al. 2000).

Secondary ion mass spectrometry (SIMS) is an attractive alternative for microanalyses of fluorine because of the much higher sensitivity compared to the electron probe. For example, Hauri et al. (2002) analyzed San Carlos olivine, using literature values for baseline volatile concentrations, and were able to report detection limits of < 1 ppm for F when counting negative secondary ions and using a Cs^+ primary beam and normal incidence electron gun for charge balance. These low detection limits were achieved because of the high useful yield of F^- ions when using a Cs^+ primary beam. Guggino et al. (2007), analyzing an aliquot of F-free silica glass as the control blank, were able to measure F concentrations below 1 ppm in olivine crystals from various tectonic suites. The primary beam diameter using SIMS is often tens of microns (as small as 5 microns using a Cs^+ primary source or 10 microns using an O^- primary source), but the area from which secondary ions are detected can be manipulated electronically and with field apertures to be substantially smaller than with EPMA for certain applications (e.g. the measurement of F, the light elements, and the alkalis where element migration and volatilization during EPMA analysis is a concern). Because of the ability of SIMS to analyze small areas (a few to tens of microns in diameter), SIMS has chiefly dominated the study of F and other volatiles in trapped melt inclusions, small mineral grains, and high-pressure experimental run products (Hauri 2002, Hervig et al. 2003).

Matrix effects are a common occurrence with SIMS measurements of crystals and glasses and are thought to be a function of the complexity involved with sputtering, ionization, and mixing inherent with analyzing materials of various chemical compositions, crystal structures, and matrix orientations, and appear to depend on the concentration and bonding regime of the element itself and that of the major elements of the matrix (e.g. Deline 1978, Kovalenko et al. 1988, Eiler et al. 1997, Ottolini 2000, Bell et al. 2009). Several attempts have been made to develop empirical correction protocols for matrix effects (e.g. Hervig et al. 1992, Eiler et al. 1997, Ottolini 2000), but the most

accepted procedure to reduce the uncertainties associated with matrix effects is to utilize a standard which is chemically and structurally similar to the unknown, or sufficiently matrix-matched (Eiler et al. 1997, Ottolini 2000, Kane 2001). SIMS measurements of F are strongly sensitive to matrix effects (e.g. Hervig et al. 1987, Kovalenko et al. 1988, Guggino and Hervig 2010, 2011), necessitating the need for F standards within a wide suite of matrixes. However, there are few well-established F concentration values for the glass standards routinely used in microanalytical laboratories.

Some workers have attempted to quantify the F content of microanalytical glass and mineral standards of various silicate and non-silicate compositions to varying degrees of uncertainty, and some of these F standards are in widespread use in microanalytical laboratories. A fluorine standard routinely used is the fluorapatite commonly known as Durango Apatite (3.53 wt.% F; Cerro de Mercado, Durango, Mexico) originally established by the US Geological Survey as a phosphate standard (Young et al. 1969). Two peralkaline obsidian standards common in microanalytical laboratories are KE-12 (4000-4400 ppm F; pantellerite; Eburru, Kenya; Macdonald and Bailey 1973, Palais and Sigurdsson 1989) and KN-18 (6400 ppm F; comendite; Naivasha, Kenya; Mosbah et al. 1991) which were analyzed for F by ion-specific electrode. Smith et al. (1981) used EPMA to analyze the F content of a synthetic fluorphlogopite for use as an F standard for their study of F in some upper-mantle minerals, namely phlogopite, kaersutite, and apatite. They checked the F content of the synthetic fluorphlogopite against a calibration curve constructed from EPMA measurements of CaF_2, fluorapatite, CdF_2, and F-scapolite, confirming the F content of the synthetic fluorphlogopite was stoichiometric at 9.02 wt.%. In an attempt to measure H and F in melt inclusions, Hervig et al (1989) used SIMS to construct a calibration curve for F using synthetically hydrated rhyolitic obsidian fragments (Stanton et al. 1985, Westrich 1987), a synthetic A-type granitic glass (Collins, et al. 1982), fragments of the Macusani rhyolite flow, Peru (London, et al. 1987), and several other rhyolite glasses. The calibration curves from the

poorly characterized glasses gave an F precision of ± 100 ppm. Hinton et al (1995) used SIMS to analyze the homogeneity of 22 trace elements, including F, in the high-silica, soda-lime-rich glass NIST 610. They assumed the nominal concentrations of 500 ppm for the trace elements and F, and made no attempt to independently quantify the F content of NIST 610. As a result, Hinton et al. (1995) found that the SIMS F values ranged from a maximum of +11 % to a minimum of -16 % about a mean, concluding that NIST 610 is moderately inhomogeneous with respect to F. Hoskin (1999) attempted to use SIMS to quantify the F concentration of NIST 610 by synthesizing five glass standards of varying concentrations of F within a matrix similar to that of NIST 610, characterizing these glasses for F using EPMA, and then constructing a calibration curve to ultimately obtain a value for NIST 610 of 295 ±16 (5.40% RSD) ppm F. However, other workers have reported F concentration values for NIST 610 that span a range of over 400 ppm (Wang et al. 2010: 205±6 ppm F; Jochum et al. 2006: 413±15 ppm F; Straub and Layne 2003: 611±101 ppm F). Jochum et al. (2000) synthesized eight microanalytical glass standards from natural samples of komatiite (GOR128-G, GOR132-G), peridotite (BM90/21-G), basalt (KL2-G, ML3B-G), andesite (StHs6/80-G), rhyolite (ATHO-G), and quartz-diorite (T1-G) matrix compositions (referred collectively as MPI-DING) and analyzed them for major, minor, and trace elements using various bulk- and micro-analytical methods. A survey of the MPI-DING glasses for F using SIMS (Jochum et al. 2006) was inconclusive, and the results are described as “information values”. Straub and Layne (2003) attempted to measure F and other volatiles in basaltic to rhyolitic glass shards from Izu arc volcanic rocks. For the high-silica glass F standard, they used UTR-2 (natural pantellerite; F=1143 ppm, Stix and Layne 1996). For the low-silica F standard, Straub and Layne (2003) derived an F value for the MORB glass JDF-D2 (300±70 ppm) using EPMA.

The aim of this study is to create an entirely new suite of F glass standards of varying F concentrations in a basaltic matrix, quantify the F content of these new glasses

using EPMA and SIMS, and then to use these F standards to construct a calibration curve that will be used to determine the F concentrations of some common basaltic microanalytical glass standards, namely ALV-519-4-1, the USGS glasses GSA-1G, GSC-1G, GSD-1G, GSE-1G, BCR-2G, BHVO-2G, and the MPI-DING basalt glass standards KL2-G and ML3B-G.

2. Experimental Methods

Six basaltic glasses with variable masses of added CaF_2 were synthesized (labeled Fba-0 to Fba-5, henceforth collectively referred to as Fba glasses). The starting material was a natural tholeiite from the East Pacific Rise (EPR-2001 unpublished) donated by G. Moore at Arizona State University. EPR-2001 powders were generated using a McCrone Micronizing Mill. The powders were sieved, and the size fraction of < 70 µm was retained for synthesizing. Six aliquots of EPR-2001 powders were mixed with different amounts of powdered CaF_2 to create six separate glasses with distinct concentrations of F (Table 3.1). Equation 1 was used to calculate the amount of CaF_2 powder to be weighed in order to achieve the desired weight percent of F in the powder mixture.

$$(x)\,g\,F\left(\frac{1\,mol\,CaF_2}{37.9968\,g\,F}\right)\left(\frac{78.0752\,g\,CaF_2}{1\,mol\,CaF_2}\right)=(y)\,g\,CaF_2 \qquad (1)$$

The total mass of each mixture was held constant at 2.5 grams, thereby diluting the original bulk chemistry of EPR-2001 with increasing CaF_2. To facilitate homogeneity of the CaF_2 within each aliquot, the mixtures were placed in individual plastic centrifuge tubes and returned to the McCrone Mill where they were shaken for 100 seconds. Fusing and quenching of the mixtures were performed in a one-atmosphere Deltech Model DT-31 controlled-atmosphere furnace. The mixtures were individually placed in an open

platinum crucible and slowly heated to fusing temperature (1470 °C for Fba-0 to Fba-4 and 1430 °C for Fba-5) and held at fusing temperature for 30 minutes. The environment was maintained at fO_2 ~ NNO by providing CO_2 at a flow rate of ~125 cm^3/s. The melts were quenched to a glass by rapidly immersing the melt-filled platinum crucible in distilled water. Each glass run was removed from the Pt crucible with a ball peen hammer and a dental pick, and the Pt crucible cleaned in a solution of HF. Random fragments of the Fba glasses were hand picked under a binocular microscope, mounted in a one-inch-diameter round epoxy mount, polished, and studied by electron-probe microanalysis (EPMA) and secondary ion mass spectrometry (SIMS).

3. Analytical Methods and Instrumentation

3.1 EPMA Analysis

Fluorine forms volatile compounds in silicate melts (e.g. HF, SiF_4, $SiOF_2$, $ClSiF_3$, and AlF_2O; Sawyer and Oppenheimer 2006). Although specific concentrations of F were weighed into the Fba powder mixtures, the Fba glasses were fused in an open crucible and loss of F during melting is likely, thus requiring the F content and homogeneity of the quenched glasses to be measured independently.

EPMA was performed on the six Fba glasses at the Arizona State University (ASU) and the University of Arizona (UofA) electron microprobe labs. The analytical conditions, techniques, and calibration standards for F varied between the two labs (Table 3.2), allowing us to test for reproducibility of the F content and homogeneity of the Fba glasses utilizing EMPA independent of technique.

3.1.1 EPMA at Arizona State University (ASU)

Major elements and F were measured on a JEOL 8600 Superprobe instrument equipped with four wavelength-dispersive spectrometers (WDS). Fluorine was measured using a TAP crystal on a single spectrometer. The EPMA analytical conditions included a 25 nA primary current, a 15 keV accelerating voltage, a 15 μm defocused beam diameter

to reduce F and Na migration, and a 45 s peak counting time. The major and minor element calibration standards included Si, Al, Fe, Mg, and Ca: GL113 (1921 Kilauea tholeiite glass); Ti: rutile; Na: Amelia Albite; K: orthoclase. The F calibration standards included Biotite-3 (Bt-3; 3.3 wt.% F) and a crystal of MgF_2 (61 wt.% F), each utilized during separate sessions (Table 3.2). Wavelength scans were conducted on the F Kα peak, and no anomalous peak shapes were observed. Atomic number, absorption, and fluorescence corrections (ZAF) data reduction was carried out using internal software routines.

3.1.2 EPMA at University of Arizona (UofA)

Major elements and F were measured with a Cameca SX100 Ultra electron microprobe microanalyzer equipped with five WDS spectrometers. Fluorine was measured simultaneously on two WDS spectrometers, each equipped with a TAP crystal. The calibration standards for major and trace elements included: Si, Mg, and Ca: diopside; Na: albite; Al: anorthoclase (Hakone); K: Orthoclase (OR1); Ti: rutile (Rutile1); Mn: rhodonite (rhod791); Fe: fayalite; Cr: Cr_2O_3 (synthetic). The calibration standards used for fluorine were Biotite-3 (Bt-3; 3.3 wt.% F) and synthetic fluorphlogopite (F-phlog; 9.02 wt.% F, stoichiometric). Corrections were applied based on the Pouchou and Pichoir (PAP) model using internal software routines.

Wavelength scans were conducted on the F standards Bt-3 and F-phlog (Fig. 3.1). The maximum counts occurred near peak position 71312 Cameca units (CU), or wavelength λ = 18.359 Å, where:

$$x \text{ Cameca Units} = (\sin\theta)\ x\ 10^5 \quad (2)$$

derived from the Bragg's Law equation:

$$n\lambda = 2d\sin\theta, \text{ or } n\lambda = 2d\left(\frac{CU}{10^5}\right), \text{ where} \quad (3)$$

2d = 25.745 Å

The wavelength (Å) can be obtained by solving equation (3). The energy (keV) of an x-ray is inversely proportional to its wavelength and can be calculated using equation (4):

$$E = \frac{hc}{\lambda} \text{ , where} \quad (4)$$

h is Planck's Constant in KeV = 4.1356678 x 10^{-18} keV
c is the speed of light in angstroms = 299792458 x 10^{10} Å/s
λ = wavelength in angstroms calculated from equation (3) above

The wavelength scans show a slight peak shift between the two standards Bt-3 and F-phlog as well as a satellite peak on the lower wavelength side (left side) of the F curve (Fig. 3.1), prompting the utilization of two methods of EPMA analysis: the peak count method and the peak-integration method. EPMA measurements spanned four separate sessions. The peak-count method utilized a 20 nA primary current, a 15 kV accelerating voltage, a 20 μm defocused beam, and a peak counting time of 45 seconds (Table 3.2). The peak integration method used a 20 nA primary current, 15 kV accelerating voltage, 20 μm de-focused beam, a 60-second counting time, and five iterations. The peak integration method sums all the counts under the peak curve based on a range CU's or wavelength values from the low wavelength side of the curve to the high wavelength side as selected by the user. The total range on either side of the F Kα peak was selected to be 2048 CU (± 0.527 Å about the peak). Background counts were collected from within 500 CU (0.130 Å) from the left and right edges of the total range. Therefore, the total range of integration was from 69764 CU (λ = 17.692 Å) to 72860 CU (λ = 18.756 Å). Eighteen to twenty analysis spots were manually chosen on each Fba glass aliquot, and the analyses were carried out unattended via computer automation.

3.2 SIMS Analysis

SIMS analysis was performed at Arizona State University (ASU) using the Cameca ims 6f. Analyses spanned two sessions where the instrument was configured to measure both negative and positive secondary ions. Table 3.2 lists the operating parameters for the SIMS analyses. A primary beam of $^{16}O^-$ ions obtained from a duoplasmatron at -12.5 kV was focused to a diameter of 20-30 μm on the sample held at -5 kV. Using a current of 3.5 nA, negative secondary ion intensities of $^{18}O^-$, $^{19}F^-$, and $^{28}Si^-$ (0 ± 60 eV excess kinetic energy) were recorded. The mass spectrometer was operated at a mass resolving power (MRP) sufficient to separate $^{19}F^-$ from $^{18}OH^-$ ($\Delta M/M$ ~2500) (Fig. 3.2). Detection of positive secondary ions was conducted with a primary beam of $^{16}O^-$ obtained from a duoplasmatron at -12.4 kV and focused to a diameter of 20-30 μm on the sample held at +9 kV. The operating current was maintained at 16.5 nA, and energy filtering was obtained by using a -75 V offset and a 40 V energy window. Positive secondary ion intensities were recorded for $^{19}F^+$ and $^{30}Si^+$. SIMS analysis was conducted on the Fba glasses; Biotite-3 and synthetic F-phlogopite; high-silica glasses NIST-610, UTR-2, and KE-12; and the USGS, MPI-DING, and ALV-519 basaltic standard glasses. All negative secondary ion intensities were normalized to that of $^{18}O^-$, and all positive secondary ion intensities were normalized to $^{30}Si^+$. Session-to-session precision was monitored by analyzing NIST-610 and UTR-2, which show historical values for negative secondary ion ratios that range from: NIST-610: $^{19}F/^{18}O$ = 0.95-1.0; UTR-2: $^{19}F/^{18}O$ = 6.75-6.8. With only one session studying positive ions, the session-to-session reproducibility of F/Si ion ratios is unknown.

4. Results

4.1 Homogeneity of the Fba Glasses

For any reference material (RM), the homogeneous distribution of elements is a fundamental requirement. Nevertheless, homogeneity of certain chemical species is not

solely dependent on the intrinsic properties of the bulk material, but is also a function of the characteristics of the chemical constituents measured under specific conditions. For example, a slowly diffusing chemical species may be considered homogeneously distributed within an RM at the analytical resolution of a bulk analysis, yet considered heterogeneously distributed under microanalytical methods. Therefore, the concept of fitness-for-purpose must be employed when determining the homogeneity of RMs (Kane and Potts 1999, Kane 2001, Jochum et al. 2006). Natural materials should all be considered heterogeneous at some level for different chemical species. Synthetic reference materials, on the other hand, may undergo processes to ensure homogeneity of certain chemical species of interest at a controlled analysis resolution. For the Fba glasses, we employed techniques mentioned in the previous section to ensure homogeneity at the microanalytical scale.

4.1.1 Homogeneity Determination using SIMS

An initial test of homogeneity was conducted on the Fba glasses using the SIMS 6f at Arizona State University detecting negative secondary ions. The quantitative test we used to determine homogeneity emulated the method of Jochum et al. (2000, 2005, and 2006), whereby they defined the heterogeneity of glasses as variations in elemental concentrations that are greater than 3 times the repeatability (% Relative Standard Error, or % RSE) of the analytical instrument after multiple measurements of homogeneous materials. Therefore, if the range of concentration values for a particular chemical species (the heterogeneity) does not exceed three times the analytical uncertainty of the instrument precision, then the heterogeneities are deemed insignificant and the RM is considered homogeneous with respect to that particular chemical species. Table 3.3 lists the average SIMS values and % RSE for F measured on 1) the homogeneous glasses used for instrument precision (silica blank, NIST-610, KE-12, and UTR-2), 2) the Fba glasses, and 3) three mica crystals that are routinely used as F standards (Bt-3, F-phlog, and Phlog 73-77). The average % RSE for the silica blank, NIST-610, KE-12, and UTR-2

is 1.13 %. Three times the average % RSE for the silica blank, NIST-610, and UTR-2 is 3.4 %. Figure 3.3 depicts graphically the data in Table 3.3 and shows that Fba-1 is the only Fba glass that lies outside the definition of homogeneity, showing heterogeneity of about 4 %. The remaining Fba glasses, the high-silica glasses, and the mica standards show less than 2 % heterogeneity of F at the scale of our analyses.

4.1.2 SIMS Output, Homogeneity, and the Limit on Quantitation

The output from SIMS analysis is in counts/second, and the counts/second of the elemental species of interest is typically normalized to the counts/second of some ubiquitous isotope within the sample matrix to obtain an elemental ratio; in our case, $^{19}F^-$ is normalized to $^{18}O^-$. Because there are no matrix-correction models for SIMS analysis, elemental concentration values require appropriate matrix-matched standards to build a calibration curve to convert the elemental ratios into a concentration value. Although homogeneity of the Fba glasses and mica standards was determined based on SIMS output, a matrix-corrected technique needs to be employed to fully quantify the F content of the Fba glasses, such as with EPMA. In addition, there are no suitable models to predict the yield of F^- ions from one matrix or another during sputtering. Tests for the effect of sample chemistry on F^- intensity continue to be empirical (e.g. Hoskin 1999, Portnyagin et al. 2002).

4.2 EPMA Analysis

4.2.1 EPMA: Peak-Count Method

EPMA analysis was performed on the Fba glasses in an attempt to quantify their F content. Witter and Kuehner (2004) document many attempts by other electron probe labs to measure trace F in various iron-bearing geologic materials using peak intensities. The main problems encountered by these workers were difficulty in resolving F Kα from Fe Lα, high minimum detection limits, and high uncertainties based on counting statistics. In spite of the above difficulties, Witter and Kuehner (2004) developed a peak-count technique (10 kV accelerating voltage, 180 nA beam current, 8 μm beam diameter, 400 s

peak count time) to measure trace amounts of F. The only drawback was their caveat that the above analytical conditions are too extreme to be used to analyze other elements in the sample, particularly the major elements. Because the Fba powders were initially created with greater than trace amounts of F (> 0.5 wt.%), we decided not to apply the analytical conditions of Witter and Kuehner (2004), and we tested analytical conditions where major elements could be included in the analysis.

Table 3.4 lists the results of EPMA analysis of the Fba glasses and the mica standards for F, major elements, and trace elements using both peak-count and peak integration methods. Our initial EPMA sessions were conducted at the ASU EPMA Lab employing the peak-count method. We used MgF_2 and Bt-3 as F calibration standards to test whether or not our method was standard-independent. Wavelength scans were conducted on MgF_2, but no anomalous peak shapes were observed. Table 3.5 shows the inter-calibration percent difference between the two F standards MgF_2 and Bt-3. Fba-1, -3, and -5 show percent differences below 10%, while Fba-2, Fba-4, and the Bt-3 check-standard show percent differences of 13%, 14%, and 15%, respectively. To confirm the results from the ASU EPMA Lab, we performed the peak-count method at the UofA EPMA Lab using Bt-3 and F-phlog as the F calibration standards. During the sessions at UofA, we slightly modified the ASU procedure by using a wider beam diameter and longer peak counting time. The results of the UofA sessions using both the Bt-3 standard and the F-phlog standard showed close agreement for Fba-1, yet large differences for Fba-2 and -3 and near 10% differences for Fba-4 and -5 are exhibited. In addition, when MgF_2 was used as the F calibration standard to analyze Bt-3 (ASU), or when Bt-3 was the F calibration standard to analyze F-phlog (UofA), the F concentration values for the analyzed standards were far removed from the literature or stochiometric F concentrations. However, when using only the Bt-3 calibration standard for F, there is close agreement between the ASU and UofA sessions (Table 3.5), confirming that the

peak-count method for F maintains inter-laboratory precision when the same F standard is used for calibration, and that the peak-count method is standard dependent.

4.2.2 EPMA: Peak Integration Method

Wavelength scans conducted at the UofA EPMA lab on the standards Bt-3 and F-phlog of the F Kα peak showed a slight peak shift and a pronounced bi-modal, non-Gaussian peak curve with a satellite peak on the low wavelength/high energy side (left side) (see Fig. 3.1). A wavelength scan of Fba-5 (3.13 wt.% F powder) showed a similar F Kα peak shape. Because F is a volatile species and is one atomic number higher than the group of elements considered ultra-light elements for the purposes of EPMA analysis (B, C, N, O; Bastin and Heijligers 1991), problems that are common with the ultra-light elements, such as peak-shape alteration and peak shifts, as well as interference between the F Kα and Fe Lα lines (e.g. Witter and Kuehner 2004), could arise while attempting to measure F. With EPMA, it is common practice to measure the peak intensities at the spectrometer settings that give the maximum count rates. However, it is sometimes not realized that integral intensities may be required to more accurately represent the x-ray signal from the sample. Peak measurements are only valid under the assumption that the peak intensity is proportional to the integral emitted intensity, which is usually a valid assumption for the K- and L-lines of medium-to-high atomic number elements where peak shifts and peak-shape alterations are uncommon (Bastin and Heijligers 1991).

Prompted by the unsatisfactory inter-calibration and inter-laboratory precision of the F analyses obtained under peak-count mode (See Table 3.5), we decided to test for anomalous peak shapes and peak shifts by performing wavelength scans on Bt-3, F-phlog, and Fba-5 at the UofA EPMA Lab (Fig. 3.1). The wavelength scans revealed good separation of the F Kα line from the Fe Lα line, but also showed a small peak shift (~ 0.03 Å) and, a non-Gaussian peak-shape alteration that included a large satellite peak on the left shoulder (Bastin and Heijligers 1991), compelling us to re-analyze the Fba glasses and the mica standards using the peak integration method at the UofA EPMA Lab. Table

3.4 lists the results of the peak integration method for two sessions using Bt-3 and F-phlog as F calibration standards, as well as the average (accepted) values for F and the major and trace element analysis from the two peak integration sessions. Table 3.5 shows the precision (as percent difference) between the peak-integration sessions using both Bt-3 and F-phlog as the F calibration standards. The precision in the F concentration values between the two calibration standards of all the Fba glasses is shown to be < 6%.

4.2.3 EPMA: Peak-count versus Peak Integration Methods

Figure 3.4 summarizes the precision of both the peak-count and peak integration methods between the different F calibration standards. The peak-count method shows wide variations in precision between standards, while the peak integration method shows that the variability between the standards Bt-3 and F–phlog is less than 6 % RSD. The peak integration method shows the best agreement between the two different F calibration standards Bt-3 and F-phlog. Therefore, we interpret the F concentration values obtained by the peak integration method as the most reliable for the Fba glasses.

4.2.4 Homogeneity with EPMA

Because the EPMA peak integration method analyzed more spots on each Fba aliquot than did the SIMS analysis, we decided to look again at the homogeneity of the Fba glasses based on the EPMA measurements. The definition of homogeneity, as proposed by Jochum et al. (2000, 2005, 2006), was again utilized. We chose to use the F values from the EPMA session where Bt-3 was used as the F calibration standard (see Table 3.4). Figure 3.5 shows the % RSE of the Fba glasses plotted in relation to the upper demarcation of 3 x the instrument precision (3 times the % RSE of repeated measurements of the synthetic F-phlogopite). The % RSE for synthetic F-phlog is 1.1 %, and three times the average % RSE is 3.3 % RSE. According to Figure 3.5, Fba-2, -3, -4, and -5 are homogeneous with respect to F, showing heterogeneities of ≤ 3 % RSE. Fba-1 shows heterogeneity of about 8 % RSE, greater than the definition limits.

4.3 Fluorine Loss during Synthesis of the Fba Glasses

In silicate melts, F forms complexes with silicon, aluminum, and hydrogen to form volatile species that exsolve upon decompression (e.g. HF, SiF_4, $SiOF_2$, $ClSiF_3$, AlF_2O; Sawyer and Oppenheimer 2006). Therefore, because the Fba glasses were fused in an open platinum crucible at one atmosphere pressure, some F loss was expected. Table 3.6 lists the F loss from the Fba glasses during fusing, and Figure 3.6 summarizes the F loss by showing that the powder mixtures with a higher initial concentration of F experienced a higher amount (wt.%) of F loss.

4.3.1 Open-system Fluorine Partitioning between CO_2 Gas and Basaltic Melt

The measurement of halogens in volcanic gases is a source of invaluable information, allowing researchers to quantify pre-eruptive volatile contents as well as the atmospheric impacts of volcanic volatiles, thus contributing to volcano monitoring (Aiuppa 2009). Fluorine, for example, is exsolved from ascending magmas at relatively shallow depths (P < 50 MPa in basaltic magmas; Spilliaert et al., 2006), and the study of F in volcanic gas emissions can offer insight into both the syn-eruptive and quiescent degassing of active volcanoes. Fluorine loss from a silicate melt into a mixed-gas atmosphere is a function of the partition coefficient of F between the melt and the gas mixture, which is itself a function of temperature, pressure, F solubility, and melt structure such as degree of polymerization. The partitioning of any element between two phases is expressed as the Nernst partition coefficient:

$$D_i^{fluid-melt} = \frac{C_i^{fluid}}{C_i^{melt}} \quad (5)$$

where D is the partition coefficient for element i and C is the concentration of element i in the fluid divided by the concentration of element i in the melt. The fluorine loss

experienced by the Fba samples during fusing prompted an investigation into the open-system partitioning of F between a CO_2 gas and basaltic melt.

Based on equation (5), the trend exhibited in Figure 3.6 clearly demonstrates that, while maintaining a constant partition coefficient, the samples with a higher initial F content will lose a larger absolute amount of F to the atmosphere. However, Table 6 lists the apparent partition coefficients (APC) of the Fba glasses calculated using equation (5), ascribing the mass loss (ΔF) as C_i^{fluid} and the F content of the glasses measured via EPMA as C_i^{melt}. The APC's are quite different for each sample. The variable APC's can be explained by the fact that the Fba glasses were fused in an open Pt crucible for 30 minutes within a CO_2 gas atmosphere flowing at a constant rate of ~125 cm^3/s. As a result, fresh CO_2 gas continually flowed past the sample during F exsolution, disallowing F to reach equilibrium between the CO_2 gas and the melt.

Using the data from Table 3.6, Figure 3.7 (a) shows a graph of the measured F content of the Fba glasses versus the APC of F between the CO_2 gas and the basaltic melt. The plot appears to show a hyperbolic fit, where X × Y = Constant. Figure 3.7 (a) appears to show that with higher initial F content, the $D_F^{CO_2-melt}$ of the Fba glasses asymptotically approaches some constant value. If indeed Figure 3.7 (a) exhibits a hyperbolic fit, then a plot of Y versus 1/X would produce a straight line. Figure 3.7 (b) shows just such a plot of the reciprocal of the measured F content of the Fba glasses versus the APC. The curve defines a straight line that intersects the y-axis at about y = 0.28, suggesting that the equilibrium partition coefficient of F between CO_2 gas and basaltic melt at one atmosphere is about 0.28±0.01. This result indicates that F is mildly incompatible in CO_2 gas, but that given continual degassing of CO_2 out of the system over a sustained period of time, a basaltic melt will become significantly depleted in F.

This attempt to determine the equilibrium partition coefficient of F between CO_2 gas and a basaltic melt at one atmosphere is solely a first order approach. More detailed and controlled experiments are necessary, the results of which can supply much needed

information to aid in the monitoring of active volcanoes volcano as well as modeling eruption dynamics and risk assessment.

5. Application of New Fba Fluorine Standards for SIMS Calibration

5.1 Matrix Effects

Both EPMA and SIMS analysis of volatile elements must overcome the influence of matrix effects on the EPMA x-ray intensity or the SIMS ion yield, respectively. The SIMS matrix effect is characterized as the variation in ion yield of a given element within different matrixes of distinct major and minor element composition, and is a complex function not only of the chemical composition of the matrix, but also crystal structure and the orientation of the matrix to the incident primary ion beam (Deline et al. 1978, Ottolini et al. 2000, 2002). While the sample matrix effects on EPMA x-ray generation are quantitatively corrected by modeling atomic number, absorption, and fluorescence (ZAF) or by Φ(ρz) methods for light elements (Bastin and Heijligers 1991; Ottolini et al. 2000; Hervig et al. 2003, Reed 2005), there is no analogous theory of matrix-effect corrections applicable for SIMS analysis. To minimize matrix effects and to increase the accuracy of SIMS analyses, appropriate standards must be used that are closely matrix-matched to the unknown samples undergoing analysis. To convert the secondary ion intensity to a concentration value, a calibration curve must be constructed from a series of SIMS measurements of the elements of interest from as many matrix-matched standard glasses as possible (Kane 2001, Straub and Layne 2003, Hervig et al. 2003).

5.2 Calibration Curves

The main use of RMs is for the calibration of analytical instruments. On instruments such as the SIMS, a calibration curve is generated by plotting secondary ion signals from the RMs versus the accepted concentration values of the elemental species of interest within those RMs. The ideal calibration should be linear with little scatter (correlation coefficient as close to 1 as possible). Small errors in calibration curves are

achieved by measuring a large number of RMs and by requiring the RMs used for the calibration curve are closely matrix-matched (Kane 2001).

Table 3.7 lists the SIMS $^{19}F/^{18}O$ negative secondary ion ratios, the SIMS 1000 x $^{19}F/^{30}Si$ positive secondary ion ratios, and the F concentration values from EPMA and the literature for the Fba glasses, the high-silica glass standards (NIST-610, UTR-2, and KE-12), and the F mica standards (Bt-3, F-phlog, and phlogopite 73-77) used in this study for instrument calibrations. Figure 3.8 (a-d) shows SIMS calibration curves generated from the data in Table 3.7. Variability in SIMS ion ratios in samples with similar F contents but variable major element compositions demonstrates matrix effects. Figure 3.8 (a) shows a plot of the SIMS output ($^{19}F/^{18}O$) for all the Fba glasses, the high-silica glasses (NIST-610, UTR-2, and KE-12), and the mica standards (Bt-3, F-phlog., and phlogopite 73-77) versus their F content (ppm) based on EPMA or literature values. The regression line shows considerable scatter (standard deviation as % RSD = 7.0 % and a correlation coefficient, R^2, = 0.919). Figure 3.8 (b) demonstrates less scatter in calibrations when samples with similar matrix composition are grouped. Iron-rich Biotite-3 appears to be co-linear with the Fba glasses but not with the two Mg-rich, Fe-poor phlogopite micas (Curve 2: % RSD = 2.3 %; R^2 = 0.992), while the phlogopite micas appear to align more closely with the Fe-poor, high-silica glasses (Curve 3: % RSD = 0.17; R^2= 0.999). Figure 3.8 (c) shows a detailed view of the calibration lines that include the high-silica glasses and the phlogopite micas. The solid line is the regression line with F-phlog as the high-F anchor (Curve 3). The dashed line is the regression if F-phlog is removed from the fit (Curve 4: % RSD = 3.4 %; R^2= 0.992). Figure 3.8 (d) shows the silica-corrected *positive* secondary ion ratios $^{19}F^+/^{30}Si^+$ for the Fba glasses, Bt-3, and F-phlog versus their F content from EPMA and the literature. The regression line (Curve 5: % RSD = 1.0%, R^2 = 0.998) displays co-linearity among the Fba glasses, Bt-3, and F-phlog, suggesting that matrix effects for the above phases may be minimized when corrected for silica content. However, SIMS matrix effects are shown to be prevalent when the silica-corrected

positive secondary ion ratios $^{19}F^{+}/^{30}Si^{+}$ for the high-silica glasses NIST-610, UTR-2, and KE-12 are compared with the basalt and mica phases (Figure 3.8 e). Two distinct regression lines can be drawn, one grouping the basalt and mica phases (Curve 5) and the other grouping the high-silica glasses (Curve 6). The difference between the slopes of the two regression lines is nearly a factor of 3.

In Figure 3.8 (a-e), the slope of each calibration line generates a calibration factor (CF) which allows one to assign an F concentration value to an unknown sample analyzed by SIMS. Although we analyzed a silica blank (a very low F ion signal observed in quartz glass), our calibration lines are forced through the origin, which simplifies the calculation of the CF to be just the reciprocal of the slope. The CF is then multiplied by the appropriate ion ratios or silica-corrected ion ratios of the unknown sample to yield the F concentration. For the calibration curves generated by the negative secondary ion ratios $^{19}F/^{18}O$, the CF for Curve 2 is 96.7 (Fig. 3.8 b), and for Curve 3 (Fig. 3.8 b) the CF is 161.6. The two CFs are different by about 50 %, or nearly a factor of 2, which would lead to significant errors in F concentrations if the standards and unknowns are not sufficiently matrix-matched for SIMS analysis. Note that the calibration factors assume 1) variation in the oxygen contents of the samples is small (the vast majority of silicates contain 62±5 mol % oxygen), and 2) matrix dependence of the $^{18}O^{-}$ ion yield is also small.

5.3 Comparison of Ion Yields for F^{-} and F^{+} Secondary Ions

In SIMS analysis, a major influence on the secondary ion yield is the ionization potential (IP) for positive ion production and the electron affinity (EA) when studying negative ions. The IP is the energy needed to remove an electron from an isolated atom or molecule in the gaseous state, thus giving the species a net positive charge. IP governs the ionic yield of positive secondary ions. The EA is the energy release associated with the capture of an electron by an isolated atom or molecule in the gaseous state, giving the species a net negative charge. EA governs the ionic yield of negative secondary ions. The IPs and EAs for the elements are known. For the elements

we measured on the SIMS: Fluorine (IP=17.42 eV, EA=3.40 eV), Oxygen (IP=13.618 eV, EA=1.462 eV), Silicon (IP=8.151 eV, EA=1.385 eV) (Wilson et al. 1989, Stern 2009). Fluorine has both a high IP and a high EA, meaning F readily forms negative secondary ions but does not easily form positive secondary ions.

Ion yields of F^- and F^+ for the Fba glasses were calculated using equation (6):

Intensity (cps) / Conc. F (ppm) / Primary Current (nA) (6)

Intensity (cps) = the average counts per second of the F signal
Conc. F (ppm) = the concentration of F in the material
Primary Current (nA) = the average primary current in nA

Table 3.8 lists the nominal F concentrations for the Fba glasses, the average intensities of the F signal from the Fba glasses for both the F^- and F^+ analyses, the average primary current for the analyses, and the calculated ion yields. The difference in the ion yield between F^- and F^+ is large. The negative secondary ion yield for F is about 130 times greater than the positive secondary ion yield for F, which translates into higher sensitivity allowing for lower detection limits and the separation of interfering peaks.

5.4 Fluorine Content of USGS, MPI-DING, and ALV-519 Basalt Reference Glasses using SIMS

Several glass RMs of basaltic composition are routinely used in laboratories for the calibration of microanalytical instruments. Although these RM's have been characterized for their major and trace element compositions to various extents, their fluorine concentrations have not yet been adequately studied. We applied the Fba calibration factors from Curve 1, Curve 2, Curve 3, and Curve 5 from Figure 3.8 above to the SIMS measurements of F in the following basaltic glasses: ALV-519; BCR-2G, BHVO-2G, GSA-1G, GSC-1G, GSD-1G, and GSE-1G (USGS); and ML3B-G and KL2-G (MPI-DING). Table 3.9 lists the results of the SIMS measurements and the F content of

the USGS, MPI-DING, and ALV-519 glasses based on the four calibration curves. Also listed in Table 3.9 are the literature values of F for the glasses, if available. Table 3.9 shows the wide variability in F values when calibration curves are not matrix-matched to unknowns. Curve 1 is composed of all the glass and crystal RM's, but the R^2 value is low (0.92) and the % RSD is high (7.0%) compared to the other curves. Curve 2 is composed of the Fba glasses and Bt-3 and is the most closely matrix-matched to these broadly basaltic glasses. Curve 3 is composed of the high-silica glasses (NIST-610, UTR-2, KE-12) and the phlogopite crystals, and shows a much higher CF than the matrix-matched values from Curve 2. Curve 5 reflects the CF from measuring positive secondary ions sputtered from Fba glasses, biotite and F-phlog.

We surmise that Curve 2 gives the most reasonable values for the concentration of F in the glass samples due to a number of factors. First, Curve 2 is based on the Fba glasses and the Bt-3 crystal and is thus most similar chemically to the unknown glass samples. Second, Curve 2 shows that the products of fusing BCR-2 and BHVO-2 to form BCR-2G and BHVO-2G lost F relative to the parent (Table 3.9, Literature Values). Because the present study experienced volatile loss of F when we fused our powder mixtures to create the Fba glasses, we find it reasonable that there would be F-loss upon synthesizing BCR-2G and BHVO-2G. Third, Curves 1 and 3 suggest glasses BCR-2G and BHVO-2G *increased* their F content upon fusing, which we find unlikely. Although Curve 1 gives an F value for ALV-519 that is close to its literature value, it still overestimates the F content of BCR-2G and BHVO-2G and the lower correlation coefficient in the regression for Curve 1 leads to relatively high uncertainties in fluorine concentrations. Curve 5 produces F concentration similar to those generated by Curve 2 for all the basaltic glasses except BHVO-2G and BCR-2G, whose F values are much lower than with Curve 2 and whose relative abundances are reversed. BHVO-2G shows lower F content than BCR-2G with Curve 5 than with any other calibration curve.

6. Conclusions

Five fluorine-bearing basaltic glasses (annotated as Fba-1, Fba-2, Fba-3, Fba-4, Fba-5) were synthesized for use as new fluorine microanalytical reference materials for the calibration of analytical instruments and for the determination of the fluorine content of low-silica glasses and minerals. To determine the F content of the newly synthesized Fba glasses, we used EPMA calibrated for F with MgF_2 (61 wt.% F), Biotite-3 (3.3 wt.% F), and synthetic fluorphlogopite (9.02 wt.% F). We performed both the peak count and peak integration methods and found that the peak integration method gave the same (within acceptable errors) F contents regardless of the standards used.

The F content of the five new RMs are Fba-1 (1320±480 ppm F), Fba-2 (5300±1100 ppm F), Fba-3 (8650±1050 ppm F), Fba-4 (14100±1100 ppm F), and Fba-5 (22400±1250 ppm F). The homogeneity of the Fba glasses was determined by both SIMS and EPMA. Based on the definition of heterogeneity as proposed by Jochum et al. (2000, 2005, 2006), SIMS and EPMA determined that Fba-1 was the only Fba glass that displayed heterogeneity at the scale of our analyses.

We constructed a SIMS calibration curve using the Fba glasses and Bt-3 to determine the F content of some common microanalytical glass standards routinely used in laboratories. The F content of these glasses are ALV-519 (76±4 ppm), BCR-2G (320±15 ppm), BHVO-2G (295±14 ppm), GSA-1G (7±1 ppm), GSC-1G (9±1 ppm), GSD-1G (18±2 ppm), GSE-1G (153±7 ppm), ML3B-G (47±2 ppm), and KL2-G (81±4 ppm).

We showed the importance of matrix-matching the RMs forming a calibration curve with the composition of the unknown samples. There could be as much as a 50 % difference in the calibration factors between curves composed of basaltic RMs and curves composed of high-silica RMs. The use of positive secondary ions for fluorine analysis by SIMS shows lower sensitivity than negative ions, but appears to show smaller effects of matrix on ion yields (at least for low-silica materials).

Lastly, we conducted a first-order attempt to determine the equilibrium partition coefficient of F between CO_2 gas and basaltic melt based solely on the amount of F loss from the Fba samples during fusing in the one-atmosphere furnace. The $D_F^{CO_2-melt}$ was determined to be 0.28±0.01, indicating that F is slightly incompatible in CO_2 gas. This D_F value may have great implications in monitoring the syn-eruptive and quiescent degassing behavior of active volcanoes.

7. References

Aiuppa, A. (2009) Degassing of halogens from basaltic volcanism: Insights from volcanic gas observations. Chemical Geology, 263, 99-109.

Aiuppa, A., Bake,r D. and Webster, J. (2009) Halogens in volcanic systems. Chemical Geology, 263, 1-18.

Alletti, M., Baker, D.R., and Freda, C. (2007) Halogen diffusion in basaltic melt. Geochimica et Cosmochimics Acta, 71, 3570-3580.

Balcone-Boissard ,H., Michel, A. and Villemant, B. (2009) Simultaneous Derermination of Fluorine, Chlorine, Bromine and Iodine in Six Geological Reference Materials Using Pyrohydrolysis, Ion Chromatography and Inductively Coupled Plasma-Mass Spectrometry. Geostandards and Geoanalytical Research, 33, 477-485.

Bastin, G.F. and Heijligers, J.M. (1991) Quantitative Electron Probe Microanalysis of Ultra-Light Elements (Boron - Oxygen). In: Heinrich K.F.J. and Newberry, D.E. (eds), Electron Probe Quantitation. Plenum Press (New York), 145-161.

Bell, D.R., Hervig, R.L., Buseck, P.R. and Aulbach, S. (2009) Lithium isotope analysis of olivine by SIMS: Calibration of a matrix effect and application to magmatic phenocrysts. Chemical Geology, 258, 5-16.

Bell, D.R. and Rossman, G.R. (1992) Water in Earth's mantle: The role of nominally anhydrous minerals. Science, 255, 1391-1397.

Boyle, D.R. (1981) The analysis of fluorine in geochemical exploration. Journal of Geochemical Exploration, 14, 175-197.

Carroll, M.R. and Webster, J.D. (1994) Solubilities of sulfur, noble gases, nitrogen, chlorine, and fluorine in magmas. In: Carroll, M.R. and Holloway, J.R. (eds), Volatiles in Magmas. Reviews in Mineralogy Volume 30. Mineralogical Society of America (Washington, D.C.), 231-279.

Chevychelov, V.Y., Botcharnokov, R.E., and Holtz, F. (2008) Partitioning of Cl and F between fluid and hydrous phonolitic melt of Mt. Vesuvius at ~850-1000 C and 200 Mpa. Chemical Geology, doi:10.1016/j.chemgeo.2008.06.025.

Collins, W., Beams, S., White, A.J.R. and Chappell, B. (1982) Nature and origin of A-type granites with particular reference to southeastern Australia. Contributions to Mineralogy and Petrology, 80, 189-200.

Deline, V., Katz, W., Evans, C. and Williams, P. (1978) Mechanism of the SIMS matrix effect. Applied Physics Letters, 33, 832-835.

Dingwell, D.B. (1985) The structures and properties of fluorine-rich magmas: A review of experimental studies. In: Taylor, R.P. and Strong, D.F. (eds), Recent Advances in the Geology of Granite-Related Mineral Deposits. Canadian Institute of Mining and Metallurgy (Montreal), 1-12.

Dingwell, D.B., Scarfe, C.M. and Cronin, D.J. (1985) The effect of fluorine on viscosities in the system Na_2O-Al_2O_3-SiO_2: implications for phonolites, trachytes and rhyolites. American Mineralogist, 70, 80-87.

Eiler, J.M., Graham, C. and Valley, J.W. (1997) SIMS analysis of oxygen isotopes: Matrix effects in complex minerals and glasses. Chemical Geology, 138, 221-244.

Gasparik, T. (1993) The role of volatiles in the transition zone. Journal of Geophysical Research, 98, 4287-4299.

Gasparik, T. (1990) Phase relations in the transition zone. Journal of Geophysical Research, 5, 15751-15769.

Guggino, S.N. and Hervig, R.L. (2011) Synthesis and Characterization of Five New F-bearing Basalt Reference Materials (Fba Glasses): Quantifying the Fluorine Content of the Basaltic Glass Standards BCR-2G, BHVO-2G. GSA-1G, GSC-1G, GSD-1G, GSE-1G, ML3B-G, KL2-G, and ALV-519-4. Abstract. American Geophysical Union Fall Meeting.

Guggino, S.N. and Hervig, R.L. (2010) Determination of fluorine in fourteen microanalytical geologic reference materials using SIMS, EPMA, and proton Induced Gamma Ray Emission (PIGE) Analysis. Abstract, American Geophysical Union Fall Meeting.

Guggino, S., Hervig, R. and Bell, D. (2007) Fluorine in olivines from plutonic, extrusive, and hypabyssal suites. American Geophysical Union Fall Meeting Abstract.

Hauri, E.H., Weinreich, T., Saal, A., Rutherford, M.C., and Van Orman, J.A. (2011) High pre-eruptive water contents preserved in lunar melt inclusions. Science, 333, 213-215.

Hauri, E., Wang, J., Dixon, J.E., King, P.L., Mandeville, C. and Newman, S. (2002) SIMS analysis of volatiles in silicate glasses 1: Calibration, matrix effects and comparisons with FTIR. Chemical Geology, 183, 99-114.

Hauri, E. (2002) SIMS analysis of volatiles in silicate glasses 2: isotopes and abundances in Hawaiian melt inclusions. Chemical Geology, 183, 115-141.

Hazen, R.M., Yang, H., Prewitt, C.T. and Gasparik, T. (1997) Crystal chemistry of superflourous phase B ($Mg_{10}Si_3O_{14}F_4$): Implications for the role of fluorine in the mantle. American Mineralogist, 82, 647-650.

Hervig, R. and Bell, D. (2005) Fluorine and hydrogen in mantle megacrysts. American Geophysical Union Fall Meeting Abstract..

Hervig, R.L., Mazdab, F.K., Moore, G. and McMillan, P.F. (2003) Analyzing hydrogen (H_2O) in silicate glass by secondary ion mass spectrometry and reflectance Fourier transform infrared spectroscopy. In: De Vivo, B. and Bodnar, R.J. (eds) Melt Inclusions in Volcanic Systems: Methods Applications and Problems. Developments in Volcanology 5. Elsevier, 83-103.

Hervig, R.L., Williams, P., Thomas, R.M., Schauer, S.N. and Steele, I.M. (1992) Microanalysis of oxygen isotopes in insulators by secondary ion mass spectrometry. International Journal of Mass Spectrometry and Ion Processes, 120, 45-63.

Hervig, R.L., Dunbar, N., Westrich, H.R., Kyle, P.R. (1989) Pre-eruptive water content of rhyolitic magmas as determined by ion microprobe analyses of melt inclusions in phenocrysts. Journal of Volcanology and Geothermal Research, 36, 293-302

Hervig, R.L., Smith, J.V. and Rivers, M.L. (1988) Fluorine content of upper mantle minerals. EOS, Transactions of the American Geophysical Union, 69, 502.

Hervig, R.L., Kortemeier, W.T. and Burt, D.M. (1987) Ion-microprobe analyses of Li and B in topaz from different environments. American Mineralogist, 72, 392-396.

Hinton, R., Harte, B. and Witt-Eickschen, G. (1995) Ion probe measurements of National Institute of Standards and Technology standard reference material SRM 610 glass, trace elements. Analyst, 120, 1315-1319.

Hirschmann, M.M., Aubaud, C., and Withers, A.C. (2005) Storage capacity of H_2O in nominally anhydrous minerals in the upper mantle. Earth and Planetary Science Letters, 236, 167-181.

Hoskin, P.W.O. (1999) SIMS Determination of μg g^{-1} - Level Fluorine in Geological Samples and its Concentration in NIST SRM 610. Geostandards Newsletter, 23, 69-76.

Jochum, K.P., Stoll, B., Herwig, K., Willbold, M., Hofmann, A.W., Amini, M., Aarburg, S., Abouchami, W., Hellebrand, E., Mocek, B., Raczek, I., Stracke, A., Alard, O., Bouman, C., Becker, S., Ducking, M., Bratz, H., Klemd, R., de Bruin, D., Canil, D., Cornell, D., de Hoog, C.J., Dalpe, C., Danushevsky, L., Eisenhauer, A., Gao, Y., Snow, J.E., Groschopf, N., Gunther, D., Latkoczy, C., Guillong, M., Hauri, E., Hofer, H.E., Lahaye, Y., Horz, K., Jacob, D.E., Kasemann, S.A., Kent, A.J.R., Ludwig, T., Zack, T., Mason, P.R.D., Meixner, A., Rosner, M., Misawa, K., Nash, B.P., Pfander, J., Premo, W.R., Sun, W.D., Tiepolo, M., Vannucci, R., Vennemann, T., Wayne, D., Woodhead, J.D. (2006) MPI-DING reference glasses for in situ microanalysis: New reference values for element concentrations and isotope ratios. Geochemistry, Geophysics, Geosystems, Technical Brief, 7, 44 p.

Jochum, K.P., Willbold, M., Raczek, I., Stoll, B., Herwig, K. (2005) Chemical Characterization of the USGS Reference Glasses GSA-1G, GSC-1G, GSD-1G, GSE-1G, BCR-2G, BHVO-2G and BIR-1G Using EPMA, ID-TIMS, ID-ICP-MS, and LA-ICP-MS. Geostandards and Geoanalytical Research, 29, 285-302.

Jochum, K.P., Dingwell, D.B., Rocholl, A., Stoll, B., Hofmann, A.W., Becker, S., Besmehn, A., Bessette, D., Dietze, H.J. and Dulski, P. (2000) The Preparation and Preliminary Characterization of Eight Geological MPI-DING Reference Glasses for In-Situ Microanalysis. Geostandards Newsletter, 24, 87-133.

Johnson, M.C., Anderson, A.T., and Rutherford, M.J. (1994) Pre-eruptive volatile contents of magmas. In: Carroll, M.R. and Holloway, J.R. (eds), Volatiles in Magmas. Reviews in Mineralogy Volume 30. Mineralogical Society of America (Washington, D.C.), 281-330.

Kane, J.S. (2001) The use of reference materials: A tutorial. Geostandards Newsletter, 25, 7-22.

Kane, J.S. and Potts, P.J. (1999) An interpretation of ISO Guidelines for the certification of geological reference materials. Geostandards Newsletter, 23, 209-221.

Köhler, J., Schönenberger, J., Upton, B., and Markl, G. (2009) Halogen and trace-element chemistry in the Gardar Province, South Greenland: Subduction-related mantle metasomatism and fluid exsolution from alkalic melts. Lithos, 113, 731-747.

Kovalenko, V., Hervig, R.L. and Sheridan, M.F. (1988) Ion-microprobe analyses of trace elements in anorthoclase, hedenbergite, aenigmatite, quartz, apatite, and glass in pantellerite: evidence for high water contents in pantellerite melt. American Mineralogist, 73, 1038-1045.

London, D., Hervig, R.L., and Morgan, G.B. (1988) Melt-vapor solubilities and elemental partitioning in peraluminous granite-pegmatite systems: Experimental results with Macusani glass at 200 MPa. Contributions to Mineralogy and Petrology, 99, 360-373.

Macdonald, R. and Bailey, D.K. (1973) Chapter N. Chemistry of Igneous Rocks Part 1. The Chemistry of Peralkaline Oversaturated Obsidians. In: Fleischer, M. (eds), Data of Geochemistry 6th Edition. Geological Survey Professional Paper 440-N-1, US Government Printing Office, Washington, 41 p.

McGee, J.J. and Keil, K. (2001) Application of electron probe microanalysis to the study of geological and planetary materials. Microscopy and Microanalysis, 7, 200-210.

Michael, P.J. (1988) The concentration, behavior and storage of H_2O in the suboceanic upper mantle: Implications for mantle metasomatism. Geochimica et Cosmochimica Acta, 52, 555-566.

Michel, A. and Villemant, B. (2003) Determination of halogens (F, Cl, Br, I), sulfur and water in seventeen geological reference materials. Geostandards Newsletter, 27, 163-171.

Mosbah, M., Metrich, N. and Massiot, P. (1991) PIGME fluorine determination using a nuclear microprobe with application to glass inclusions. Nuclear Instruments and Methods in Physics Research Section B: Beam Interactions with Materials and Atoms, 58, 227-231.

Moune, S., Sigmarsson, O., Thordarson, T. and Gauthier, P.J. (2007) Recent volatile evolution in the magmatic system of Hekla volcano, Iceland. Earth and Planetary Science Letters, 255, 373-389.

Mysen, B.O., Cody, G.D. and Smith, A. (2004) Solubility mechanisms of fluorine in peralkaline and meta-aluminous silicate glasses and in melts to magmatic temperatures. Geochimica et Cosmochimica Acta, 68, 2745-2769.

Nicolson, K. (1983) Fluorine determination in geochemistry: errors in the electrode method of analysis. Chemical Geology, 38, 1-22.

O'Leary, J.A., Gaetani, G.A. and Hauri, E.H. (2010) The effect of tetrahedral Al^{3+} on the partitioning of water between clinopyroxene and silicate melt. Earth and Planetary Science Letters, 297, 111-120.

Ottolini, L., Cámara, F., Hawthorne, F.C. and Stirling, J. (2002) SIMS matrix effects in the analysis of light elements in silicate minerals: Comparison with SREF and EMPA data. American Mineralogist, 87, 1477-1485.

Ottolini, L., Cámara, F. and Bigi, S. (2000) An investigation of matrix effects in the analysis of fluorine in humite-group minerals by EMPA, SIMS, and SREF. American Mineralogist, 85, 89-102.

Palais, J.M. and Sigurdsson, H. (1989) Petrologic evidence of volatile emissions from major historic and pre-historic volcanic eruptions. In Berger, A., Dickinson, R.E., Kidson, J.W. (eds), Understanding Climate Change, Geophysical Monograph 52, 31-53.

Pan, Y. and Fleet, M.E. (1996) Rare earth element mobility during prograde granulite facies metamorphism: significance of fluorine. Contributions to Mineralogy and Petrology, 123, 251-262.

Portnyagin, M., Simakin, S. and Sobolev, A. (2002) Fluorine in primitive magmas of the Troodos Ophiolite complex, Cyprus: analytical methods and main results. Geochemistry International, 40, 625-632.

Reed, S.J.B. (2005) Electron Microprobe Analysis and Scanning Electron Microscopy in Geology. Cambridge University Press, Cambridge.

Robert, J.L., Bény, J.M., Della Ventura, G. and Hardy, M. (1993) Fluorine in micas: crystal-chemical control of the OH-F distribution between trioctahedral and dioctahedral sites. European Journal of Mineralogy, 5, 7-18.

Sawyer, G.M. and Oppenheimer, C. (2006) Volcanic fluorine emissions: Observations by Fourier transform infrared spectroscopy. In: Tressaud, A. (eds), Fluorine and the Environment: Atmospheric Chemistry, Emissions, & Lithosphere. Elsevier (San Francisco), 165-185.

Scaillet, B. and Macdonald, R. (2004) Fluorite stability in silicic magmas. Contributions to Mineralogy and Petrology, 147, 319-329.

Sigvaldason, G.E and Oskarsson, N (1986) Fluorine in basalts from Iceland. Contributions to Mineralogy and Petrology, 94, 263-271.

Smith, J.V. (1981) Halogen and Phosphorous Storage in the Earth. Nature, 289, 762-765.

Smith, J., Delaney, J., Hervig, R. and Dawson, J. (1981) Storage of F and Cl in the upper mantle: Geochemical implications. Lithos, 14, 133-147.

Spilliaert, N., Métrich, N. and Allard, P. (2006) S–Cl–F degassing pattern of water-rich alkali basalt: Modeling and relationship with eruption styles on Mount Etna volcano. Earth and Planetary Science Letters, 248, 772-786.

Stanton, T.R., Holloway, J.R., Hervig, R.L., Stolper, E. (1985) Isotope effect on water diffusivity in silicic melts: an ion microprobe and inrared analysis. EOS, Transactions of the American Geophysical Union, 66, 1131 (abstract).

Stecher, O. (1998) Fluorine geochemistry in volcanic rock series: examples from Iceland and Jan Mayen. Geochimica et Cosmochimica Acta, 62, 3117-3130.

Stern, R.A. (2009) Chapter 1: An introduction to secondary ion mass spectrometry (SIMS) in geology. In: Fayek, M. (eds) Secondary Ion Mass Spectrometry in the Earth Sciences: Gleaning the Big Picture from a Small Spot. Mineralogical Association of Canada Short Course, vol. 41, p. 1-18.

Stix, J. and Layne, G.D. (1996) Gas saturation and evolution of volatile and light lithophile elements in the Bandelier magma chamber between two caldera-forming eruptions. Journal of Geophysical Research, 101, 25181-25196.

Stolpe,r E. (1982) The speciation of water in silicate melts. Geochimica et Cosmochimica Acta, 46, 2609-2620.

Straub, S.M. and Layne, G.D. (2003) The systematics of chlorine, fluorine, and water in Izu arc front volcanic rocks: Implications for volatile recycling in subduction zones. Geochimica et Cosmochimica Acta, 67, 4179-4203.

Sykes, D., Rossman, G.R., Veblen, D.R., Grew, E.S. (1994) Enhanced H and F incorporation in borian olivine. American Mineralogist, 79, 904-908.

Symonds, R.B., Rose, W.I., Bluth, G.J.S. and Gerlach, T.M. (1994) Volcanic-gas studies: methods, results, and applications. In: Carroll, M.R. and Holloway, J.R. (eds), Volatiles in Magmas. Reviews in Mineralogy Volume 30. Mineralogical Society of America (Washington, D.C.), 1-66.

Tagirov, B., Schott, J., Harrichourry, J.C. and Salvi, S. (2002) Experimental study of aluminum speciation in fluoride-rich supercritical fluids. Geochimica et Cosmochimica Acta, 66, 2013-2024.

Wang, Q., Makishima, A., Nakamura, E. (2010) Determination of fluorine and chlorine by pyrohydrolysis and ion chromatography: Comparison with alkaline fusion digestion and ion chromatography. Geostandards and Geoanalytical Research, 34, 175-183.

Watson, E.B. (1994) Diffusion in volatile-bearing magmas. In: Carroll, M.R. and Holloway, J.R. (eds), Volatiles in Magmas. Reviews in Mineralogy Volume 30. Mineralogical Society of America (Washington, D.C.), 371-411.

Westrich, H.R. (1987) Determination of water in volcanic glasses by Karl-Fischer titration. Chemical Geology, 63, 335-340.

Williams-Jones, A.E., Samson, I.M. and Olivo, G.R. (2000) The genesis of hydrothermal fluorite-REE deposits in the Gallinas Mountains, New Mexico. Economic Geology, 95, 327-341.

Wilson, R.G., Stevie, F.A., Magee, C.W. (1989) Secondary Ion Mass Spectrometry: A Practical Handbook for Depth Profiling and Bulk Impurity Analysis. Jon Wiley and Sons. New York.

Witter, J.B. and Kuehner, S.M. (2004) A simple empirical method for high-quality electron microprobe analysis of fluorine at trace levels in Fe-bearing minerals and glasses. American Mineralogist, 89, 57-63.

Young, E., Myers A., Munson, E. and Conklin, N. (1969) Mineralogy and geochemistry of fluorapatite from Cerro de Mercado, Durango, Mexico. US Geological Survey Professional Paper, 650, D84-D93.

8. Figure Captions

Figure 3.1. Wavelength scans of Biotite-3 and Synthetic Fluor-phlogopite using the Cameca SX-100 electron microprobe at the University of Arizona EPMA lab. The scans were conducted simultaneously on two spectrometers using TAP crystals. Peak positions showed a small peak shift of <0.05 Å. Each scan also shows the presence of a satellite peak on the lower wavelength side, prompting the use of integral analysis of F.

Figure 3.2. SIMS high-resolution mass spectrum of NIST-610. Negative secondary ion intensities of F show the separation between the $^{19}F^-$ and $^{18}OH^-$ peaks. Mass resolving power (M/ΔM) is 2500.

Figure 3.3. SIMS 6f determination of homogeneity of the Fba glasses and mica F standards. See text for details. The repeatability of the SIMS with respect to F was conducted on the homogeneous glasses silica blank, NIST-610, KE-12, and UTR-2 [average % Relative Standard Error (% RSE) = 1.92]. The dashed line represents 3 times the instrument repeatability (3 times the average % RSE of silica blank, NIST-610, KE-12, and UTR-2). All the Fba-glasses (except Fba-1) and the mica standards exhibit homogeneity with respect to F.

Figure 3.4. Precision of both the peak-count and peak integration methods between various F calibration standards expressed as percent difference. The peak-count method shows wide variations in precision between standards, while the peak integration method (solid black circles and line) shows that the variability between the standards Bt-3 and F–phlog is less than 6 %.

Figure 3.5. EPMA (peak integration method) determination of homogeneity of the Fba glasses with respect to F as defined by Jochum et al. (2000, 2005, 2006). See text for details. The repeatability of the EPMA was conducted on synthetic F-phlog (% RSE = 3.06). The dashed line represents 3 times the instrument repeatability (3 times the % RSE of F-phlog). Based on EPMA analysis, Fba-1 exhibits heterogeneities above the defined threshold of 3.06 % RSE, while Fba-2, -3, -4, and -5 show homogeneous distribution of F. Biotite-3 was used as the calibration standard for the analyses.

Figure 3.6. Fluorine concentration (wt.%) of pre-fusing initial powder aliquots versus the mass loss of fluorine (wt.%) after fusing. The trend shows that a larger portion of F loss occurred with higher initial F concentration.

Figure 3.7 (a) Fluorine content of the Fba glasses versus the apparent partition coefficient (APC) of F between CO_2 gas and the basaltic melt. The Nernst partition coefficient (see Equation 5), was calculated for each Fba glass using the data from Table 3.6 (see text for details), and the plot appears to show a hyperbolic curve. (b) The reciprocal of the measured F content of the Fba glasses versus the APC. The curve defines a straight line that intersects the y-axis at y=0.28, suggesting that the equilibrium partition coefficient of F between CO_2 fluid and melt, $D_F^{fluid-melt}$, is about 0.28±0.01.

Figure 3.8. SIMS calibration curves generated from the data in Table 7 showing the variability in fluorine measurements due to matrix effects. All the regression lines were forced through the origin. (a) All the Fba glasses, high-silica glasses, and mica standards plotted together. Regression line has a % RSD of 7.0%. (b) Bt-3 appears to plot more co-linear with the Fba glasses than with the phlogopite micas (Curve 2, % RSD = 2.3 %). Phlogopite micas appear to plot more co-linear with the high-silica glasses (Curve 3, % RSD = 0.17 %). (c). Detailed view of the calibration lines that include the high-silica glasses and the phlogopite micas. Solid line (Curve 3) is the regression line with F-phlog as the high-F anchor (% RSD = 0.17 %). Dashed line (Curve 4) is the regression line without KE-12 (F = 4000 ppm) as the high-F anchor (% RSD = 3.4 %). (d) The silica-corrected positive secondary ion ratios $^{19}F^{+}/^{30}Si^{+}$ for the Fba glasses, Bt-3, and F-phlog lie on the same regression line and show that matrix effects appear to be minimized for basalts and micas when corrected for silica content. %RSD of the regression line is 1.0 %. (e) The silica-corrected positive secondary ion ratios $^{19}F^{+}/^{30}Si^{+}$ for the Fba glasses, Bt-3, F-phlog, and the high-silica glasses NIST-610, UTR-2, and KE-12. Two distinct regression lines are shown demonstrating the pervasiveness of matrix effects with SIMS.

Table 3.1. Masses of EPR-2001 and CaF_2 (96 % pure) powders to achieve desired F concentrations in final powder mixtures.

Sample Name	Mass of EPR-2001 (g)	Mass of CaF_2 (g)	Total mass of pwdr mix (g)	[a]Mass of F in pwdr mix (g)	[a]Conc. of F in pwdr mix (ppm)
Fba-0	2.5012	0	2.5012	0	0
Fba1	2.4732	0.0272	2.5004	0.0132	0.5294
Fba2	2.4464	0.0539	2.5003	0.0262	1.0491
Fba3	2.4197	0.0807	2.5004	0.0393	1.5707
Fba4	2.3932	0.1076	2.5008	0.0524	2.0940
Fba5	2.3401	0.161	2.5011	0.0784	3.1328

a. Mass and concentration of F in powder mixture does not include the initial amount of F present in EPR-2001.

Table 3.2. Analytical Instruments, operating conditions, and fluorine standards for analysis of the Fba glasses.

Instrumentation				Operating Conditions							Calibration Standards	
Method	Lab	Instr.	Anal. Type	Beam Current	Accel. Voltage	Beam Size	Prim. Beam	Second. Beam	Crystal	Energy Filtering	Fluorine Standard	F Conc.
SIMS	ASU	Cameca ims 6f	Spot	3.5 nA	-5 keV	30 µm	$^{16}O^-$	negative	--	None	NIST 610[1] UTR-2[1]	295 (ppm)[2] 1143 (ppm)[2]
SIMS	ASU	Cameca ims 6f	Spot	16.5 nA	+9 keV	30 µm	$^{16}O^-$	positive	--	40V window -75V offset	NIST 610 UTR-2	
EPMA	ASU	JEOL 8600 Superprobe	Peak-Count	25 nA	15 keV	15 µm	e^-	F Kα	TAP	--	MgF_2 Biotite-3	61 (wt.%) 3.3 (wt.%)[3]
EPMA	UofA	Cameca SX100	Peak-Count	10 nA	15 keV	20 µm	e^-	F Kα	TAP	--	syn. F-phlog.	9.02 (wt.%)[4]
EPMA	UofA	Cameca SX100	Peak-Integr.	20 nA	15 keV	20 µm	e^-	F Kα	TAP	--	Biotite-3 syn. F-phlog.	

1. NIST 610 and UTR-2 are used as internal calibration standards to check the precision of the instrument.
   Typical $^{19}F/^{18}O$ ion ratios for NIST 610 is 0.95 to 1.0. Typical $^{19}F/^{18}O$ ion ratios for UTR-2 is 6.8 to 7.0.
2. NIST 610 = 295 ppm (Hoskins, 1999); UTR-2 = 1143 ppm (Stix, personal communication).
3. G. Moore personal comm.
4. Syntetic fluorphlogopite = 9.02 wt.%, stoichiometric (Smith et al. 1981)

Table 3.3. Average SIMS values and % RSD of the homogeneous F standard glasses, the Fba glasses, and mica standards.

	Sample	n	^{19}F / ^{18}O	1σ	std error	% RSE
F Stds	Silica Blank	3	0.0069	0.00023	1.3E-04	1.9
	NIST-610	4	0.95	0.014	6.9E-03	0.7
	UTR-2	2	6.35	0.093	0.0661	1.0
	KE-12	3	23.49	0.35	0.2035	0.9
Fba Glasses	Fba-1	7	17.52	1.84	0.6954	4.0
	Fba-2	7	67.90	1.15	0.4364	0.6
	Fba-3	5	102.92	1.73	0.7740	0.8
	Fba-4	6	154.11	2.47	1.0079	0.7
	Fba-5	6	231.23	4.58	1.8704	0.8
Mica Stds	F-phlog.	5	562.62	14.40	6.4389	1.1
	Phlog. 73-77	4	6.71	0.20	0.1012	1.5
	Bt-3	6	337.16	15.06	6.1464	1.8

Table 3.4. Electron probe microanalysis of the major, trace, and fluorine abundances of the Fba glasses, Bt-3, and F-phlogopite. Both the peak-count and peak-integration methods are shown. All elemental and oxide values in wt.%.

Sample	n	F	1 σ	% [b]RSE	SiO_2	TiO_2	Al_2O_3	FeO	MgO	CaO	Na_2O	K_2O	MnO	Total
Peak Count Method														
EPMA Lab: ASU; F Standard: MgF_2 (61 % m/m F); 25 nA; 15 keV; 15 µm beam; 45 s														
Fba-0	5	bdl	--	--	47.4 (1)[a]	1.2 (2)	18.3 (4)	8.7 (3)	7.6 (1)	12.3 (0.4)	2.5 (2)	0.11 (36)	--	98.1
Fba-1	7	0.20	0.08	15	49.6 (1)	1.3 (2)	16.6 (1)	8.8 (1)	8.2 (1)	13.0 (2)	2.6 (2)	0.10 (16)	--	100.3
Fba-2	8	0.64	0.12	7	49.1 (0.4)	1.3 (2)	16.6 (1)	8.7 (2)	8.1 (1)	13.6 (1)	2.5 (3)	0.10 (14)	--	100.6
Fba-3	8	1.01	0.14	5	48.4 (0.4)	1.3 (2)	16.8 (1)	8.5 (2)	7.9 (0.3)	14.2 (1)	2.5 (2)	0.10 (16)	--	100.7
Fba-4	7	1.39	0.07	2	46.4 (1)	1.2 (4)	18.8 (1)	8.3 (1)	7.8 (0.3)	14.6 (1)	2.3 (3)	0.08 (14)	--	100.9
Fba-5	10	2.26	0.13	2	44.9 (2)	1.2 (2)	18.2 (2)	8.3 (3)	7.6 (1)	16.0 (1)	2.3 (3)	0.08 (16)	--	100.9
Bt-3	4	2.80	0.12	2	38.1 (3)	2.3 (2)	11.0 (2)	17.2 (2)	13.5 (2)	bdl	0.6 (5)	8.4 (4)	--	94.0
EPMA Lab: ASU; F Standard: Bt-3 (3.3 % m/m F); 25 nA; 15 keV; 15 µm beam; 45 s														
Fba-0	7	bdl	--	--	48.7 (1)	1.3 (2)	19.3 (2)	8.7 (1)	8.1 (1)	11.9 (2)	2.5 (3)	0.09 (3)	--	100.6
Fba-1	7	0.19	0.09	19	48.7 (1)	1.3 (2)	16.0 (2)	9.0 (2)	7.7 (2)	13.2 (1)	2.5 (2)	0.10 (9)	--	98.7
Fba-2	7	0.73	0.14	7	48.0 (1)	1.2 (2)	16.0 (1)	8.8 (2)	7.6 (1)	13.9 (1)	2.5 (2)	0.10 (14)	--	98.9
Fba-3	7	1.04	0.09	3	47.3 (1)	1.2 (4)	16.2 (2)	8.7 (2)	7.5 (2)	14.5 (1)	2.5 (2)	0.10 (11)	--	99.0
Fba-4	7	1.59	0.11	3	45.7 (1)	1.2 (3)	18.3 (1)	8.3 (2)	7.4 (1)	14.6 (1)	2.3 (1)	0.07 (13)	--	99.4
Fba-5	10	2.46	0.12	2	44.1 (2)	1.1 (3)	17.8 (2)	8.4 (3)	7.1 (4)	16.0 (1)	2.3 (3)	0.08 (8)	--	99.3
Bt-3	4	3.28	0.07	1	39.3 (0.4)	2.2 (2)	11.2 (1)	17.9 (1)	13.8 (1)	bdl	0.7 (2)	8.2 (1)	--	96.5
EPMA Lab: UofA; F Standard: Bt-3 (3.3 % m/m F); 25 nA; 15 keV, 20 µm, 45 s														
Fba-0	--	--	--	--	--	--	--	--	--	--	--	--	--	--
Fba-1	3	0.24	0.02	5	49.5 (0.2)	1.3 (2)	16.8 (0.4)	9.0 (2)	8.6 (1)	13.0 (0.3)	2.5 (2)	0.10 (4)	0.17 (5)	101.2
Fba-2	3	0.71	0.01	1	48.7 (0.2)	1.3 (1)	17.0 (1)	8.8 (1)	8.5 (1)	13.6 (0.1)	2.4 (3)	0.10 (4)	0.16 (9)	101.3
Fba-3	3	1.11	0.07	4	48.1 (0.2)	1.2 (1)	17.2 (0.1)	8.7 (0.3)	8.4 (1)	14.2 (0.2)	2.3 (3)	0.10 (2)	0.17 (11)	101.5
Fba-4	3	1.71	0.05	2	46.4 (0.3)	1.2 (1)	19.1 (0.2)	8.3 (1)	8.1 (1)	14.5 (0.4)	2.2 (1)	0.09 (5)	0.16 (9)	101.8
Fba-5	3	2.48	0.04	1	45.1 (0.4)	1.2 (1)	18.8 (0.3)	8.1 (3)	7.9 (1)	15.9 (1)	2.1 (4)	0.09 (2)	0.15 (17)	101.9
Bt-3	1	3.33	0.48	14	39.6 (1)	2.2 (2)	11.4 (2)	17.8 (2)	15.0 (3)	bdl	0.6 (15)	9.1 (2)	0.92 (7)	99.9
F-phlog	4	6.99	0.42	3	42.8 (1)	bdl	12.8 (2)	bdl	30.0 (2)	bdl	bdl	11.1 (1)	bdl	103.4
EPMA Lab: UofA; F Standard: F-phlog (9.02 % m/m F); 25 nA; 15 keV, 20 µm, 45 s														
Fba-0	1	bdl	--	--	48.3 (1)	1.3 (4)	19.3 (2)	8.6 (4)	8.2 (4)	12.0 (2)	2.5 (9)	0.10 (21)	0.15 (26)	100.5
Fba-1	4	0.24	0.06	13	48.8 (0.2)	1.3 (0.4)	16.7 (1)	8.9 (2)	8.3 (0.4)	12.9 (0.3)	2.5 (3)	0.11 (7)	0.16 (6)	100.0
Fba-2	7	0.88	0.15	7	48.2 (0.2)	1.3 (2)	16.8 (1)	8.8 (1)	8.2 (1)	13.5 (1)	2.4 (2)	0.10 (4)	0.16 (5)	100.4
Fba-3	4	1.28	0.08	3	47.4 (0.3)	1.3 (1)	17.0 (0.4)	8.7 (1)	8.2 (1)	14.1 (0.2)	2.4 (3)	0.10 (3)	0.16 (9)	100.5
Fba-4	6	1.87	0.26	6	45.6 (0.2)	1.2 (1)	19.0 (0.4)	8.3 (1)	8.0 (1)	14.4 (1)	2.3 (3)	0.09 (9)	0.14 (7)	100.9
Fba-5	5	2.70	0.11	2	44.4 (1)	1.2 (2)	18.5 (1)	8.2 (4)	7.8 (1)	16.0 (1)	2.2 (4)	0.08 (11)	0.14 (9)	101.3
F-Phlog	1	9.21	1.25	14	44.7 (1)	bdl	11.5 (2)	bdl	27.7 (3)	bdl	bdl	11.2 (2)	bdl	104.4

Table 3.4. Continued.

Sample	n	F	1 σ	% [b]RSE	SiO_2	TiO_2	Al_2O_3	FeO	MgO	CaO	Na_2O	K_2O	MnO	Total
Peak Integration Method														
EPMA Lab: UofA; F Standard: Bt-3 (3.3 % m/m F); 20 nA; 15 keV; 20 µm beam diameter; 60 s; 5 repeats														
Fba-0	--	--	--	--	--	--	--	--	--	--	--	--	--	--
Fba-1	15	0.13	0.04	8	48.6 (0.2)	1.3 (2)	16.5 (1)	8.8 (1)	8.1 (1)	12.6 (0.4)	2.5 (2)	0.10 (4.4)	0.11 (11)	98.7
Fba-2	23	0.54	0.08	3	47.9 (0.3)	1.3 (2)	16.5 (1)	8.7 (1)	8.0 (1)	13.1 (0.3)	2.5 (1)	0.10 (6.3)	0.12 (11)	98.8
Fba-3	21	0.85	0.07	2	47.2 (0.3)	1.3 (1)	16.8 (0.4)	8.6 (1)	7.9 (1)	13.6 (0.2)	2.4 (2)	0.09 (6.8)	0.11 (11)	98.9
Fba-4	22	1.38	0.10	1	45.2 (0.4)	1.2 (1)	18.7 (1)	8.2 (1)	7.7 (1)	14.0 (1)	2.3 (1)	0.09 (6.2)	0.10 (17)	98.9
Fba-5	18	2.22	0.14	2	44.1 (1)	1.2 (1)	18.3 (1)	8.2 (4)	7.5 (1)	15.4 (1)	2.2 (1)	0.08 (7.6)	0.08 (14)	99.4
F-Phlog	8	9.20	0.28	1	42.8 (1)	bdl	12.8 (1)	bdl	29.1 (0.4)	bdl	bdl	11.2 (0.5)	bdl	104.9
EPMA Lab: UofA; F Standard: F-phlog (9.02 % m/m F); 20 nA; 15 keV; 20 µm beam diameter; 60 s; 5 repeats														
Fba-0	--	--	--	--	--	--	--	--	--	--	--	--	--	--
Fba-1	17	0.14	0.06	10	48.9 (0.2)	1.3 (1)	16.8 (1)	8.8 (1)	8.3 (1)	12.5 (0.4)	2.4 (2)	0.10 (8)	0.12 (8)	99.5
Fba-2	20	0.51	0.13	6	48.3 (0.3)	1.3 (1)	16.9 (1)	8.7 (1)	8.2 (1)	13.1 (0.4)	2.4 (2)	0.10 (7)	0.13 (9)	99.7
Fba-3	20	0.88	0.13	3	47.7 (0.2)	1.2 (1)	17.1 (1)	8.5 (1)	8.1 (1)	13.6 (0.3)	2.4 (2)	0.09 (7)	0.12 (8)	99.9
Fba-4	18	1.44	0.11	2	45.6 (0.3)	1.2 (1)	19.0 (0.4)	8.1 (1)	7.9 (1)	14.0 (1)	2.2 (2)	0.09 (7)	0.10 (11)	99.9
Fba-5	21	2.25	0.10	1	44.4 (1)	1.2 (1)	18.5 (1)	8.3 (3)	7.7 (1)	15.4 (0.1)	2.2 (2)	0.08 (9)	0.10 (13)	100.2
Bt-3	5	3.37	0.19	3	38.3 (0.2)	2.2 (1)	11.4 (0.4)	17.4 (1)	14.0 (1)	bdl	0.6 (3)	9.1 (0.4)	0.61 (2)	97.0
Accepted fluorine and bulk concentration values for the Fba glasses: Avereage of both UofA EPMA peak integration sessions														
Fba-1	32	0.13	0.05	6	48.7 (0.4)	1.3 (2)	16.6 (1)	8.8 (1)	8.2 (2)	12.5 (0.4)	2.5 (2)	0.10 (7)	0.11 (10)	99.1
Fba-2	43	0.53	0.11	3	48.1 (1)	1.3 (1)	16.7 (1)	8.7 (1)	8.1 (2)	13.1 (0.3	2.5 (2)	0.10 (7)	0.12 (11)	99.2
Fba-3	41	0.87	0.10	2	47.5 (1)	1.3 (1)	17.0 (1)	8.5 (1)	8.0 (2)	13.6 (0.3)	2.4 (2)	0.10 (7)	0.12 (11)	99.4
Fba-4	40	1.41	0.11	1	45.4 (1)	1.2 (1)	18.8 (1)	8.2 (1)	7.8 (2)	14.0 (1)	2.3 (2)	0.09 (7)	0.10 (15)	99.4
Fba-5	39	2.24	0.12	1	44.3 (1)	1.2 (1)	18.4 (1)	8.3 (4)	7.6 (2)	15.4 (1)	2.2 (2)	0.08 (9)	0.09 (20)	99.8

bdl = below detection limit

a. Numbers in parenthese are the % RSD of the EPMA analyses.

b. % RSE is the percent relative standard error

Table 3.5. Results of the peak-count and peak-integration methods on the Fba glasses and mica standards using the various F standards used in the analyses, showing inter-laboratory and inter-calibration precision.

Method	Peak Count								Peak Integration			
EPMA Lab	ASU			UofA			ASU	UofA	UofA			
Standards	MgF_2	Bt-3		Bt-3	F-phlog		Bt-3	Bt-3	Bt-3	F-phlog		
Sample	F (wt.%)	F (wt.%)	%diff	F (wt.%)	F (wt.%)	%diff	F (wt.%)	F (wt.%)	% diff	F (wt.%)	F (wt.%)	%diff
Fba-1	0.20	0.19	8.8	0.24	0.24	0.4	0.19	0.24	26.7	0.13	0.14	5.6
Fba-2	0.64	0.73	12.8	0.71	0.88	20.6	0.73	0.71	2.4	0.54	0.51	6.0
Fba-3	1.01	1.04	2.8	1.11	1.28	13.8	1.04	1.11	7.0	0.85	0.88	2.7
Fba-4	1.39	1.59	13.7	1.71	1.87	9.0	1.59	1.71	6.8	1.38	1.44	4.5
Fba-5	2.26	2.46	8.4	2.48	2.70	8.7	2.46	2.48	0.7	2.22	2.25	1.4
Bt-3	2.80	3.28	15.7	3.33	3.30[a]	0.8	3.28	3.33	1.5	3.30[a]	3.37	2.1
F-phlog	na	na	na	6.99	9.21	27.3	na	6.99	na	9.09	9.02[a]	0.8

a. nominal F concentration values for these standards.

na: not analyzed

Table 3.6. Mass loss of F during fusing and calculated apparent partition coefficients (APC) of F between the CO_2 atmosphere and the basaltic melt.

Sample	Initial F Content Powders (wt.%)	Measured F Content EPMA (wt.%)	Mass Loss ΔF (wt.%)	Apparent Partition Coefficient (APC) ΔF/Meas	1/APC
Fba-1	0.53	0.13	0.40	3.08	7.69
Fba-2	1.05	0.53	0.52	0.98	1.89
Fba-3	1.57	0.87	0.70	0.81	1.15
Fba-4	2.09	1.41	0.68	0.48	0.71
Fba-5	3.13	2.24	0.89	0.40	0.45

Table 3.7. Results of SIMS, EPMA, and literature F concentration values of the Fba glasses, high silica glass standards, and mica standards.

Samples		SIMS				EPMA and Literature			
Sample Composition	Sample Name	(-) secondaries		(+) secondaries		F (wt.%)	1 σ	F (ppm)	1 σ
		$^{19}F/^{18}O$	1 σ	1000* ($^{19}F/^{30}Si$)	1 σ				
Fba Glasses	Fba-1	17.52	1.84	3.15	0.28	0.13	0.05	1320	480
	Fba-2	67.90	1.15	12.60	0.21	0.53	0.11	5300	1100
	Fba-3	102.12	2.50	19.88	0.07	0.87	0.10	8650	1050
	Fba-4	152.82	4.08	30.26	0.47	1.41	0.11	14100	1100
	Fba-5	231.23	4.58	49.32	0.77	2.24	0.12	22400	1250
High SiO_2 Glasses	NIST-610[a]	0.95	0.01	0.26	0.01	0.018	8.E-04	180	8
	UTR-2[a]	6.35	0.09	0.49	0.03	0.105	2.E-03	1048	21
	KE-12[b]	23.49	0.35	1.87	0.02	0.400	--	4000	--
	SiO2 Blnk	0.01	0.00	0.00	0.00	0.000	0	0	0
Mica Stds	F-phlogopite	562.62	14.40	192.65	11.04	9.09	0.21	90900	2100
	Phlog. 73-77[c]	6.71	0.20	--	--	0.090	--	902	--
	Biotite3	337.16	15.06	79.11	0.50	3.37	0.19	33700	1900

a. Chapter 2 of this work
b. Moune et al. (2007)
c. Hervig (personal communication)

Table 3.8. Nominal F concentrations for the Fba glasses, the average intensities of the F signal from the Fba glasses for both the F^- and F^+ analyses, the average primary current, and the calculated ion yields.

Samples			F^- Secondary Ions						F^+ Secondary Ions					Yield Ratio	
Fba Glass	F (ppm)	σ	I (nA)	σ	F^- (cps)	1 σ	(A) F^- Ion Yield	1 σ	I (nA)	σ	F^+ (cps)	1 σ	(B) F^+ Ion Yield	1 σ	A/B	1 σ
Fba-1	1320	480	3.15	0.04	23637	3777	5.7	3.0	3.15	0.04	216	29	0.052	0.027	109	85
Fba-2	5300	1100	3.17	0.04	106479	5835	6.3	1.7	3.17	0.04	805	67	0.048	0.015	132	76
Fba-3	8650	1040	3.16	0.05	160924	10960	5.9	1.2	3.16	0.05	1233	103	0.045	0.0098	131	55
Fba-4	14100	1070	3.22	0.03	212528	18706	4.7	0.82	3.22	0.03	1458	39	0.032	0.0036	146	42
Fba-5	22400	1230	3.35	0.02	350137	42638	4.7	0.85	3.35	0.02	2912	147	0.039	0.0043	120	35

Table 3.9. Fluorine concentration values of ALV-519, USGS, and MPI-DING basaltic glass reference materials using the calibration curves 1-3 and 5 from Figure 3.8 a-d.

	F and SiO_2 Content: Literature Values			SIMS						Curve 1: (-)		Curve 2: (-)		Curve 3: (-)		Curve 5: (+)	
				(-) secondary ions			(+) secondary ions			CF 143.5	%RSD 7.0	CF 96.7	%RSD 2.3	CF 161.6	%RSD 0.17	CF 1097.6	%RSD 1.0
Samples	F (ppm)	2σ	SiO_2 (wt.%)	n	$^{19}F/^{18}O$	2σ	n	1000 x ($^{19}F^+/^{30}Si^+$) x SiO_2	2 σ	F (ppm)	2σ	F (ppm)	2σ	F (ppm)	2σ	F (ppm)	2σ
ALV-519	95[a]	10	48.50	4	0.783	0.020	5	0.072	0.008	112	16	76	4	127	1	79	9
USGS basaltic microanalytical refeence glasses																	
BCR-2G	448[b]	27	54.40	4	3.307	0.221	5	0.208	0.010	475	66	320	15	534	4	228	11
BHVO-2G	402[c]	48	49.30	5	3.051	0.195	5	0.228	0.015	438	61	295	14	493	3	250	17
	376[d]	68	49.30														
GSA-1G	na	na	51.20	3	0.070	0.005	3	0.008	0.001	10	1	7	0	11	0	8	1
GSC-1G	na	na	52.60	3	0.089	0.003	3	0.009	0.001	13	2	9	0	14	0	9	1
GSD-1G	na	na	53.20	3	0.185	0.017	3	0.017	0.001	27	4	18	1	30	0	18	1
GSE-1G	na	na	53.70	3	1.586	0.050	5	0.137	0.010	228	32	153	7	256	2	150	11
MPI-DING basaltic microanalytical reference glasses																	
ML3B-G	70[e]	na	51.40	7	0.488	0.170	4	0.053	0.005	70	10	47	2	79	1	58	5
KL2-G	177[e]	na	50.30	4	0.839	0.039	6	0.070	0.009	120	17	81	4	136	1	77	10

a. Hauri et al. (2011)
b. Michel and Villemant (2003) as BCR-2 powder
c. Michel and Villemant (2003) as BHVO-2 powder
d. Balcone-Boissard et al. (2009) as BHVO-2 powder
e. Jochum et al. (2006) info only
na: not analysed
CF: calibration factor
% RSD is that of the calibration line

Figure 3.1

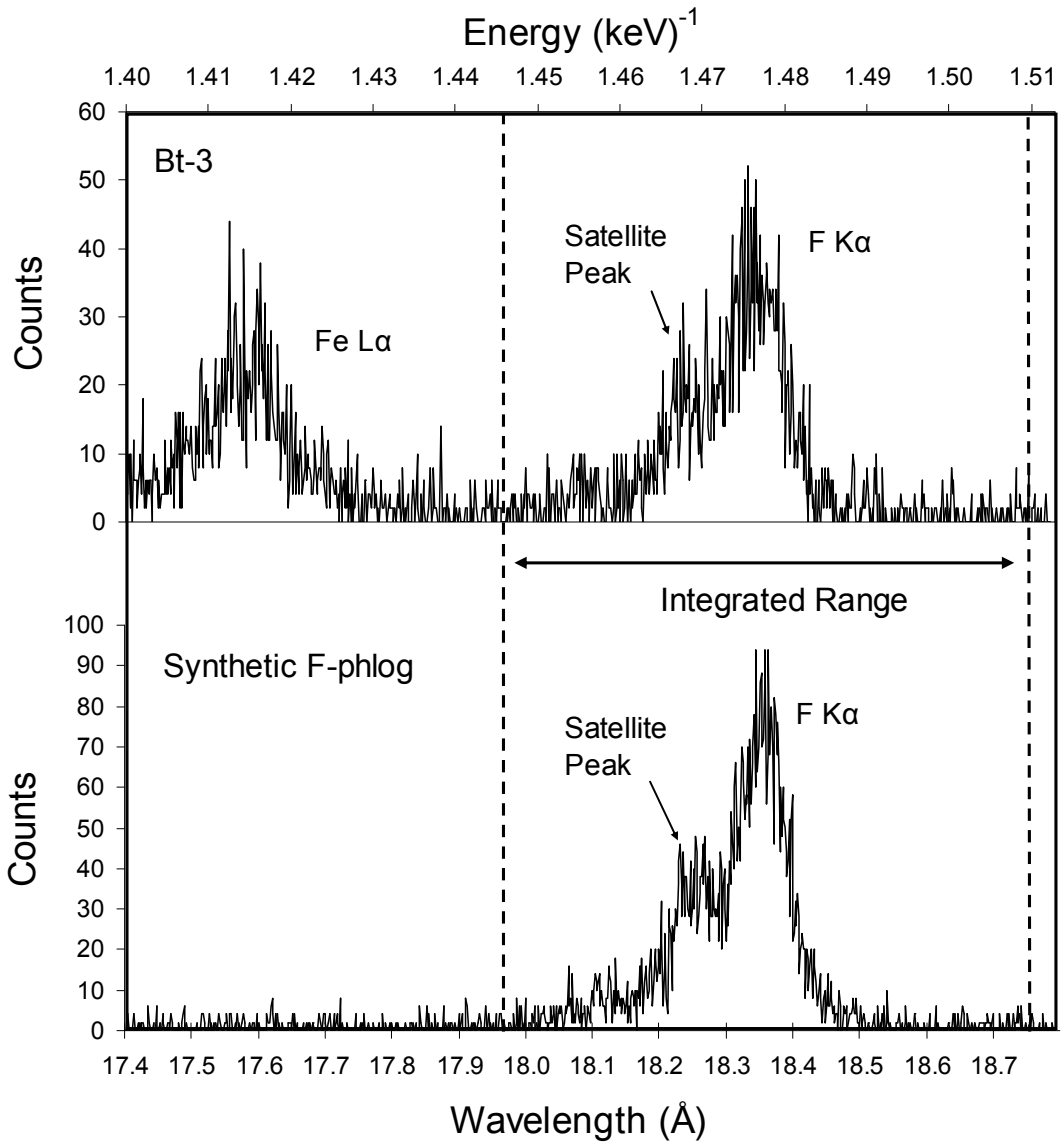
Energy (keV)$^{-1}$
1.40 1.41 1.42 1.43 1.44 1.45 1.46 1.47 1.48 1.49 1.50 1.51
Bt-3
Satellite Peak
F Kα
Fe Lα
Counts
Integrated Range
Synthetic F-phlog
Satellite Peak
F Kα
Counts
17.4 17.5 17.6 17.7 17.8 17.9 18.0 18.1 18.2 18.3 18.4 18.5 18.6 18.7
Wavelength (Å)

Figure 3.2

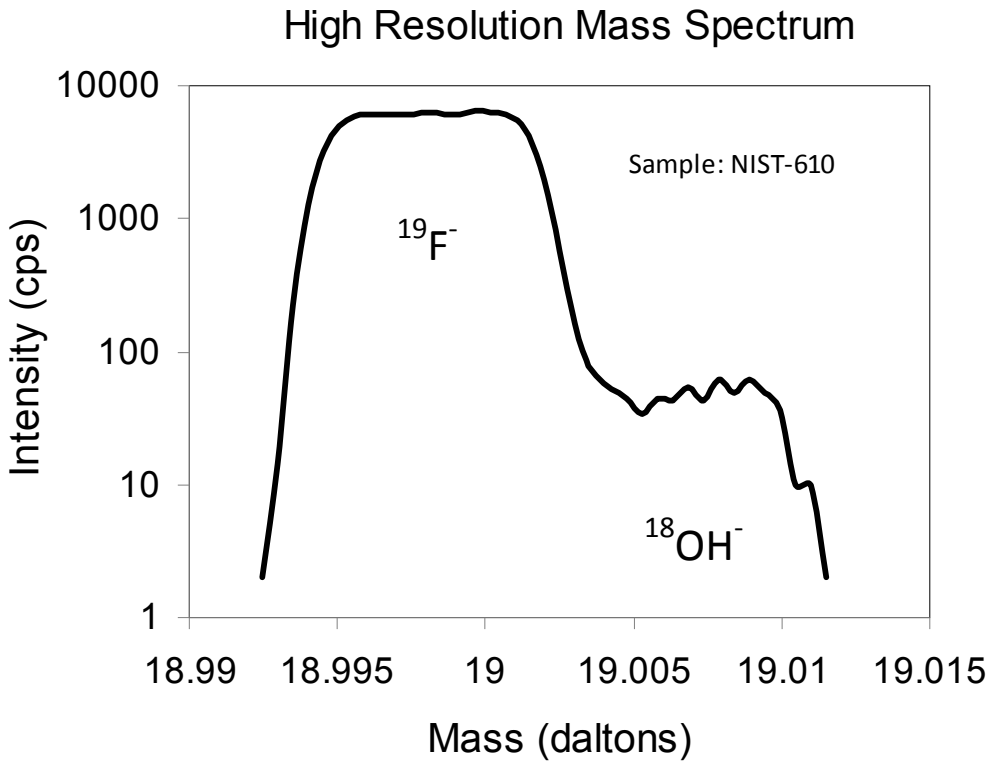
High Resolution Mass Spectrum
Sample: NIST-610
$^{19}F^-$
$^{18}OH^-$
Intensity (cps)
10000
1000
100
10
1
18.99
18.995
19
19.005
19.01
19.015
Mass (daltons)

Figure 3.3

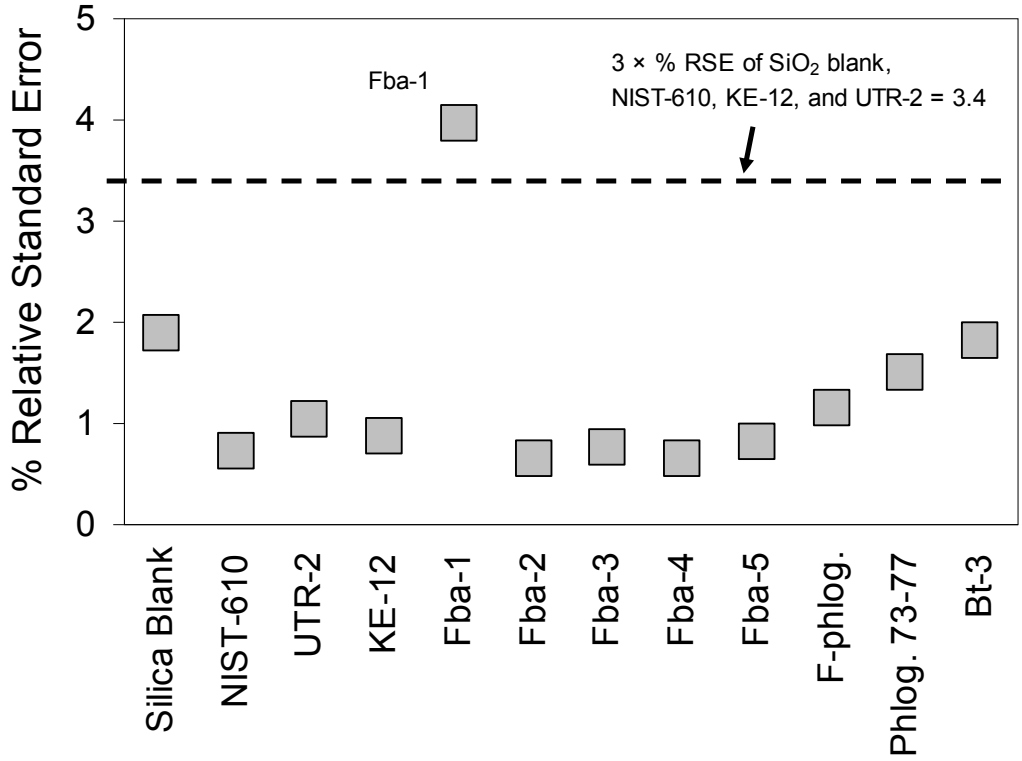
% Relative Standard Error
5
4
3
2
1
0
Fba-1
3 × % RSE of SiO2 blank,
NIST-610, KE-12, and UTR-2 = 3.4
Silica Blank
NIST-610
UTR-2
KE-12
Fba-1
Fba-2
Fba-3
Fba-4
Fba-5
F-phlog.
Phlog. 73-77
Bt-3

Figure 3.4

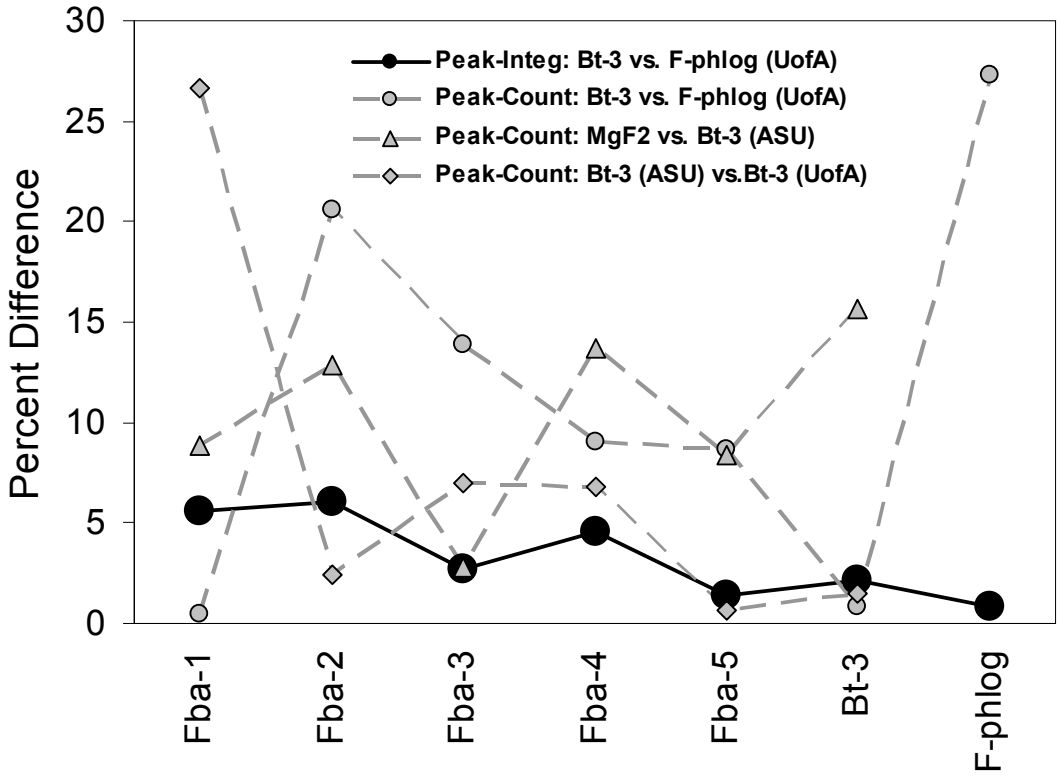
Peak-Integ: Bt-3 vs. F-phlog (UofA)
Peak-Count: Bt-3 vs. F-phlog (UofA)
Peak-Count: MgF2 vs. Bt-3 (ASU)
Peak-Count: Bt-3 (ASU) vs.Bt-3 (UofA)
Percent Difference
30
25
20
15
10
5
0
Fba-1
Fba-2
Fba-3
Fba-4
Fba-5
Bt-3
F-phlog

Figure 3.5

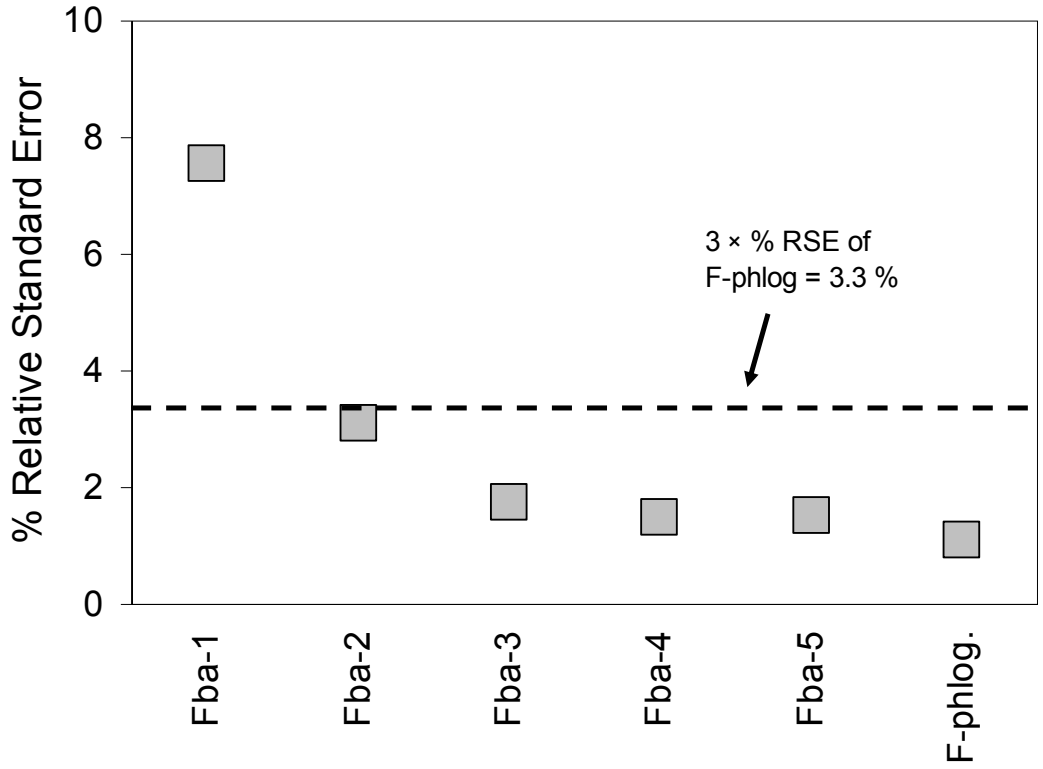
% Relative Standard Error
10
8
6
4
2
0
3 × % RSE of
F-phlog = 3.3 %
Fba-1
Fba-2
Fba-3
Fba-4
Fba-5
F-phlog.

Figure 3.6

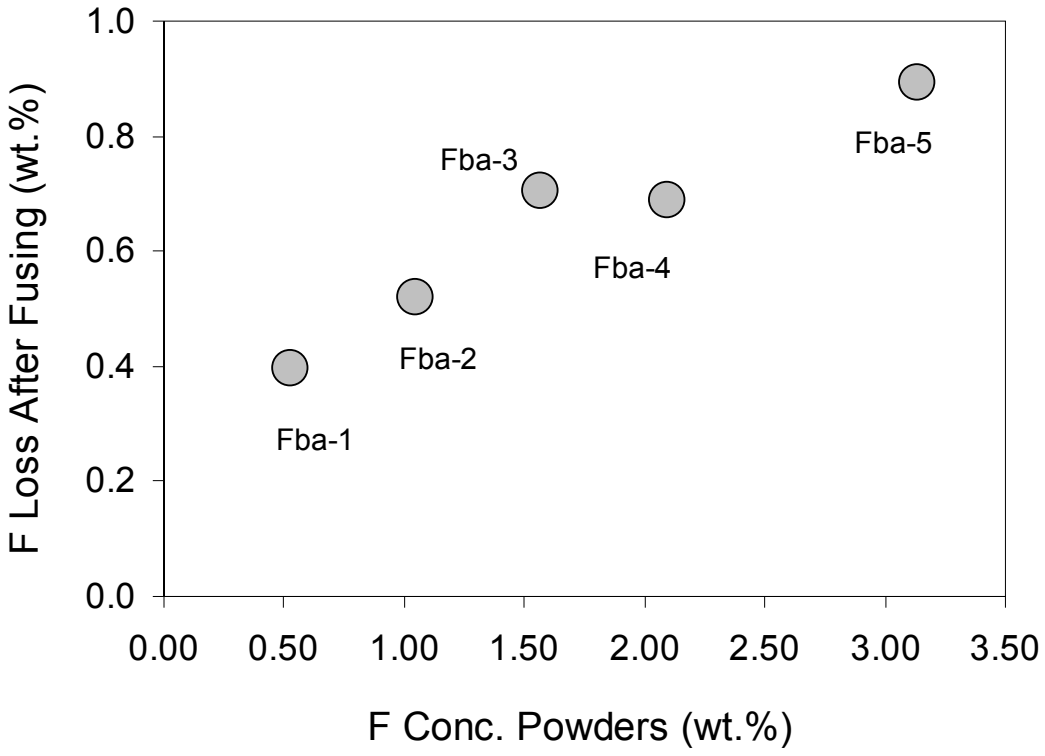
1.0
0.8
0.6
0.4
0.2
0.0
F Loss After Fusing (wt.%)
Fba-1
Fba-2
Fba-3
Fba-4
Fba-5
0.00
0.50
1.00
1.50
2.00
2.50
3.00
3.50
F Conc. Powders (wt.%)

Figure 3.7 (a)

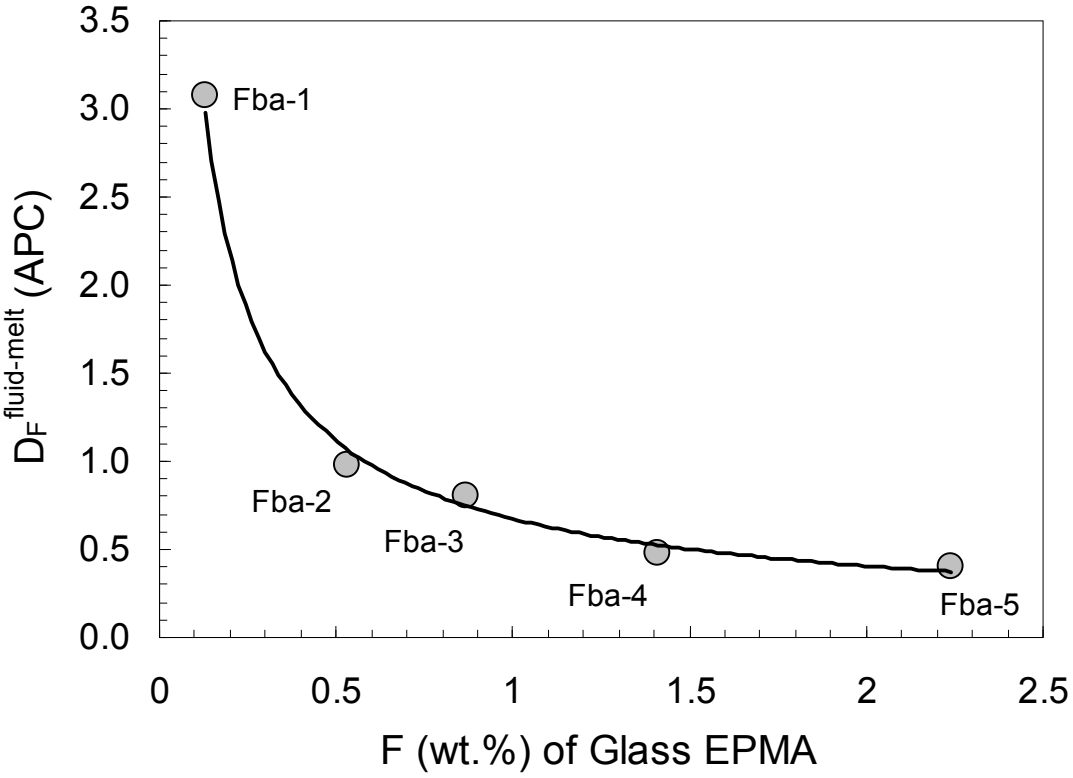
3.5
3.0
2.5
2.0
1.5
1.0
0.5
0.0
$D_F^{fluid\text{-}melt}$ (APC)
Fba-1
Fba-2
Fba-3
Fba-4
Fba-5
0
0.5
1
1.5
2
2.5
F (wt.%) of Glass EPMA

Figure 3.7 (b)

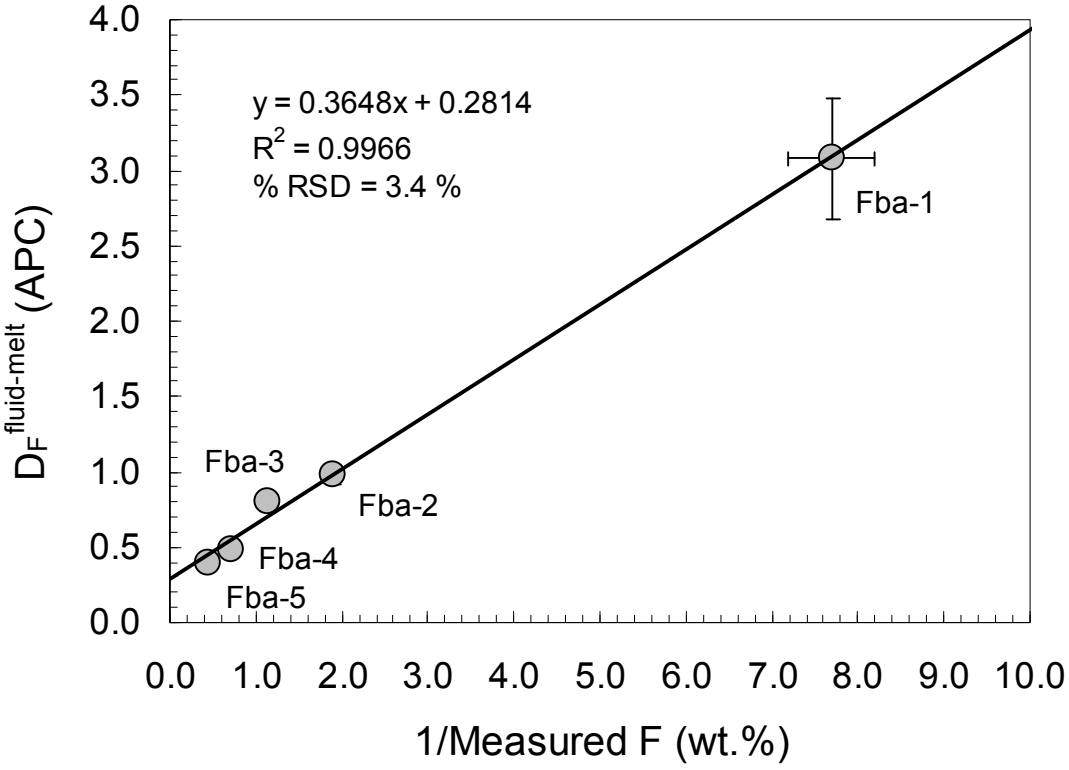
y = 0.3648x + 0.2814
R2 = 0.9966
% RSD = 3.4 %
Fba-1
Fba-2
Fba-3
Fba-4
Fba-5
DF fluid-melt (APC)
1/Measured F (wt.%)
0.0
0.5
1.0
1.5
2.0
2.5
3.0
3.5
4.0
0.0
1.0
2.0
3.0
4.0
5.0
6.0
7.0
8.0
9.0
10.0

Figure 3.8 (a)

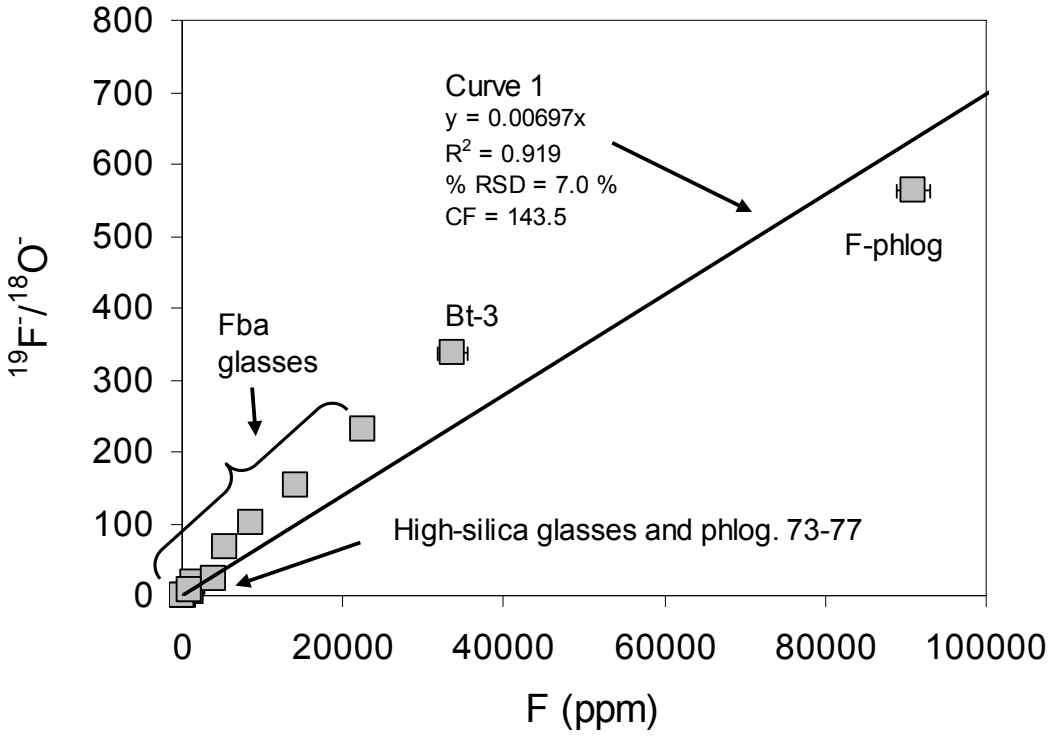
800
700
600
500
400
300
200
100
0
$^{19}F^-/^{18}O^-$
Curve 1
y = 0.00697x
R^2 = 0.919
% RSD = 7.0 %
CF = 143.5
F-phlog
Bt-3
Fba
glasses
High-silica glasses and phlog. 73-77
0
20000
40000
60000
80000
100000
F (ppm)

Figure 3.8 (b)

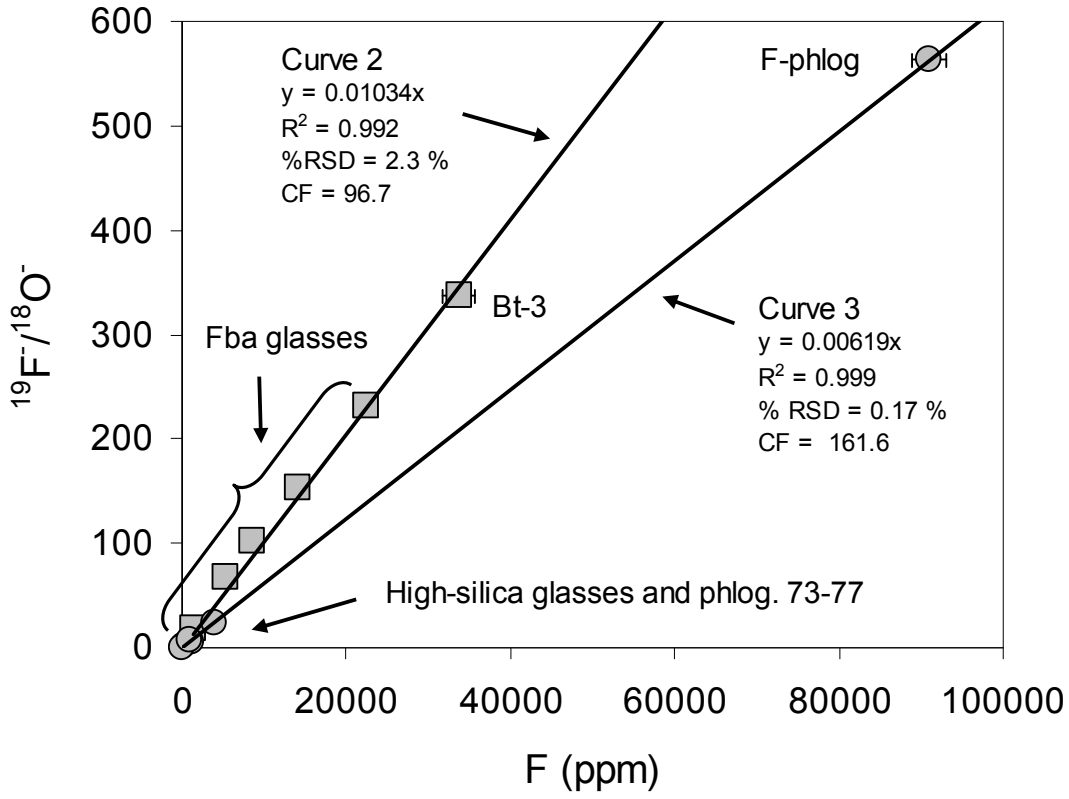
600
500
400
300
200
100
0
$^{19}F^-/^{18}O^-$
Curve 2
y = 0.01034x
R^2 = 0.992
%RSD = 2.3 %
CF = 96.7
F-phlog
Bt-3
Fba glasses
Curve 3
y = 0.00619x
R^2 = 0.999
% RSD = 0.17 %
CF = 161.6
High-silica glasses and phlog. 73-77
0
20000
40000
60000
80000
100000
F (ppm)

Figure 3.8 (c)

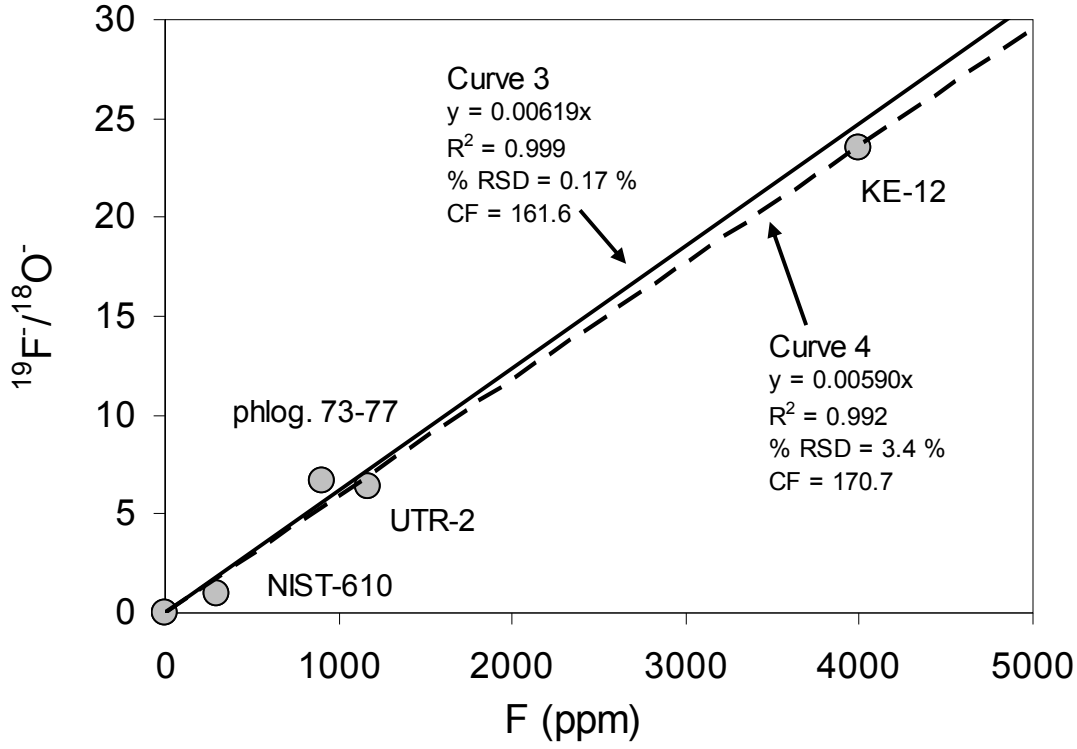
Curve 3
y = 0.00619x
R2 = 0.999
% RSD = 0.17 %
CF = 161.6
Curve 4
y = 0.00590x
R2 = 0.992
% RSD = 3.4 %
CF = 170.7
KE-12
phlog. 73-77
UTR-2
NIST-610
19F-/18O-
F (ppm)
0
5
10
15
20
25
30
0
1000
2000
3000
4000
5000

Figure 3.8 (d)

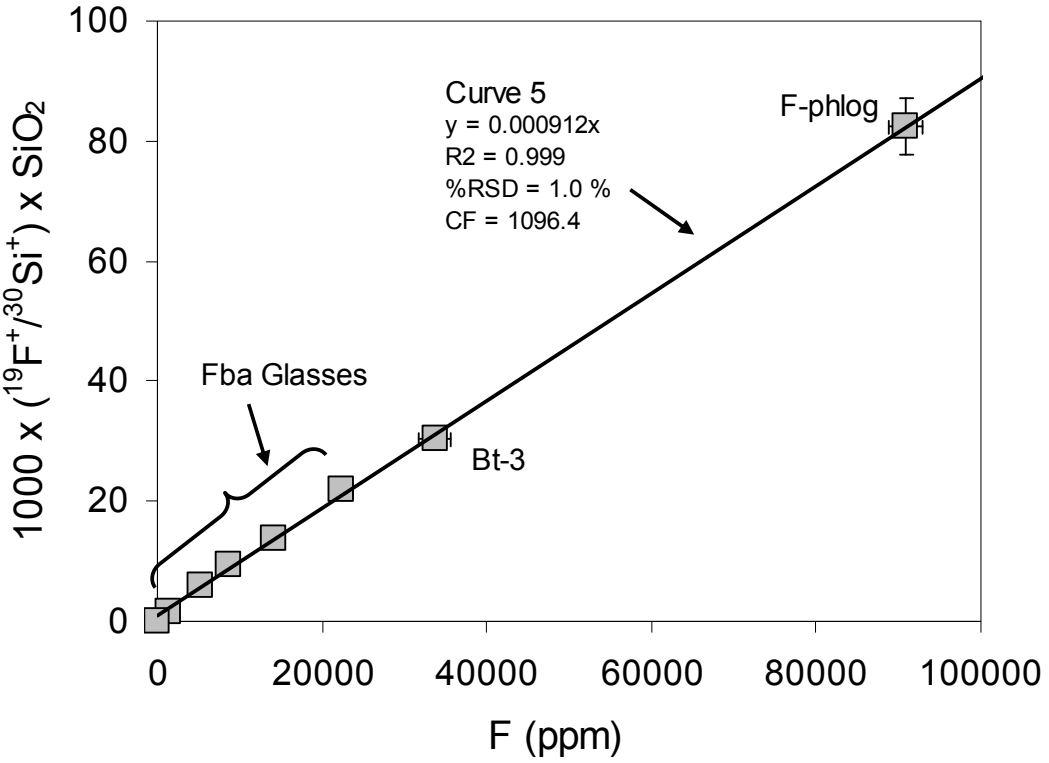
100
80
60
40
20
0
1000 x ($^{19}F^{+}/^{30}Si^{+}$) x SiO_2
Curve 5
y = 0.000912x
R2 = 0.999
%RSD = 1.0 %
CF = 1096.4
F-phlog
Fba Glasses
Bt-3
0
20000
40000
60000
80000
100000
F (ppm)

Figure 3.8 (e)

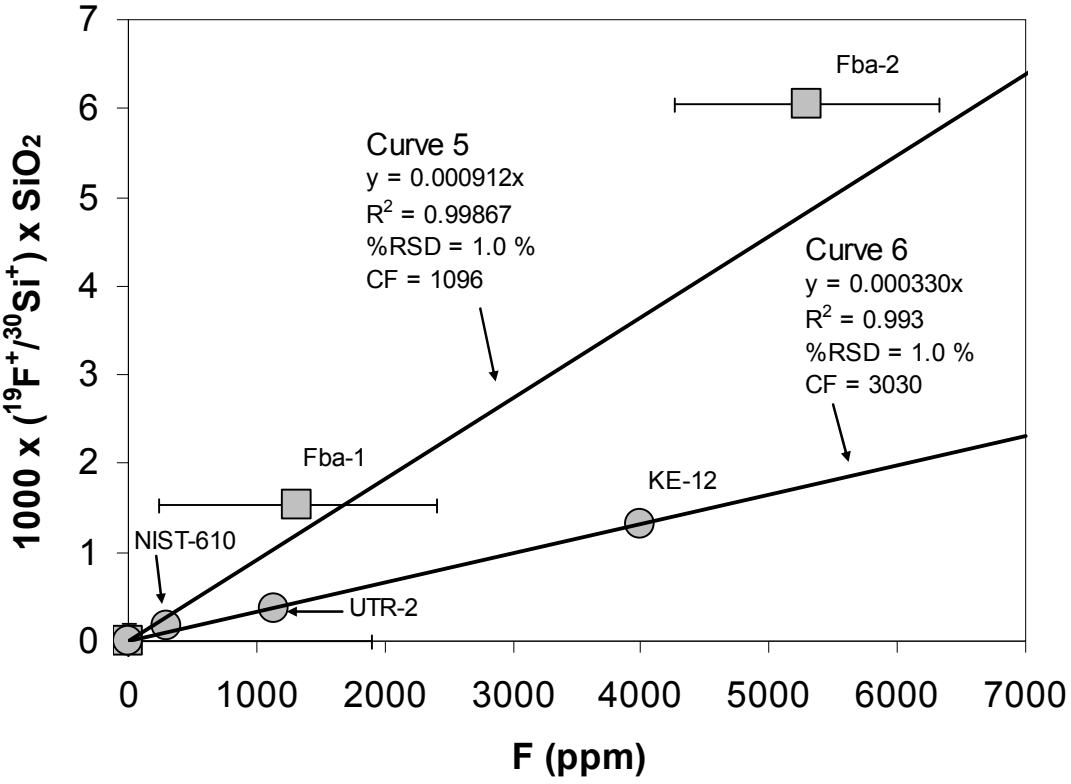
1000 x ($^{19}F^{+}/^{30}Si^{+}$) x SiO_2
F (ppm)
Curve 5
y = 0.000912x
R^2 = 0.99867
%RSD = 1.0 %
CF = 1096
Curve 6
y = 0.000330x
R^2 = 0.993
%RSD = 1.0 %
CF = 3030
Fba-1
Fba-2
KE-12
NIST-610
UTR-2
0
1
2
3
4
5
6
7
0
1000
2000
3000
4000
5000
6000
7000

CHAPTER 4

FLUORINE IN OLIVINE: DEVELOPMENT OF A TECHNIQUE TO MEASURE FLUORINE IN NOMINALLY ANHYDROUS MINERALS USING SIMS

ABSTRACT

Olivine crystals from a range of geologic and tectonic environments were measured for fluorine using SIMS employing a Cs^+ primary beam and a normal incidence electron gun for charge-compensation. A suite of microanalytical glass standards of both low-silica basaltic (Fba glasses from Chapter 3 of this work) and high-silica rhyolitic (NIST-610, UTR-2, and KE-12) compositions were analyzed for $^{19}F^-$ using both a Cs^+ primary beam and an O^- primary beam, and the results were compared. Both methods yielded $^{19}F^-$ secondary ion count rates that allowed for sub-ppm detection of F in mineral phases. The $^{19}F^-/^{18}O^-$ ion ratios obtained by both primary-beam methods were plotted against each other, and strong linear relationships emerged that showed two separate regression lines connecting the low-silica and the high-silica glasses, illustrating matrix effects independent of primary beam used. SIMS calibration curves were constructed using the basaltic and rhyolitic glass standards from above that were analyzed using a Cs^+ primary beam. Two calibration curves connecting glasses of similar compositions were noted: basaltic curve (calibration factor = 422.8) and rhyolitic curve (calibration factor = 512.3), demonstrating matrix effects of about 20 %. Olivine samples from the classic paper by Simkin and Smith (1970) were analyzed for F using SIMS and a Cs^+ primary beam. The majority of the crystals lacked geologic context, but a few, like the Hawaiian suite of genetically related olivines from basalts and andesites and the olivine crystals from the Kiglapait Layered Intrusion, showed that F behaves as an incompatible element. The most F-rich olivine was recovered from a kimberlite, pointing to a role of nominally anhydrous phases in hosting volatile elements at high *P* and *T*.

1. Introduction

Fluorine is the lightest of the halogens and the most electronegative element in the periodic table. Fluorine behaves as a moderately volatile element, and it is relatively depleted in the bulk Earth compared to CI chondrites. Due to their large ionic radii, the heavier halogens Cl, Br, and I are highly incompatible in most crystallizing assemblages, and are partitioned into the liquid and/or fluid phase during the evolution of silicate magmas. Fluorine is not as strongly incompatible (Rowe and Schilling 1979, Stecher 1998) and may be retained within mineralogical reservoirs within the mantle (e.g. apatite, micas, amphiboles, and humite-group minerals) and the crust (e.g. fluorite, topaz, apatite). In the Earth's crust, F concentration is around 500 ppm, while in the bulk mantle the concentration of F is about 25 ppm (McDonough and Sun 1995).

Few investigations have been conducted to determine how fluorine is stored within the Earth, or what governs its geochemical behavior in igneous systems (Smith et al. 1981, Carroll and Webster 1994, Stecher 1998, Ottolini et al. 2000, Straub and Layne 2003). During melting of the mantle, fluorine behaves as an incompatible element, but unlike other halogens is not readily lost by near-surface degassing of mafic magmas, nor gained (as are H_2O and Cl) by assimilation of altered oceanic crust or associated brines (Straub and Layne 2003). This implies that connections made between F in basalts and F in the mantle source of the basalt are more robust than for many other volatile species, such as H_2O, CO_2, N_2, Cl, Br, and the noble gases. However, minerals commonly associated as being reservoirs for F (micas, amphiboles and apatite) are not stable at conditions in the mantle where many melts are formed (Straub and Layne 2003), and the likelihood that these are the main mineralogical repositories for F in the mantle is small. Therefore, we propose that other more stable mineralogical reservoirs exist for F storage, namely the nominally anhydrous minerals (NAMs) such as olivine, garnet, and pyroxene. Early investigations of the abundance of F in NAMs from mantle-derived garnet and spinel lherzolites (Hervig et al. 1988, Hervig and Bell 2005) show that F exists in

significant concentrations (a few to over 100 ppm), and this range is similar to that for H_2O on a molar basis. Hervig et al. (1988) measured F in mantle olivines, clinopyroxenes, orthopyroxenes, and garnet from a garnet lherzolite using both secondary ion mass spectrometry (SIMS) and proton-induced gamma-ray emission (PIGE) spectrometry and found that these minerals contain F concentrations from about 3 to 120 ppm, with olivine containing the most abundant F. In the study by Hervig and Bell (2005), the authors examined F in coexisting olivine, pyroxene, and mica megacrysts in mica peridotites from African kimberlites. The olivine crystals show a wide range in F concentration (30-100 ppm), and when compared to the F content of the coexisting micas, a strong correlation emerges that shows a consistent correlation [$F_{mica}/F_{olivine}$ ~ 100:1], suggesting that F actually substitutes into the olivine structure and is not an artifact of humite intergrowths or other secondary phases (Engi 1980, Hermann et al. 2007). Nominally anhydrous minerals are likely the dominant H reservoir within Earth's interior (Bell and Rossman 1992, Ingrin and Skogby 2000), and preliminary observations of F behavior and partitioning suggest that NAMs may also be the host for most of the F on Earth.

In this study, we have obtained many of the olivine grain mounts from the classic electron probe work of Simkin and Smith (1970) where they measured major and selected minor elements in olivine from a wide range of volcanic and plutonic rocks that represent diverse tectonic environments. The olivine crystals from the Simkin and Smith (1970) samples (DP, DR, EA, EB, EC, EP, EQ; their nomenclature) were analyzed for F using SIMS and served as a preliminary investigation into the behavior of fluorine in these phases and to further test hypotheses concerning F in diverse environments.

2. Methods

2.1 Samples

Olivine grain mounts were selected from the work of Simkin and Smith (1970) based on the variety of tectonic and volcanic environments and the availability of geochemical data. The grain mounts consist of fractured olivine grains mounted on a one-inch brass disc within distinct one-eighth-inch drilled holes filled with epoxy (Fig. 4.1). The mounts were covered in the original carbon coat used by Simkin and Smith (1970) for electron microprobe analysis. The old carbon coat was removed by polishing the mounts with 3 μm and 1 μm alumina polishing paper, sonicated in de-ionized water and ethanol, and then sputter-coated with a thin film (~ 10-20 nm) of Au in order to minimize sample charging during SIMS analysis. The sample selected for SIMS analysis were on the grain mounts labeled DP, DR, EA, EB, EC, EP, and EQ (nomenclature from Simkin and Smith 1970).

2.2 SIMS Measurements

2.2.1 Primary Beams

Fluorine was measured using the Cameca IMS 6f secondary ion mass spectrometer (SIMS) (Fig. 4.2) located at Arizona State University (ASU). The IMS 6f was delivered to ASU in 1999, and at the time the IMS 6f was the latest version of the “single collector” type of magnetic sector SIMS, in which the design of the instrument incorporated all the necessary improvements for a multitude of tasks, as opposed to the later development of several instruments focused for specific applications (see Schuhmacher et al. 1999). The IMS 6f contains two mass-filtered ion sources located at the head of the primary column: 1) a surface ionization cesium source where a Cs gun produces Cs^+ ions by thermally ionizing vaporized Cs at a tungsten frit and 2) a duoplasmatron where (most commonly) positive and negative oxygen ion beams are produced as a plasma discharge within a hollow Ni-cathode. When in use, the two primary ion sources are held at a fixed potential with respect to ground and the extracted

ion beam is accelerated toward the sample via a potential difference. Ions extracted from the sources are focused by a lens and aligned by a deflector set so that the ions pass along the central path of the primary beam mass filter (PBMF, Fig. 4.2). The PBMF selects for specific masses of ions from the sources and serves to provide an isotopically pure ion beam. That is, when a primary beam comprised of only ^{16}O is selected, no other isotopes of oxygen are allowed to impact the sample, thus reducing contamination of the sample. However, the gas source must be free of any other ionic species with interfering mass (e.g. NH_2 will interfere with ^{16}O). The primary beam passes through the main flight tube and is focused by a series of electrostatic lenses while deflectors align the beam through the center of each subsequent lens and apertures. Near the sample, deflectors affect the position of the primary beam on the sample surface and, as controlled by the user, can also divert the beam into the Faraday cup so the primary ion current can be measured. Stigmators can be adjusted to change the shape of the ion beam on the sample surface.

An important consideration in the selection of a primary ion beam is the magnitude of the ion yield for the secondary ion of interest and whether positive or negative ion yields are favored (Wilson et al. 1989). Both Cs^+ ion sources and ionic oxygen species from the duoplasmatron offer their unique advantages for analyzing particular types of secondary ionic species. The duoplasmatron can operate with any gas, including air, but oxygen gas is most commonly used. Samples bombarded with an oxygen beam become saturated in oxygen, which is strongly electronegative, to depths of about 10 nm, enhancing the production of sputtered positive secondary ions of most metallic elements as well as liberating anions. When insulating samples are analyzed for either positive or negative secondary ions, sputtering with an O^- primary beam is the preferred technique because sample charging is kept at a minimum due to the continual influx of negatively-charged oxygen ions and the dissipation of charge via the conductive Au coating applied to the sample prior to analysis.

Because of their greater mass, Cs^+ primary beams sputter material more effectively than O^- primary beams. The Cs^+ primary beam is well known for its ability to enhance the production of negative secondary ions from the target, and the negative secondary ion yield is much greater than when using an O^- primary beam. Because of the increased negative secondary ion yield, the Cs^+ primary beam can be focused to a diameter smaller than those generated by the duoplasmatron, where the size of the beam is controlled by and proportional to the primary beam current (~ 5 μm at 1 nA current), decreasing the minimum detection limit.

The Cs^+ primary beam enhances the production of sputtered negative secondary ions due to the accumulation and saturation of Cs^+ ions on the receding surface of the target. These surface Cs^+ ions temporarily become adatoms (adsorbed atoms) that act to significantly lower the work function of the target solid (Stern 2009, Wittmaack 2012). The work function is defined as the minimum energy (in eV) required to remove an electron from a solid to a point immediately outside the solid surface. Lowering the work function increases the production of "free" electrons available to combine with non-metallic elements (e.g. O^-, C^-, H^-, Cl^-, and F^-). In SIMS analysis, reduced work functions are commonly thought to be responsible for the high yields of negative secondary ions as well as the decrease in the yields of positive secondary ions. Wittmaack (2012) surmised that implanted Cs atoms from a Cs^+ primary beam exert a great amount of stress on the surrounding matrix in which they are implanted, and a portion of these atoms migrate toward the surface following vacancies produced by ion bombardment. Depending on the bombardment parameters (i.e. primary ion energy, angle of impact, and mean current density), the residence time of adatoms is short. However, for his model to work, Wittmaack (2012) recognized that there must be a balance between Cs implantation, transport, and removal from the surface under stationary bombardment conditions, which he was not able to quantify in his study. An implication for the Cs^+ transport model of Wittmaack (2012) would be that the rate of Cs^+ accumulation on the surface of the target

solid is matrix dependent, whereby the less stress the Cs atom experiences from the matrix would result in a slower migration of the Cs atom to the surface. The implication that the secondary ion yield from a Cs^+ primary beam may be matrix dependent is a topic for further study.

When a Cs^+ primary beam is used, a positive charge on the sample builds up due to the accumulation of Cs^+ ions on the surface and the resulting repulsion of negative ions and electrons. Sample charging is controlled by employing a normal incidence electron gun to neutralize charge build-up on the sample (see NEG in Fig. 4.2).

2.2.2 Analytical Parameters

Standards

A suite of microanalytical glass standards were analyzed using both Cs^+ and O^- primary beams to produce negative secondary ions of $^{19}F^-$, $^{18}O^-$, and $^{28}Si^-$, and the results were used to compare the respective secondary ion yields. The standard glasses represent both low-silica basaltic and high-silica rhyolitic compositions: Basaltic (Fba glasses from Chapter 3 of this work): Fba-1 (F = 1320±480 ppm), Fba-2 (F = 5300±1100 ppm), Fba-3 (8650±1040 ppm), Fba-4 (F = 14100±1070 ppm), Fba-5 (F = 22400±1240 ppm); and Rhyolitic: NIST-610 (F = 180 ppm), KE-12 (F = 4000 ppm), UTR-2 (F = 1048 ppm). SIMS analyses using a Cs^+ primary beam utilized a primary current that ranged from 1.89 - 2.26 nA, a primary beam diameter of about 10 μm, and a normal-incidence electron gun to neutralize positive charge build-up in the sputtered crater. The Cs source was held at +10 kV with respect to ground, while the samples were held at -5000 V, yielding an impact energy on the sample surface of 15 keV. No energy filtering was applied to the negative secondary ion signal. The mass spectrometer was operated at a mass resolving power (MRP) sufficient to separate $^{19}F^-$ from $^{18}OH^-$ ($M/\Delta M$ ~2500) (Fig. 4.3). SIMS analysis using the $^{16}O^-$ primary beam utilized a duoplasmatron held at a constant high voltage of -12.5 kV to sputter a crater on the glass surface held at a constant potential of -5000 V, yielding an impact energy on the sample surface of 7.5

keV. The $^{16}O^-$ primary beam utilized a primary current that ranged from 3.07 – 3.57 nA with a primary beam diameter of about 15 μm. The use of negative primary ions eliminated the need for a normal-incidence electron gun because positive charge build-up was avoided. No energy filtering was applied, and the mass spectrometer was operated at a mass resolving power (MRP) sufficient to separate $^{19}F^-$ from $^{18}OH^-$ (M/ΔM ~2500) (Fig. 4.3). Secondary ion intensities were collected for $^{18}O^-$, $^{19}F^-$, and $^{28}Si^-$.

Samples

The samples from the Simkin and Smith (1970) suite labeled DP, DR, EA, EB, EC, EP, and EQ were analyzed using the Cs^+ primary beam to produce negative secondary ions of $^{19}F^-$, $^{18}O^-$, and $^{28}Si^-$. The average primary current was 1.5 nA, with a primary beam diameter of about 10 μm and a normal-incidence electron gun to neutralize positive charge build-up in the sputtered crater. The Cs source was held at +10 kV with respect to ground, while the sample was held at -9 kV, yielding an impact energy on the sample surface of 19 keV. No energy filtering was applied to the negative secondary ion signal. The mass spectrometer was operated at a mass resolving power (MRP) sufficient to separate $^{19}F^-$ from $^{18}OH^-$ (M/ΔM ~2500).

2.2.3 Quantifying SIMS Measurements

A significant limitation to SIMS measurements is converting secondary ion signal intensities to actual concentrations for the material being analyzed. The output from SIMS analysis is in counts/second (cps) for each species measured, but the cps values for the ions of interest within the same solid may vary significantly from one analysis to another due to subtle and systematic variations in analytical parameters during each separate analysis. However, because these variations can be systematic, the count rates for each measured ionic species may be proportional within each analysis. Therefore, it is common practice to normalize the cps of the species of interest to the cps of some ubiquitous isotope within the sample matrix, resulting in an ion ratio of high reproducibility. In our case, $^{19}F^-$ (cps) was normalized to $^{18}O^-$ (cps).

In SIMS analysis, secondary ion signals are strongly dependent on 1) the properties of the particular element of interest, namely the ionization potential (IP) and the electron affinity (EA) and 2) the chemical and electronic environment (termed matrix effects) of the solid in which the element resides (Ottolini et al. 2002, Stern 2009). The IP is the energy needed to remove an electron from an isolated atom or molecule in the gaseous state, thus giving the species a net positive charge. IP governs the ionic yield of positive secondary ions. The EA is the energy release associated with the capture of an electron by an isolated atom or molecule in the gaseous state, giving the species a net negative charge. EA governs the ionic yield of negative secondary ions. The IPs and EAs for the elements are known (e.g. for fluorine: IP=17.42 eV, EA=3.40 eV; for oxygen: IP=13.618 eV, EA=1.462 eV; for silicon: IP=8.151 eV, EA=1.385 eV) (Wilson et al. 1989, Stern 2009). Matrix effects are a complex function not only of the chemical composition of the matrix, but also the crystal structure and the orientation of the matrix to the incident primary ion beam, and it combines the nature of the undisturbed solid itself as well as the changing conditions on the surface of the solid during sputtering and implantation of primary-beam ions.

There are no matrix-correction models for SIMS analysis. Therefore, to minimize matrix effects and to increase the accuracy of SIMS analyses, quantitative analysis requires an empirical calibration with appropriate reference materials that are closely matrix-matched to the unknown samples undergoing analysis. To convert the secondary ion intensity to a concentration value, a calibration curve must be constructed from a series of SIMS measurements of the elements of interest from as many matrix-matched standard glasses as possible (Kane 2001, Straub and Layne 2003, Hervig et al. 2003).

Tests for the effect of sample chemistry on F^- intensity continue to be empirical (e.g. Hoskin 1999, Portnyagin et al. 2002). Examination of matrix effects for F analysis with SIMS were conducted by calibrating with glass standards composed of different matrix chemistries and various concentrations of F. Fluorine calibrations were obtained

by analyzing several bulk-analyzed high-silica glasses (NIST 610, UTR-2, and KE-12) and newly synthesized low-silica basaltic glass standards (Fba-1, Fba-2, Fba-3, Fba-4, Fba-5; see Chapter 3).

3. Results and Discussion

3.1 Fluorine Secondary Ion Yields under Cs^+ and O^- Primary Beam Bombardment

The low-silica basaltic and high-silica rhyolitic glass standards utilized in this study were analyzed by SIMS using both Cs^+ and O^- primary beams to compare the ion yields of $^{19}F^-$ negative secondary ions. Table 4.1 lists the results of SIMS measurements of $^{19}F^-$ on the basaltic and high-silica glass standards, including the average operating current for each glass, the $^{19}F^-/^{18}O^-$ ratios, the $^{19}F^-$ counts per second, and the calculated $^{19}F^-$ secondary ion yields for each glass. Secondary ion yield for $^{19}F^-$ is defined as the average $^{19}F^-$ cps per F concentration of the standard per nA of operating current, or:

$$\text{F (cps) / F (ppm) std / nA } (O^- \text{ or } Cs^+) \quad (1)$$

Table 4.1 shows the ion yield ratios for $^{19}F^-$ using Cs^+ and an O^- primary beams, or $^{19}F^-\ \text{Yield}_{(Cs^+\ \text{Prim.Beam})} \Big/ {}^{19}F^-\ \text{Yield}_{(O^-\ \text{Prim.Beam})}$. The Cs^+ primary beam generally produces a greater $^{19}F^-$ ion yield than does the O^- primary beam, and we found that the difference ranges from a factor of 3 to a factor of 8. Ideally, the difference in secondary ion yields between the two primary beams should be similar within error, but variations in analytical parameters within and between sessions may account for this disparity, such as subtle misalignment of the electron gun, subtle and inconsistent alignment of the field apertures, and operator inexperience. Figure 4.4 shows a plot of the $^{19}F^-$ secondary ion yield ratios for the two primary beams. The graph shows comparable ratios for the basaltic glasses and NIST-610, but the yield appears to increase for the two pantellerite glasses UTR-2 and KE-12, with KE-12 showing the highest ratio. Although the error bars

overlap somewhat, the conspicuously higher ratios for the pantellerite glasses suggests the possibility of a systematic cause that may require further investigation, such as matrix effects resulting from minor changes in chemistry or inaccurate bulk analyses of their F contents.

Although the secondary ion yields for $^{19}F^-$ are greater when using the Cs^+ primary beam as compared to the O^- primary beam, there are disadvantages to using the Cs^+ primary beam. Because Cs^+ ions are implanted into the sample while negative ions and electrons are accelerated away from the sample, the surface of the crater becomes positively charged. To mitigate positive charge build-up on the sample, a normal incidence electron gun is employed which directs electrons toward the sputtered crater. However, because the electron gun must maintain a continuous flood of electrons at the point of charge build-up (the sputter crater), difficulties arise involving 1) steering the electron gun to the correct spot and 2) preventing the electron beam from drifting off the spot during analysis and while driving the sample to a new analysis location. In addition, Pivovarov and Guryanov (2010), while studying the detection limits of F and Cl in doped Si and SiO_2 wafers using a Cs^+ beam and electron-gun charge neutralization, discovered that simultaneous use of the electron beam and primary ion beam can increase the background yield of F and Cl negative ions. They attribute this phenomenon to a process called dissociative electron attachment (DEA), by which a low-energy electron (0-15 eV) is temporarily captured by a sputtered residual gas molecule of two or more atoms that had been deposited on the sample surface. The electron capture produces a transient negative molecular ion that then dissociates and produces a negative atomic ion. The cross section (probability of occurrence) of the DEA process is enhanced if the molecule contains an atom with high electron affinity, like a halogen (Pivovarov and Guryanov 2010). For samples with > 1 ppm F, this effect is not likely to be important. But for sub-ppm analysis of F, background due to DEA may become a significant factor.

3.2 Comparing $^{19}F/^{18}O$ Ion Ratios between Cs^+ and O^- Primary Beams

Table 4.1 lists the $^{19}F\text{-}/^{18}O^-$ ion ratios obtained for the standard glasses using both the Cs^+ and O^- primary beams. The right-most two columns of Table 4.1 show the $^{19}F\text{-}/^{18}O^-$ Relative Ratios (RR), the $^{19}F\text{-}/^{18}O^-$ generated from the O^- primary beam divided by the $^{19}F\text{-}/^{18}O^-$ generated from the Cs^+ primary beam, as well as the 1-sigma uncertainty. Inspection of the RR for all the glasses shows that the $^{19}F^-/^{18}O^-$ ion ratios using the O^- primary beam are consistently 2-5 times greater than the ratios when using the Cs^+ primary beam. However, when inspecting the glasses separately based on silica content, the low-silica Fba glasses show RR's that are consistently 4.5 – 4.8, while the high-silica glasses show RR's that are consistently 2.3 – 3.0, illustrating the influence of matrix effects on both techniques. Figure 4.5 shows a comparison between the $^{19}F/^{18}O$ ion ratios for the low-silica Fba glasses and the high-silica glasses generated from O^- primary beam versus the Cs^+ primary beam. Regression lines drawn through the data distinguish between the low-silica Fba glasses (slope = 4.5; R^2 = 0.999) and the high-silica glasses (slope = 2.97; R^2 = 0.992) with a difference in slopes of about 41 %. The results from both techniques show excellent linearity relative to the glass bulk chemistry and silica content, indicating that whether fluorine ions are generated by Cs^+ or O^- impacts, the signal increases in the same way (the simplest explanation is that, in both cases, the F- signal increases linearly with concentration. However, we cannot rule out a similar, non-linear increase with concentration). The equations for the regression lines show slopes of 4.52 (basaltic Fba glasses) and 2.97 (high-silica glasses), indicating that the $^{19}F/^{18}O$ ratios obtained with an O^- primary beam are about 4.5 and 3 times greater, respectively, than those obtained with a Cs^+ primary beam. The slopes of the regression lines can be used as correction factors when assessing results from both Cs^+ and O^- techniques or when converting results from one technique to the other.

3.3 Matrix Effects and the Use of the Fba Standards

Because SIMS output is in counts per second, an empirical method must be employed to convert SIMS output to elemental concentration data. This is accomplished by creating a calibration curve consisting of geologic reference materials that have been sufficiently characterized for the element of interest and analyzed on the SIMS. The measured $^{19}F^-$ secondary ion intensities on unknowns were normalized to the intensity for $^{18}O^-$ (a minor isotope of oxygen) and compared with fluorine concentrations determined on previously-characterized reference materials. SIMS analyses are subject to matrix effects, requiring the use of appropriately matrix-matched standards when constructing the calibration curve. A pronounced matrix effect has been observed when analyzing F on the SIMS, and Chapter 3 demonstrates that the calibration factors from high-silica and low-silica, basaltic calibration curves differ by as much as a factor of two when utilizing an O^- primary beam. The glass standards analyzed for F in this study using the Cs^+ primary beam (Fba glasses, NIST-610, KE-12, and UTR-2) were used to construct SIMS calibration curves to assess the extent of matrix effects when measuring F using the Cs^+ primary beam (Fig. 4.6 a, b). Figure 4.6 (a) shows the SIMS calibration curve (Curve 1) using the low-silica Fba glasses and the silica blank. Curve 1 shows an excellent linear trend with the regression line forced through the origin, an $R^2 = 0.995$, and a calibration factor (CF; inverse of slope) of 422.8. Figure 4.6 (b) shows a SIMS calibration curve (Curve 2) constructed using the high-silica glasses and the silica blank, and the regression line is forced through the origin. Curve 2 shows excellent linearity, with an $R^2 = 0.999$ and CF = 512.3. The difference in slopes between Curves 1 and 2 demonstrates matrix effects in SIMS analysis of $^{19}F^-$ when utilizing a Cs^+ primary beam. The extent of matrix effects between the low-silica basaltic glasses and the high-silica glasses is about 20 %, or a factor of ~1.2, much less than the matrix effects of 50 % (factor of 2; see Chapter 3) when using an O^- primary beam to measure $^{19}F^-$. Although moderate

compared with an O^- primary beam, matrix effects is a factor that must be considered when utilizing a Cs^+ primary beam to generate negative secondary ions of F.

Both the low-silica basaltic and the high-silica rhyolitic glass standards of this study have bulk chemistries much different than that of the unknown olivine samples, rendering the use of "appropriately matrix-matched standards" for SIMS analysis of F in olivines a relative concept. In Chapter 3, it was demonstrated that matrix effects has a profound impact on calculating the F content of samples that have different matrix chemistries as the standards, and that using the high-silica glasses overestimate the F content of low-silica glasses. For our study of F in olivine grains, we decided to use the calibration factor (CF = 422.8) generated from Curve 1 (Fig. 4.6 a). Although the matrix chemistry of the Fba glasses are not an exact match to the chemistry of olivine, their silica, Mg, and Fe content are closer to that of olivine than the high-silica glass standards. However, we recognize that the application of the Fba calibration curve toward assessing the F content of olivine may be uncertain, and the change in olivine content from Fo90 to Fo05 may itself be subject to matrix effects which the Fba calibration curve may not alleviate.

3.4 Fluorine Content of the Olivine Samples

Tables 4.2- 4.5 categorize the olivine grains by the cooling rate of host rock (e.g. extrusive, hypabyssal, plutonic) and olivine grains from xenoliths. Listed in Tables 4.2-4.5 are the original olivine grain sample names from the Simkin and Smith (1970) paper, the collection location of the olivine grains, a description of the host rock, major element data of the olivine grains, the forsterite (Fo) content of the olivine grains, the SIMS $^{19}F^-/^{18}O^-$ ion ratios, and the F content of the olivine grains calculated using the calibration factor (422.8) from Curve 1 (Fig. 4.6 a). The F contents of all the olivine samples span a range from less than 1 ppm to about 37 ppm, with the vast majority of the olivine grains containing less than 1 ppm F. Figure 4.7 (a-c) shows histograms that demonstrate the

range of F content among the samples analyzed. The geological context of most of these samples is unknown, so our discussions are limited.

3.4.1 Fluorine Content of Kimberlitic Olivine

One sample stands out in Figure 4.7 (a-c); the olivine from kimberlite. This sample (F = 37±3 ppm) shows nearly five times as much F as any other olivine from the *plutonic* suite of samples from this study, and is at least twice as rich in F as most other olivines from the *extrusive - hypabyssal* and *xenolith* suites. This observation matches well with earlier studies (Hervig et al., 1988; Hervig and Bell, 2005) and suggests that olivine can be a host for fluorine at upper mantle pressures (*P*) and temperatures (*T*). Whether this is a result of increased compatibility of olivine for F at high pressures, the *P* and *T* exceeding the stability limits of micas, amphiboles, and apatite (fluorine reservoirs), a local high-F bulk composition in the kimberlite, or a combination of effects that remains to be determined.

3.4.2 Fluorine Content of the Extrusive and Hypabyssal Rocks

Extrusive rocks include ol-nephelinites, picrite basalts, tholeiite basalts, and andesites. The hypabyssal rocks are peridotites, picrites, and teschenites, and their olivine F contents are generally low, averaging < 1 ppm. The F content of olivines from the extrusive and hypabyssal suites ranges from < 1 ppm to about 15 ppm (Fig. 4.7 a). One outlier, an olivine grain from a picrite basalt from Igdlorssuit, Greenland, records an F content of about 15 ppm. The olivine grains from ol-nephelinites from Mt. Nyiragongo, East Africa, and the pillow basalts from Keflavik, Iceland show F contents consistently ≤ 1 ppm. The low abundance of F in the Icelandic mid-oceanic ridge (MORB) pillow basalt olivines may reflect a depleted magma source. Rowe and Schilling (1979) measured whole-rock F content from the interiors of pillow basalts from the Reykjanes Ridge, Iceland, and they found the total F content of these rocks ranged from 82 ppm to 270 ppm. They concluded that two magma sources exist that could erupt the multi-modal abundance of F in these Icelandic basalts, one source more depleted than the other in F

as well as in trace elements. Olivine grains from ocean island basalts (OIB) and andesites show F contents that range from < 1 ppm to about 8 ppm. Fluorine from olivines within the less evolved basalts tends to range from about 1 to 5 ppm, while the more evolved ocean-island andesites contain F contents that range from 6 to 8 ppm (Figure 4.8 a, b). Figure 4.8 (b) highlights the F content of olivine grains in the genetically-related basalts and andesites from the Hawaiian Islands suite. The Hawaiian olivine samples show a moderate increase in their F content with decreasing Fo content, the basalts showing a wider range in F content than do the andesites. There appears to be a fairly sharp dividing line separating the F content of the olivines from andesites and from the basalts, again demonstrating the incompatibility of F in olivine and the reluctance of F to be lost from magma during degassing and fractionation.

3.4.3 Fluorine Content of the Plutonic Rocks

Plutonic rocks of this study include depleted dunites and harzburgites from ophiolites, a peridotite, an ol-bearing rapakivi, and wehrlites and troctolites from layered intrusions. The overall F content of olivines in these plutonic rocks range from << 1 ppm to about 8 ppm, excluding the olivine from kimberlite discussed above (Fig. 4.7 c). The F content of olivines from ultramafic cumulates (dunites and harzburgites from ophiolites; wehrlite and diorite from Nain intrusive, Newfoundland; upper troctolite from Kiglapait Layered Intrusion) show a wide range of F values (0.4 – 8 ppm) and span a number of different tectonic and igneous environment (ophiolites and layered intrusions). Figure 4.9 shows a plot of the forsterite (Fo) content of the olivine samples from plutonic rocks versus their F content. The range of Fo spans from fayalitic to forsteritic, but the F content remains low regardless of Fo content. Unlike the extrusive suites, there appears to be no correlation between Fo and F content within the olivine grains from these plutonic rocks. However, using the Kiglapait Layered Intrusion as a case study, we will show that the F content of olivines from layered cumulates can also reflect the precipitation of fluorine-compatible phases from the cooling magma.

3.4.4 Olivines from the Kiglapait Layered Intrusion

Olivines from the Kiglapait layered intrusions were represented in the Simkin & Smith collection, and these samples contain enough geological context and stratigraphic integrity to warrant further discussion. The Kiglapait Layered Intrusion, Labrador, is a Precambrian layered gabbroic intrusion of the Skaergaard type about 560 km^2 in area. The Kiglapait has recognizable border zones and a layered series, with generally cumulate troctolite comprising the Lower Zone and gray olivine gabbro making up the Upper Zone. The intrusion displays extreme fractionation within an arguably closed system and has served as a natural laboratory over the decades for the study of fractionation trends. From modal and mineral analyses of its layers, the composition of the parent magma is estimated to have been alkali-basalt (Morse 1965). During fractional crystallization of a mafic magma body where olivine and plagioclase are the initial crystallizing phases, the growing olivine crystals consume Mg over Fe at a faster rate such that the later stages of olivine crystallization result in olivine crystals that are more fayalitic. Hence, the Mg/Fe ratio of olivine decreases with fractionation of the magma. The F content of the olivine grains taken from the Kiglapait ranges in abundance from 0.9 ppm to 8.0 ppm. If F behaves as an incompatible element in olivine, then there should be recognizable fractionation trends with F abundances in olivine such that F will show a negative correlation with the Mg/Fe ratio of the olivine crystals. Figure 4.10 shows that this is not the case. The F abundance in the olivine crystals decreases markedly as the Mg/Fe ratio decreases, pointing toward the crystallization of trace to modal amounts of hydrous and/or fluoride phases that would begin consuming the F from the magma. Figure 4.11 shows a plot of the F content of the olivine crystals versus the percent solidification of the intrusion (estimates from Morse 1965; Note: Morse 1965 used the concept of percent solidification as a means of stratigraphic control within the Kiglapait layered intrusion). Within the troctolite lower zone, F displays a normal trend of increasing concentration in the olivine crystals as F is concentrated in the melt during fractionation of

F-poor minerals. However, three olivine grains from rocks presumed to represent > 80% crystallization show much lower F than the earlier olivine. While apatite (a typically F-rich mineral) was unambiguously identified after 95% crystallization, the low F olivines indicate that this phase must have begun to precipitate earlier, possibly in trace amounts, resulting in an increasingly F-poor melt. The above interpretation is based on the analysis of only five olivine grains. More samples representing a more complete stratigraphic and spatial perspective of the Kiglapait Layered Intrusion is desirable.

4. Summary and Conclusions

Olivine crystals from a range of geologic and tectonic environments were measured for fluorine using SIMS employing a Cs^+ primary beam and a normal incidence electron gun for charge-compensation. Because previous measurements of $^{19}F^-$ on SIMS in this work utilized an O^- primary beam, a suite of microanalytical glass standards of both low-silica basaltic (Fba glasses from Chapter 3 of this work) and high-silica rhyolitic (NIST-610, UTR-2, and KE-12) compositions were analyzed for $^{19}F^-$ using both a Cs^+ primary beam and an O^- primary beam, and the results were compared. Both methods yielded $^{19}F^-$ secondary ion count rates that allowed for sub-ppm detection of F in mineral phases. The $^{19}F^-/^{18}O^-$ ion ratios obtained by both primary-beam methods were plotted against each other, and strong linear relationships emerged that showed two separate regression lines connecting low-silica and the high-silica glasses, thus illustrating the influence of matrix effect regardless of primary beam used. To convert SIMS $^{19}F^-/^{18}O^-$ ion ratios to F concentrations, we constructed SIMS calibration curves using the basaltic and rhyolitic glass standards from above analyzed with SIMS using a Cs^+ primary beam. Two calibration curves connecting glasses of similar compositions were noted: basaltic curve (calibration factor = 422.8) and rhyolitic curve (calibration factor = 512.3), demonstrating a moderate control of matrix effects in F analysis of about 20 %. Nevertheless, because of the added risk of introducing uncertainty when using a normal incidence electron gun

to eliminate charging when employing the Cs^+ primary beam, coupled with the effectiveness of using an O^- primary beam to detect sub-ppm levels of F in geologic materials, we decided to conduct all future F analyses on the SIMS using the O^- primary beam method.

Fluorine measurements were carried out using SIMS and a Cs^+ primary beam on olivine samples from the classic paper by Simkin and Smith (1970). The olivine grains reflect a wide range of various source rocks, cooling histories, and fractionation trends. The majority of the crystals lacked geologic context, but a few, like the Hawaiian suite of genetically related olivines from basalts and andesites and the olivine crystals from the Kiglapait Layered Intrusion showed that F behaves as an incompatible element. The most F-rich olivine was recovered from a kimberlite, pointing to a role of nominally anhydrous phases in hosting volatile elements at high *P* and *T*.

5. References

Bell, D.R. and Rossman, G.R. (1992) Water in Earth's mantle: The role of nominally anhydrous minerals. Science, 255, 1391-1397.

Brown, G.M. (1956) The layered ultrabasic rocks of Rhum, Inner Hebrides. Philosophical Transactions of the Royal Society of London, 240: 1-54.

Carroll, M.R. and Webster, J.D. (1994) Solubilities of sulfur, noble gases, nitrogen, chlorine, and fluorine in magmas. In: Carroll, M.R. and Holloway, J.R. (eds), Volatiles in Magmas. Reviews in Mineralogy Volume 30. Mineralogical Society of America (Washington, D.C.), 231-279.

Engi, M. and Lindsley, D.H. (1980) Stability of titanian clinohumite: Experiments and thermodynamic analysis. Contributions to Mineralogy and Petrology, 72, 415-424.

Hermann, J., Fitz Gerald, J.D., Malaspina, N., Berry, A.J. and Scambelluri, M. (2007) OH-bearing planar defects in olivine produced by the breakdown of Ti-rich humite minerals from Dabie Shan (China). Contributions to Mineralogy and Petrology, 153, 417-428.

Hervig, R.L. and Bell, D.R. (2005) Fluorine and hydrogen in mantle mega-crysts. American Geophysical Union Fall Meeting Abstract.

Hervig, R.L., Mazdab, K., Moore, G., McMillan, P.F. (2003) Analysing hydrogen (H_2O) in silicate glass by secondary ion mass spectrometry and relectance Fourier transform infrared spectroscopy. In: De Vivo, B. and Bodnar, R.J. (eds) Melt Inclusions in Volcanic Systems: Methods Applications and Problems. Developments in Volcanology 5. Elsevier, 83-103.

Hervig, R.L., Smith, J.V. and Rivers, M.L. (1988) Fluorine content of upper mantle minerals. EOS, Transactions of the American Geophysical Union, 69, 502.

Hoskin, P.W.O. (1999) SIMS Determination of μg g^{-1} - level fluorine in geological samples and its concentration in NIST SRM 610. Geostandards Newsletter, 23, 69-76.

Ingrin, J. and Skogby, H. (2000) Hydrogen in nominally anhydrous upper-mantle minerals: Concentration levels and implications. European Journal of Mineralogy, 12, 543-570

Kane, J.S. (2001) The use of Reference Materials: A tutorial. Geostandards Newsletter, 25, 7-22.

MacDonald, G.A. and Katsura, T. (1964) Chemical composition of Hawaiian lavas. Journal of Petrology, 5, 82-133.

McDonough, W.F. and Sun, S.S. (1995) The composition of the Earth. Chemical Geology, 120, 223-253.

Moores, E.M. (1969) The petrology and structure of the Vourinos ophiolitic complex of Northern Greece. Geological Society of America Special Paper 118.

Morse, S.A. (1965) The Kiglapait layered intrusion, Labrador. Geological Society of America Memoir, 112p.

Moune, S., Sigmarsson, O., Thordarson, T. and Gauthier, P.J. (2007) Recent volatile evolution in the magmatic system of Hekla volcano, Iceland. Earth and Planetary Science Letters, 255, 373-389.

Ottolini, L., Cámara, F., Hawthorne, F.C. and Stirling, J. (2002) SIMS matrix effects in the analysis of light elements in silicate minerals: Comparison with SREF and EMPA data. American Mineralogist, 87, 1477-1485.

Ottolini, L., Cámara, F. and Bigi, S. (2000) An investigation of matrix effects in the analysis of fluorine in humite-group minerals by EMPA, SIMS, and SREF. American Mineralogist, 85, 89-102.

Pivovarov, A.L. and Guryanov, G.M. (2010) F and Cl detection limits in secondary ion mass spectrometry measurements of Si and SiO2 samples. Journal of Vacuum Science and Technology, A, 28, 1181-1186.

Portnyagin, M., Simakin, S. and Sobolev, A. (2002) Fluorine in primitive magmas of the Troodos Ophiolite complex, Cyprus: analytical methods and main results. Geochemistry International, 40, 625-632.

Rowe, E. and Schilling, J.G. (1979) Fluorine in Iceland and Reykjanes ridge basalts. Nature, 279, 33-37.

Sahama, Th.G. (1962) Petrology of Mt. Nyiragongo: A review. Transactions of the Edinburgh Geological Society, 19, 1-28.

Sahama, T.G. and Hytönen, K. (1958) Calcium-bearing magnesium-iron olivines. American Mineralogist, 43, 862-871.

Schuhmacher, M., Rasser, B., De Chambost, E., Hillion, F., Mootz, T. and Migeon, H.N. (1999) Recent instrumental developments in magnetic sector SIMS. Fresenius' Journal of Analytical Chemistry, 365, 12-18.

Simkin, T. and Smith, J. (1970) Minor-element distribution in olivine The Journal of Geology, 304-325.

Simkin, T. (1967) Flow differentiation in the picritic sills of north Skye, in Wyllie, P.J. (eds) Ultramafic and related Rocks: John Wiley and Sons, New York, p. 64-69.

Simkin, T. (1966) Zoned olivines and the cooling history of a picritic sill (abs) Geological Society of America Special Paper, 101, 202-203.

Simonen, A. (1961) Olivine from Rapakivi. Geological Survey of Finland Compte rendus, 33, 371-376.

Smith, J., Delaney J., Hervig, R. and Dawson, J. (1981) Storage of F and Cl in the upper mantle: Geochemical implications. Lithos, 14, 133-147.

Stecher, O. (1998) Fluorine geochemistry in volcanic rock series: examples from Iceland and Jan Mayen. Geochimica et Cosmochimica Acta, 62, 3117-3130.

Stern, R.A. (2009) Chapter 1: An introduction to secondary ion mass spectrometry (SIMS) in geology. In: Fayek, M. (eds) Secondary Ion Mass Spectrometry in the Earth Sciences: Gleaning the Big Picture from a Small Spot. Mineralogical Association of Canada Short Course, vol. 41, p. 1-18.

Straub, S.M. and Layne, G.D. (2003) The systematics of chlorine, fluorine, and water in Izu arc front volcanic rocks: Implications for volatile recycling in subduction zones. Geochimica et Cosmochimica Acta, 67, 4179-4203.

Westrich, H.R. (1990) Materials compatibility studies for the magma energy extraction project. Geothermics, 19, 341-357.

Wheeler, E.P. (1965) Fayalitic olivine ion northern Newfoundland-Labrador. Canadian Mineralogist, 8, 339-346.

Wilkinson,J. (1958) The petrology of a differentiated teschenite sill near Gunnedah, New South Wales. American Journal of Science, 256, 1-39.

Wilson, R.G., Stevie, F.A., Magee, C.W. (1989) Secondary Ion Mass Spectrometry: A Practical Handbook for Depth Profiling and Bulk Impurity Analysis. Jon Wiley and Sons. New York.

Wittmaack, K. (2012) Mechanisms responsible for inducing and balancing the presence of Cs adatoms in dynamic Cs based SIMS. International Journal of Mass Spectrometry. 313, 68-72.

Yagi, K. (1960) Petrochemistry of the alkalic rocks of the Ponape island, western Pacific Ocean. International Geological Congress, pt. 13, 108-122

Yagi, K. (1964) Pillow lavas of Keflavik, Iceland and their genetic significance. Journal of the Faculty of Science, Hokkaido University. Series 4, Geology and Mineralogy, 12, 171-183.

Yoder, H.S. and Tilley, C.E. (1962) Origin of basalt magmas: An experimental study of natural and synthetic rock systems. Journal of Petrology, 3, 342-532.

6. Figure Captions

Figure 4.1. Selected olivine grain mounts from the original study by Simkin and Smith (1970). Mounts are 1-inch-diameter brass discs with pre-drilled holes for samples. Olivine grains set into epoxy within the small round drill-holes and polished with 3 μm and 1 μm alumina paper.

Figure 4.2. Plan view of the Cameca secondary ion mass spectrometer (SIMS) ims 6f.

Figure 4.3. SIMS high resolution mass spectrum of F from an analysis of NIST 610 using the SIMS 6f showing the separation between the ^{19}F and ^{18}OH peaks. Mass resolving power (M/ΔM/) is 2500.

Figure 4.4. Plot of the ratio of the $^{19}F^-$ secondary ion yields generated by both the Cs^+ and O^- primary beams for the glass standards used in this study. Ideally, the ratio of ion yields should be consistent for all materials. The Fba glasses and NIST-610 are within error, but the pantellerite glasses UTR-2 and KE-12 show higher ion yield ratios.

Figure 4.5. The $^{19}F/^{18}O$ ratios for the low- and high-silica glasses generated from the O^- primary beam versus those generated from the Cs^+ primary beam. The ion ratios from both primary beams show excellent linear relationships connecting glasses of similar compositions, thus illustrating the occurrence of matrix effects regardless of primary beam used.

Figure 4.6. SIMS calibration curves for the low- and high-silica glass standards based on the SIMS Cs^+ primary-beam method. a) The low-silica basaltic glasses show an excellent linear trend and produce a calibration factor of 422.8. b) the high-silica rhyolitic glasses show an excellent linear trend and produce a calibration factor of 512.3. Moderate matrix effects of about 20 % are noted for F analysis with this method.

Figure 4.7. Histograms showing the F content of the olivine samples from this study. a) Extrusive and hypabyssal suites. b) Xenoliths. c) Plutonic suites.

Figure 4.8. Forsterite content of the olivines from extrusive suites versus their F content. (a) Overall, the data show a weak trend of increasing F content of the olivine crystals with increasing Fe content. (b) The genetically related Hawaiian suites of basalts and andesites show increasing F content of the olivines with decreasing Fo content due to magma evolution, demonstrating the incompatible nature of F within olivine and melt.

Figure 4.9. Forsterite content of the olivine samples from the plutonic suites versus their F content. The Fo content spans the range from highly fayalitic to forsteritic, but there appears to be no correlation between Fo content and F content in these olivine samples.

Figure 4.10. Mg/Fe ratio of the olivine grains from the Kiglapait Layered Intrusion versus their F content. The trend shows decreasing F content with increasing fayalite content, which is not what would be expected if F does indeed behave as an incompatible element during fractional crystallization of a closed system.

Figure 4.11. The F content of olivine grains from the Kiglapait Layered Intrusion versus the percent solidified (PCS) within the intrusion during its cooling history. PCS is a proxy for the stratigraphic position where the olivine grains were collected. The graph shows an increase in the F content with fractional crystallization until phases begin to crystallize that consume F more readily that olivine. In the Upper Zone, the appearance of modal apatite causes the F content of olivine to drop off precipitously.

Table 4.1. Average SIMS measurements and secondary ion yields of $^{19}F^-$ on the high silica glass standards using both Cs+ and O- primary beams.

			O- Primary Beam								Cs+ Primary Beam								Yield Ratio		$^{19}F^-/^{18}O^-$ Relative Ratios	
Sample	F (ppm)	σ	I (nA)	σ	$^{19}F^-/^{18}O^-$	σ	$^{19}F^-$ (cps)	σ	$^{19}F^-$ Yield†	σ	I (nA)	σ	$^{19}F^-/^{18}O^-$	σ	$^{19}F^-$ (cps)	σ	$^{19}F^-$ Yield	σ	Cs^+/O^-	σ	O^-/Cs^+	σ
Fba-1	1320	480	3.15	0.04	17.48	1.81	23637	3777	5.7	1.0	2.00	0.08	3.67	0.03	58658	7244	22.3	3.6	3.9	1.3	4.8	0.5
Fba-2	5300	1100	3.17	0.04	67.90	1.15	106479	5835	6.3	0.4	2.01	0.05	14.09	0.40	222326	8349	20.8	1.3	3.3	0.4	4.8	0.2
Fba-3	8650	1040	3.16	0.05	102.12	2.50	160924	10960	5.9	0.5	2.04	0.09	22.33	0.06	303126	10402	17.2	1.3	2.9	0.5	4.6	0.1
Fba-4	14100	1070	3.22	0.03	152.82	4.08	212528	18706	4.7	0.5	2.14	0.08	33.89	1.86	647184	74263	21.5	3.3	4.6	1.2	4.5	0.4
Fba-5	22400	1230	3.35	0.02	231.23	4.58	350137	42638	4.7	0.6	2.03	0.07	51.51	1.58	850825	53825	18.7	1.9	4.0	0.9	4.5	0.2
NIST-610[a]	180	--	3.31	0.09	0.95	0.01	3127	252	5.2	0.6	1.94	0.04	0.41	0.03	7593	504	21.8	1.9	4.2	0.8	2.3	0.2
KE-12[b]	4000	--	3.55	0.02	23.49	0.35	35207	2725	2.5	0.2	1.93	0.02	7.75	0.07	151188	11819	19.6	1.7	7.9	1.3	3.0	0.1
UTR-2[c]	1048	--	3.32	0.08	5.83	0.61	11392	55	3.3	0.1	1.97	0.06	2.42	0.01	41184	3018	20.0	2.1	6.1	0.8	2.4	0.3

a. NIST-610 F (ppm) content from Chapter 3 of this work.
b. KE-12 F (ppm) from Moune et al. (2007)
c. UTR-2 F (ppm) content from Chapter 3 of this work.
† Yield: Ion yield = F (cps)/F (ppm)/operating current (nA)

Table 4.2. List of olivine samples from extrusive suites showing collection location, description of host rock, major element, and F data.

Sample	Location	Host Rock	Mg	Fe	Ca	Mn	Ni	Fo	$^{19}F/^{18}O$	sd	F (ppm)	sd
Mount Nyirgongo, East Africa (Sahama and Hytonen, 1958; Sahama, 1962)												
EQ1	Kabfumu, 10 km ENE of summit	Olivine-melilite nephelinite	26.9	5.6	0.38	0.24	0.13	83	0.0062	0.0002	0.6	0.02
EQ7	Baruta crater, north of main crater	Olivine nephelinite	27.1	4.6	0.35	0.23	0.15	85	0.0073	0.0012	0.7	0.12
Isle of Skye, Scotland (Simkin, 1967)												
EA1	Druim Fada	Basalt	24.5	6.0	0.21	0.22	0.21	80	0.054	0.0248	5.2	2.4
EA2	Ru Idrigal	Basalt	24.0	7.6	0.21	0.25	0.18	76	0.026	0.0045	2.6	0.44
EA3	Scamadal	Basalt	24.2	8.4	0.22	0.24	0.22	74	0.039	0.0227	4.7	2.0
EA4	Strathaird	Basalt	26.2	4.9	0.22	0.20	0.24	84	0.017	0.0131	2.5	1.2
EA5	Portree	Basalt	23.2	9.4	0.25	0.28	0.17	71	0.019	0.0100	1.3	0.17
Keflavik, Iceland (Yagi, 1964)												
EP1	Stapafell quarry, Keflavick	Upper center pillow basalt (Phen: ol: 4%, Grndms: ol: 3.2%, pl: 31.3%, mag: 5.3%, gl: 56.4%)	28.2	5.0	0.17	0.16	0.21	85	0.0040	0.0013	0.4	0.13
EP2	Stapafell quarry, Keflavick	Lower center pillow basalt (Phen: ol: 24.4%, Grndms: ol: 2.2%, pl: 26.6%, mag: 3.1%, gl: 43.7%)	28.1	4.6	0.19	0.17	0.23	86	0.0041	0.0013	0.4	0.12
EP3	Stapafell quarry, Keflavick	Lower rim pillow basalt (Phen: ol: 15.8%, Grndms: ol: 1.6%, pl: 24.0%, mag: 0.6%, glass: 58.0%)	28.1	6.4	0.20	0.19	0.19	81	0.0033	0.0001	0.3	0.01
EP4	Stapafell quarry, Keflavick	Nearby center pillow basalt	28.4	5.0	0.19	0.16	0.21	85	0.0056	0.0001	0.5	0.02
Pacific Island Suites (Yagi, 1960)												
EP5	Sado Island, Japan	Picrite basalt	28.8	4.4	0.15	0.15	0.17	87	0.0069	0.0015	0.7	0.15
EP8	Ponape Island, Caroline Islands, Western Pacific Ocean: Roi Rock, Oné, Kitiu	Olivine Ti-augite nepheline dolerite (picrite basalt) (Phen: ol: 20.2%, Ti-aug: 32.8%, mag: 4.1%; Grndms: pl: 20.6%, ne: 10.1%, ol: 1.0%, Ti-aug: 4.4%, mag: 3.8%, ap: 1.2%, anl: 0.9%, bt: 0.9%)	24.1	8.9	0.13	0.24	0.07	73	0.011	0.0065	1.1	0.63
EP9	Ponape Island, Caroline Islands, Western Pacific Ocean: North end of Parām Island	Kaersutite-bearing olivine Ti-augite basalt (Phen: pl: 2.3%, ol: 0.35, Ti-aug: 0.8%, krs: 0.1%, mag: 1.0%; Grndms: 95.5% pl, ol, mag, ap, Ti-aug	24.8	7.8	0.03	0.24	0.14	76	0.0057	0.0001	0.6	0.02
EP10	Truk Island, Caroline Islands	Melilite nepheline basalt	27.6	5.0	0.17	0.17	0.17	85	0.0072	0.0014	0.7	0.13
Hawaiian Chain, Central Pacific Ocean (Yoder and Tilley, 1962, McDonald and Katsura, 1964)												
EA6	Mauna Loa, 1887 Flow, southwest rift	Hypersthene basalt (Phen: ol; Microphen: cpx, opx, pl; Grndms: subcalcic aug and pl; hy rimmed with pgt, ilm, mag; brown interstitial glass.	25.1	3.6	0.36	0.19	0.26	87	0.0231	0.0104	1.7	0.60
EA7	Kilauea, Prehistoric Flow, National Park Quarry	Tholeiite (Phen: ol; Grndms: sub-calcic aug, ilm, mag, devitrified glass)	25.2	7.0	0.21	0.21	0.17	78	0.0161	0.0114	1.8	1.5
EA8	Kilauea, 1960 Flow at Kapoho, East Rift Zone	Tholeiite (cellular trachylite) (Phen: aug, pl, ol; Grndms: glass)	24.9	7.2	0.27	0.25	0.18	77	0.0123	0.0003	1.2	0.02
EA10	North of Keauhou, Hualalai, Prehistoric Flow	Alkali basalt (Microphen: ol; Grndms: aug, pl, mag)	26.1	4.5	0.14	0.20	0.25	85	0.0080	0.0032	0.6	0.01
DP1	Hualalai, Kaupuleh, 1801 Flow	Olivine basalt	24.9	7.0	0.14	0.18	0.16	78	0.0256	0.0093	2.5	0.90
DP6	Hualalai, Kaupuleh, 1801 Flow	Olivine basalt	24.9	4.3	0.14	0.18	0.16	85	0.0353	0.0038	3.4	0.37
DP9	Maui, Haleakala Crater Floor	Picrite basalt	23.3	8.1	0.15	0.23	0.10	74	0.0275	0.0098	2.7	0.95
DP12	Maui, Haleakala Observatory	Picrite basalt	23.5	9.0	0.15	0.24	0.09	72	0.0193	0.0077	1.9	0.75
DP10	Maui, Haleamuu Trail, Maui	Andesite	23.2	8.5	0.21	0.21	0.09	73	0.0441	0.0062	4.3	0.60
DP11	Maui, Haleakala Observatory	Andesite	23.0	8.2	0.14	0.24	0.10	74	0.0544	0.0040	5.3	0.38
DP13	Maui, Kalahaku Overlook	Andesite	23.4	9.5	0.16	0.25	0.09	71	0.0401	0.0035	3.9	0.34

Table 4.3. List of olivine samples from xenoliths showing collection location, description of host rock, major element, and F data.

Sample	Location	Host Rock	Mg	Fe	Ca	Mn	Ni	Fo	$^{19}F/^{18}O$	sd	F (ppm)	sd
Pacific Island Suite (Yagi 1960)												
EP6	Ponape Island, Caroline Islands, Western Pacific Ocean	Olivine nodule in nepheline basalt	30.00	4.05	0.00	0.13	0.25	88	0.010	0.0012	1.0	0.1
DP2	Hawaii, Hualalai, Kaupulehu, 1801	Olivine nodule within olivine basalt	26.90	5.57	0.10	0.15	0.27	83	0.038	0.014	3.7	1.3
DP3	Hawaii, Hualalai, Kaupulehu, 1802	Olivine nodule within olivine basalt	25.60	6.38	0.07	0.19	0.25	80	0.037	0.016	3.5	1.6
DP4	Hawaii, Hualalai, kaupulehu, 1801	Olivine nodule in olivine basalt	26.00	6.79	0.08	0.17	0.22	79	0.028	0.0029	2.7	0.3
DP7	Hawaii, Hualalai, Kaupulehu, 1802	Olivine nodule within olivine basalt	26.80	5.04	0.05	0.15	0.28	84	0.028	0.013	2.7	1.3
DP8	Olivine nodule within olivine basalt	Troctolite nodule	22.40	10.05	0.07	0.27	0.02	69	0.015	0.0047	1.5	0.5
Lanzarote, Canary Islands, Eastern Altlantic Ocean (Simkin and Smith 1970)												
EQ8	East end of 1730 fissure	Olivine-orthopyroxene block in alkalic basalt	30.00	3.53	0.09	0.15	0.30	89	0.0084	0.0011	0.8	0.1
EQ9	Center of 1730 fissure	Dunite xenolith	30.30	3.03	0.03	0.11	0.29	91	0.0062	0.0028	0.6	0.3
EQ10	1730 basalt flow	Peridotite xenolith	30.00	3.18	0.02	0.11	0.30	90	0.0034	0.0005	0.3	0.0
EQ11	Sub-Recent cinder cone	Large single olivine crystal	30.20	3.22	0.01	0.15	0.29	90	0.0062	0.0008	0.6	0.1
EQ12	Sub-Recent cinder cone	Dunite block	30.10	2.94	0.15	0.11	0.30	91	0.0051	0.0015	0.5	0.1
University of Chicago Petrographic Collection (Simkin and Smith 1970)												
DP14	Dreis Eifel, Rhine	Olivine bomb	28.80	3.90	0.07	0.11	na	88	0.115	0.068	11.2	6.6

Table 4.4. List of olivine samples from hypabyssal suites showing collection location, description of host rock, and major element data.

Sample	Location		Mg	Fe	Ca	Mn	Ni	Fo	$^{19}F/^{18}O$	sd	F (ppm)	sd
University of Chicago Petrographic Collection (Simkin and Smith 1970)												
DR3	Cullins, Skye, Scotland	Peridotite dike	28.70	3.96	0.23	0.15	0.29	88	0.0021	0.0006	0.2	0.1
Isle of Skye, Scotland (Simkin, 1966)												
DR14	Bornaskitaig Sill	Flow differentiated picritic sill and chilled olivine dolerite.	26.30	6.87	0.20	0.19	0.27	79	0.0063	0.0004	0.6	0.04
South East Australia (Wilkinson, 1958)												
EQ13	Black Jack Sill, 200 miles north-northwest of Sydney. Samples collected 20 feet above lower contact.	Teschenite: (ol: 23.0%, cpx: 19.7%, iron ore: 10.2%, feldspar: 38.0%, zeo: 9.1%)	24.30	7.31	0.17	0.20	0.18	77	0.0067	0.0006	0.6	0.1
Greenland (Simkin, 1966)												
EB13	Igdlorssuit	Picrite	30.40	10.15	0.20	0.12	0.38	75	0.10	0.12	9.8	11.4

Table 4.5. List of olivine samples from plutonic suites showing collection location, description of host rock, and major element data.

Sample	Location	Host Rock	Mg	Fe	Ca	Mn	Ni	Fo	$^{19}F/^{18}O$	sd	F (ppm)	sd
University of Chicago Petrographic Collection (Simkin and Smith 1970)												
DR2	Thetford, Quebec	Forsterite: ophiolite complex	31.6	1.9	0.01	0.07	0.44	94	0.0020	0.0002	0.2	0.02
DR9	Mooihoek, South Africa	Dunite: Bushveld layered intrusion	23.1	8.7	0.03	0.27	0.23	73	0.0055	0.0011	0.5	0.1
DR11	Grevenoir, Auvergne	Dunite (olivinfels)	29.3	3.6	0.08	0.14	0.3	89	0.0053	0.0004	0.5	0.04
DR12	Elliot County, Kentucky, USA	Kimberlite	29.1	5.5	0.06	0.13	0.27	84	0.19	0.1019	18.0	1.9
Vourinos Ophiolite Complex, Greece (Moores, 1969)												
EB7	Voidolakkos Valley, North Side	Harzburgite, strongly banded	29.7	3.7	0.01	0.12	0.35	89	0.0047	0.0007	0.5	0.1
EB8	Voidolakkos Valley, South Side	Dunite: 97% olivine with scattered, discreet serpintinite veins	30.7	3.4	0.1	0.11	0.36	90	0.0031	0.0004	0.3	0.04
EB10	Kounivo, Southern Area	Dunite: 40% serpentinite meshwork	31.4	3.1	0.09	0.1	0.37	91	0.0066	0.0001	0.6	0.01
EB11	0.5 km South of Chromion Village	Harzburgite, 90% seriate olivine, granular	30.5	3.9	0.02	0.12	0.33	89	0.0030	0.0001	0.3	0.01
North Carolina, USA (Simkin and Smith, 1970)												
EB12	Balsam Gap, Jackson County	Dunite with chromite, some serpentine, talc, vermiculite, chlorite, tremolite, anthophyllite	20.2	2.8	0.01	0.13	0.34	88	0.0045	0.0019	0.4	0.2
Lemi, Finland (Simonen 1961)												
EC7	Rapakivi massif of Viipuri, south-eastern Finland	Olivine-bearing, green hornblende rapakivi	1	25.0	0.05	0.83	0.01	4	0.049	0.0012	4.7	0.1
Rhum, Scotland (Brown, 1956; Simkin and Smith, 1970)												
EB5	Hallival-Askival Layered Ultamafic Intrusion	Layer 12. Harrisitic peridotite	28.5	5.6	0.07	0.18	0.22	83	0.045	0.0116	4.3	1.1
Nain Intrusive, Newfoundland-Labrador (Wheeler, 1965)												
EC8	Massif west of Tallifer Lake, south flank (Lat. 57°06'.0N, Long. 62°49'.2W)	Ilmenite-plagioclase wehrlite (ol: 49.9%; cpx: 21.9%; pl: 16.0%; black ore: 8.1%; ap: 2.0%; other: 2.1%)	1.3	26.8	0.06	0.75	0.01	5	0.0048	0.0001	0.5	0.2
EC9	Tallifer Lake, west end massif, east ridge (Lat. 57°06'.2N, Long. 62°48'.7W)	Clinopyroxene-olivine diorte (ol: 20.6%; cpx: 9.8%; pl: 64.9%; black ore: 2.8%; ap: 1.1%; other: 0.8%)	2.3	23.4	0.04	0.61	0.01	9	0.0061	0.0001	0.6	0.2
EC10	Tallifer Lake	Clinopyroxene-olivine diorite	1.1	23.7	0.05	0.77	0.01	4	0.016	0.0004	1.5	0.1
Kiglapait Layered Intrusion, Labrador (Morse, 1969)												
EC1	Lower Zone: 33% Solidified	Troctolite: (pl: 75.0; ol: 23.3%; aug: 1.4%)	18.8	12.9	0.03	0.38	0.06	59	0.041	0.0010	4.0	1.0
EC3	Lower Zone: 38% Solidified	Troctolite: (pl: 75.0; ol: 23.3%; aug: 1.4%)	21.3	10.2	0.02	0.32	0.09	68	0.057	0.0014	5.5	1.0
EC4	Upper Zone: 85.8% Solidified	Troctolite	15.9	14.9	0.03	0.43	0.04	52	0.017	0.0004	1.7	0.3
EC6	Upper Zone: 97.0% Solidified	Troctolite: (ap: 7.2%; bt: 0.9%)	3.7	23.8	0.04	0.95	0.01	13	0.0075	0.0002	0.7	0.1
EC5	Upper Zone: 99.98% Solidified	Troctolite	0.4	31.4	0.05	1.56	0.01	1	0.0063	0.0002	0.6	0.2

Figure 4.1

Figure 4.2

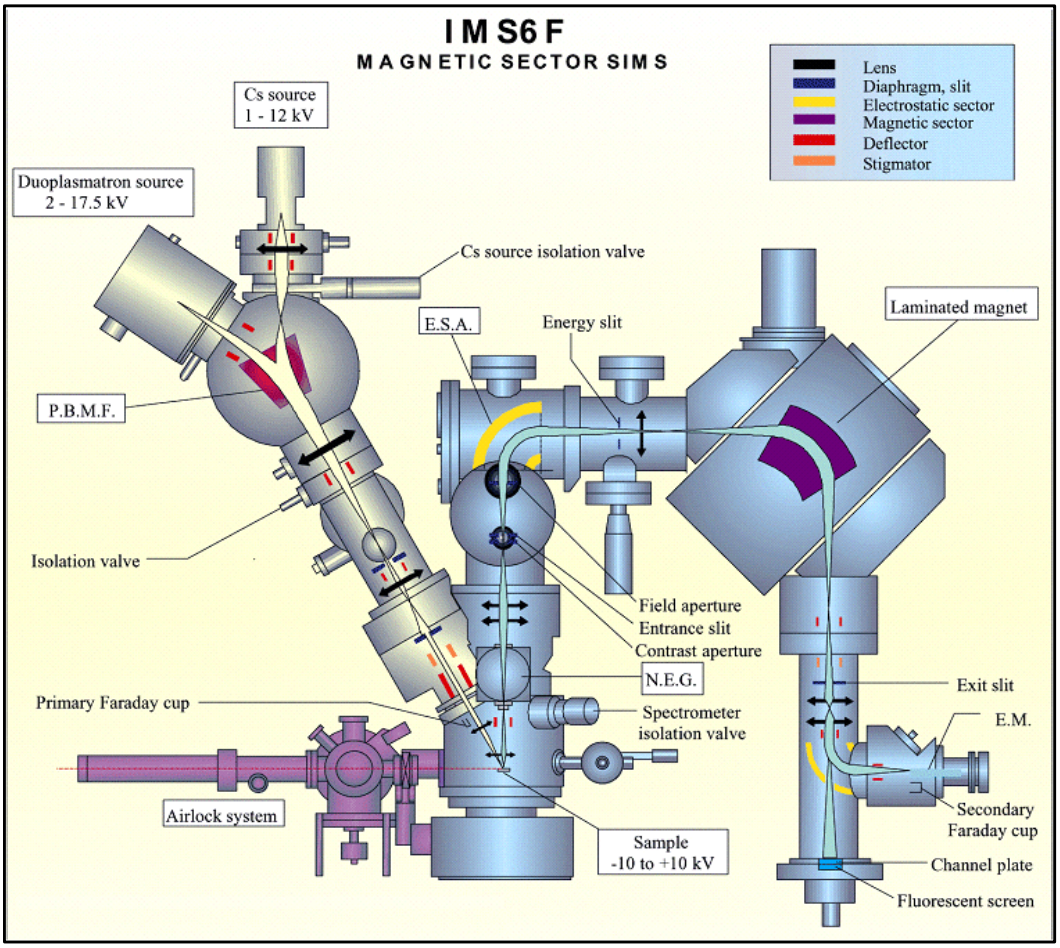
IMS6F
MAGNETIC SECTOR SIMS
Lens
Diaphragm, slit
Electrostatic sector
Magnetic sector
Deflector
Stigmator
Cs source
1 - 12 kV
Duoplasmatron source
2 - 17.5 kV
Cs source isolation valve
E.S.A.
Energy slit
Laminated magnet
P.B.M.F.
Isolation valve
Field aperture
Entrance slit
Contrast aperture
N.E.G.
Exit slit
E.M.
Primary Faraday cup
Spectrometer
isolation valve
Airlock system
Sample
-10 to +10 kV
Secondary
Faraday cup
Channel plate
Fluorescent screen

Figure 4.3

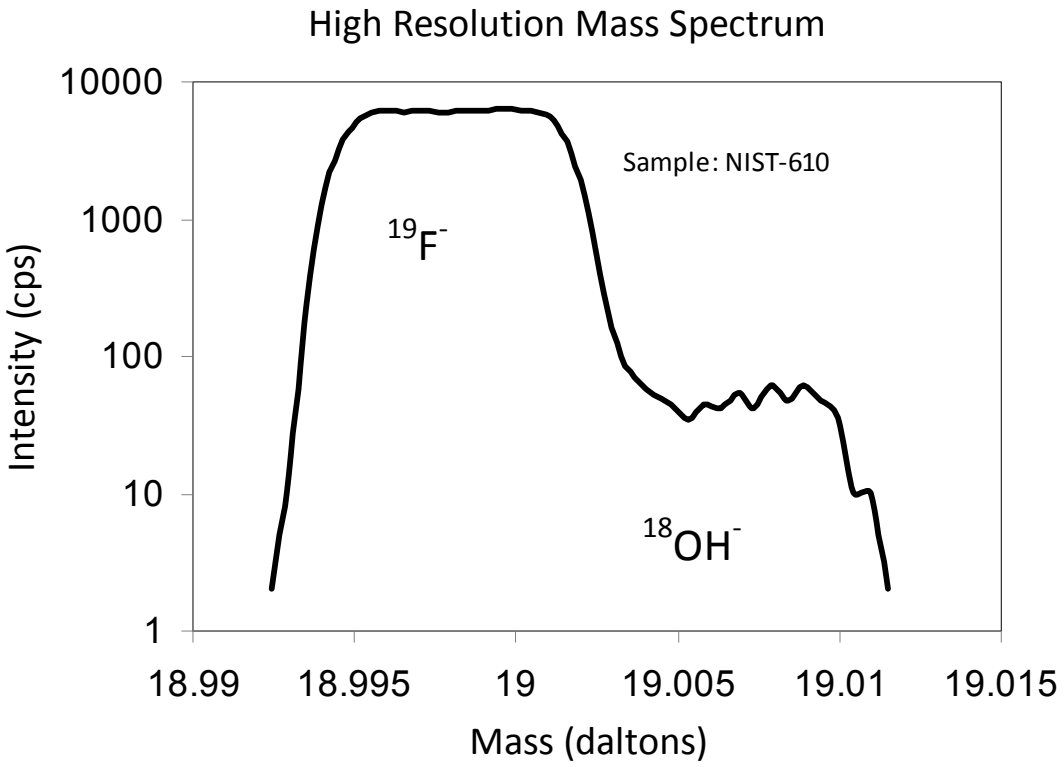
High Resolution Mass Spectrum
Sample: NIST-610
$^{19}F^-$
$^{18}OH^-$
Intensity (cps)
10000
1000
100
10
1
18.99
18.995
19
19.005
19.01
19.015
Mass (daltons)

Figure 4.4

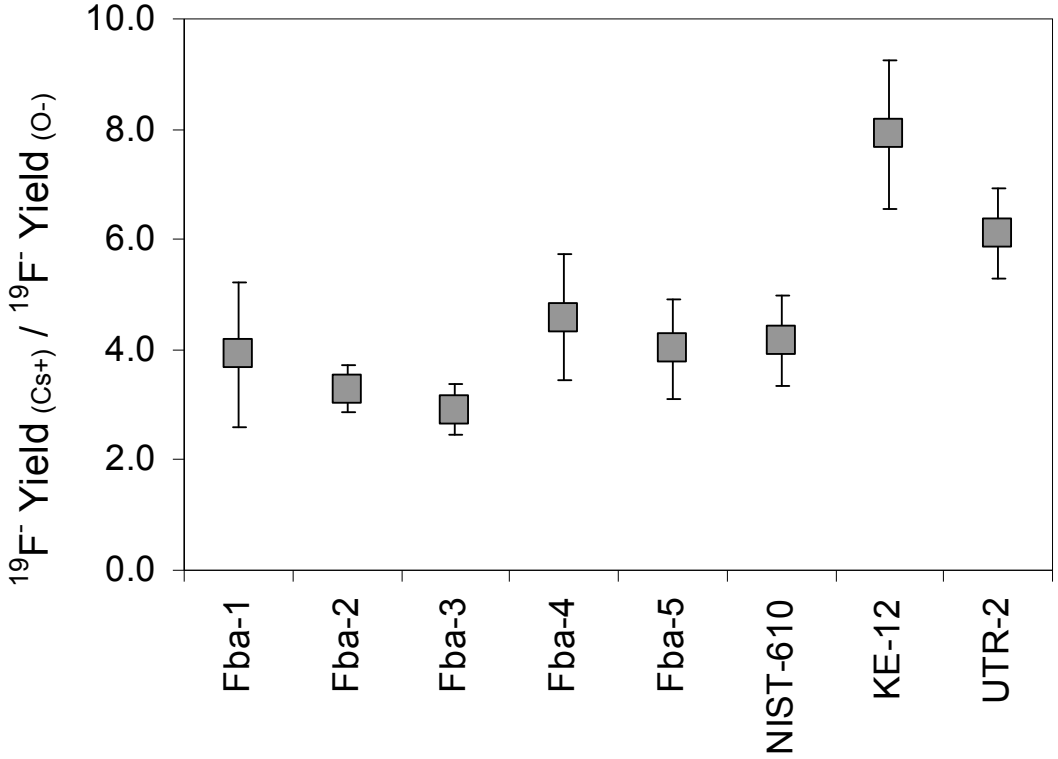
$^{19}F^-$ Yield $_{(Cs+)}$ / $^{19}F^-$ Yield $_{(O-)}$
10.0
8.0
6.0
4.0
2.0
0.0
Fba-1
Fba-2
Fba-3
Fba-4
Fba-5
NIST-610
KE-12
UTR-2

Figure 4.5

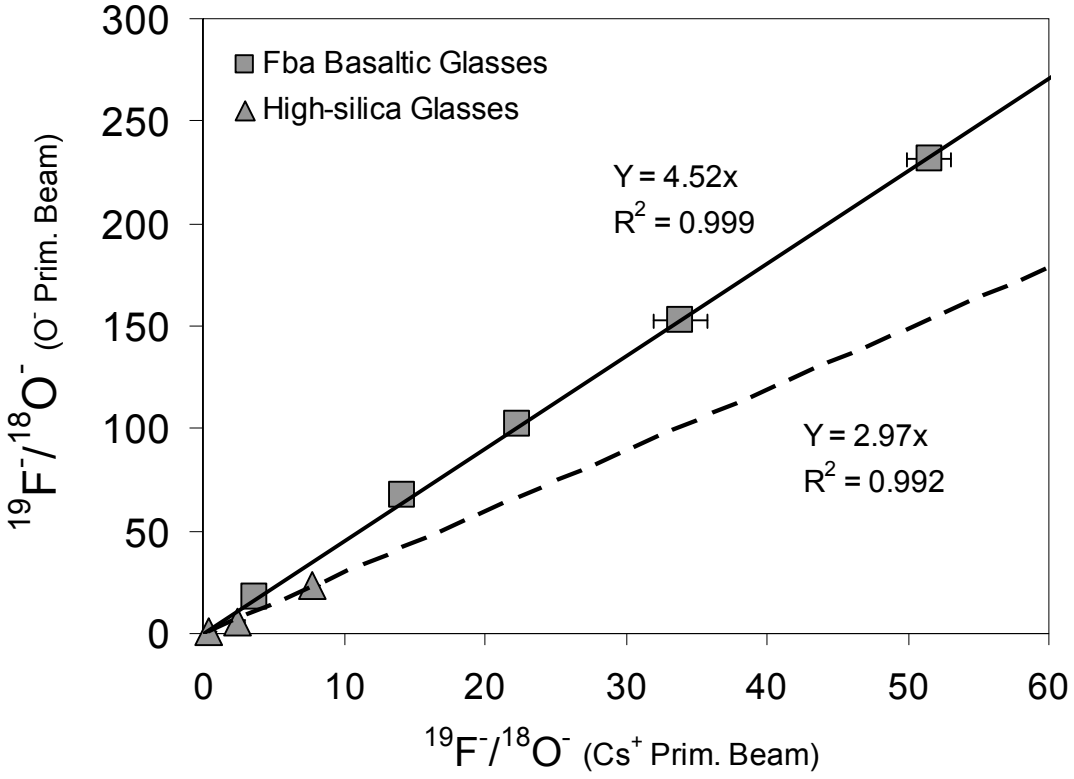
Fba Basaltic Glasses
High-silica Glasses
Y = 4.52x
R2 = 0.999
Y = 2.97x
R2 = 0.992
19F-/18O- (O- Prim. Beam)
19F-/18O- (Cs+ Prim. Beam)
0
50
100
150
200
250
300
0
10
20
30
40
50
60

Figure 4.6 (a)

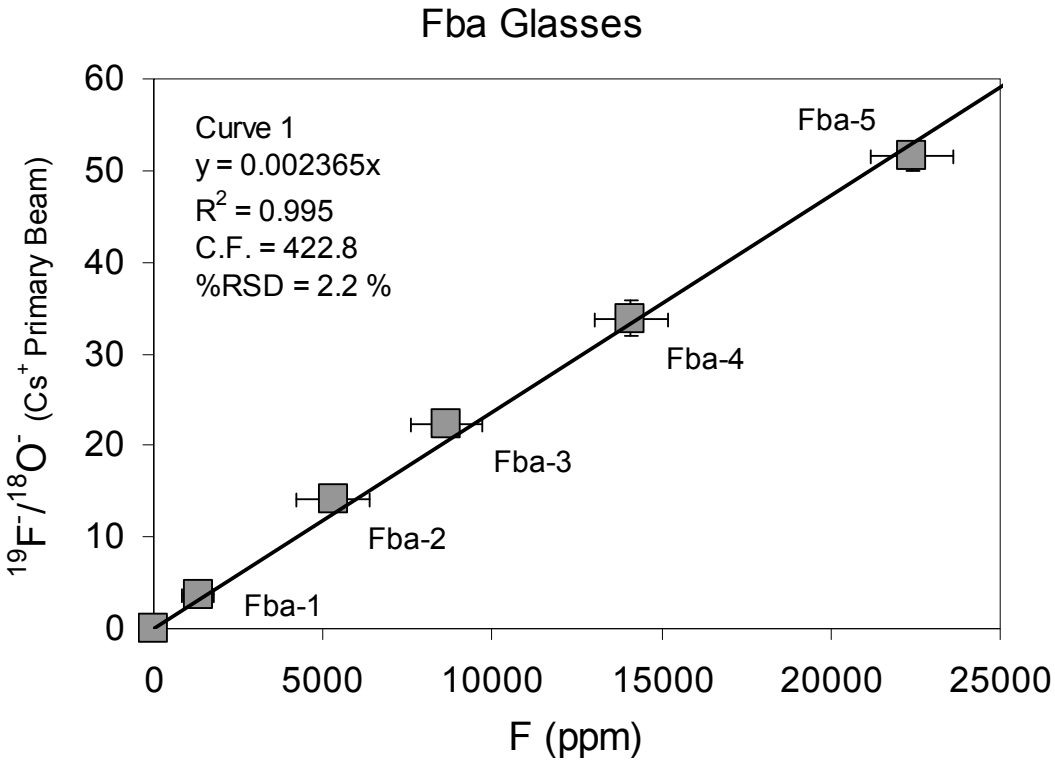
Fba Glasses
Curve 1
y = 0.002365x
R2 = 0.995
C.F. = 422.8
%RSD = 2.2 %
Fba-1
Fba-2
Fba-3
Fba-4
Fba-5
19F-/18O- (Cs+ Primary Beam)
F (ppm)
0
10
20
30
40
50
60
0
5000
10000
15000
20000
25000

Figure 4.6 (b)

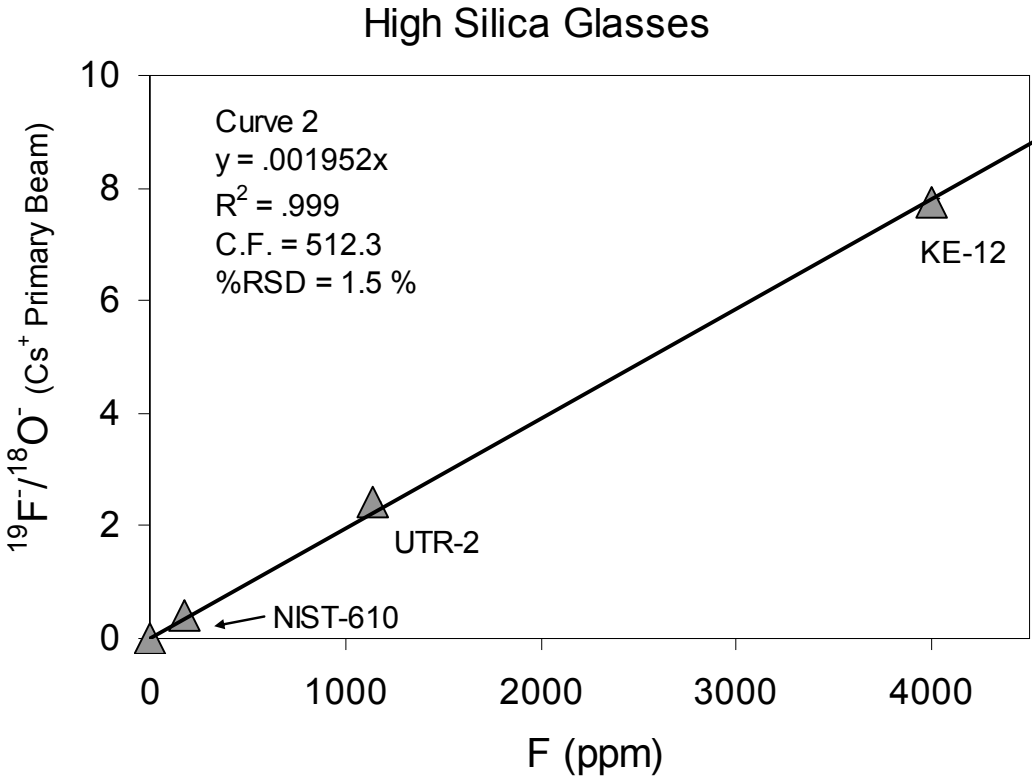
High Silica Glasses
Curve 2
y = .001952x
R2 = .999
C.F. = 512.3
%RSD = 1.5 %
KE-12
UTR-2
NIST-610
19F-/18O- (Cs+ Primary Beam)
F (ppm)
0
2
4
6
8
10
0
1000
2000
3000
4000

Figure 4.7 (a)

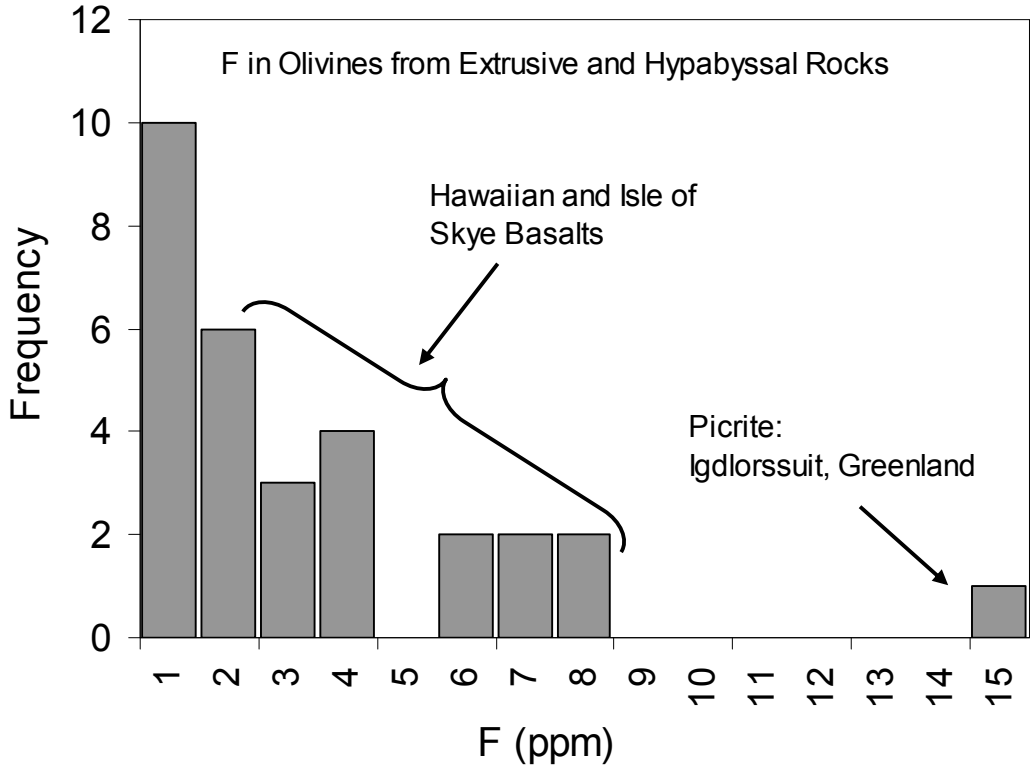
F in Olivines from Extrusive and Hypabyssal Rocks
Hawaiian and Isle of Skye Basalts
Picrite: Igdlorssuit, Greenland
Frequency
F (ppm)
0
2
4
6
8
10
12
1
2
3
4
5
6
7
8
9
10
11
12
13
14
15

Figure 4.7 (b)

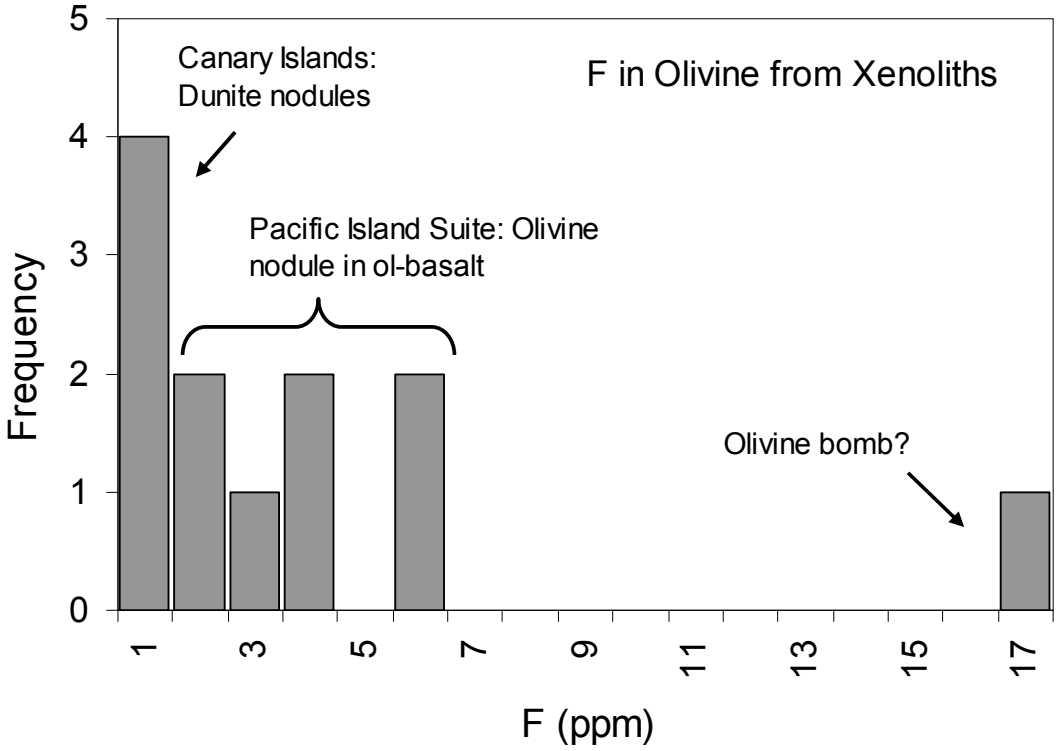
F in Olivine from Xenoliths
Canary Islands:
Dunite nodules
Pacific Island Suite: Olivine
nodule in ol-basalt
Olivine bomb?
Frequency
F (ppm)
0
1
2
3
4
5
1
3
5
7
9
11
13
15
17

Figure 4.7 (c)

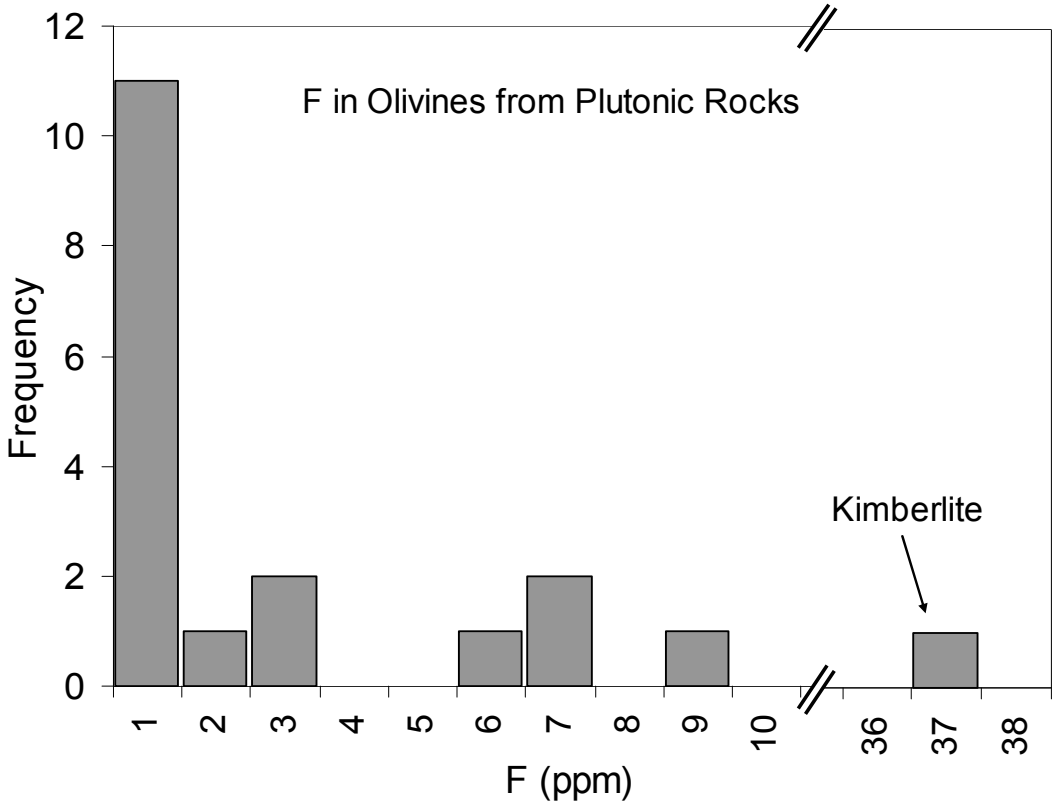
F in Olivines from Plutonic Rocks
Frequency
F (ppm)
Kimberlite
0
2
4
6
8
10
12
1
2
3
4
5
6
7
8
9
10
36
37
38

Figure 4.8 (a)

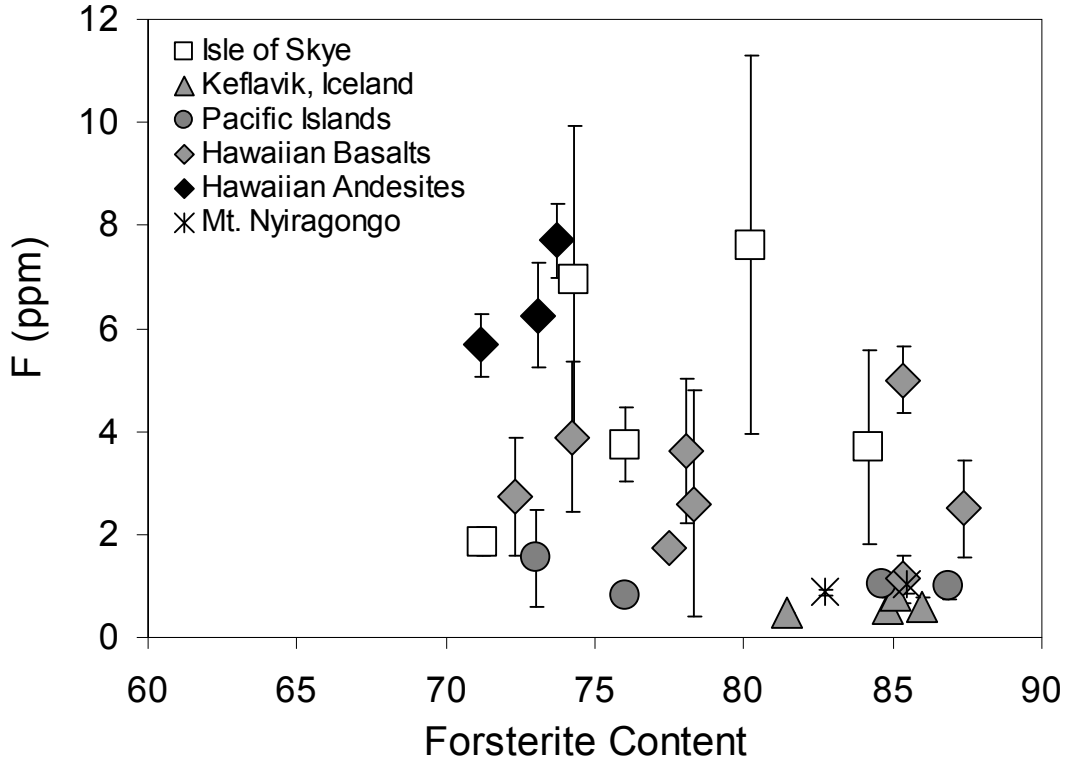
Isle of Skye
Keflavik, Iceland
Pacific Islands
Hawaiian Basalts
Hawaiian Andesites
Mt. Nyiragongo
F (ppm)
Forsterite Content
0
2
4
6
8
10
12
60
65
70
75
80
85
90

Figure 4.8 (b)

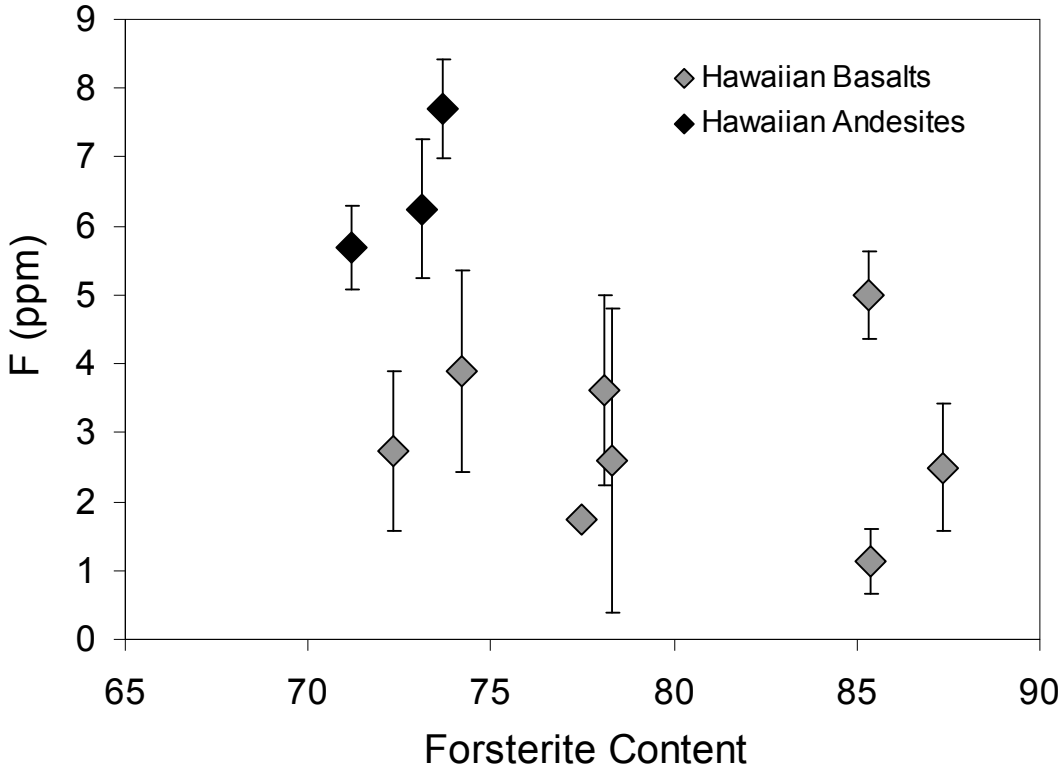
Hawaiian Basalts
Hawaiian Andesites
F (ppm)
Forsterite Content
0
1
2
3
4
5
6
7
8
9
65
70
75
80
85
90

Figure 4.9

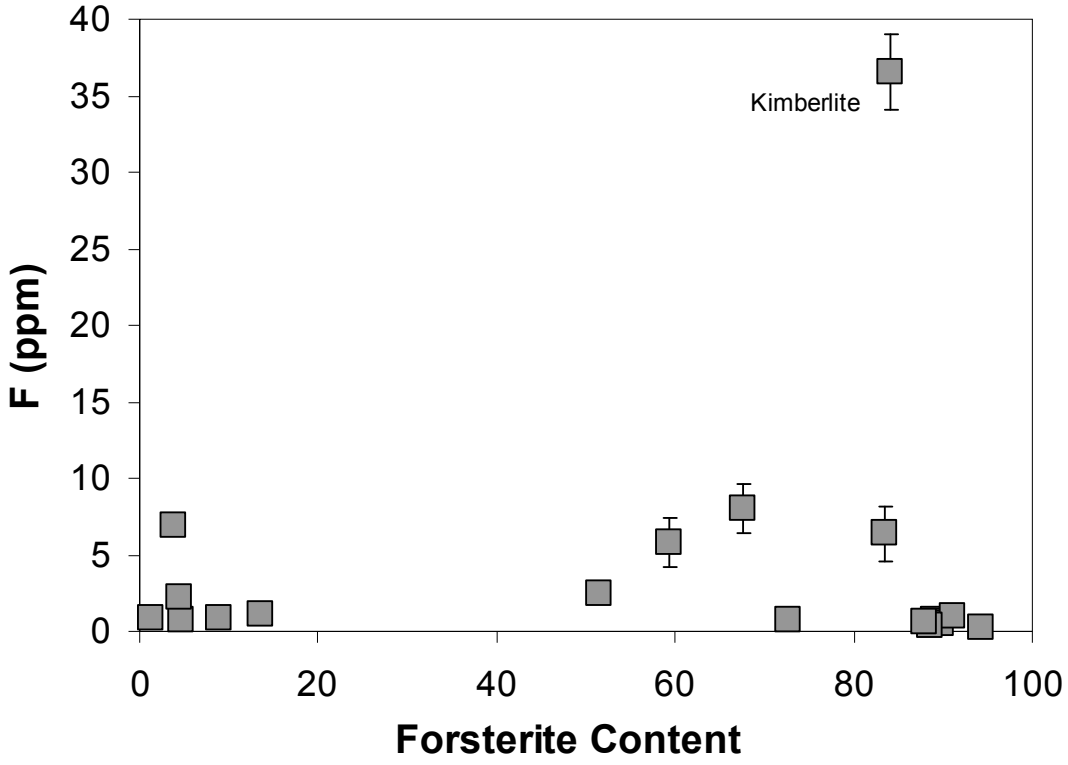
40
35
30
25
20
15
10
5
0
F (ppm)
Kimberlite
0
20
40
60
80
100
Forsterite Content

Figure 4.10

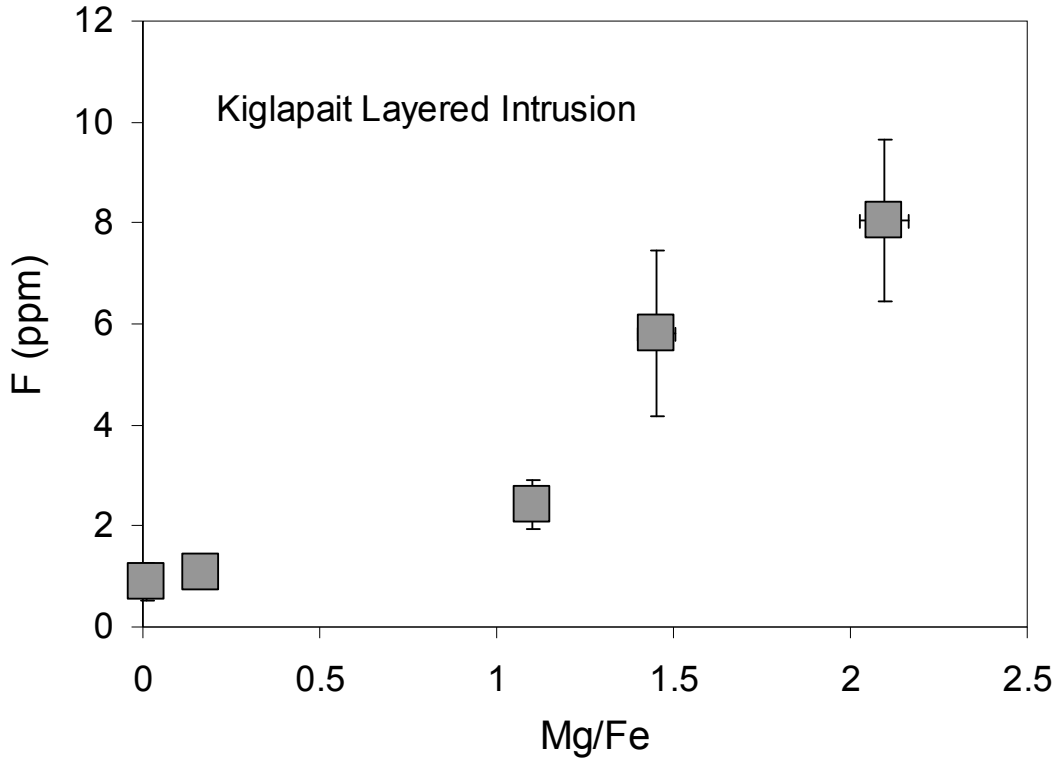
Kiglapait Layered Intrusion
F (ppm)
Mg/Fe
0
2
4
6
8
10
12
0
0.5
1
1.5
2
2.5

Figure 4.11

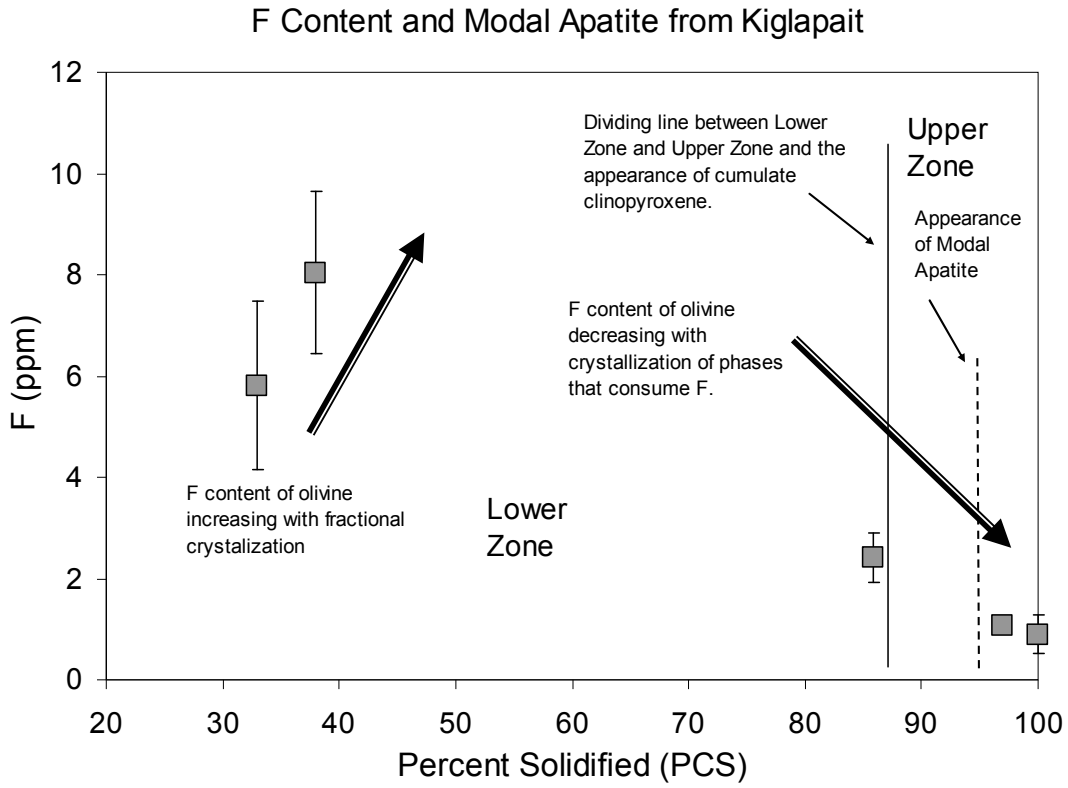
F Content and Modal Apatite from Kiglapait
F (ppm)
Percent Solidified (PCS)
Dividing line between Lower Zone and Upper Zone and the appearance of cumulate clinopyroxene.
Upper Zone
Appearance of Modal Apatite
F content of olivine decreasing with crystallization of phases that consume F.
F content of olivine increasing with fractional crystalization
Lower Zone

CHAPTER 5

FLUORINE PARTITIONING BETWEEN NOMINALLY ANHYDROUS MINERALS (CLINOPYROXENE, OLIVINE, AND PLAGIOCLASE) AND SILICATE MELT

ABSTRACT

We report fluorine partition coefficients for clinopyroxene, olivine, plagioclase, and hornblende within melts of olivine-minette, augite-minette, basaltic andesite, and latite compositions. The samples used in this study were run products from previously-published experiments at *P-T* conditions ranging from 0.607 to 20 kbars and 1,000 to 1,175°C. The partition coefficients for Cpx and olivine varied with each melt composition such that $D_F^{\min / melt}$ for ol-minette < aug-minette < basaltic andesite < latite. Crystal chemical and melt structural controls on $D_F^{\min / melt}$ were investigated. Crystal chemical controls strongly influence the incorporation of F into Cpx, but none affected olivine. Positive correlations were observed between $D_F^{Cpx / melt}$ and the jadeite component, the ferrrosilite component, the Fe/Mg ratio, Al^{3+}, and fO_2. A number of different coupled substitutions among monovalent and trivalent cations can be charge-balanced by the incorporation of F^- at oxygen sites. The cation sites where Fe^{3+} and Al^{3+} are most likely to enter are the tetrahedral and M1 octahedral sites. The preferred site for Na^+ is the larger M2 site. Both the tetrahedral site and the M2 sites are joined by the O3 oxygen site, and we propose that this is the likely oxygen site for F substitution. Melt structure was found to have a strong influence on D_F for both Cpx and olivine. We found a strong positive correlation between melt polymerization and D_F. For Cpx, D_F increased by a factor of 7 as NBO/T decreased by a factor of 8 (melt polymerization increased by a factor of 8). For olivine, D_F increased by a factor of 14 as NBO/T decreased by a factor of 5. Melt polymerization has a stronger influence on $D_F^{Oliv / melt}$ compared to $D_F^{Cpx / melt}$.

1. Introduction

The study of the volatile content (H_2O, CO_2, S, Cl, and F) within the various constituents of igneous systems (e.g. volcanic gas emissions, igneous rocks, minerals, melt inclusions, and glass) expands our understanding of the behavior and effects of volatiles within magmas, including the generation of magmas at subduction zones, mid-ocean ridges, and hotspots, as well as fluid-flux melting, magma rheology, eruption dynamics, and volatile storage in magmas, the crust, and the mantle (e.g. Smith 1981, Smith et al. 1981, London et al. 1988, Micheal 1988, Symonds et al. 1994, Carroll and Webster 1994, Johnson et al. 1994, Watson 1994, Hirschmann et al. 2005, Alletti et al. 2007, Chevychelov et al. 2008, Aiuppa et al. 2009, Dalou et al. 2011). Although the most abundant volatile species include H_2O, CO_2, and SO_2, the role of halogens (F, Cl, Br, I) in geological processes has been gaining increasing attention within the past decade (see Aiuppa et al., 2009). Halogens have been shown to substantially affect the chemical and physical properties of magmas and have been shown to be useful geochemical tracers in establishing the constraints on the genesis and fluid evolution of magmatic systems within various tectonic environments. In addition, halogen abundances may constrain the volatile budgets of the lithosphere and lower mantle (Dingwell 1985, Sigvaldason, G.E and Oskarsson, N. 1986, Symonds et al. 1994, Carroll and Webster 1994, Johnson et al. 1994, Watson 1994, Hauri 2002, Straub and Layne 2003, Aiuppa et al. 2009, Köhler et al. 2009).

Fluorine is a volatile constituent of magmas and hydrous mantle minerals, yet few investigations have been conducted to determine the geochemical behavior of fluorine in igneous systems. Fluorine is the most reactive of the halogens, possessing the highest electronegativity of all the elements and allowing it to readily ionize and induce ionization (Sawyer and Oppenheimer 2006). Fluorine forms many complexes within fluids and melt, preferentially bonding with the alkaline earth metals, Al, Na, and Si, as well as metal complexes that play a role in the transport of ore-forming metals, rare earth

elements (REEs), and high field strength elements (HFSEs) in volatile-rich systems (Carroll and Webster 1994, Pan and Fleet 1996, Williams-Jones et al. 2000, Tagirov et al. 2002, Köhler et al. 2009, Aiuppa et al. 2009). Fluorine forms the volcanic gas species HF, SiF_4, $SiOF_2$, $ClSiF_3$, AlF_2O (Sawyer and Oppenheimer 2006, Aiuppa 2009), yet fluorine is the last volatile element to be exsolved from ascending magma and does so at pressures much lower than for carbon, water, sulfur, and chlorine (e.g. S: ~140 MPa, Cl: ~100 MPa, F: <10 MPa) (Spilliaert et al 2006). Fluorine's capacity to form complexes renders fluorine highly soluble in silicate melts compared to other magmatic volatile species, allowing F to behave as an incompatible element through the general retention of F in silicate melts during differentiation and degassing upon magma ascent (Dingwell et al. 1985, Carroll and Webster 1994; Stecher 1998, Mysen et al. 2004, Scaillet and MacDonald 2004, Aiuppa et al. 2009). This implies that the association between fluorine in basalts and fluorine in the mantle source region is more robust than for many other volatile species, and measurements of fluorine in glasses quenched at depth, such as melt inclusions, may provide important information regarding the pre-eruptive and source-region volatile dynamics at depths where other more insoluble volatile species are lost to degassing (Carroll and Webster 1994, Roggensack et al. 1997).

Compared to oxygen and other halogens, the ionic radius of fluorine is relatively small, and its small ionic radius allows it to fit within the structure of silicate melts and mineral phases. The ionic radius of F^- (1.33 Å, octahedral coordination) is similar to that of OH^- and O^{2-} (1.40 Å) (Shannon 1976), allowing F to substitute for hydroxyl and oxygen in silicate minerals and melt (Stolper 1982, Stecher 1998). Fluorine substitution for hydroxyl routinely occurs in micas, amphiboles, apatites, humite group minerals, and in accessory minerals of the crust such as fluorite and topaz (e.g. Smith 1981, Smith et al. 1981, Robert et al. 1993), and these nominally hydrous minerals are thought to be the main reservoirs for fluorine in the Earth's crust. Likewise, fluorine storage in the mantle occurs in nominally-hydrous mantle-derived accessory phases such as primary apatites,

amphiboles, and phlogopite (Delaney et al. 1980, Smith 1981, Smith et al. 1981, Matson et al. 1986, O'Reilly and Griffin 2000, Aiuppa et al. 2009). At the higher temperatures of the Earth's upper mantle (compared to the crust), fluoridated phases might be expected to be more common than hydroxyl end members because of their enhanced thermal stability. In support of this, Straub and Layne (2003) show that at subduction zones, fluorine within oceanic lithosphere remains relatively fixed to the subducting slab, a major portion of fluorine returning to the deep mantle, while H and Cl are separated out during decomposition of hydrous phases at lower pressures. Hence, there is an inference that a stable mineralogical repository for fluorine exists under the temperature and pressure conditions of the mantle, and that the F/H ratio should increase within recycled materials.

It has been shown that fluorine is incorporated at trace levels within nominally anhydrous minerals (NAMs) of the upper mantle such as olivine and clinopyroxene (Hervig et al. 1988, Hervig and Bell 2005, Guggino et al. 2007, O'Leary et al. 2010), and the range of F incorporation is similar to that for H_2O on a molar basis. Hoskin (1999) suggests, because clinopyroxene contains a major fraction of the mantle's water budget (Bell and Rossman 1992), that F may substitute within this phase as well as within olivine (Sykes et al. 1994), implicating the Earth's mantle as a major reservoir for fluorine. At pressures and temperatures that approximate the conditions within the transition zone of the mantle, Gasparik (1990, 1993) synthesized a new hydrous phase with the formula $Mg_{10}Si_3O_{14}(OH,F)_4$ coexisting with stishovite. This "superfluorous" or "superhydrous" phase B shows 1) that F and OH can substitute at these pressures and temperatures and 2) the potential for F–rich phases to be stable at high pressure and temperature (Hazen 1997).

Quantifying the behavior of fluorine in NAMs has been attempted in only a handful of studies. Reconnaissance studies have been performed to determine the abundance and geochemical significance of fluorine in olivine and clinopyroxene megacrysts from South African kimberlites and olivine phenocrysts from intrusive,

extrusive, and hypabyssal suites from various tectonic environments, showing that fluorine behaves as an incompatible element during fractional crystallization and that the partitioning of fluorine within these mineral phases may be related to increasing iron content within the minerals (Stecher 1998, Hervig and Bell 2005, Guggino et al. 2007). Bromiley and Kohn (2007) added a variety of fluorides (e.g. MgF_2, CaF_2, NaF) to capsules containing forsterite, held the charges at 10-20 kb and 1300-1600˚C and found that up to 0.45 wt.% fluorine can be incorporated into forsterite from MgF_2. A more comprehensive study of fluorine, chlorine, and trace element partitioning between basaltic melt and NAMs, namely olivine, orthopyroxene, clinopyroxene, plagioclase, and garnet, was performed by Dalou et al. (2011) under conditions of 8-25 kbars and 1265-1430°C. Their results show that fluorine partitioning within these phases is globally ordered as $D^{Cpx/melt} > D^{Opx/melt} > D^{Grt/melt} > D^{Ol/melt} > D^{Plag/melt}$. In the present study, we determined the Nernst partition coefficients of fluorine between olivine, clinopyroxene, and plagioclase mineral phases and olivine-minette, augite-minette, basaltic andesite, and latite melts. The objective of this study is to compare the partitioning of fluoride with that of hydroxide within these mineral phases to assess the likelihood of chemical controls on these anionic species and to address any similarities that may exist due to the similarities in the fluoride and hydroxide ionic radii and charge.

2. Sample Suites

The samples used in this study were obtained from a suite of pre-existing experimental run products from published phase equilibrium experiments, and were generously donated by their respective authors. The experiments from which the samples were derived were performed independently of the present study, and hence the fluorine concentration of the original starting materials was unknown. For consistency, the present study preserved the original sample nomenclature. The sample starting materials and major element compositions are listed in Table 5.1 and include a high-K latite from

Camp Creek, Arizona, USA (samples LIW and LOA; Esperanca and Holloway 1986), an olivine-bearing, xenolith-free mafic minette lamprophyre from Buell Park, Arizona, USA (samples MIW and MOA; Esperanca and Holloway 1987), an augite minette from the Mascota Volcanic Field, western Mexico (sample 56-B; Righter and Carmichael 1996), and a basaltic andesite from the Western Mexican Volcanic Belt (samples PEM; Moore and Carmichael 1998). The experimental run conditions from the respective authors (see Table 5.1) are listed in Table 5.2.

2.1 Chemical Equilibrium of Sample Suites

The attainment of chemical equilibrium of the sample suites (LIW, LOA, MIW, MOA, 56B, PEM) with respect for the major elements was established by their original authors. The equilibrium criteria for the latite (LIW, LOA) and olivine-minette (MIW, MOA) samples are discussed in Esperanca (1984), and included 1) the presence of euhedral crystals, 2) performing reversal runs and changing the duration of runs to test for modal phase consistence, and 3) measuring the partition coefficient of Fe and Mg between olivine and melt and comparing them to known values. Righter and Carmichael (1996) determined equilibrium by 1) determining phase boundaries by comparing runs at isothermal conditions with those whose temperatures were slowly cooled to the final temperature, 2) changing the duration of runs while maintaining identical run conditions to test for consistency in the phase assemblages, 3) observing the absence of compositional zoning in the run products, and 4) measuring the partition coefficient of Fe and Mg between olivine and melt and comparing them to known values. Moore and Carmichael (1998) established equilibrium by 1) observing euhedral crystal shapes, 2) comparing phase assemblages of identical runs with significantly longer run times, and 3) observing the lack of compositional zoning within crystal phases.

Chemical equilibrium with respect to F was not considered during the original phase equilibria experiments. However, our SIMS analyses of fluorine in the glass phases of the run products show that fluorine was homogeneously distributed within the

melt before quenching. The quantitative test we used to determine homogeneity within the glass phases emulated the method of Jochum et al. (2000), Jochum et al. (2005), and Jochum et al. (2006) whereby, as they attempted to establish homogeneity of geologic glass reference materials, their definition of heterogeneity is based on variations in elemental concentrations that are 3 times greater than the repeatability of the analytical instrument after multiple measurements of previously characterized homogeneous glasses. Therefore, if the range of concentration values for a particular chemical species (the heterogeneity) does not exceed three times the analytical uncertainty of the instrument precision, then the heterogeneities are deemed insignificant and the material is considered homogeneous with respect to that particular chemical species. During multiple sessions of SIMS analysis, the precision of SIMS measurements was monitored by measuring the $^{19}F^{-}/^{18}O^{-}$ ratios of the geologic reference glasses NIST-610 (Session-to-session precision of 7.4 %RSD) and UTR-2 (session-to-session precision of 5.6 %RSD). Table 5.3 shows the SIMS results as $^{19}F^{-}/^{18}O^{-}$ ratios, the 1σ standard deviations, and the percent relative standard deviations for the glass phases of the experimental sample suites of this study. The percent relative standard deviations of the SIMS $^{19}F^{-}/^{18}O^{-}$ ratios for the glass phases were calculated from *n* number of spot analyses within the glasses, and the range for each sample suite is as follows: LIW (2-4 %RSD), LOA (1-10 %RSD), MIW (2-6 %RSD), MOA (9 %RSD), 56B (19 %RSD), and PEM (1-5 %RSD). All sample suites show percent relative standard deviations lower than three times the precision of the SIMS. Additionally, the diffusivity of fluorine within a basaltic melt is on the order of 10^{-10} to 10^{-11} m^2s^{-1} at the temperatures under which the experiments were run (Aletti et al. 2007). Given the duration of the experiments (LIW, LOA, MIW, MOA: 6 hours; 56B: 72 hours; PEM: 48-96 hours) and the scale of the samples, there would have been sufficient time for fluorine to equilibrate within the melt (e.g. Dalou et al. 2011). However, the equilibration time of fluorine in mineral phases is uncertain due to the lack of fluorine diffusion data. The ionic radius of F is similar to that of oxygen, and we estimate the

diffusivity of F in olivine, pyroxene, and plagioclase is probably less than that for most cations and similar to that of oxygen. In his review of diffusion studies of oxygen in various mineral phases, Farver (2010) shows that the range of oxygen diffusivities is similar in olivine (10^{-16} to 10^{-20} m^2s^{-1}), clinopyroxene (10^{-16} to 10^{-22} m^2s^{-1}), and plagioclase (10^{-17} to 10^{-21} m^2s^{-1}). If the diffusion of F in these mineral phases is similar to that of oxygen, it would be impossible for F to equilibrate via diffusion in the experimental crystals within the durations of the experiments. However, Dalou et al (2011) surmise that if the partitioning of F into the crystals is at a constant rate during equilibrium crystal growth, then the diffusion of F within the melt itself (10^{-10} m^2s^{-1}) is sufficiently rapid to maintain melt homogeneity during crystal growth such that F can equilibrate within the growing crystal, and that near equilibrium fluorine abundances are achieved within the first few hours of annealing.

2.2 Criteria for Selection of Crystals and Glass for Analysis

We used several criteria to select samples for analysis and interpretation. First, the area for analysis had to be large enough to accommodate the beam diameters of both SIMS analysis and EPMA. The EPMA beam diameter (1-2 μm) was small enough to pose no problem with either crystal size or areas of crystal-free glass. However, the beam diameter of the SIMS (20 to 25 μm) forced us to bias our analyses in favor of crystals and crystal-free areas of glass to spots greater than the SIMS beam diameter. Later inspection of the sputter craters with a reflecting petrographic microscope showed that many analyses of crystals had overlapped the edges of crystals and sampled glass as well. These analyses were discarded. Second, crystals with disequilibrium morphologies, such as hopper, skeletal, and dendritic morphologies, saw-tooth edges, and central melt inclusions were all ignored or discarded.

3. Analytical Methods

3.1 SIMS Analysis

Secondary ion mass spectrometry (SIMS) analysis was performed at Arizona State University (ASU) using the Cameca ims 6f. We used an $^{16}O^-$ primary beam obtained from a duoplasmatron at -12.5 kV with a primary current ranging from 2.5 to 3 nA to sputter secondary ions from the sample surface. The low primary current allowed us to achieve a primary beam diameter of about 20 to 25 μm. The use of negative primary ions eliminated the need for a normal-incidence electron gun because positive charge build-up was avoided. Negative secondary ions were accelerated to -5000eV, and no energy filtering was applied. The mass spectrometer was operated at a mass resolving power (MRP) sufficient to separate $19F^-$ from $^{18}OH^-$ ($M/\Delta M$ ~2500) (Fig. 5.1). Secondary ion intensities were collected for $^{18}O^-$, $^{19}F^-$, and $^{28}Si^-$. The output from SIMS analysis is in counts/second (cps), and the cps of the elemental species of interest is typically normalized to the cps of some ubiquitous isotope within the sample matrix to obtain an elemental ratio. In our case, $^{19}F^-$ was normalized to $^{18}O^-$. Analyses spanned multiple sessions. Session-to-session precision was monitored by analyzing NIST-610 and UTR-2, which show historical values for negative secondary ion ratios that range from $^{19}F^-/^{18}O^-$ = 0.95-1.0 for NIST-610 and $^{19}F^-/^{18}O^-$ = 6.75-6.8 for UTR-2. Negative secondary ion ratios $^{19}F^-/^{18}O^-$ were measured in crystals and adjacent glass of the experimental run products used in this study (Fig. 5.2).

3.2 EPMA Analysis

Electron probe microanalysis (EPMA) of the major elements was performed at the ASU electron microprobe laboratory for the mineral phases from the LIW and LOA samples (Esperanca and Holloway 1986) and the MIW and MOA samples (Esperanca and Holloway 1987). EPMA was conducted at Arizona State University using a JEOL 8600 Superprobe equipped with four wavelength-dispersive spectrometers (WDS) and TAP crystals on each of the four spectrometers. The EPMA analytical conditions included

a 10 nA primary current, a 15 keV accelerating voltage, a 1-2 μm focused beam diameter, and a 45 s peak counting time. The major and minor element calibration standards included Si, Al, Fe, Mg, and Ca: GL113 (1921 Kilauea tholeiite glass); Ti: rutile; Na: Amelia Albite; K: orthoclase. Atomic number, absorption, and fluorescence corrections (ZAF) data reduction was carried out using internal software routines.

3.3 Fluorine Standards for SIMS Analysis (Fba Glasses)

Because there are no matrix-correction models for SIMS analysis, the determination of elemental concentration values of unknown samples from SIMS output requires appropriate matrix-matched standards that have been well-characterized for the relevant element. For fluorine measurements, the SIMS $^{19}F^{-}/^{18}O^{-}$ measurements of standards are plotted against their fluorine concentrations, and a calibration curve is constructed to convert the SIMS $^{19}F^{-}/^{18}O^{-}$ ratios of the unknowns into concentration values. There are few well characterized low-silica, basaltic fluorine glass standards for use with SIMS analysis. As a consequence, we synthesized five in-house fluorine basalt glass standards, collectively known as Fba glasses, with the following fluorine contents: Fba-1: 0.13±0.05 wt.%, Fba-2: 0.53±0.11wt.%, Fba-3: 0.87±0.10 wt.%, Fba-4: 1.41±0.11 wt.%, Fba-5: 2.24±0.12 wt.% (See Chapter 3; Guggino and Hervig 2011). Table 5.4 lists the experimental conditions during synthesis of the Fba glasses, along with the $^{19}F^{-}/^{18}O^{-}$ ratios from SIMS and F concentrations of each Fba glass standard determined by EPMA.

3.3.1 EPMA on Fluorine Standards (Fba Glasses)

Homogeneity of the Fba glasses was established and the average fluorine contents were determined by EPMA at the University of Arizona Electron Microprobe laboratory (see Table 5.4). EPMA was conducted using a Cameca SX100 equipped with five WDS spectrometers. Fluorine was measured simultaneously on two WDS spectrometers, each equipped with a TAP crystal, utilizing the peak integration method, a 20 nA primary current, 15 kV accelerating voltage, 20 μm de-focused beam, a 60-second counting time, and five iterations. The calibration standards for major and trace elements

included: Si, Mg, and Ca: diopside; Na: albite; Al: anorthoclase (Hakone); K: Orthoclase (OR1); Ti: rutile (Rutile1); Mn: rhodonite (rhod791); Fe: fayalite; Cr: Cr_2O_3 (synthetic). The calibration standards used for fluorine were Biotite-3 (Bt-3; 3.3 wt.% F) and synthetic fluorphlogopite (F-phlog; 9.02 wt.% F, stoichiometric). Corrections were applied based on the Pouchou and Pichoir (PAP) model using internal software routines.

3.3.2 SIMS Analysis of Fluorine Standards (Fba Glasses)

SIMS analysis on the Fba glasses was performed at Arizona State University (ASU) using the Cameca ims 6f. During analyses, the instrument was configured to measure negative secondary ions. Detection of negative secondary ions was conducted with a primary beam of $^{16}O^-$ ions obtained from a duoplasmatron at -12.5 kV and focused to a diameter of 20-30 μm on the sample held at -5 kV. Using a current of 3.5 nA, negative secondary ion intensities of $^{18}O^-$, $^{19}F^-$, and $^{28}Si^-$ (0 ± 60 eV excess kinetic energy) were recorded. The mass spectrometer was operated at a mass resolving power (MRP) sufficient to separate $^{19}F^-$ from $^{18}OH^-$ (M/ΔM ~2500). Figure 5.3 shows a calibration curve constructed from the Fba glasses and the mica fluorine standard Biotite-3 (Bt-3), where SIMS measurements of $^{19}F^-/^{18}O^-$ ratios (Table 5.4) are plotted against the actual fluorine concentrations of the Fba glasses and Bt-3. The calibration curve has a %RSD of 1.73 %, and the calibration factor (CF) is 96.7.

4. Analytical Results

4.1 Major and Trace Element Composition

Major and trace element composition from EPMA, the $^{19}F^-/^{18}O^-$ ratios from SIMS, and the calculated fluorine concentration values from our SIMS calibration curve (Fig. 5.3) of the glass and mineral phases from our samples are reported in Table 5.5. We conducted EPMA analysis only on the mineral phases from samples LIW, LOA, MIW, and MOA while the rest of the analyses are literature values from the respective authors. The silicate melts from the experimental run products range in composition that consists of a

high-K olivine-minette (average SiO_2=51.9 wt.%; Al_2O_3=13.5 wt.; Na_2O+K_2O=7.11 wt.%; Mg# 0.54), high-K augite-minette (average SiO_2=58.8 wt.%; Al_2O_3=16.0 wt.; Na_2O+K_2O=11.01wt.%; Mg# 0.45), basaltic andesite (average SiO_2=54.7wt.%; Al_2O_3=17.2 wt.; Na_2O+K_2O=5.2 wt.%; Mg# 0.57), and a high-K latite (average SiO_2= 62.6 wt.%; Al_2O_3=16.6 wt.; Na_2O+K_2O=7.16 wt.%; Mg# 0.47). The fluorine concentration of the silicate melts range from 1150 to 2250 ppm (high-K olivine-minette), 1092 ppm (augite-minette), 115 to 195 ppm (basaltic andesite), and 750 to 1050 ppm (high-K latite). Composition of each mineral phase varies little among the different silicate melt compositions. For the olivine-minette samples, the Cpx show a Mg# from 0.88-0.90 and a CaO content from 19.7-22.9 wt.%, and the Fo content of the olivine varies from 0.82-0.83. The augite-minette sample shows the Cpx with a Mg# of 0.87 and a CaO content of 22.3 wt.%. The Cpx and olivine crystals from the basaltic andesite samples show the greatest variation in compositions compared with the other samples (Cpx: Mg# 0.69-0.96, CaO content 21.4-22.0 wt.%; olivine: Fo content 0.83-0.96). The anorthite content [An = Ca/(Ca+Na)] of plagioclase in two basaltic andesite experiments were 0.65 and 0.81, respectively.

4.2 Partition Coefficients

The Nernst partition coefficient is defined as $D_i^{\min/melt} = C_i^{\min} / C_i^{melt}$, where *D* is the partition coefficient for element *i* and *C* is the concentration of element *i* in the mineral divided by the concentration of element *i* in the melt. The F partition coefficients for all the mineral phases are reported in Table 5.5 and show a range of values for each mineral phase both within the same melt composition and between melt compositions. Figure 5.4a illustrates the range in $D_F^{\min/melt}$ values for olivine (Oliv), clinopyroxene (Cpx), and plagioclase. Figure 5.4b exhibits a notable increase in $D_F^{Oliv,Cpx/melt}$ with increasing silica content of the melt in order of ol-minette > aug-minette > basaltic andesite > latite.

4.3 Clinopyroxene Partition Coefficients

Figure 5.4a reveals that, among the samples studied, $D_F^{Cpx/melt}$ in the ol-minette shows the lowest values with a range from 0.04-0.10 (average = 0.08±0.02). $D_F^{Cpx/melt}$ for the aug-minette sample shows larger values and a smaller range than for ol-minette (0.11-0.17, average = 0.13±0.03). The basaltic andesite samples show an increase in the $D_F^{Cpx/melt}$ values with a range from 0.17-0.21 (average = 0.19±0.02), showing the smallest range in Cpx partition values of all the samples. The high-K latite samples show an increase in the $D_F^{Cpx/melt}$ values and the largest range of values compared with the lower silica samples (0.12-0.27 with a low-value outlier of 0.07; average = 0.18±0.07). Dalou et al. (2011) reported $D_F^{Cpx/melt}$ in a basaltic melt to have a range of 0.04 to 0.15 (average = 0.10±0.04), and our results are in agreement.

4.4 Olivine Partition Coefficients

The samples that contain olivine are the ol-minettes and the basaltic andesites, and similar to the partitioning behavior of Cpx in our study, $D_F^{Oliv/melt}$ exhibits an apparent increase with an increase in silica content of the melt (Fig. 5.4b). The $D_F^{Oliv/melt}$ values for the minette samples show a range from 0.01-0.07 (average = 0.03±0.02), while the $D_F^{Oliv/melt}$ for the basaltic andesites show an increase in values by factors of 2 to 13 and a smaller range (0.13-0.16; average = 0.14±0.01) compared to the ol-minettes. Dalou et al. (2011) reported one $D_F^{Oliv/melt}$ value for olivine in a basaltic melt (0.12±0.07), and our results are in agreement.

4.5 Plagioclase and Hornblende Partition Coefficients

Two plagioclase crystals and one hornblende crystal were measured from the basaltic andesite samples. Although hornblende is not a nominally anhydrous mineral, we report its F partition coefficient here (Table 5.5). The $D_F^{Plag/melt}$ was calculated from two

values (0.06 and 0.08; average = 0.07±0.01). Dalou et al. (2011) report a $D_F^{Plag/melt}$ value for one plagioclase crystal (0.10), and our results are in agreement within one standard deviation. The $D_F^{Hbd/melt}$ was calculated from one F measurement from a single crystal, recording an F partition coefficient of 3.63±0.36 (analytical precision). An OH deficient, Ti-rich pargasite was synthesized from a natural basanite by LaTourrette et al. (1995), and the $D_F^{Amph/melt}$ was found to be 1.65±0.14, a factor of 2 lower than our results for hornblende.

5. Discussion

5.1 Crystal Chemical Controls on the Incorporation of F in NAMs

Fluorine clearly substitutes into nominally anhydrous silicates, but as anions their incorporation into the silicate crystal structure of NAMs may follow different mechanisms and controls than for cations. The negative charge and ionic radius of F^- likely allows it to substitute for oxygen, and the similar charge and ionic radius of F^- and OH^- allow researchers to consider analogous substitution behavior among the two species. Smyth (1989) determined the electrostatic potential (in units of volts) of approximately 500 anion sites in 165 rock-forming minerals as a way to aid in predicting the oxygen sites that would most likely accommodate fluorine and hydroxyl substituents. The electrostatic potentials for hydroxyl and fluorine oxygen sites exist within a broad range of values (5 to 22 V; average within upper mantle minerals = 12.4±2.2 V) that are much lower than the range of electrostatic potentials from oxygen sites that cannot easily accommodate hydroxyls or F (average 27.3±1.4 V) (Smyth 1987, 1989). In order for an oxygen site to accommodate a hydroxyl or F, the site needs to 1) have a low Pauling bond-strength sum, 2) have a low enough electrostatic potential, and 3) must not be bonded to Si. Smyth (1987, 1989) found that among the silicates, there was no circumstance of a hydroxyl or F bonding to Si or entering an oxygen site of coordination number less than six, thus showing the difficulty of wholesale replacement of Si-O and ^{IV}Al-O bonds with Si-

F or ^{IV}Al-F bonds. When Smyth (1987) studied 28 anion sites from 11 high-pressure mantle phases, he found that only one site (O1) from the phase β-Mg_2SiO_4 wadsleyite matched all three criteria to host a hydroxyl or F. The NAMs of the present study all contain oxygens that bond to at least one Si, and the average electrostatic potentials are high (olivine: 26.8±0.20 V; clinopyroxene: 27.5±0.6 V; plagioclase: 29.1±0.7 V). Consequently, the low abundances of F in these minerals and the relatively low $D_F^{NAM\,/\,melt}$ may be due to the high energy cost for F to enter the oxygen sites. Nevertheless, there are other crystal chemical controls that may regulate the incorporation of F in NAMs. Because F has a charge of -1 and oxygen has a charge of -2, mechanisms for charge balance must occur for F^- to substitute for O^{2-}, which may be accomplished by coupled substitutions, point defects, and M-site vacancies.

5.2 Fluorine in Olivine

All the oxygens in olivine are in tetrahedral coordination with one Si and 3 divalent metals, making the electrostatic potential at the O1, O2, and O3 sites high (Smyth, 1989). In their paper on F partitioning into lherzolite phases, Dalou et al. (2011) were not able to satisfactorily resolve the mechanism by which F is substituted into olivine. They did speculate on two substitution mechanisms: 1) F enters the smaller O1 and O2 oxygen sites and is coordinated with M-site cations for charge balance. With this mechanism, a monovalent cation would have to replace Mg or Fe in an M site or a trivalent cation would have to substitute for Si in the tetrahedral site. Sodium and Li have been detected in olivine at levels up to tens of parts per million (ppm), with the higher values found in mantle-derived olivines. Trivalent aluminum (Al^{3+}) in olivine does not exist in tetrahedral coordination at pressures greater than about 2 GPa (Smyth 1987), but in clinopyroxene tetrahedral Al^{3+} can exists at pressures of 20 kbar and higher. 2) F is incorporated into the clinohumite defect where it substitutes for OH and consequently stabilizes clinohumite to much higher temperatures than that of OH-bearing humite (< 1000°C) (Engi and Lindsley 1980; Hermann et al. 2007). However, Dalou et al (2011) did

not discuss the possibility that the behavior of F incorporation into olivine may be analogous to OH incorporation. Smyth (1987) suggested that OH along with F can be incorporated into β-Mg_2SiO_4 wadsleyite through charge balancing with M-site vacancies. He proposed that because the Ca-Eskola pyroxene end-member ($Ca_{0.5}[]_{0.5}AlSi_2O_6$) is a major vacancy-bearing constituent of mantle-derived omphacites (Wood and Henderson 1977, Smyth 1980, McCormick 1986) and is stable at temperatures greater than 1250 °C (Smyth et al. 1984), that a similar charge-balancing mechanism can occur in β-Mg_2SiO_4 wadsleyite where significant amounts of F and OH can substitute at the O1 site. Similarly, Zhao et al. (2004) argue that metal vacancies within olivine under anhydrous conditions comprise one of the majority point defects, and that these metal vacancies make up the primary water-derived defect complex in olivine. Kohlstedt and Mackwell (1999) used experimental data to suggest that OH substitution in olivine is achieved through M-site vacancies via the following reaction:

$$MeSiO_3 \text{ (opx)} + H2O = Me[]SiO_2(OH)_2 \text{ (olivine)} \quad (1)$$

where [] represents an octahedral vacancy in the olivine and Me represents a metal (e.g. Mg or Fe). If we substitute F_2 for H_2O in equation (1), we come up with an analogous equation where orthopyroxene in the presence of fluorine gas will produce a fluoridated olivine with a metal vacancy:

$$MeSiO_3 \text{ (opx)} + F_2 = Me[]SiO_2(F_2) \text{ (olivine)} + ½\ O_2 \quad (2)$$

Equation (2) produces oxygen, and F-rich olivines might be associated with relatively oxidized assemblages. If we change F_2 to a more likely volatile fluoride constituent in mantle fluids such as HF, then a more realistic reaction would be:

$MeSiO_3$ (opx) + HF = $HMe[]SiO_3F$ (olivine) (3)

If equation (3) is a viable process for incorporating F in olivine, then a simple test would be to look for a positive correlation between H and F abundances in olivine. Unfortunately, that goes beyond the scope of this study. However, Nakamura and Schmalzried (1983) showed that under anhydrous conditions, the concentration of metal vacancies in olivine increases exponentially with increasing iron content, and Zhao et al (2004) showed that under hydrous conditions the concentration of defect complexes between metal vacancies and hydroxyl ions likewise increase exponentially with increasing iron content (Fig. 5.5a). Therefore, we propose that if F behaves similarly to OH with respect to solubility in olivine, then there should be a comparable increase in F concentration with increasing iron content in olivine. Hervig and Bell (2005) measured major elements and F in a group of iron-rich olivine megacrysts from southern African kimberlites found a strong correlation of increasing F content (70 – 240 ppm F) with increasing Fe content (Fo84 – Fo80). However, Figure 5.5b shows that Fe and F are not correlated for the olivine crystals we sampled. If the solubility of F were to increase with increasing Fe content in olivine crystals as does OH, then we would expect to see a higher $D_F^{Oliv\,/\,melt}$ in olivine crystals that contain higher Fe content. Figure 5.6 shows a plot of $D_F^{Oliv\,/\,melt}$ versus the magnesium number (Mg#) of the olivine crystals sampled. Although the olivine crystals from the basaltic andesites show a higher F partition coefficient than the olivine crystals from the minettes, the data show no correlations between Mg# and F partitioning. The substitution mechanism for F in olivine remains inconclusive and requires further study.

5.3 Fluorine in Pyroxene

5.3.1 Elastic Strain Model

Crystal chemical controls on the substitution mechanism for F in pyroxenes are not well known. In orthopyroxene phases from their experiments, Dalou et al. (2011) used a lattice-strain model (Frei et al. 2009) and Raman spectra to ascribe F to the O1 site (the smaller of the O sites) where it is coordinated with two M1 cations, one M2 cation, and one tetrahedral cation (Fig. 5.7). The lattice-strain model predicted that, given the similar ionic radii between F^- and O^{2-}, the charge deficit caused by the substitution of F^- into the O^{2-} site involves the lengthening of the cation-anion distance, thus relaxing the strain energy and revealing a negative correlation between D_F and the strain-energy component of the model. Raman spectra on the Opx phases found distinct negative correlations between F abundances and certain vibration modes. Given the similar ionic radii between F^- and O^{2-}, the charge difference between the two anions results in a decrease in anion-cation bonding force, reducing the vibrational frequency. Dalou et al. (2011) show negative correlations between F content and the Mg-O, O-Si-O, and Ca-O vibrational modes. Thus, the lattice-strain model predicted a reduction in strain energy at F sites, and Raman spectroscopy was able to identify those sites where the vibrational frequency was lower due to F incorporation at those sites. Nevertheless, Dalou et al (2011) express concern that more work needs to be done on this model for F incorporation into Opx.

When applying the lattice-strain model to clinopyroxene phases, Dalou et al. (2011) found a positive correlation between end-member pyroxene component and the ideal crystal strain-free radius of the M1 and M2 sites. They found a positive correlation between the Ca-Tschermaks (CaTs) component and the radius of the M1 site, resulting from the substitution of Al^{3+} for Mg^{2+} and a shortening of the M1-O bond length. However, with no subsequent correlation between F incorporation and strain energy, there was no role for F to play in the lattice-strain model for Cpx. Raman spectroscopy revealed that there is a decrease in the Ca-anion stretch vibration mode with an increase in F content

of the crystal, suggesting that F substitutes into the O3 site associated with the M2 cation site. Nevertheless, Dalou et al. (2011) state that the correlation between F incorporation into Cpx and pyroxene end-member chemistry is inconclusive.

5.3.2 Fluorine in Pyroxene: End-Member Components

There are several possible substitution mechanisms for F within the Cpx phases from our study. For example, Figure 5.8a shows a positive correlation between the F (ppm) and Na_2O (wt.%) content of Cpx, which may be described by the following reaction of diopside with Na from a melt:

$$Mg_2Si_2O_6 \text{ (pyx)} + NaF \text{ (melt)} = NaMgSi_2O_5F \text{ (pyx)} + MgO \text{ (melt)} \quad (4)$$

Equation (4) suggests that Na enters the pyroxene structure by replacing Mg in the M2 site. Fluorine enters the Cpx structure at an O site, possibly following the model of Dalou et al. (2011) as described above where F substitutes for oxygen at the O3 site associated with the M2 cation. Figure 5.8b shows a negative correlation between Na_2O and MgO, suggesting a loss of Mg^{2+} as it is replaced by Na^{+} as indicated by equation (4). The trend depicted in Figure 5.8b is not a 1:1 correlation, and other cations like Ca^{2+} and Li^{+} may replace Mg in the M2 site. Compared to other monovalent cations that may substitute for Mg in the M2 site (in VIII-fold coordination), Na^{+} (1.18 Å) is slightly larger than Mg^{2+} (0.89 Å) by about 25 %, keeping the elastic strain energy low and allowing F to substitute for O3 (Dalou et al. 2011). However, other substitution mechanisms are possible as long as charge balance is maintained. Trivalent cations such as Al^{3+} may substitute within the M1 or T sites to balance the charge as F^{-} replaces O^{2-}. Adding alumina to equation (4) may result in a coupled substitution of Na^{+} and Al^{3+} as follows:

$$Mg_2Si_2O_6 \text{ (pyx)} + NaF \text{ (melt)} + Al_2O_3 \text{ (melt)} = NaAl(Al,Si)O_5F \text{ (modified jadeite)} + 2MgO \text{ (melt)} + SiO_2 \text{ (melt)} \quad (5)$$

Equation (5) shows a fictive mechanism by which Na^+ and Al^{3+} replace both Mg^{2+} ions within the M1 and M2 sites, respectively, to form the jadeite component of pyroxene. To accommodate F within jadeite, an additional Al^{3+} must substitute for one Si^{4+} cation in the tetrahedral site. This mechanism suggests a loss of Mg as F enters the structure of a "modified" jadeitic pyroxene, and Figure 5.8 (c) shows a strong negative correlation between Al_2O_3 and MgO of our Cpx samples.

The effects of pyroxene end-member components on the incorporation of F into the pyroxene structure have not been adequately determined. Dalou et al. (2011) investigated crystal chemical controls for F and Cl incorporation into Cpx, but found none with statistical significance for F. They did find positive correlations between Cl and the jadeite and Ca-Tschermaks components of Opx and proposed a thermodynamic model to demonstrate the incorporation of Cl into the jadeite component of Opx phases. We will adopt this model for F and follow the substitution equation of Dalou et al. (2011) using the Kroger-Vink notation (Kroger and Vink 1956):

$$\begin{aligned} &Na'_{Mg} + Al^{\bullet}_{Mg} + Si^{\times}_{Si} + O^{\times}_{0} + F^{\times}_{melt} + 2MgO^{\times}_{melt} \\ &\quad = Na^{\times}_{melt} + Al'_{Si} + SiO^{\times}_{2\,melt} + O^{\times}_{melt} + F^{\bullet}_{O} + 2Mg^{\times}_{Mg} \end{aligned} \tag{6}$$

where superscript symbols represent the charge states of the lattice: $'$ represents a negatively charged, $^{\bullet}$ represents a positively charged, and ^{x} indicates a neutrally charged lattice site. Subscripts indicate the locations where the species are found (melt or lattice site). Equation (6) demonstrates that as F^- is substituted into the O^{2-} site, Al^{3+} substitutes into the Si^{4+} site. The reaction should progress to the right with increasing jadeite component. A thermodynamic expression of equation (6) can be written as:

$$\Delta G = -RT \ln \left(\frac{a^{melt}_{Na}\, a^{melt}_{SiO_2}\, a^{pyx}_{F}\, a^{pyx}_{Al}\, a^{pyx}_{Enstatite}}{a^{pyx}_{Jadeite}\, a^{melt}_{F}\, a^{melt\ 2}_{MgO}} \right) \tag{7}$$

where, from equation (6), $2Mg_{Mg}^{\times}$ represents the enstatite component of pyroxene and $Na'_{Mg} + Al^{\bullet}_{Mg} + Si^{\times}_{Si} + O^{\times}_{0}$ represents the jadeite component. From equation (7), the activities of oxygen and Si in pyroxene and oxygen in the melt are considered unity. The partition coefficient can now be expressed as activities of components such that:

$$D_F^{pyx/melt} = \frac{[F]^{px}}{[F]^{melt}} \propto \frac{a_F^{pyx}}{a_F^{melt}},$$

$$D_F^{pyx/melt} \propto \frac{a_{Jadeite}^{pyx}\, a_{MgO}^{melt\ 2}}{a_{Na}^{melt}\, a_{SiO_2}^{melt}\, a_{Al}^{pyx}\, a_{Enstatite}^{pyx}} \exp\left(-\frac{\Delta G}{RT}\right). \quad (8)$$

Under the assumption that the ratio of the activity coefficients ($\gamma_F^{pyx} / \gamma_F^{melt}$) is constant over the range of experimental conditions of our samples, equation (8) shows that $D_F^{pyx/melt}$ is correlated positively with $a_{Jadeite}^{pyx}$ and negatively with $a_{Enstatite}^{pyx}$. The data for the Cpx phases of our study show good agreement with equation (8), and we found that $D_F^{Cpx/melt}$ shows a moderately positive correlation with the jadeite component of our samples and a strong negative correlation with the enstatite component (Fig. 5.9 a, b).

The Ca-Tschermaks (CaTs) component of clinopyroxene involves the substitution of Al^{3+} for Mg^{2+} in the M1 site and Al^{3+} for Si^{4+} in the tetrahedral (T) site. We showed in equation (5) that the substitution of F^- into the O^{2-} O3 site balances the Al^{3+} substitution into the Si^{4+} site. However, because [F] << [Al], the substitution of Al^{3+} into the Si^{4+} site may also be charge-balanced by Al^{3+} replacing Mg^{2+} in the M1 site as per the Tschermaks substitution. The Tschermaks component can be expressed by the following reaction:

$$Al^{\bullet}_{Mg} + O^{\times}_{O} + F^{\times}_{melt} + Mg^{\times}_{melt} = Al^{\times}_{melt} + O^{\times}_{melt} + F^{\bullet}_{O} + Mg^{\times}_{Mg} \quad (9)$$

Figure 5.9c shows the jadeite + CaTs component (mol %) versus $D_F^{Cpx/melt}$. The correlation is strong, suggesting that multiple substitution mechanisms occur to charge-balance F incorporation into pyroxene.

5.3.3. Total Iron Content of Cpx and Fe^{2+} – F Avoidance in Silicate Minerals

The Fe content of our Cpx samples comprises the second most abundant cation next to Mg to compete for the M1 octahedral site. Therefore, we suggest that the strong negative correlation between $D_F^{Cpx/melt}$ and the enstatite (Mg) component of our samples (Fig. 5.9b) is due mainly to closure, and hence F incorporation into Cpx should correlate positively with an increase in the ferrosilite (Fe) content of Cpx. Figure 5.10 (a) shows a plot of $D_F^{Cpx/melt}$ versus the ferrosilite content of the Cpx samples, and as anticipated a strong positive correlation exists. The ferrosilite content of the Cpx phases shows an orderly, systematic increase relative to the evolved state of the parent rock, illustrating a greater uptake of Fe into Cpx during differentiation of the host magma. The ol-minette suite represents the most primitive of the sample suites of this study, and their Cpx phases show the lowest mole percent of ferrosilite, and hence the lowest Fe content. The ferrosilite content of the Cpx phases from the aug-minette, basaltic andesite, and latite suites increase in the order of melt evolution, respectively, with the latite suites showing the largest values of Fe content as well as the largest range. The Fe/Mg ratio is typically used to describe trends in fractional crystallization and magma differentiation, where the Fe content increases within the system (melt and crystals) as Mg is consumed by earlier crystallizing phases. Figure 5.10 (b) shows a plot of $D_F^{Cpx/melt}$ versus the Fe/Mg ratio of the Cpx phases. The trend is nearly identical to that depicted in Figure 5.10 (a), but the correlation coefficient is slightly better. During magma evolution, the magma necessarily becomes more enriched in incompatible elements, in our case F, which is demonstrated by an increase in the incorporation of F into Cpx with a concomitant increase in the Fe content of Cpx.

The increase in $D_F^{Cpx/melt}$ with Fe content is in contrast to the iron-fluorine 'avoidance' noticed in other silicate phases. It has been observed that hydrous silicate minerals, such as natural micas and amphiboles that contain a high Mg/Fe ratio, show a preference for the incorporation of F over OH, and that F solubility is enhanced with increasing Mg content (e.g., Ekstrom 1972, Rosenberg and Foit 1976, Mason 1992). Experimental studies have shown that Mg^{2+} forms stronger bonds with F^- than does Fe^{2+}, and this "preference" should allow F to substitute for oxygen with greater ease in phases with a higher relative Mg content. Fluorine's preference for Mg over Fe is due to the exothermicity of the exchange reaction:

$$Mg(OH)_2 + FeF_2 \rightarrow MgF_2 + Fe(OH)_2 \qquad \Delta H = -116.7\ kcal/mole \qquad (10)$$

More work needs to be done to determine if an increase in the Fe content of Cpx does indeed promote an increase in $D_F^{Cpx/melt}$, or if other parameters associated with magma evolution, such as melt viscosity, play a greater role.

5.3.4 Fluorine in Pyroxene: Fe^{3+} Substitutions

An increase in OH^- or F^- content of pyroxene requires a charge balance through the coupled substitutions of monovalent and trivalent cations in the M1 and M2 sites, respectively, or a trivalent cation substituting for Si^{4+} in the T site. In any event, the likelihood of increased presence of trivalent cations such as Al^{3+}, Cr^{3+}, or Fe^{3+} in hydrated or fluoridated pyroxenes is great (Bromiley et al. 2004, Stalder 2004, Stalder et al 2005). Ferric iron may substitute into the M1 and M2 cation sites, substituting for Mg^{2+} and Ca^{2+}, respectively, as well as in the tetrahedral site where it replaces Si. Some possible cation substitution reactions involving ferric iron and H^+ are the following (Stalder 2004):

$$Fe^{3+}_{tetr} + H^{+} = Si^{4+}_{tetr} \quad (11)$$

$$Fe^{3+}_{tetr} + Fe^{3+}_{oct} = Si^{4+}_{tetr} + Mg^{2+}_{oct} \quad (12)$$

$$Fe^{3+}_{oct} + H^{+} = 2\ Mg^{2+} \quad (13)$$

Reaction (11) shows the Fe^{3+} substitution in the tetrahedral site as H^{+} bonds to oxygen for charge balance. Reaction (12) shows the Fe-Tschermaks substitution, which is not likely to generate much H^{+} incorporation because H^{+} is not required for charge balance. In addition, reaction (11) may not generate much H^{+} either due to the incorporation of tetrahedral Fe^{3+} through reaction (12). Reaction (13) shows the coupled substitution of Fe^{3+} and H^{+} in the M1 octahedral site. The ionic radius of Fe^{3+} (0.55 Å in VI-fold coordination; 0.78 Å in VIII-fold coordination) is smaller than the ionic radius of Mg^{2+} (0.72 Å in VI-fold coordination; 0.89 Å in VIII-fold coordination), and therefore it is unlikely that a significant fraction of Fe^{3+} will substitute for Ca^{2+} (1.00 Å in VI-fold coordination; 1.12 Å in VIII-fold coordination) in the M2 site, leaving most of the Fe^{3+} in the M1 site (Bromiley et al. 2004). Nevertheless, dissolving ferric iron into pyroxene requires a coupled substitution mechanism whereby Fe^{3+} in the M1 site is charge-balanced by H^{+} bonded to oxygen in an interstitial site, by Na^{+} in the M2 site, or Al^{3+} in the tetrahedral site. Stalder (2004) notes that reaction (13) may be the most likely mechanism for H^{+} incorporation into pyroxenes until hematite saturation is achieved.

Because $D_F^{Cpx/melt}$ shows an increase with increasing Fe content of the crystals, we decided to test reaction (13). However, we measured F^{-} in our samples, not H^{+}. Analogous reactions involving F^{-} instead of H^{+} would be:

$$Fe^{3+}_{oct} + F^{-} + [] = 2\ Mg^{2+} + O^{2-} \quad (14)$$

$$Fe^{3+}_{tetr} + F^{-} = Si^{4+}_{tetr} + O^{2-} \quad (15)$$

In equation (14), Fe^{3+} replaces 2 Mg^{2+} ions as F^- replaces an oxygen anion for charge balance, leaving a metal vacancy. Equation (15) shows a mechanism by which Fe^{3+} may substitute for Si^{4+} in the tetrahedral site as F^- replaces O^{2-} for charge balance. Figure 5.11 shows a strong negative correlation between octahedral Mg^{2+} and total Fe, indicating the possibility that reaction 14 has occurred in our samples, whereby Fe^{3+} substitutes for Mg^{2+} in the octahedral site and is charge balanced by either H^+ in the cation site or by F^- in one of the oxygen sites plus a metal vacancy in the M2 site. However, because Fe^{2+} and Mg^{2+} are major components in pyroxenes, Figure 5.11 may simply show solid solution substitutions between Mg- and Fe-pyroxenes.

If ferric iron has indeed been incorporated into our Cpx samples and is causing an increase in the partitioning of F into our samples, then there should be a positive correlation between $D_F^{Cpx/melt}$ and the oxygen fugacity of the system, where a higher fO_2 of the melt will generate Fe^{3+} cations. Table 5.2 lists the log fO_2 of the sample suites we studied, and the values show generally reducing conditions during the experimental runs. Nevertheless, the log fO_2 values range from -14.9 to -7.3 (nearly seven orders of magnitude), and the relative increase in the oxidizing conditions may result in a concomitant increase in the occurrence of Fe^{3+} and an increase in the partitioning of F into the pyroxene crystals. Figure 5.12 shows a plot of log fO_2 versus $D_F^{Cpx/melt}$ for the sample suites of this study. Within the interval of fO_2 log units, the ol-minette, aug-minette, and basaltic andesite samples show an increase in $D_F^{Cpx/melt}$ with an increase in fO_2. The ol-minette samples show little variation in D_F as fO_2 increases from -13.8 to -10.0 log units. However, an increase in the fO_2 in the aug-minette and the basaltic andesite samples depicts a substantial rise in $D_F^{Cpx/melt}$. This may be due in part to an increase in the Fe^{3+} content of the crystals as the system becomes relatively more oxidizing. Figure 5.12 also shows the average total iron content (FeO in the legend) for each suite of Cpx samples. The lowest average Fe content exists in the ol-minette

samples, and these samples show only a slight response in $D_F^{Cpx/melt}$ as fO_2 becomes more oxidizing. However, the aug-minette and the basaltic andesite Cpx samples contain more total iron than Cpx from the ol-minettes, and their $D_F^{Cpx/melt}$ values increase substantially. It appears the average total Fe content of the Cpx phases may play a role in the amount of ferrous iron available for oxidation when conditions are more oxidizing. Stalder (2004) suggests that an increasing Fe content in the starting material does indeed lead to enhanced Fe^{3+} content simply because there is more iron to oxidize. The highest average total Fe content occurs in the latite Cpx phases, but these samples show no correlation between $D_F^{Cpx/melt}$ and fO_2. Their range in log $fO2$ units is narrow, but their $D_F^{Cpx/melt}$ values range as high as the basaltic andesite values. The latite samples also contain the highest silica content and are the most evolved of the suites studied. Other factors that control F incorporation into pyroxenes, like melt viscosity (see a later section of the text) may dominate with pyroxenes in these more evolved rocks. We recognize that our results for Fe^{3+} substitution are inconclusive and more work needs to be done.

5.3.5 Fluorine in Pyroxene: Al^{3+} Substitution and Comparison to H^+ in Pyroxene

Within the past decade or so there have been many studies on the relation between the incorporation of H and Al in pyroxenes, including studies that show a strong correlation between increasing H_2O solubility with increasing Al content and increasing $D_H^{pyx/melt}$ with increasing Al_2O_3 content, including an increase in Al in tetrahedral sites (Rauch and Keppler 2002, Stalder and Skogby 2002, Stalder 2004, Aubaud et al. 2004, 2008; Hauri et al. 2006; Grant et al. 2007; Tenner et al. 2009). The incorporation of OH into aluminous pyroxene may be the result of a coupled substitution that charge-balances Al within the tetrahedral site, forming a molecule such as $Mg_2Al^{IV}HSiO_6$, where H occupies an interstitial site. Hauri et al. (2006) suggests that tetrahedral Al^{3+} is the main driver of the increase in $D_H^{Cpx/melt}$ in aluminous pyroxenes. Plots from the literature of

$D_H^{Cpx/melt}$ versus total alumina content (Al_2O_3; Fig. 5.13a) and $D_H^{Cpx/melt}$ versus tetrahedral Al content (Al (IV); Fig. 5.13b) show trends that indicate the majority of Al that substitutes into pyroxene due to coupled substitutions with H^+ enters tetrahedral sites. Indeed, studies within the past few years have shown that the dominant mechanism for incorporating H in aluminous pyroxenes occurs as Al^{3+} substitutes for Si^{4+} within tetrahedral sites (Hauri et al. 2006; Tenner et al. 2009; O'Leary et al. 2010) and is charge-balanced by H^+ occupying an interstitial site where it bonds to the O3 oxygen (located at the SiO_4-tetrahedron faces and pointing toward the interstice between the M2 positions along the crystallographic b-axis sites (see Fig. 5.7). For the incorporation of Al and H, a number of reactions have been proposed (Stalder and Skogby 2002, Stalder 2004):

$$Si^{4+} = 4H^+ \quad (16)$$

$$Mg^{2+} = 2H^+ \quad (17)$$

$$Al^{3+} + H^+ = Si^{4+} \quad (18)$$

$$2Mg^{2+} = Al^{3+} + H^+ \quad (19)$$

$$Si^{4+} + Mg^{2+} = 2Al^{3+} \quad (20)$$

Equations 16-20 can be combined to form an expression that accommodates the Al^{3+} and H^+ substitution mechanism whereby the Tschermak's-type Al substitution in pyroxene is coupled with a defect in which H is used to charge balance tetrahedral Al:

$$MgAl^{VI}Al^{IV}SiO_6 \text{ (pyx)} + H_2O + 2Mg_2SiO_4 \text{ (oliv)} = 2Mg_2Al^{IV}HSiO_6 \text{ (pyx)} + MgSiO_3 \text{ (pyx)} \quad (21)$$

where an aluminous pyroxene co-exists with forsterite (Tenner et al. 2009). Obviously, the Tschermak's molecule places Al^{3+} in both the tetrahedral sites and the M1 octahedral

sites. In the case of octahedral Al, charge balance may be achieved by H^+ occupying M2 vacancies to form the molecule $HAl^{VI}Si_2O_6$ (Stalder and Skogby 2002; Kohn et al. 2005; Aubaud et al. 2008). Equation (20) generates a vacancy in one octahedral site. Eclogite pyroxenes, with a large Ca-Eskola component [$CaAl(AlSi)O_6 + 3SiO_2 = Ca[]Al_2Si_4O_{12}$; where [] represents a vacancy], are known to contain large amounts of OH, and these hydroxyl ions are stabilized by association with octahedral Al, bonding at oxygen sites associated with octahedral vacancies. However, the Ca-Eskola component occurs at pressures between 4-8 GPa, pressures much greater than the experimental conditions of our samples (Smyth et al. 1991; Katayama and Nakashima 2003; Aubaud et al. 2008; Zhao et al. 2011).

The incorporation of F in pyroxenes as a function of Al content is not well known. Trivalent cation substitution mechanisms were addressed above, and substitution reactions for Al^{3+} can emulate reactions (14) and (15) above:

$$Al^{3+}_{oct} + F^- + [] = 2\ Mg^{2+} + O^{2-} \quad (22)$$

$$Al^{3+} + F^- = Si^{4+} + O^{2-} \quad (23)$$

Reaction (22) describes the formation of the Eskola component whereby Al^{3+} substitutes in the M1 site with F^- replacing one O^{2-} for charge balance and generating a vacancy in the M2 site. Reaction (23) places Al^{3+} in a tetrahedral site with F^- replacing one O^{2-} for charge balance, forming the Tschermaks component. Both reactions (22) and (23) can be combined to form a fictive reaction analogous to reaction (5) above:

$$Mg_2Si_2O_6\ (pyx) + Me^{1+}F\ (melt) + Al_2O_3\ (melt) = Me^{1+}Al^{VI}(Al^{IV},Si)O_5F\ (pyx) + 2MgO\ (melt) + SiO_2\ (melt) \quad (24)$$

where Me^{1+} is a monovalent cation in the M2 site.

We attempted to apply the H_2O-Al solubility and partitioning mechanisms to fluorine by testing F partitioning versus Al content of the pyroxene phases from our samples. The results show similarities between H and F incorporation into pyroxenes. When compared against total Al_2O_3 and tetrahedral Al content, F incorporation into pyroxene appears to be enhanced by increasing Al content of the pyroxenes, although the correlations are moderate at best (Fig. 5.14 a,b). Dalou et al. (2011) suggest that F is substituted into the O3 site, the largest of the oxygen sites, which is associated with the M2 cation site. Indeed, F may substitute into the smaller O2 and O1 oxygen sites, although greater effort is required in order to charge balance a trivalent cation in the M1 octahedral site. However, the O3 oxygen bridges the tetrahedral site with the M2 site, and F replaces O3 to charge balance both sites. We agree with Dalou et al. (2011) that F more likely substitutes into the O3 oxygen site to charge balance both monovalent cations in the M2 site as well as trivalent cations in the tetrahedral site.

5.4 Melt Viscosity and F Partition Coefficient

Fluorine behaves as an incompatible element within magmas within which hydrous or fluorous phases have not crystallized (e.g. Stecher, 1998). As a result, the abundance of F will increase in the melt with differentiation, allowing more F to be available for incorporation into crystallizing phases. However, given a constant $D_F^{\text{min}/\,melt}$, the abundance of F in the crystal is proportional to the abundance of F in the melt. The observed positive correlation between $D_F^{Cpx\,/\,melt}$ and the Fe/Mg ratio of our Cpx phases (See Fig. 5.10 b) suggests that the “preference” of F for Cpx increases with magma differentiation. As discussed previously, the incorporation of F within silicate minerals has been documented to favor phases with higher magnesian content (Fe-F avoidance), and this observation has been thermodynamically modeled (see equation 10). Because the Cpx phases in this study appear to counter the Fe-F avoidance, we decided to investigate other factors related to magma differentiation, in addition to the crystal chemical controls, that may effect the partitioning of F into Cpx.

Previous studies have shown that the partitioning of cations between nominally anhydrous mantle phases and melt is strongly influenced by the structure of the melt, as well as any crystal chemical controls within the mineral itself (e.g. Gaetani and Grove 1995; Kushiro and Mysen 2002; Gaetani 2004). By far, the structure of the crystal dominates the control on cation partitioning and relative compatibilities, yet melt structure is likely to contribute moderate controls on partitioning (Gaetani 2004), and any effect attributable to melt structure is likely to be subtle. Although silicate melts lack the long-range order and structure of crystals, they nevertheless contain transient and ephemeral structural units of SiO_4^{4-} tetrahedra that are variably connected to form polymeric units whereby 0-4 tetrahedral oxygens are bonded to other tetrahedra via bridging oxygens or to non-tetrahedral polyhedrons via non-bridging oxygens (Mysen 1988). The degree to which a melt contains connected and ordered tetrahedra describes its polymerization, and it has been demonstrated that when considering a broad range of melt compositions, increasing melt polymerization leads to increased partitioning of cations into crystals, similar to the manner consistent with immiscible silicate liquids (Gaetani 2004). Smaller cations are more sensitive to melt depolymerization, and Dalou et al (2011) showed that this tendency affects smaller anions as well. Dalou et al. (2011) plotted $D_F^{Opx/melt}$ and $D_{Cl}^{Opx/melt}$ against melt viscosity and found that $D_F^{Opx/melt}$ exhibits a strong, positive correlation with viscosity whereas $D_{Cl}^{Opx/melt}$ does not. Even though both F^- and Cl^- have the same charge, the smaller anion F^- concentrates in a more depolymerized melt and is more readily influenced by changes in melt viscosity. We tested the correlation between the D_F of our samples and the viscosity of the melt from which the crystals grew. To calculate the viscosity, we utilized a spreadsheet model constructed by Giordano et al. (2008) called grdViscosity, which can be downloaded from the internet (http://www.eos.ubc.ca/~krussell/VISCOSITY/grdViscosity.html). Figure 5.15 shows a moderate correlation between D_F and melt viscosity for both the Cpx and olivine phases,

in agreement with Dalou et al. (2011). Clearly, $D_F^{Cpx/melt}$ increases with increasing viscosity for Cpx, but $D_F^{Oliv/melt}$ shows only two clusters, rendering it difficult to conclude a trend, although a positive correlation may be extrapolated.

Many variables control melt viscosity, such as temperature, pressure, volatile content, crystallinity, and melt composition. The most significant contributor to melt viscosity is the degree of polymerization of the melt, which itself varies as a function of the silica content of the magma insofar as the higher the silica content the greater the degree of polymerization. A common method for quantifying melt polymerization is to calculate the ratio of non-bridging oxygens (oxygens that are bonded to one cation in tetrahedral coordination and one cation in a different coordination state) to cations in tetrahedral coordination, or NBO/T. As melt polymerization increases, NBO/T decreases in response to an increase in the number of bridging oxygens present in the melt. With greater melt polymerization, NBO/T will approach zero. Hence, NBO/T = O means a melt is fully polymerized and all four oxygens in the SiO^{4-} tetrahedron are bonded to bridging oxygens forming a silicate framework. A melt with NBO/T = 4 is theoretically not polymerized at all and the SiO_4^{4-} tetrahedra exist as isolated silicate structures (Mysen 1988; Gaetani 2004). We calculated NBO/T for the glass portions of the samples from our study using the method of Mysen (1985, 1988), and we plotted NBO/T versus $D_F^{Cpx/melt}$ and $D_F^{Oliv/melt}$ for our samples (Figure 5.16a,b). Our plots show a strong correlation between melt polymerization and F partitioning into Cpx and olivine. The dashed lines in Figure 5.16a and 5.16b indicate, by inspection, the value of NBO/T at which melt polymerization may become the most important factor controlling partitioning. Figure 5.16a shows that polymerization begins to affect $D_F^{Cpx/melt}$ at approximately NBO/T = 0.3. Whereas, Figure 5.16b shows that polymerization begins to affect $D_F^{Oliv/melt}$ at about NBO/T = 0.35. For Cpx, D_F increased by a factor of 7 as NBO/T decreased by a factor of 8 (melt polymerization increased by a factor of 8). For olivine, D_F

increased by a factor of 14 as NBO/T decreased by a factor of 5. It appears that melt polymerization has a greater effect on the partitioning of F into olivine than into Cpx.

A simple reaction model to describe the increase in $D_F^{Cpx/melt}$ with an increase in polymerization is as follows:

$$SiO_2 \text{ (melt)} + NaF \text{ (melt)} + Al_2O_3 \text{ (melt)} = NaAl^{VI}Al^{IV}SiO_5F \text{ (pyx)} \quad (25)$$

whereby an increase in the silica content (polymerization) of the melt drives the reaction toward the right, promoting the incorporation of F into pyroxene.

6. Conclusion

We report the F partition coefficients for clinopyroxene, olivine, plagioclase, and hornblende within melts of olivine-minette, augite-minette, basaltic andesite, and latite compositions taken from previously-published experimental run products for *P-T* conditions that range from 0.607 to 20 kbars and 1,000 to 1,175°C. The partition coefficients of F for clinopyroxene and olivine are shown to be << 1.0. D_F varied with each melt composition and showed a progressive increase with increasing silica content of the melt (from lowest D_F to highest): ol-minette > aug-minette > basaltic andesite > latite. We investigated some possible crystal chemical and melt structural controls on D_F.

Previously published work on the partitioning of F into Cpx and olivine found no controls on F partitioning based on mineral chemistry. We demonstrated that crystal chemical controls strongly influence the incorporation of F into Cpx (in particular the Al content), but we found none that affected olivine. It appears that the F substitution mechanism into olivine is dominantly controlled by melt viscosity and the degree of melt polymerization, whereby an increase in polymerization and viscosity leads to an increase in D_F. Fluorine incorporation into Cpx was found to be promoted by a combination of chemical and end-member-component factors. We demonstrated a positive correlation

between $D_F^{Cpx/melt}$ and the pyroxene jadeite (Na^+) component and a much stronger correlation when the jadeite and the Tschermaks components are added together, demonstrating the occurrence of multiple substitution mechanisms involving Na and Al as F is incorporated into the pyroxene crystal for charge balance. A strong negative correlation between $D_F^{Cpx/melt}$ and the enstatite component (Mg^{2+}) and a strong positive correlation between $D_F^{Cpx/melt}$ and Fe/Mg ratio shows that F incorporation correlates with an increase in the Fe content of pyroxenes, in contrast to the F – Fe avoidance known to occur in biotite, phlogopite, amphibole, and other silicate phases.

When we looked at $D_F^{Cpx/melt}$ versus individual cations such as Na^+, Fe^{3+}, and Al^{3+}, we found positive correlations. A number of different coupled substitutions among monovalent and trivalent cations can be charge-balanced by the incorporation of F^- at oxygen sites. The cation site where Fe^{3+} and Al^{3+} are most likely to enter is the tetrahedral site, although they will enter the M1 octahedral site as well. The preferred site for Na^+ is the larger M2 site. Both the tetrahedral site and the M2 site are connected by the O3 oxygen site, and we propose that this is the likely oxygen site for F substitution, which agrees with the findings of Dalou et al. (2011). In addition, we found that within minettes and basaltic andesites, an increase in the oxygen fugacity of the system results in the possible generation of Fe^{3+} in the Cpx within octahedral and tetrahedral sites, allowing for the incorporation of F via charge balancing. We found a positive correlation between log fO_2 and $D_F^{Cpx/melt}$, and the higher the initial iron content of the system, the greater the $D_F^{Cpx/melt}$. However, the influence of fO_2 on F incorporation occurs when other dominant mechanisms are not present. The Cpx samples from latites showed no correlation between fO_2 and $D_F^{Cpx/melt}$, but a strong correlation emerged with melt polymerization.

Melt structure was found to have a strong influence on D_F for both Cpx and olivine. We calculated the viscosity of the glass portion of our samples, and we found a moderate positive correlation between D_F and viscosity. We also calculated the degree of melt polymerization as NBO/T (non-bridging oxygens divided by the number of tetrahedral cations in the melt). We found a strong positive correlation between melt polymerization and D_F. For Cpx, D_F increased by a factor of 7 as NBO/T decreased by a factor of 8 (melt polymerization increased by a factor of 8). For olivine, D_F increased by a factor of 14 as NBO/T decreased by a factor of 5. We show that melt polymerization has a stronger influence on $D_F^{Oliv/melt}$ compared to $D_F^{Cpx/melt}$.

7. References

Aiuppa, A., Baker, D.R., and Webster, J.D. (2009) Halogens in volcanic systems. Chemical Geology, 263, 1018.

Alletti, M., Baker, D.R. and Freda, C. (2007) Halogen diffusion in a basaltic melt. Geochimica et Cosmochimica Acta, 71, 3570-3580.

Aubaud, C., Hirschmann, M.M., Withers, A.C. and Hervig R.L. (2008) Hydrogen partitioning between melt, clinopyroxene, and garnet at 3 GPa in a hydrous MORB with 6 wt.% H_2O. Contributions to Mineralogy and Petrology, 156, 607-625.

Aubaud, C., Hauri, E.H. and Hirschmann, M.M. (2004) Hydrogen partition coefficients between nominally anhydrous minerals and basaltic melts. Geophysical Research Letters, 31, L20611.

Bell, D.R. and Rossman, G.R. (1992) Water in Earth's mantle: The role of nominally anhydrous minerals. Science, 255, 1391-1397.

Bromiley, D.W. and Kohn, S.C. (2007) Comparisons between fluoride and hydroxide incorporation in nominally anhydrous and fluorine-free mantle minerals. Goldschmidt conference abstracts.

Bromiley, G.D., Keppler, H., McCammon, C., Bromiley F.A. and Jacobsen S.D. (2004) Hydrogen solubility and speciation in natural, gem-quality chromian diopside. American Mineralogist, 89, 941-949.

Carroll, M.R. and Webster, J.D. (1994) Solubilities of sulfur, noble gases, nitrogen, chlorine, and fluorine in Magmas. In: Carroll, M.R. and Holloway, J.R. (eds), Volatiles in Magmas. Reviews in Mineralogy Volume 30. Mineralogical Society of America (Washington, D.C.), 231-279.

Chevychelov, V.Y., Botcharnokov, R.E., and Holtz, F. (2008) Partitioning of Cl and F between fluid and hydrous phonolitic melt of Mt. Vesuvius at ~850-1000 C and 200 Mpa. Chemical Geology, doi:10.1016/j.chemgeo.2008.06.025.

Dalou, C., Koga, K.T., Shimizu, N., Boulon, J. and Devidal, J.L. (2011) Experimental determination of F and Cl partitioning between lherzolite and basaltic melt Contributions to Mineralogy and Petrology, 1-19.

Delaney, J., Smith, J., Carswel,l D. and Dawson, J. (1980) Chemistry of micas from kimberlites and xenoliths--II. Primary-and secondary-textured micas from peridotite xenoliths. Geochimica et Cosmochimica Acta, 44, 857-872.

Dingwell, D.B. (1985) The structures and properties of fluorine-rich magmas: A review of experimental studies. In: Taylor, R.P. and Strong, D.F. (eds), Recent Advances in the Geology of Granite-Related Mineral Deposits. Canadian Institute of Mining and Metallurgy (Montreal), 1-12.

Dingwell, D.B., Scarfe, C.M., and Cronin, D.J. (1985) The effect of fluorine on viscosities in the system Na_2O-Al_2O_3-SiO_2: implications for phonolites, trachytes, and rhyolites. American Mineralogist, 70, 80-87.

Ekstrom, T.K. (1972) The distribution of fluorine among some coexisting minerals. Contributions to Mineralogy and Petrology, 34, 192-200.

Engi, M. and Lindsley, D.H. (1980) Stability of titanian clinohumite: Experiments and thermodynamic analysis. Contributions to Mineralogy and Petrology, 72, 415-424.

Esperanca, S. (1984) An experimental and geochemical study of the high-K latites and associated nodules from camp Creek, Arizona. PhD Dissertation, Arizona State University, p. 87

Esperança, S. and Holloway, J.R. (1987) On the origin of some mica-lamprophyres: experimental evidence from a mafic minette. Contributions to Mineralogy and Petrology, 95, 207-216.

Esperança, S. and Holloway, J.R. (1986) The origin of the high-K latites from Camp Creek, Arizona: constraints from experiments with variable fO_2 and aH_2O. Contributions to Mineralogy and Petrology, 93, 504-512.

Farver, J.R. (2010) Oxygen and hydrogen diffusion in minerals. In Diffusion in Minerals and Melts. Reviews in Mineralogy and Geochemistry (eds. Y. Zhang and D.J. Cherniak). Mineralogical Society of America. 72, 447-507.

Frei, D., Liebscher, A., Franz, G., Wunder, B., Klemme, S., and Blundy, J.D. (2009) Trace element partitioning between orthopyroxene and anhydrous silicate melt on the lherzolite solidus from 1.1 to 3.2 Gpa and 1,230 to 1,535 C in the model system Na_2O-CaO-MgO-Al_2O_3-SiO_2. Contributions to Mineralogy and Petrology, 157, 473-490.

Gaetani, G.A. (2004) The influence of melt structure on trace element partitioning near the peridotite solidus. Contributions to Mineralogy and Petrology, 147, 511-527.

Gaetani, G.A. and Grove T.L. (1995) Partitioning of rare earth elements between clinopyroxene and silicate melt: Crystal-chemical controls. Geochimica et Cosmochimica Acta, 59, 1951-1962.

Gasparik, T. (1993) The role of volatiles in the transition zone. Journal of Geophysical Research, 98, 4287-4299.

Gasparik, T. (1990) Phase relations in the transition zone. Journal of Geophysical Research, 5, 15751-15769.

Giordano, D., Russell, J.K. and Dingwel,l D.B. (2008) Viscosity of magmatic liquids: A model. Earth and Planetary Science Letters, 271, 123-134.

Grant, K.J., Kohn, S.C. and Brooker, R.A. (2007) The partitioning of water between olivine, orthopyroxene and melt synthesized in the system albite-forsterite-H_2O. Earth and Planetary Science Letters, 260, 227-241.

Guggino, S.N. and Hervig, R.L. (2011) Synthesis and Characterization of Five New F-bearing Basalt Reference Materials (Fba Glasses): Quantifying the Fluorine Content of the Basaltic Glass Standards BCR-2G, BHVO-2G. GSA-1G, GSC-1G, GSD-1G, GSE-1G, ML3B-G, KL2-G, and ALV-519-4. American Geophysical Union Fall Meeting Abstract.

Guggino, S.N., Hervig, R.L., and Bell, D.R. (2007) Fluorine in olivines from plutonic, extrusive, and hypabyssal suites. American Geophysical Union Fall Meeting Abstract.

Hauri, E.H., Gaetani, G.A. and Green, T.H. (2006) Partitioning of water during melting of the Earth's upper mantle at H_2O-undersaturated conditions. Earth and Planetary Science Letters, 248, 715-734.

Hauri, E. (2002) SIMS analysis of volatiles in silicate glasses, 2: isotopes and abundances in Hawaiian melt inclusions. Chemical Geology, 183, 115-141.

Hazen, R.M., Yang, H., Prewitt, C.T., Gasparik, T. (1997) Crystal chemistry of superfluorous phase B ($Mg_{10}Si_3O_{14}F_4$): Implications for the role of fluorine in the mantle. American Mineralogist, 82, 647-650.

Hermann ,J., Fitz Gerald, J.D., Malaspina, N., Berry, A.J. and Scambelluri, M. (2007) OH-bearing planar defects in olivine produced by the breakdown of Ti-rich humite minerals from Dabie Shan (China). Contributions to Mineralogy and Petrology, 153, 417-428.

Hervig, R.L. and Bell, D.R. (2005) Fluorine and hydrogen in mantle mega-crysts. American Geophysical Union Fall Meeting Abstract.

Hervig, R.L., Smith, J.V. and Rivers, M.L. (1988) Fluorine content of upper mantle minerals. EOS, Transactions of the American Geophysical Union, 69, 502.

Hirschmann, M.M., Aubaud, C., and Withers, A.C. (2005) Storage capacity of H_2O in nominally anhydrous minerals in the upper mantle. Earth and Planetary Science Letters, 236, 167-181.

Hoskin, P.W.O. (1999) SIMS Determination of μg g^{-1} - level fluorine in geological samples and its concentration in NIST SRM 610. Geostandards Newsletter, 23, 69-76.

Jochum, K.P., Stoll, B., Herwig, K., Willbold, M., Hofmann, A.W., Amini, M., Aarburg, S., Abouchami, W., Hellebrand, E., Mocek, B., Raczek, I., Stracke, A., Alard, O., Bouman, C., Becker, S., Ducking, M., Bratz, H., Klemd, R., de Bruin, D., Canil, D., Cornell, D., de Hoog, C.J., Dalpe, C., Danushevsky, L., Eisenhauer, A., Gao, Y., Snow, J.E., Groschopf, N., Gunther, D., Latkoczy, C., Guillong, M., Hauri, E., Hofer, H.E., Lahaye, Y., Horz, K., Jacob, D.E., Kasemann, S.A., Kent, A.J.R., Ludwig, T., Zack, T., Mason, P.R.D., Meixner, A., Rosner, M., Misawa, K., Nash, B.P., Pfander, J., Premo, W.R., Sun, W.D., Tiepolo, M., Vannucci, R., Vennemann, T., Wayne, D., Woodhead, J.D. (2006) MPI-DING reference glasses for in situ microanalysis: New reference values for element concentrations and isotope ratios. Geochemistry, Geophysics, Geosystems, Technical Brief, 7, 44 p.

Jochum, K.P., Willbold, M., Raczek, I., Stoll, B., Herwig, K. (2005) Chemical characterization of the USGS reference glasses GSA-1G, GSC-1G, GSD-1G, GSE-1G, BCR-2G, BHVO-2G and BIR-1G using EPMA, ID-TIMS, ID-ICP-MS, and LA-ICP-MS. Geostandards and Geoanalytical Research, 29, 285-302.

Jochum, K.P., Dingwell, D.B., Rocholl, A., Brigitte Stoll, B., Hofmann, A.W., Becker, S., Besmehn, A., Bessette, D., Dietze, H.J., Dulski, P., Erzinger, J., Hellebrand, E., Hoppe, P., Horn, I., Janssens, K., Jenner, G.A., Klein, M., McDonough, W.F., Maetz, M., Mezger, K., Münker, C., Nikogosian, I.K., Pickhardt, C., Raczek, I., Rhede, D., Seufert, H.M., Simakin, S.G., Sobolev A.V., Spettel, B., Straub, S., Vincze, L., Wallianos, A., Weckwerth, G., Weyer, S., Wolf, D., Zimmer, M. (2000) The preparation and characterisation of eight geological MPI-DING reference glasses for in-situ microanalysis. Geostandards Newsletter, 24, 87-13.

Johnson, M.C., Anderson, A.T., and Rutherford, M.J. (1994) Pre-eruptive volatile contents of magmas. In: Carroll, M.R. and Holloway, J.R. (eds), Volatiles in Magmas. Reviews in Mineralogy Volume 30. Mineralogical Society of America (Washington, D.C.), 281-330.

Katayama, I. and Nakashima, S. (2003) Hydroxyl in clinopyroxene from the deep subducted crust: Evidence for H_2O transport into the mantle. American Mineralogist, 88, 229-234.

Köhler, J., Schönenberger, J., Upton, B., and Markl, G. (2009) Halogen and trace-element chemistry in the Gardar Province, South Greenland: Subduction-related mantle metasomatism and fluid exsolution from alkalic melts. Lithos, 113, 731-747.

Kohlstedt, D.L. and Mackwell, B. (1999) Solubility and diffusion of "water" in silicate minerals. In: Wright K. and Catlow R. (eds), Microscopic Properties and Processes in Minerals. Kluwer (Dordrecht,), 539-559.

Kohn, S., Roome, B., Smith, M. and Howes, A. (2005) Testing a potential mantle geohygrometer; The effect of dissolved water on the intracrystalline partitioning of Al in orthopyroxene. Earth and Planetary Science Letters, 238, 342-350.

Kroger, F.A. and Vink, H.J. (1956) Relations between te concentrations of imperfections in crystalline solids. In: Seitz, F. and Turnbull, D. (eds). Solid State Physics, v. 3, pp. 307-435. Academic Press, Inc., New York.

Kushiro, I. and Mysen, B.O. (2002) A possible effect of melt structure on the Mg-Fe^{2+} partitioning between olivine and melt. Geochimica et Cosmochimica Acta, 66, 2267-2272.

La Tourrette, T., Hervig, R.L., and Holloway, J.R. (1995) Trace element partitioning between amphibole, phlogopite, and basanite melt. Earth and Planetary Science Letters, 135, 13-30.

London, D., Hervig, R.L. and Morgan, G.B. (1988) Melt-vapor solubilities and elemental partitioning in peraluminous granite-pegmatite systems: Experimental results with Macusani glass at 200 MPa. Contributions to Mineralogy and Petrology, 99, 360-373.

Mason, R.A. (1992) Models of order and iron - fluorine avoidance. Canadian Mineralogist, 30, 343-354.

Matson, D.W., Muenow, D.W. and Garcia, M.O. (1986) Volatile contents of phlogopite micas from South African kimberlite. Contributions to Mineralogy and Petrology, 93, 399-408.

McCormick, T.C. (1986) Crystal-chemical aspects of nonstoichiometric pyroxenes. American Mineralogist, 71, 1434-1440.

Michael, P.J. (1988) The concentration, behavior and storage of H_2O in the suboceanic upper mantle: Implications for mantle metasomatism. Geochimica et Cosmochimica Acta, 52, 555-566.

Moore, G. and Carmichael, I. (1998) The hydrous phase equilibria (to 3 kbar) of an andesite and basaltic andesite from western Mexico: Constraints on water content and conditions of phenocryst growth. Contributions to Mineralogy and Petrology, 130, 304-319.

Mysen, B.O., Cody, G.D. and Smith, A. (2004) Solubility mechanisms of fluorine in peralkaline and meta-aluminous silicate glasses and in melts to magmatic temperatures. Geochimica et Cosmochimica Acta, 68, 2745-2769.

Mysen, B.O. (1988) Structure and Properties of Silicate Melts. Developments in Geochemistry 4. Elsevier, New York, 354 p.

Mysen, B.O., Virgo, D. and Seifert, F.A. (1985) Relationships between properties and structure of aluminosilicate melts. American Mineralogist, 70, 88-105.

Nakamura, A. and Schmalzried, H. (1983) On the nonstoichiometry and point defects of olivine. Physics and Chemistry of Minerals, 10, 27-37.

O'Leary, J.A., Gaetani, G.A. and Hauri, E.H. (2010) The effect of tetrahedral Al^{3+} on the partitioning of water between clinopyroxene and silicate melt. Earth and Planetary Science Letters, 297, 111-120.

O'Reilly, S.Y. and Griffin, W. (2000) Apatite in the mantle: Implications for metasomatic processes and high heat production in Phanerozoic mantle. Lithos, 53, 217-232.

Pan, Y. and Fleet, M.E. (1996) Rare element mobility during prograde granulite facies metamorphism: significance of fluorine. Contributions to Mineralogy and Petrology, 123, 251-262.

Rauch, M. and Keppler, H. (2002) Water solubility in orthopyroxene. Contributions to Mineralogy and Petrology, 143, 525-536.

Righter, K. and Carmichael, I.S.E. (1996) Phase equilibria of phlogopite lamprophyres from western Mexico: Biotite-liquid equilibria and P-T estimates for biotite-bearing igneous rocks. Contributions to Mineralogy and Petrology, 123, 1-21.

Robert, J.L., Bény, J.M., Della, Ventura, G. and Hardy, M. (1993) Fluorine in micas: crystal-chemical control of the OH-F distribution between trioctahedral and dioctahedral sites. European Journal of Mineralogy, 5, 7-18.

Roggensack, K., Hervig, R.L., McKnigh,t S.B. and Williams, S.N. (1997) Explosive basaltic volcanism from Cerro Negro volcano: Influence of volatiles on eruptive style. Science, 277, 1639-1642.

Rosenberg, P.E. and Foit, F.F. (1976) Fe2+ - F avoidance in silicates. Geochimica et Cosmochimica Acta, 41, 345-346.

Sawyer, G.M. and Oppenheimer, C. (2006) Volcanic fluorine emissions: Observations by Fourier transform infrared spectroscopy. In: Tressaud, A. (eds), Fluorine and the Environment: Atmospheric Chemistry, Emissions, & Lithosphere. Elsevier (San Francisco), 165-185.

Scaillet, B. and Macdonald, R. (2004) Fluorite stability in silicic magmas. Contributions to Mineralogy and Petrology, 147, 319-329.

Shannon, R. (1976) Revised effective ionic radii and systematic studies of interatomic distances in halides and chalcogenides. Acta Crystallographica Section A: Crystal Physics, Diffraction, Theoretical and General Crystallography, 32, 751-767.

Sigvaldason, G.E and Oskarsson, N (1986) Fluorine in basalts from Iceland. Contributions to Mineralogy and Petrology, 94, 263-271.

Smith, J.V. (1981) Halogen and phosphorous storage in the Earth. Nature, 289, 762-765

Smith, J., Delaney, J., Hervig, R. and Dawson, J. (1981) Storage of F and Cl in the upper mantle: Geochemical implications. Lithos, 14, 133-147.

Smyth, J.R., Bell, D.R., Rossman, G.R. (1991) Incorporation of hydroxyl in upper mantle clinopyroxenes. Nature, 351, 732-735.

Smyth, J.R. (1989) Electrostatic characterization of oxygen sites in minerals. Geochimica et Cosmochimica Acta, 53, 1101-1110.

Smyth, J.R. (1987) β-Mg_2SiO_4: A potential host for water in the mantle? American Mineralogist, 72, 1051-1055.

Smyth, J.R., McCormick, T.C., Caporuscio, F.C. (1984) Petrology of a suite of eclogite inclusions from the Bobbejaan kimberlite: 1 Two unique corundum grospydites. In: Kornprobst, J (eds) Kimberlites II: The Mantle and Crust-Mantle Relationships, p. 121-132. Elsevier, New York.

Smyth, J.R. (1980) Cation vacancies and the crystal chemistry of breakdown reactions in kimberlitic omphacites. American Mineralogist, 65, 1185-1191.

Spilliaert, N., Métrich,N. and Allard, P. (2006) S–Cl–F degassing pattern of water-rich alkali basalt: Modeling and relationship with eruption styles on Mount Etna volcano. Earth and Planetary Science Letters, 248, 772-786.

Stalder R., Klemme S., Ludwig T. and Skogby H. (2005) Hydrogen incorporation in orthopyroxene: Iinteraction of different trivalent cations. Contributions to Mineralogy and Petrology, 150, 473-485

Stalder, R. (2004) Influence of Fe, Cr and Al on hydrogen incorporation in orthopyroxene. European Journal of Mineralogy, 16, 703-711.

Stalder, R. and Skogby, H. (2002) Hydrogen incorporation in enstatite. European Journal of Mineralogy, 14, 1139-1144.

.Stecher, O. (1998) Fluorine geochemistry in volcanic rock series: Examples from Iceland and Jan Mayen. Geochimica et Cosmochimica Acta, 62, 3117-3130.

Stolper, E. (1982) The speciation of water in silicate melts. Geochimica et Cosmochimica Acta, 46, 2609-2620.

Straub, S.M. and Layne, G.D. (2003) The systematics of chlorine, fluorine, and water in Izu arc front volcanic rocks: Implications for volatile recycling in subduction zones. Geochimica et Cosmochimica Acta, 67, 4179-4203.

Sykes, D., Rossman, G.R., Veblen, D.R. and Grew, E.S. (1994) Enhanced H and F incorporation in borian olivine. American Mineralogist, 79, 904-908.

Symonds, R.B., Rose, W.I., Bluth, G.S.J., and Gerlach, T.M. (1994) Volcanic-gas studies: Methods, results, and applications. In: Carroll, M.R. and Holloway, J.R. (eds), Volatiles in Magmas. Reviews in Mineralogy Volume 30. Mineralogical Society of America (Washington, D.C.), 1-66.

Tagirov, B., Schott, J., Harrichourry, J.C. and Salvi, S. (2002) Experimental study of aluminum speciation in fluoride-rich supercritical fluids. Geochimica et Cosmochimica Acta, 66, 2013-2024.

Tenner, T.J., Hirschmann, M.M., Withers, A.C. and Hervig, R.L. (2009) Hydrogen partitioning between nominally anhydrous upper mantle minerals and melt between 3 and 5 GPa and applications to hydrous peridotite partial melting. Chemical Geology, 262, 42-56.

Watson, E.B. (1994) Diffusion in volatile-bearing magmas. In: Carroll, M.R. and Holloway, J.R. (eds), Volatiles in Magmas. Reviews in Mineralogy Volume 30. Mineralogical Society of America (Washington, D.C.), 371-411.

Williams-Jones, A.E., Samson, I.M. and Olivo, G.R. (2000) The genesis of hydrothermal fluorite-REE deposits in the Gallinas Mountains, New Mexico Economic Geology, 95, 327-341.

Wood, B. and Henderson, C. (1978) Compositions and unit-cell parameters of synthetic non-stoichiometric tschermakitic clinopyroxenes. American Mineralogist, 63, 66-72.

Zhao, Y.H., Ginsberg, S. and Kohlstedt, D. (2004) Solubility of hydrogen in olivine: Dependence on temperature and iron content. Contributions to Mineralogy and Petrology, 147, 155-161.

Zhao, S., Nee, P., Green, H.W., Dobrzhinetskaya, L.F. (2011) Ca-Eskola component in clinopyroxene: Experimental studies at high pressures and high temperatures in multi-anvil apparatus. Earth and Planetary Science Letters, 307, 517-524.

8. Figure Captions

Figure 5.1. SIMS high resolution mass spectrum of F from an analysis of NIST 610 using the SIMS 6f showing the separation between the ^{19}F and ^{18}OH peaks. Mass resolving power (M/ΔM) is 2500.

Figure 5.2 Sample MOA-2 showing SIMS craters in a euhedral Cpx crystal and in adjacent glass. Magnification is 1000x. The craters are approximately 10 μm in diameter.

Figure 5.3. SIMS F calibration curve generated from the data in Table 5.4 using the synthetic Fba glasses, Biotite-3, and a silica blank. The regression line was forced through the origin and has a % RSD of 1.73%. A calibration factor (CF) of 96.7 was calculated from the equation of the regression line, and this CF was multiplied by the SIMS $^{19}F^{-}/^{18}O^{-}$ ratios to obtain F concentration values of the phases analyzed in this study.

Figure 5.4. Range of F partition coefficients for the mineral phases Cpx, olivine, and plagioclase within melts of different chemistries and silica content. a) The range in $D_F^{Cpx,Oliv\,/\,melt}$ appears to increase with increasing evolution of the host magma. Arrow points to a low $D_F^{Cpx\,/\,melt}$ outlier for the latite Cpx's. b) First-order observation that $D_F^{Cpx,Oliv\,/\,melt}$ increases with increasing silica content of the melt.

Figure 5.5. Semi-log plots of OH and F concentrations in olivine as a function of mole fraction of fayalite content. a) Modified from Zhao et al. (2004). Solubility of OH/H normalized to a water fugacity of 300 MPa versus X_{Fa} showing the solubility of OH in olivine increases exponentially with increasing Fe content of the olivine. Solid lines result from a non-linear least-squares regression of the experimental data from the authors, and dashed lines represent an overestimated extrapolation fit toward higher forsterite content. b) Data from current study showing F content (ppm x 10^3) versus X_{Fa}. Our data show no correlation between F content of the olivine crystals with increasing Fe content.

Figure 5.6. $D_F^{Oliv\,/\,melt}$ plotted against the magnesium number (Mg#) of the olivine crystals from the current study. $D_F^{Oliv\,/\,melt}$ of the basaltic andesites are 2 to 13 times higher than for the minettes, yet the Fe content appears to have no effect on F partitioning.

Figure 5.7. Generalized model of enstatite cut perpendicular to the c-axis [001]. Large grey circles (Oxygen), open circles (Magnesium), small solid circles (Silicon). Lattice sites for oxygen and magnesium are indicated. Probable locations for H^+ are indicated with an asterisk.

Figure 5.8. Possible mechanism for F replacing oxygen in the O3 site where charge balance is maintained by a coupled substitutions of Na^+ replacing Mg^{2+} in the M2 site (see equation 4 in text). a) Positive correlation between F (ppm) and Na_2O (wt.%) content of Cpx, indicating F incorporation may be due to increasing Na content. b) Negative correlation between Na_2O (wt.%) and MgO (wt.%) indicating the Mg content of Cpx is lowered as Na replaces Mg in the M2 site. c) strong negative correlation between the Al_2O_3 (wt.%) and MgO (wt.%) contents of the Cpx phases.

Figure 5.9. Variation in F partitioning with different pyroxene end-member compositions.. a) $D_F^{Cpx/melt}$ shows a moderately positive correlation with jadeite composition (mol %). b) a strong negative correlation with the enstatite component (mol %). c) The jadeite + Tschermaks component versus $D_F^{Cpx/melt}$, showing a strong positive correlation.

Figure 5.10. Ferrosilite content and Fe/Mg ratio versus $D_F^{Cpx/melt}$. a) Fluorine partitioning into the Cpx phases shows a positive correlation with the ferrosilite content (mol%) of Cpx, and this trend follows the order of the magmatic evolution of the host rock. b) The graph shows a strong positive correlation between the incorporation of F into Cpx and the Fe/Mg ratio of Cpx. The Fe/Mg ratio is typically used to describe fractional crystallization, and this graph may simply indicate that F incorporation in Cpx is a function of the incompatible nature of F, and that the correlation with increasing Fe is not causal.

Figure 5.11. Magnesium and iron crystal chemistry of Cpx phases from EPMA analysis. The plot shows a strong negative correlation between octahedral Mg^{2+} and total Fe content of the clinopyroxenes in atoms per formula unit (based on 6 oxygens).

Figure 5.12. Plot of log fO_2 versus $D_F^{Cpx/melt}$ for the sample suites of this study. The oxygen fugacity spans nearly seven orders of magnitude from -14.7 to -7.3 log units. Within this interval, the ol-minette, aug-minette, and basaltic andesite samples show an increase in D_F with an increase in fO_2 (trend line). This may be due to an increase in the Fe^{3+} content of the crystals (see text). The latite samples show no correlation between D_F and fO_2. This may be due other dominant factors that control F incorporation into pyroxenes, like melt viscosity (see a later section of the text). FeO (see legend) is the average total iron content of the samples.

Figure 5.13. Literature data of $D_H^{Cpx/melt}$ vs. the Al content of pyroxenes. a) $D_F^{Cpx/melt}$ vs. Al_2O_3 content and b) $D_F^{Cpx/melt}$ vs. the tetrahedral Al component. The equations for the regression lines show a better fit between $D_F^{Cpx/melt}$ and Al^{IV}, indicating that this substitution mechanism favors Al^{3+} entering the tetrahedral sites. Data from previous studies: Aubaud et al. (2004), Hauri et al. (2006), Grant et al. (2007), Abaud et al. (2008), and Tenner et al. (2009).

Figure 5.14. Current data of $D_F^{Cpx/melt}$ vs. the Al content of pyroxenes. a) Al_2O_3 content of the Cpx phases from our study vs. $D_F^{Cpx/melt}$ and b) tetrahedral Al content of the Cpx phases from our study vs. $D_F^{Cpx/melt}$. Similar to the partitioning of H_2O into Cpx, F partitioning appears to be enhanced by increasing Al content.

Figure 5.15. Variations in melt viscosity with D_F, including both Cpx and olivine samples from this study. Graph shows a moderate trend of increasing D_F with increasing melt viscosity, particularly for the Cpx phases.

Figure 5.16. Plots of NBO/T vs. a) $D_F^{Cpx/melt}$ and b) $D_F^{Oliv/melt}$ for the Cpx and olivine samples from this study. The dashed line represents the approximate NBO/T value by inspection at which melt structure becomes a significant control on mineral/melt partitioning of F. Error bars are 1σ.

Table 5.1. Major element compositions of the starting materials for the experimental samples analyzed in this study.

Oxide	ol-Minette[a]	aug-Minette[b]	Basaltic Andesite[c]	Latite[d]
SiO2	49.13	53.59	55.25	59.17
TiO2	2.02	1.76	0.74	1.02
Al2O3	10.51	13.83	17.41	14.33
FeO	7.74	5.94	5.98	5.09
MgO	9.87	5.34	6.68	3.55
CaO	9.06	6.85	7.28	5.58
Na2O	2.06	3.33	3.97	2.54
K2O	4.86	6.27	1.18	5.55
P2O5	0.97	1.37	0.27	0.34
H2O+	2.36	0.34	0.61	2.38
Sum	98.58	98.62	99.57	99.55

a. Esperanca and Holloway (1987)
b. Righter and Carmichael (1996)
c. Moore and Carmichael (1998)
d. Esperanca and Holloway (1986)

Table 5.2. Experimental run conditions of the samples used in this study.

Sample Name	*T* (°C)	*P* (kb)	log fO_2	Average a_{H2O}	Analyzed Phases
Latite					
LIW-39	1060	9.7	-14.9	0.17	gl,cpx
LIW-37	1125	9.8	-12.9	0.17	gl,cpx
LIW-40	1085	10	-13.4	0.17	gl,cpx
LIW-51	1150	15	-12.4	0.17	gl,cpx
LOA-8	1150	15	-10.1	0.24	gl,cpx
LOA-13	1083	10.2	-10.8	0.39	gl,cpx
LOA-15	1070	6.5	-11	0.39	gl,cpx
LOA-18	1070	15	-11	0.39	gl,cpx
Ol-Minette					
MIW-6	1125	10	-12.9	0.19	gl,cpx,ol
MIW-12	1175	20	-12	0.19	gl,cpx
MIW-18	1150	10	-12.5	0.19	gl,cpx,ol
MIW-20	1135	15	-12.6	0.19	gl,cpx,ol
MIW-23	1125	17.4	-12.9	0.19	gl,cpx
MIW-26	1070	10	-13.8	0.19	gl,cpx
MOA-2	1150	10	-10	0.22	gl,cpx,ol
MOA-4	1125	10	-10.4	0.22	gl,cpx
Aug-Minette					
56B	1050	0.969	-7.25	~1.0	gl, cpx
Basaltic Andesite				1	
PEM22-1	1050	0.989	-7.8	1	gl,cpx,ol
PEM22-4	1075	1.055	-6.2	1	gl,ol
PEM22-5	1125	0.769	-6.4	1	gl,ol
PEM22-6	1075	0.607	-6.4	1	gl,ol,plag
PEM22-12	1050	2.082	-3.8	1	gl,ol
PEM22-17	1000	1.613	-9.5	1	gl,cpx
PEM22-18	1025	2.04	-8.3	1	gl,cpx,ol,plag
PEM22-19	1000	3.027	-9.5	1	gl,ol,hbd

Table 5.3. SIMS results ($^{19}F/^{18}O$) of the glass phases from the experimental sample suites of this study, including the percent relative standard deviation (% RSD).

Sample	Phase	n	$^{19}F/^{18}O$	1 σ	% RSD
LIW-39	glass	4	8.30	0.34	4
LIW-37	glass	3	7.58	0.10	1
LIW-40	glass	3	8.91	0.14	2
LIW-51	glass	2	8.27	0.06	1
LOA-8	glass	6	9.18	0.95	10
LOA-13	glass	7	10.56	0.83	8
LOA-15	glass	1	8.07	0.05	1
LOA-18	glass	3	9.96	0.56	6
MIW-6	glass	4	14.38	0.58	4
MIW-12	glass	4	17.65	0.46	3
MIW-18	glass	5	17.67	1.03	6
MIW-20	glass	7	18.82	0.42	2
MIW-23	glass	4	14.59	0.49	3
MIW-26	glass	3	12.13	0.52	4
MOA-2	glass	15	23.14	1.98	9
MOA-4	glass	6	13.46	1.24	9
56B	glass	7	11.30	2.16	19
PEM22-1	glass	2	2.00	0.001	0.07
PEM22-4	glass	2	1.67	0.08	5
PEM22-5	glass	2	1.99	0.10	5
PEM22-6	glass	1	1.81	0.01	0.4
PEM22-12	glass	2	1.24	0.03	3
PEM22-17	glass	3	1.70	0.04	2
PEM22-18	glass	8	1.56	0.07	5
PEM22-19	glass	1	1.20	0.04	3

Table 5.4. Experimental conditions during synthesis of the Fba glasses, their $^{19}F^{-}/^{18}O^{-}$ ratios from SIMS, and their F concentration values from EPMA. The $^{19}F^{-}/^{18}O^{-}$ and F content for the standards Biotite-3 and a silica blank are shown as well.

Sample	Starting Material	Dopant	Fusing *T* (°C)	Time at fusing *T* (min)	fO_2	SIMS $^{19}F^{-}/^{18}O^{-}$	1σ	F (ppm)	1σ
Fba-1	Tholeite	CaF_2	1470	30	NNO	17.52	1.84	1323	481
Fba-2	Tholeite	CaF_2	1470	30	NNO	67.90	1.15	5297	1090
Fba-3	Tholeite	CaF_2	1470	30	NNO	102.12	2.50	8651	1035
Fba-4	Tholeite	CaF_2	1470	30	NNO	152.82	4.08	14063	1068
Fba-5	Tholeite	CaF_2	1430	30	NNO	231.23	4.58	22400	1234
Bt-3	--	--	--	--	--	340.14	14.05	33700	1900
Blank	--	--	--	--	--	0.0069	0.00	0	0

Table 5.5. Average of SIMS and EPMA data from this study and the literature, including calculated mg# and F partition coefficients.

Sample	Phase	SiO_2	TiO_2	Al_2O_3	FeO	MgO	CaO	Na_2O	K_2O	P_2O_5	Sum	mg#	n	$^{19}F/^{18}O$	1 σ	F (ppm)	1 σ	D_F	1 σ
[a]LIW-39	glass	62.0	1.2	17.5	5.0	2.6	4.3	2.1	5.1	0.3	93.6	0.48	4	8.30	0.34	802	47	--	--
	cpx	51.8	0.4	2.8	7.6	14.0	22.2	0.9	0.0	na	99.8	0.77	1	1.82	0.01	176	4	0.22	0.02
LIW-37	glass	60.0	1.1	16.1	5.3	3.3	5.4	2.7	6.2	na	93.4	0.53	3	7.58	0.10	733	22	--	--
	cpx	53.6	0.4	1.4	5.9	17.4	20.5	0.3	0.0	na	99.6	0.84	1	1.04	0.01	101	3	0.14	0.01
LIW-40	glass	62.0	1.2	17.1	5.1	2.0	4.1	2.5	5.7	0.3	91.2	0.42	3	8.91	0.14	862	28	--	--
	cpx	52.8	0.6	2.3	6.9	16.2	20.8	0.4	0.0	na	100.0	0.81	3	1.56	0.41	150	42	0.17	0.05
LIW-51	glass	60.5	1.1	16.6	5.4	3.2	5.7	2.2	5.5	0.2	91.3	0.51	2	8.27	0.06	800	19	--	--
	cpx	52.0	0.7	3.1	6.8	15.7	20.2	0.6	0.0	na	99.1	0.80	2	1.02	0.15	98	17	0.12	0.02
[a]LOA-8	glass	62.8	1.0	16.6	5.2	2.1	4.3	2.2	5.8	na	92.5	0.42	6	9.18	0.95	888	108	--	--
	cpx	51.6	0.4	2.6	8.3	15.1	20.3	0.6	0.1	na	99.3	0.77	6	2.25	0.18	218	21	0.25	0.04
LOA-13	glass	66.6	1.1	16.4	4.3	2.5	4.3	0.8	3.9	na	88.0	0.51	7	10.56	0.83	1021	98	--	--
	cpx	51.9	0.4	1.9	7.0	14.9	22.9	0.6	0.0	na	99.4	0.77	7	2.18	0.43	211	45	0.21	0.04
LOA-15	glass	64.2	1.0	16.7	5.1	2.0	4.9	0.8	4.8	na	91.4	0.41	1	8.07	0.05	780	18	--	--
	cpx	51.5	0.4	2.7	8.3	13.6	22.6	0.8	0.0	na	99.9	0.74	4	2.29	0.15	221	18	0.28	0.06
LOA-18	glass	62.5	1.2	15.8	5.0	2.8	5.3	1.5	5.6	na	92.3	0.50	3	9.96	0.56	963	70	--	--
	cpx	53.0	0.4	1.9	7.6	16.6	19.7	0.5	0.0	na	99.7	0.80	9	0.72	0.16	70	17	0.07	0.02
[a]MIW-6	glass	52.5	2.5	14.5	9.9	5.1	7.0	2.6	5.7	na	92.6	0.48	4	14.38	0.58	1391	80	--	--
	cpx	54.1	0.5	1.0	3.5	17.5	23.1	0.5	0.0	na	100.2	0.90	4	1.40	0.18	135	19	0.10	0.01
	olivine	38.9	0.0	0.0	16.1	42.3	0.3	0.1	0.0	na	97.8	0.82	1	0.14	0.00	13	0	0.01	0.00
MIW-12	glass	47.5	2.5	11.2	16.8	7.2	8.2	1.7	4.7	na	92.7	0.43	4	17.65	0.46	1707	74	--	--
	cpx	53.8	0.5	1.0	3.8	17.8	22.3	0.5	0.0	na	99.7	0.89	9	1.47	0.68	142	69	0.08	0.04
MIW-18	glass	51.1	2.5	11.1	8.1	8.9	9.8	2.3	5.2	1.1	96.4	0.66	5	17.67	1.03	1708	129	--	--
	cpx	53.7	0.7	0.9	4.0	17.0	22.9	0.3	0.0	na	99.5	0.88	11	1.59	0.36	154	38	0.09	0.02
	olivine	39.1	0.0	0.0	15.8	43.0	0.2	0.1	0.0	na	98.3	0.83	5	0.86	0.47	83	47	0.05	0.01
MIW-20	glass	50.5	2.8	13.2	8.8	7.1	7.7	2.6	6.2	1.3	93.6	0.59	7	18.82	0.42	1820	72	--	--
	cpx	53.7	0.5	1.1	4.3	18.1	21.6	0.4	0.0	na	99.6	0.88	9	0.84	0.23	81	23	0.04	0.01
	olivine	39.3	0.0	0.0	15.3	43.5	0.2	0.1	0.0	na	98.4	0.83	2	0.32	0.26	31	26	0.02	0.01
MIW-23	glass	52.5	2.7	13.8	9.5	6.5	6.7	1.9	4.9	1.5	94.7	0.55	4	14.59	0.49	1411	72	--	--
	cpx	53.2	0.6	1.1	4.4	17.2	22.3	0.4	0.0	na	99.2	0.88	9	1.21	0.30	117	31	0.08	0.02
MIW-26	glass	53.2	2.3	14.9	9.3	5.1	6.1	2.3	5.1	1.7	99.0	0.49	3	12.13	0.52	1173	70	--	--
	cpx	53.3	0.6	0.8	4.2	17.0	23.2	0.4	0.0	na	99.5	0.88	4	1.03	0.14	99	15	0.08	0.01
[a]MOA-2	glass	53.3	3.1	16.0	8.4	5.1	6.1	1.7	6.1	na	93.8	0.52	15	23.14	1.98	2237	230	--	--
	cpx	53.8	0.5	0.9	4.0	17.6	22.4	0.4	0.0	na	99.7	0.89	14	1.45	0.24	140	26	0.06	0.01
	olivine	38.6	0.0	0.0	17.3	42.6	0.3	0.0	0.0	na	99.0	0.81	4	0.99	0.24	96	25	0.04	0.00
MOA-4	glass	55.0	2.3	13.6	8.0	7.6	9.4	0.7	3.3	na	92.6	0.63	6	13.46	1.24	1302	142	--	--
	cpx	53.3	0.5	0.9	3.8	17.3	22.5	0.3	0.0	na	98.6	0.89	7	1.18	0.46	114	46	0.09	0.04

Table 5.5 Continued. Average of SIMS and EPMA data from this study and the literature, including calculated mg# and F partition coefficients.

Sample	Phase	SiO_2	TiO_2	Al_2O_3	FeO	MgO	CaO	Na_2O	K_2O	P_2O_5	Sum	mg#	n	$^{19}F/^{18}O$	1 σ	F (ppm)	1 σ	D_F	1 σ
[b]56B	glass	58.8	1.1	16.0	3.0	1.4	2.5	3.9	7.1	na	96.9	0.45	7	11.30	2.16	1092	227	--	--
	cpx	53.7	0.7	1.4	4.7	17.0	22.3	0.3	0.0	na	100.3	0.87	15	1.50	0.31	145	32	0.13	0.03
[b]PEM22-1	glass	56.1	0.9	17.0	5.0	3.1	5.4	5.1	1.8	na	97.9	0.52	2	2.00	0.001	193	3	--	--
	cpx	50.6	0.9	5.1	7.5	15.1	21.4	0.3	0.0	na	101.0	0.78	6	0.42	0.14	41	14	0.21	0.07
	olivine	39.5	0.0	0.0	16.3	45.7	0.1	na	0.0	na	101.5	0.83	10	0.25	0.05	25	5	0.13	0.03
PEM22-4	glass	na	na	na	na	na	na	na	na	na	na	na	2	1.67	0.08	161	10	--	--
	olivine	40.6	0.0	0.0	11.2	47.7	0.2	na	0.0	na	99.7	0.88	9	0.26	0.09	26	9	0.16	0.05
PEM22-5	glass	na	na	na	na	na	na	na	na	na	na	na	2	1.99	0.10	192	13	--	--
	olivine	40.4	0.0	0.0	10.8	48.0	0.2	na	0.0	na	99.4	0.89	7	0.26	0.08	25	8	0.13	0.04
PEM22-6	glass	58.5	0.9	16.9	5.0	2.8	5.4	2.2	1.7	na	95.9	0.50	1	1.81	0.01	175	4	--	--
	olivine	39.9	0.0	0.0	15.3	44.1	0.2	na	0.0	na	99.6	0.84	4	0.24	0.09	23	10	0.13	0.05
	plag	51.4	0.1	29.9	0.9	0.1	13.0	3.9	0.2	na	99.4	0.64[c]	4	0.15	0.02	14	3	0.08	0.01
PEM22-12	glass	51.8	0.6	17.5	4.5	5.2	6.4	3.1	1.3	na	95.5	0.68	2	1.24	0.03	119	5	--	--
	olivine	41.5	0.0	0.1	3.7	53.9	0.2	na	0.0	na	99.5	0.96	1	0.17	0.00	17	1	0.14	0.01
PEM22-17	glass	55.7	0.8	17.4	3.3	3.1	5.6	4.2	1.5	na	96.2	0.63	3	1.70	0.04	165	7	--	--
	cpx	50.1	0.8	4.2	6.9	15.4	21.5	0.4	0.0	na	99.4	0.80	5	0.30	0.12	29	13	0.17	0.07
PEM22-18	glass	53.2	1.0	17.6	4.9	3.3	6.5	3.9	1.2	na	96.5	0.55	8	1.56	0.07	151	9	--	--
	cpx	50.5	0.7	4.2	6.1	15.4	22.0	0.3	na	na	100.2	0.82	4	0.29	0.02	28	3	0.19	0.02
	olivine	40.1	0.0	0.8	15.6	42.4	0.4	0.1	0.0	na	99.4	0.83	11	0.22	0.05	22	5	0.14	0.03
	plag	47.2	0.1	32.6	0.8	0.2	16.4	2.1	0.1	na	99.5	0.81[c]	1	0.10	0.01	9	1	0.06	0.01
PEM22-19	glass	53.0	0.5	16.7	4.8	3.4	5.2	3.8	1.3	na	95.0	0.56	1	1.20	0.04	116	6	--	--
	olivine	39.4	0.0	0.0	15.8	43.8	na	na	0.0	na	99.3	0.83	7	0.17	0.07	17	7	0.14	0.06
	hbd	42.9	1.5	12.2	9.1	16.2	11.0	2.4	0.4	na	95.7	0.76	1	4.35	0.08	421	15	3.63	0.36

a. Major element data for mineral phases of samples LIW, LOA, MIW, and MOA were measured via EPMA this study. Major element data for all glass phases taken from their respective authors.
b. Major element data of the mineral phases and glasses for 56B and the PEM samples from the respective authors.
c. Anorthite content for plagioclase: [moles Ca/(moles Ca + moles Na)]
na = not analized

Figure 5.1

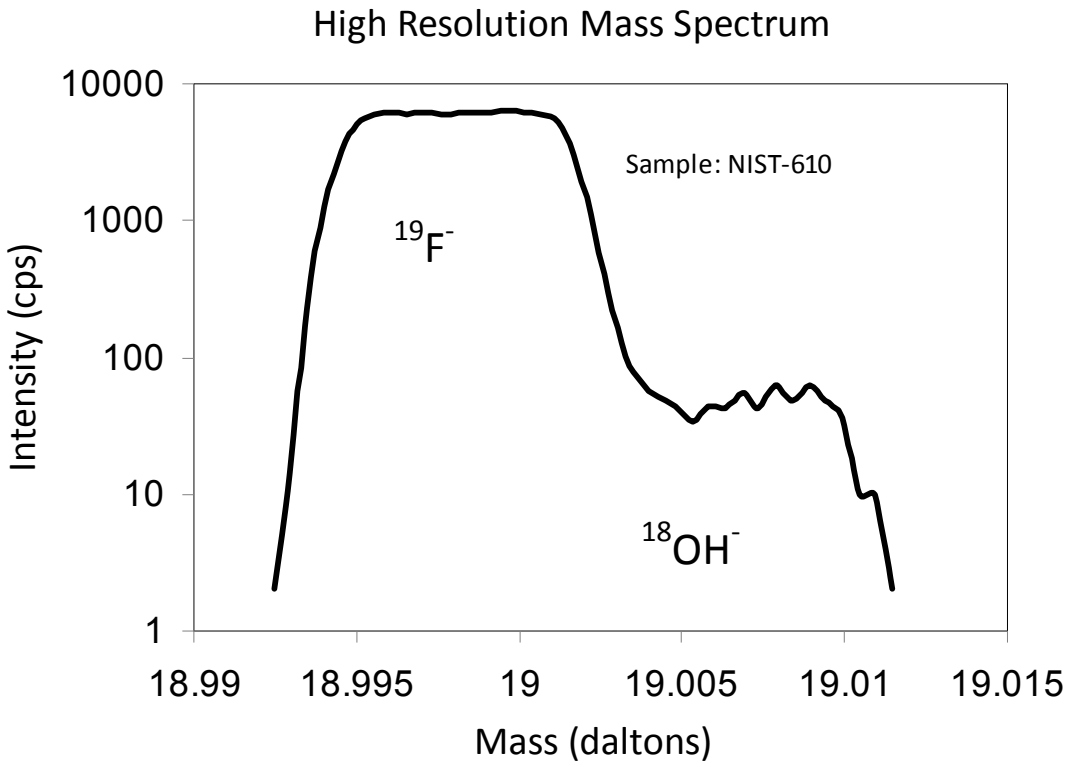
High Resolution Mass Spectrum
Intensity (cps)
10000
1000
100
10
1
Sample: NIST-610
$^{19}F^-$
$^{18}OH^-$
18.99
18.995
19
19.005
19.01
19.015
Mass (daltons)

Figure 5.2

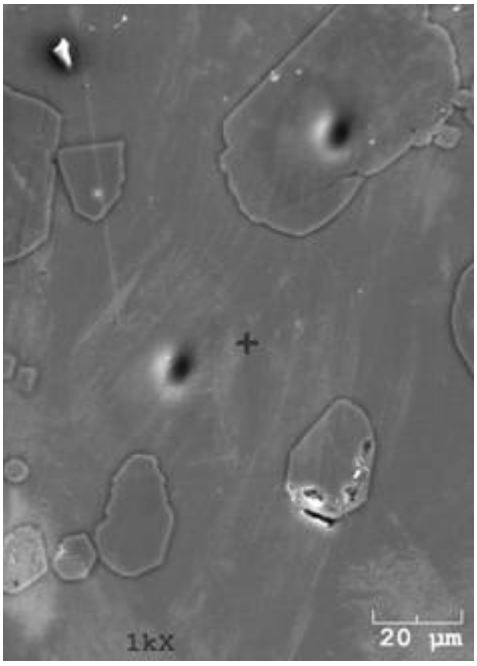

Figure 5.3

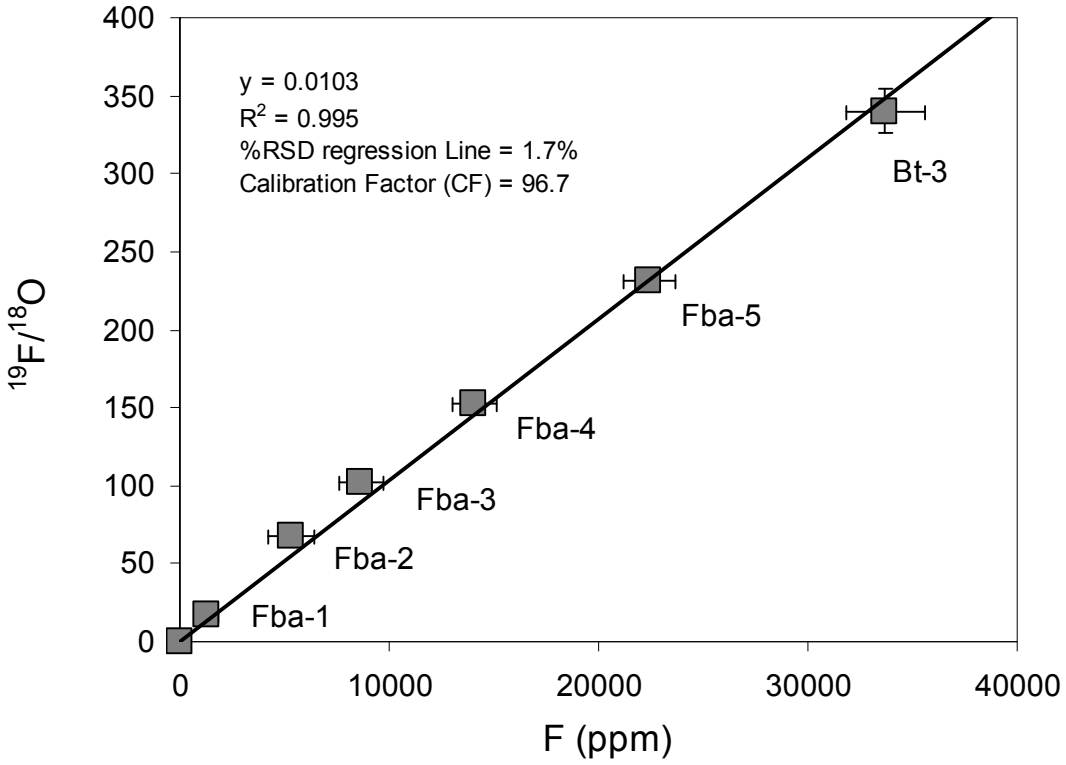
y = 0.0103
R2 = 0.995
%RSD regression Line = 1.7%
Calibration Factor (CF) = 96.7
Fba-1
Fba-2
Fba-3
Fba-4
Fba-5
Bt-3
19F/18O
F (ppm)
0
50
100
150
200
250
300
350
400
0
10000
20000
30000
40000

Figure 5.4 (a)

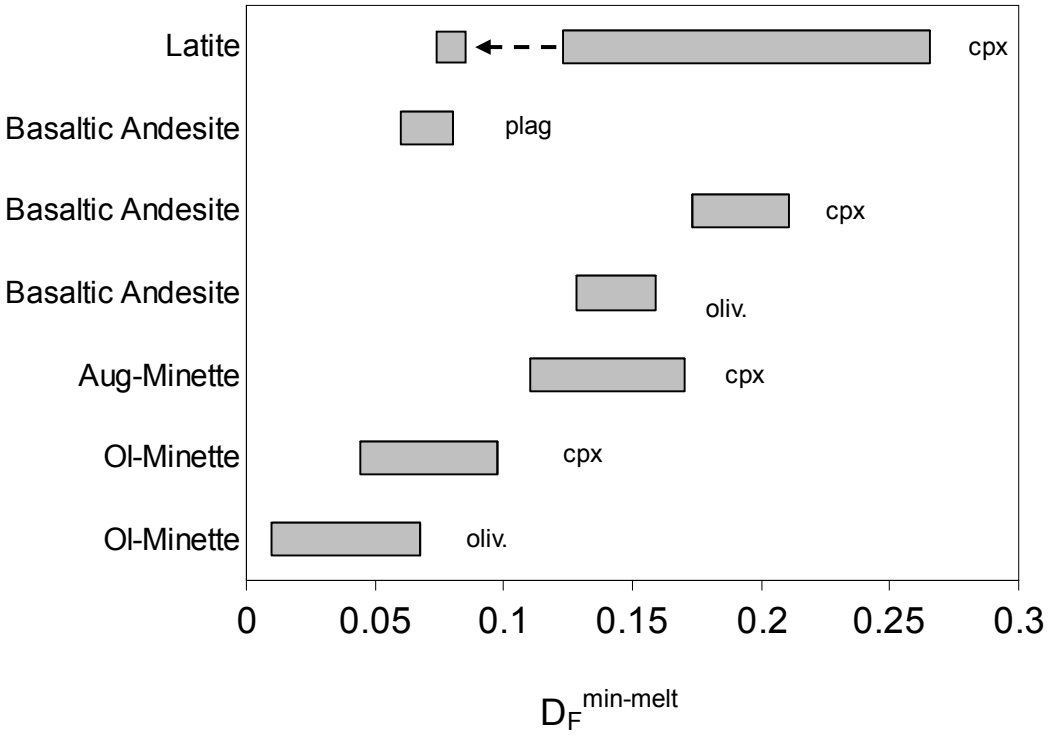
Latite
Basaltic Andesite
Basaltic Andesite
Basaltic Andesite
Aug-Minette
Ol-Minette
Ol-Minette
cpx
plag
cpx
oliv.
cpx
cpx
oliv.
0
0.05
0.1
0.15
0.2
0.25
0.3
$D_F^{min\text{-}melt}$

Figure 5.4 (b)

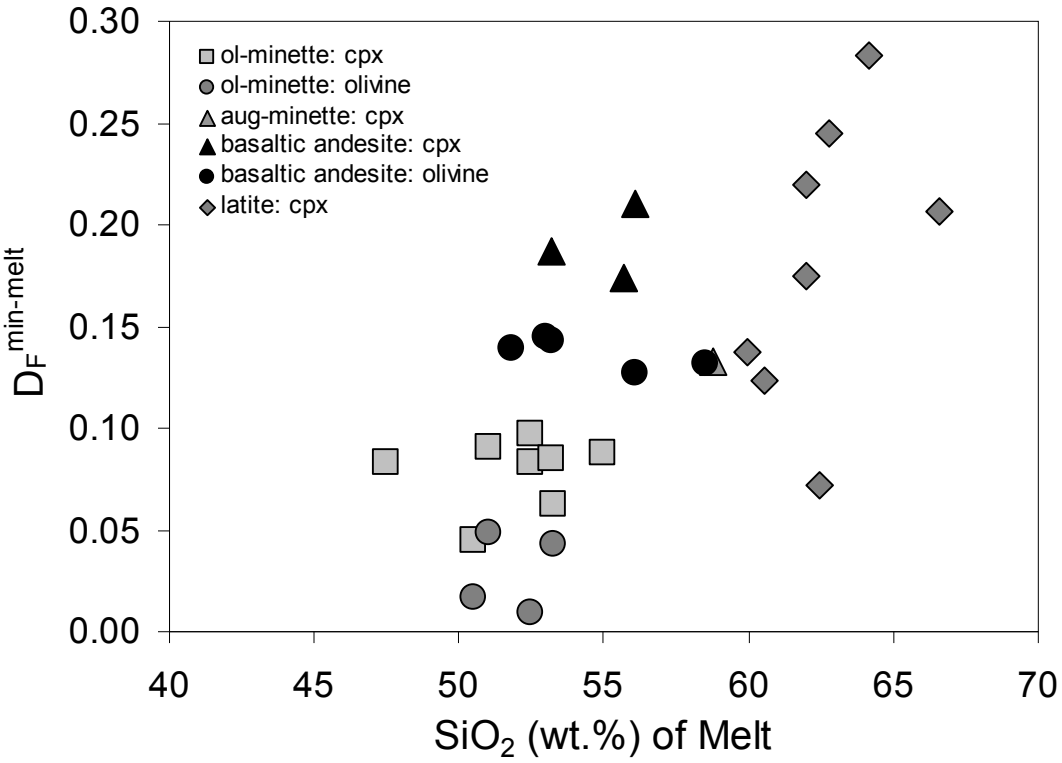
0.30
0.25
0.20
0.15
0.10
0.05
0.00
$D_F^{min\text{-}melt}$
ol-minette: cpx
ol-minette: olivine
aug-minette: cpx
basaltic andesite: cpx
basaltic andesite: olivine
latite: cpx
40
45
50
55
60
65
70
SiO_2 (wt.%) of Melt

Figure 5.5 (a)

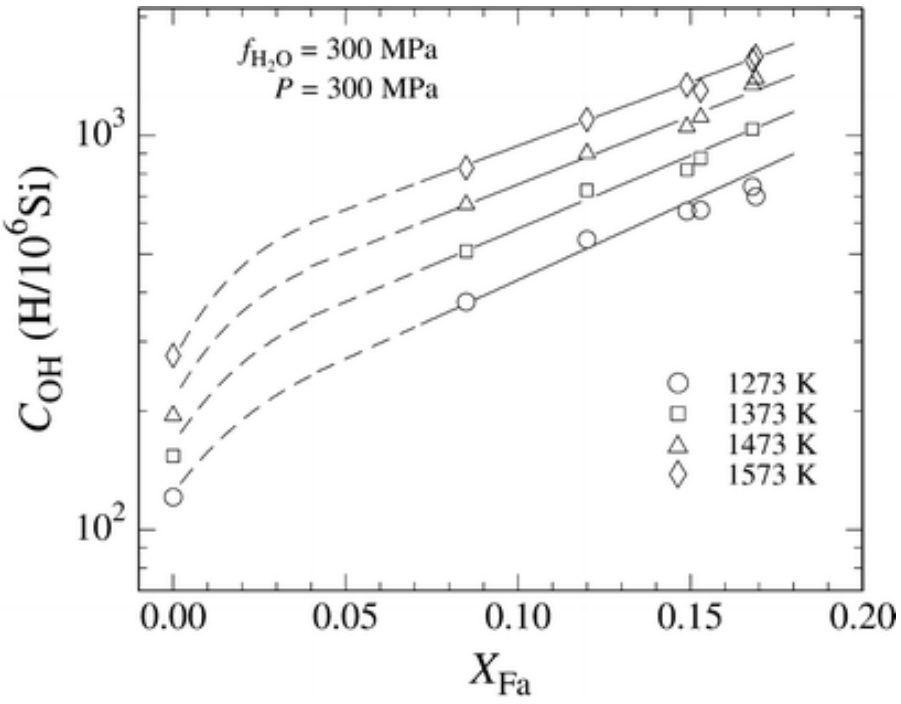
f_{H_2O} = 300 MPa
P = 300 MPa
10^3
10^2
C_{OH} (H/10^6Si)
1273 K
1373 K
1473 K
1573 K
0.00
0.05
0.10
0.15
0.20
X_{Fa}

Figure 5.5 (b)

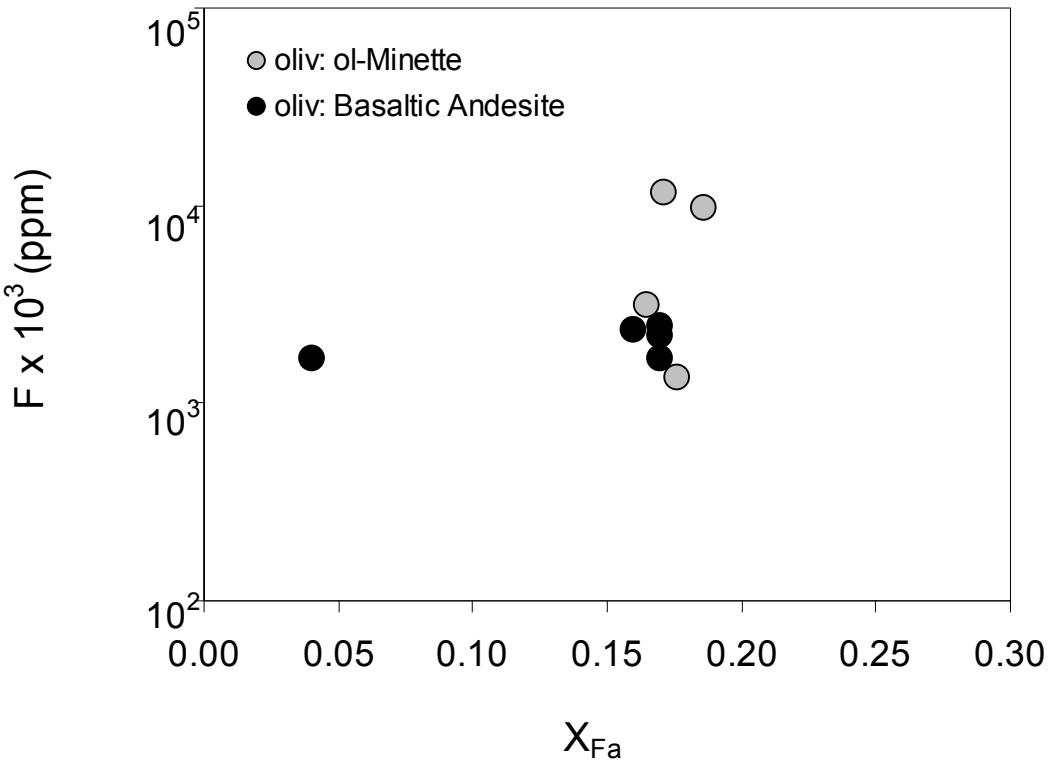
oliv: ol-Minette
oliv: Basaltic Andesite
F x 10^3 (ppm)
10^5
10^4
10^3
10^2
0.00
0.05
0.10
0.15
0.20
0.25
0.30
X_Fa

Figure 5.6

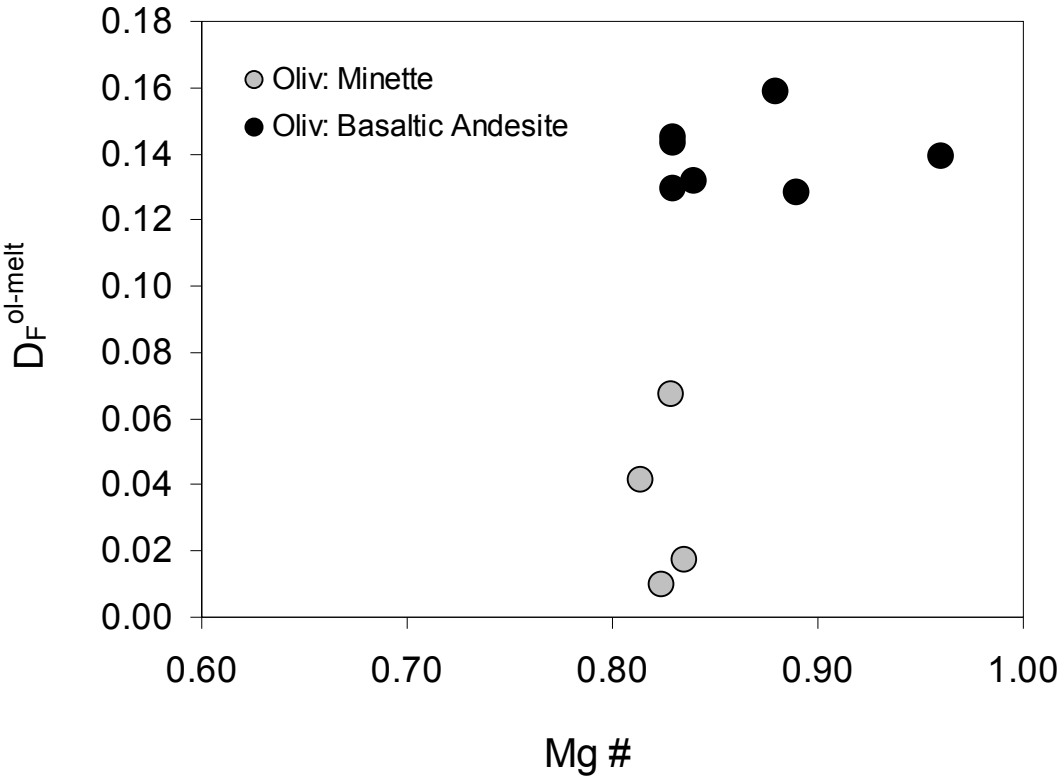
0.18
0.16
0.14
0.12
0.10
0.08
0.06
0.04
0.02
0.00
$D_F^{ol\text{-}melt}$
Oliv: Minette
Oliv: Basaltic Andesite
0.60
0.70
0.80
0.90
1.00
Mg #

Figure 5.7

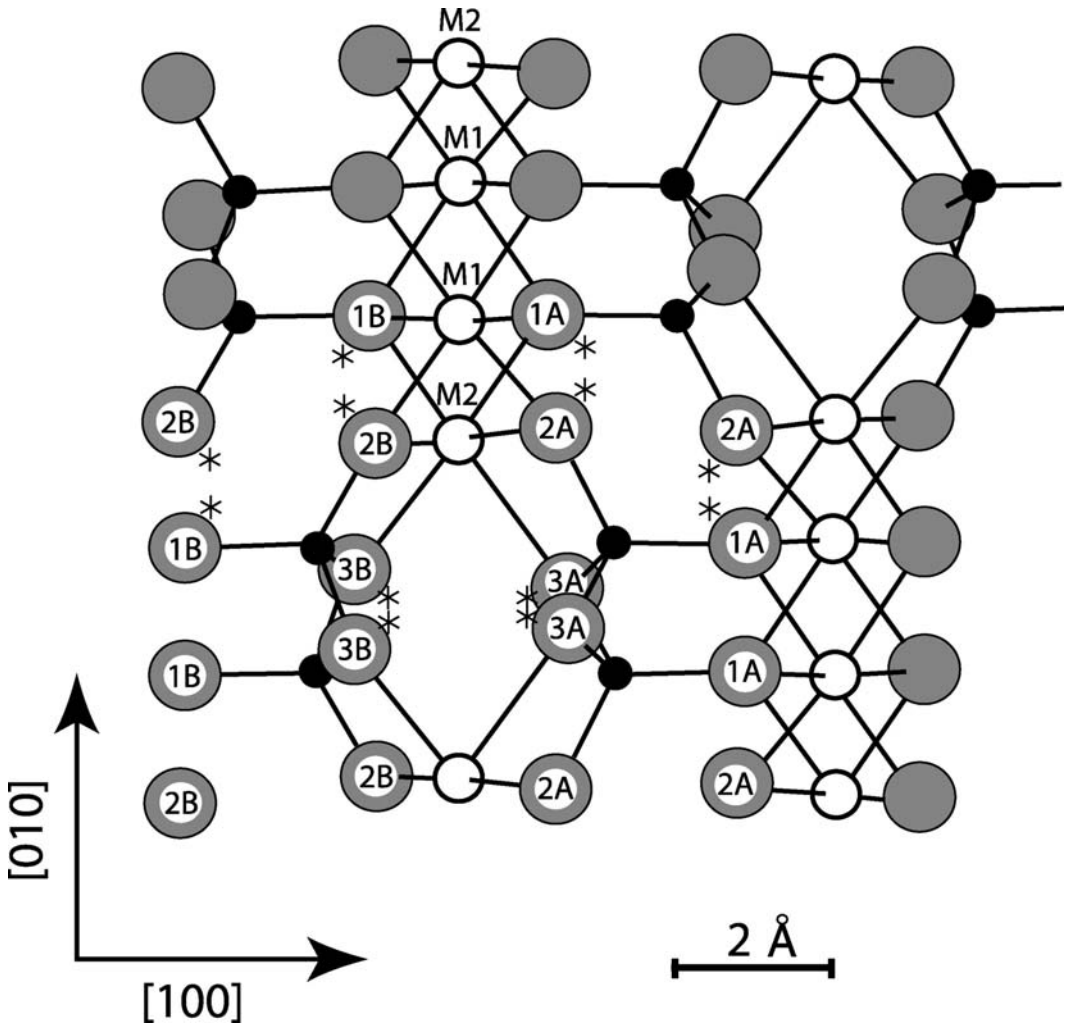
M2
M1
M1
1B
1A
M2
2B
2B
2A
2A
1B
3B
3A
1A
3B
3A
1B
1A
2B
2A
2A
2B
[010]
[100]
2 Å

Figure 5.8 (a)

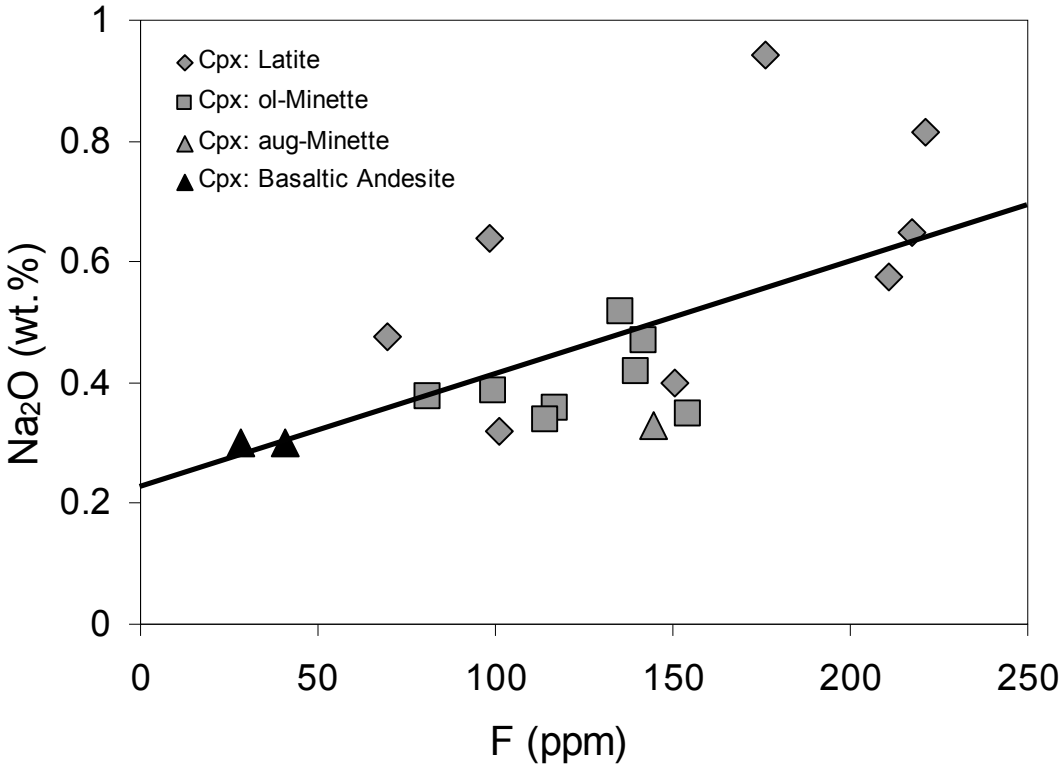
Cpx: Latite
Cpx: ol-Minette
Cpx: aug-Minette
Cpx: Basaltic Andesite
Na2O (wt.%)
F (ppm)
0
0.2
0.4
0.6
0.8
1
0
50
100
150
200
250

Figure 5.8 (b)

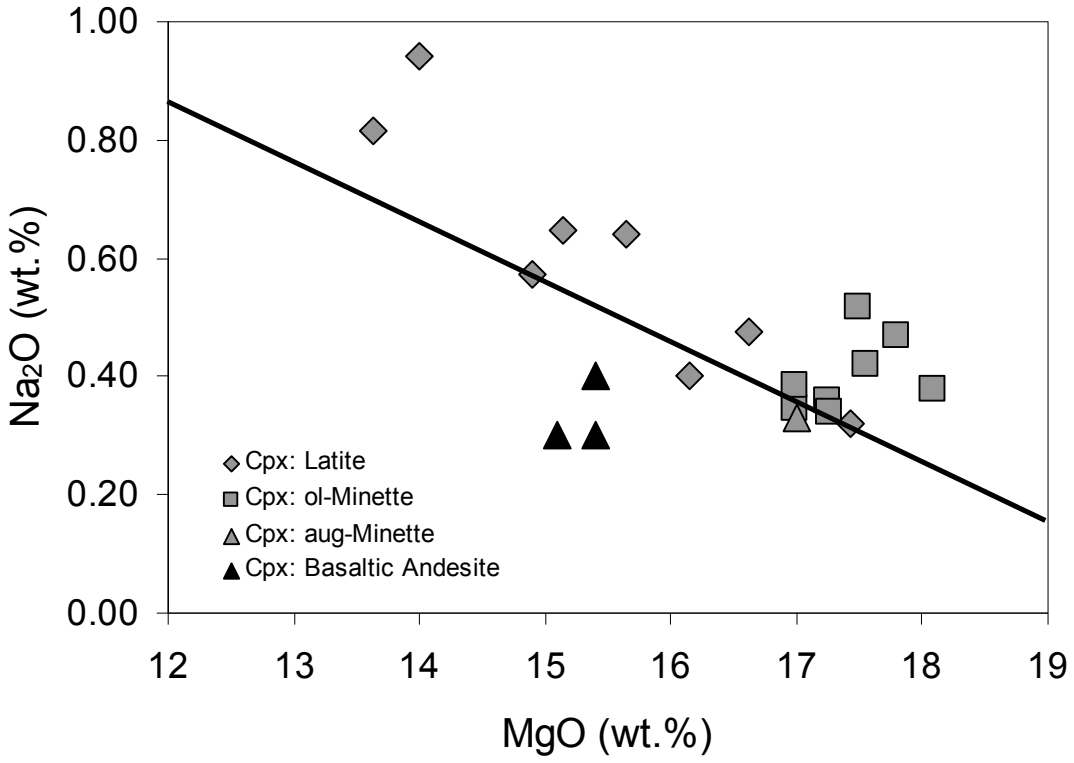
1.00
0.80
0.60
0.40
0.20
0.00
Na2O (wt.%)
12
13
14
15
16
17
18
19
MgO (wt.%)
Cpx: Latite
Cpx: ol-Minette
Cpx: aug-Minette
Cpx: Basaltic Andesite

Figure 5.8 (c)

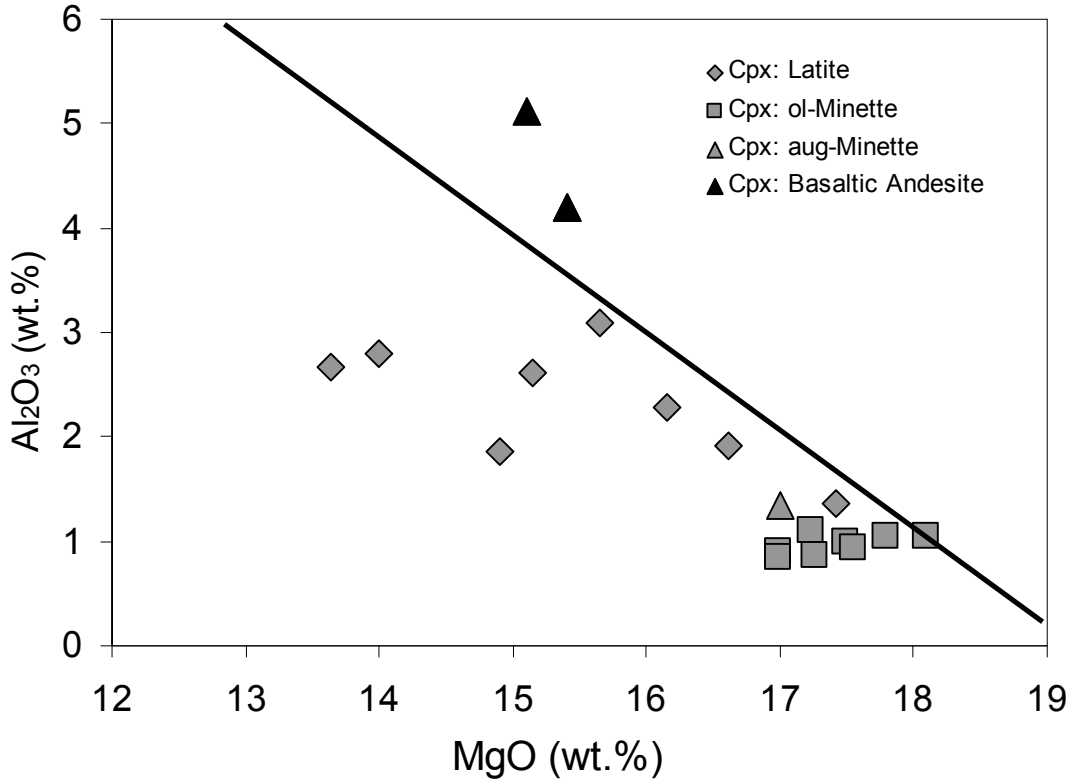
Cpx: Latite
Cpx: ol-Minette
Cpx: aug-Minette
Cpx: Basaltic Andesite
Al2O3 (wt.%)
MgO (wt.%)
0
1
2
3
4
5
6
12
13
14
15
16
17
18
19

Figure 5.9 (a)

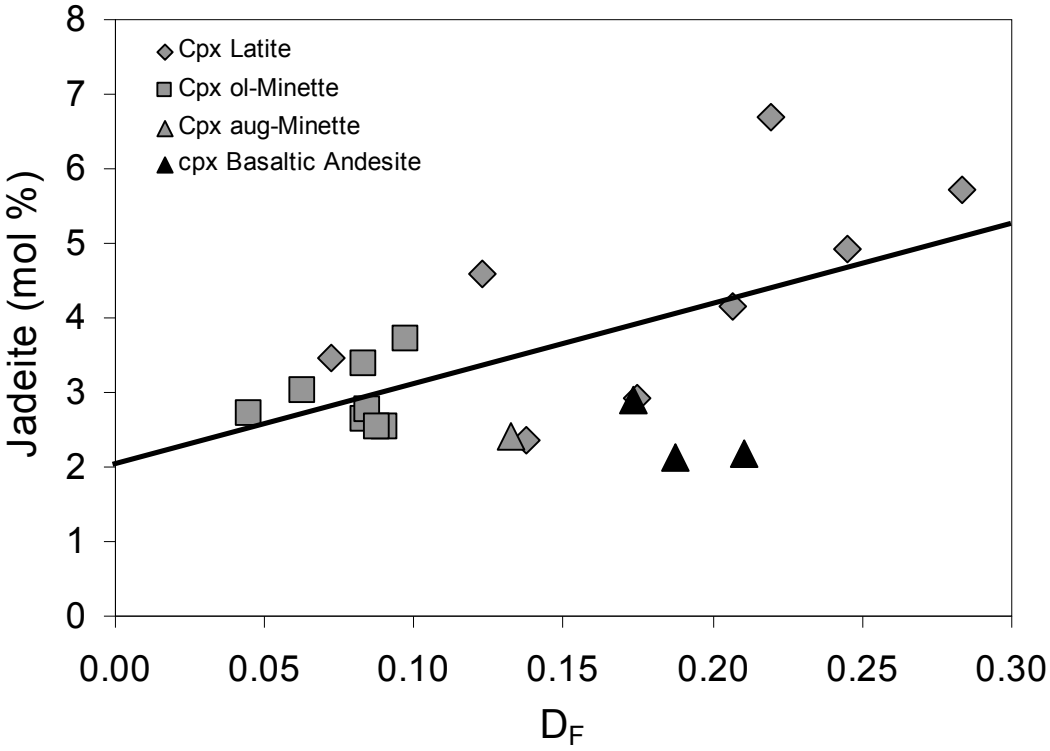
Cpx Latite
Cpx ol-Minette
Cpx aug-Minette
cpx Basaltic Andesite
Jadeite (mol %)
0
1
2
3
4
5
6
7
8
0.00
0.05
0.10
0.15
0.20
0.25
0.30
D_F

Figure 5.9 (b)

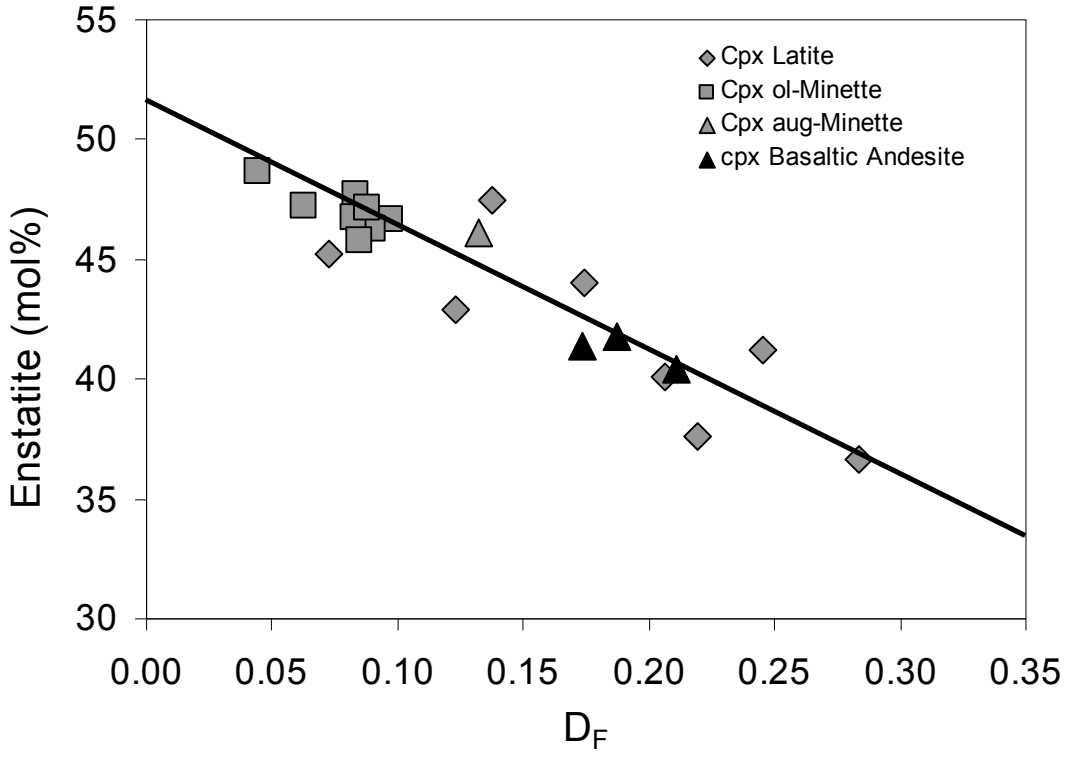
Cpx Latite
Cpx ol-Minette
Cpx aug-Minette
cpx Basaltic Andesite
Enstatite (mol%)
55
50
45
40
35
30
0.00
0.05
0.10
0.15
0.20
0.25
0.30
0.35
D_F

Figure 5.9 (c)

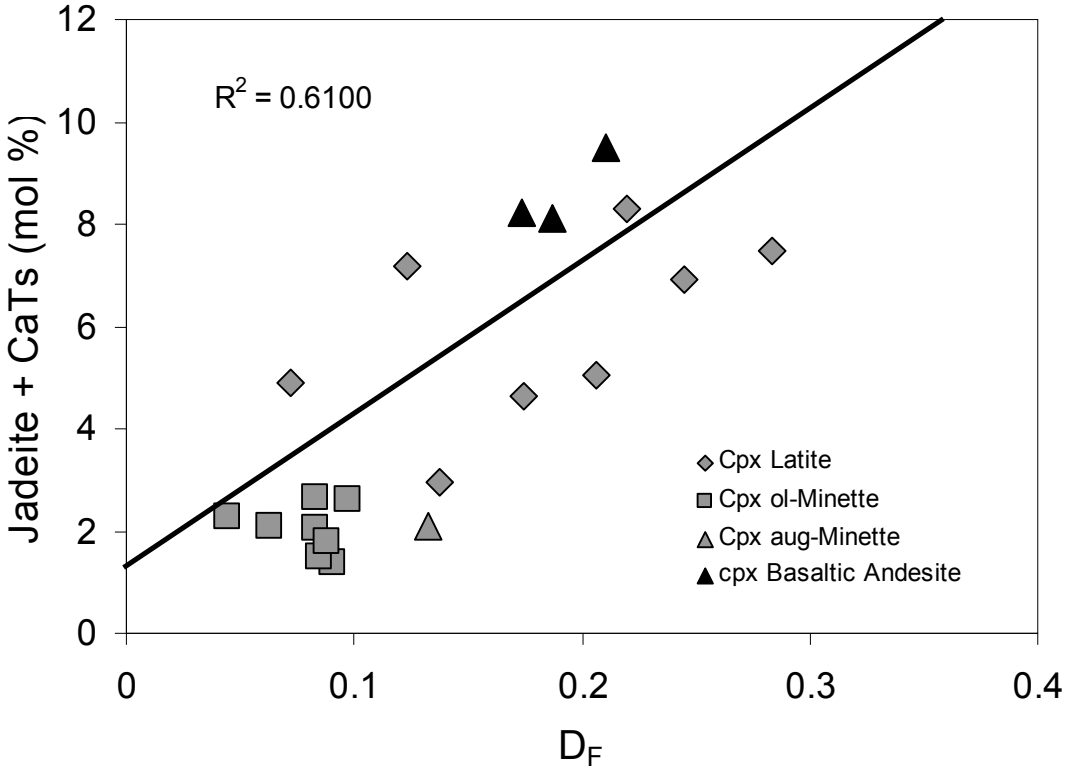
12
10
8
6
4
2
0
Jadeite + CaTs (mol %)
R2 = 0.6100
0
0.1
0.2
0.3
0.4
DF
Cpx Latite
Cpx ol-Minette
Cpx aug-Minette
cpx Basaltic Andesite

Figure 5.10 (a)

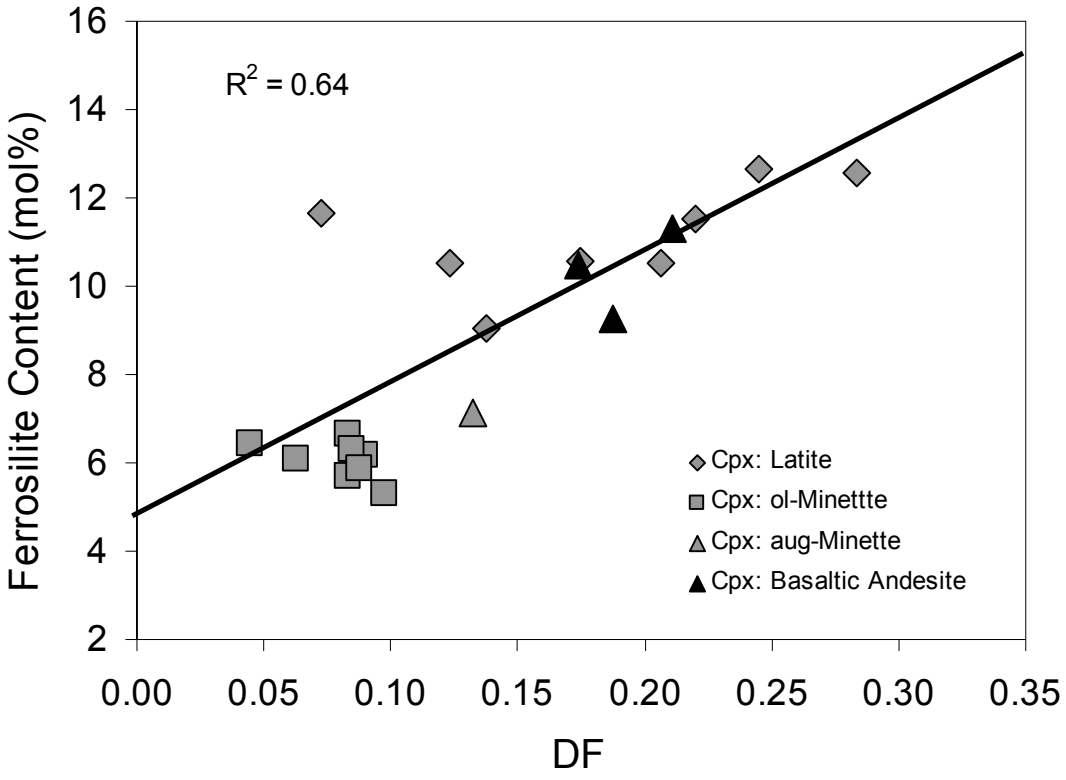
16
14
12
10
8
6
4
2
Ferrosilite Content (mol%)
R2 = 0.64
0.00
0.05
0.10
0.15
0.20
0.25
0.30
0.35
DF
Cpx: Latite
Cpx: ol-Minettte
Cpx: aug-Minette
Cpx: Basaltic Andesite

Figure 5.10 (b)

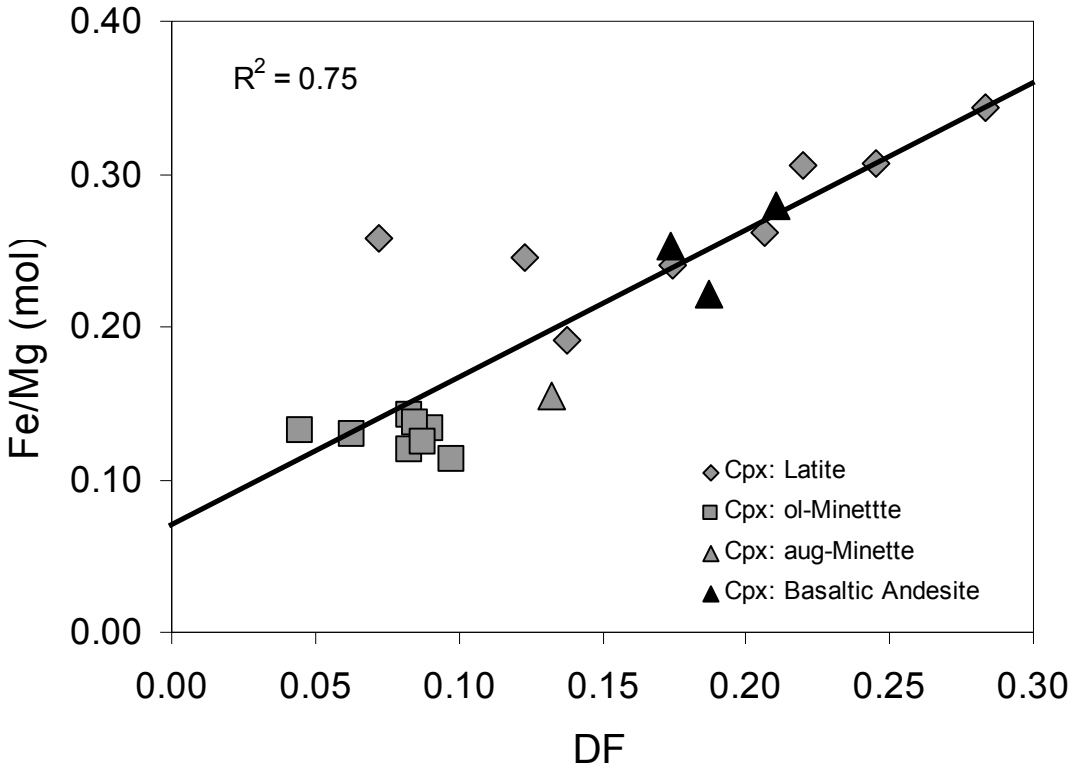
0.40
0.30
0.20
0.10
0.00
Fe/Mg (mol)
R2 = 0.75
0.00
0.05
0.10
0.15
0.20
0.25
0.30
DF
Cpx: Latite
Cpx: ol-Minettte
Cpx: aug-Minette
Cpx: Basaltic Andesite

Figure 5.11

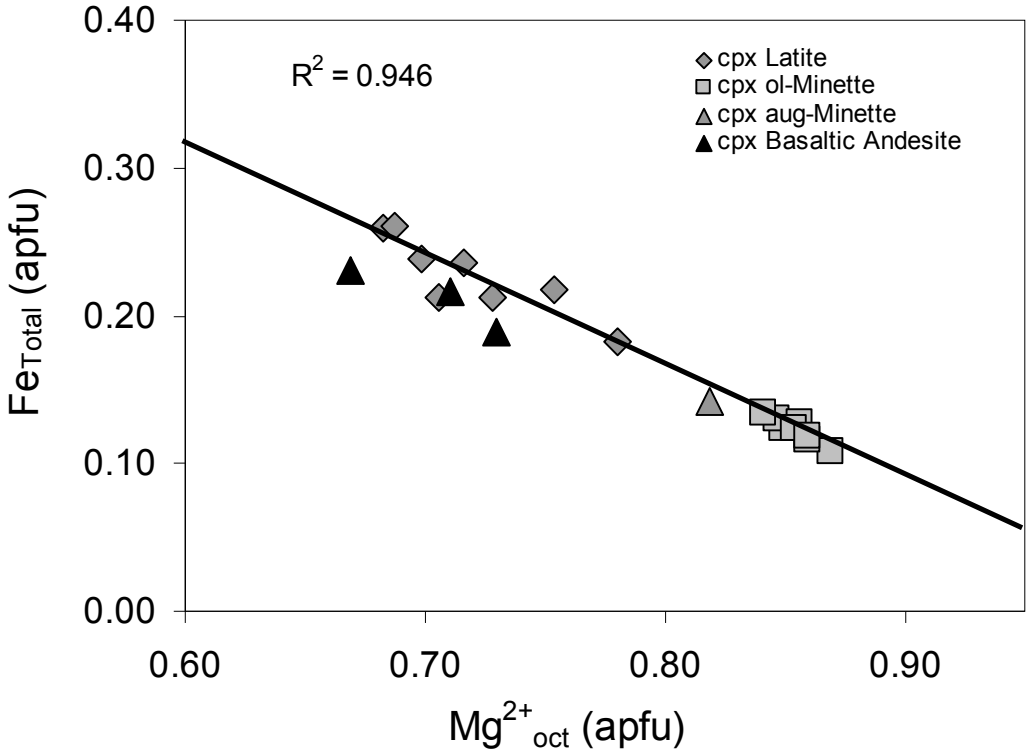
0.40
0.30
0.20
0.10
0.00
0.60
0.70
0.80
0.90
Fe_{Total} (apfu)
Mg^{2+}_{oct} (apfu)
R^2 = 0.946
cpx Latite
cpx ol-Minette
cpx aug-Minette
cpx Basaltic Andesite

Figure 5.12

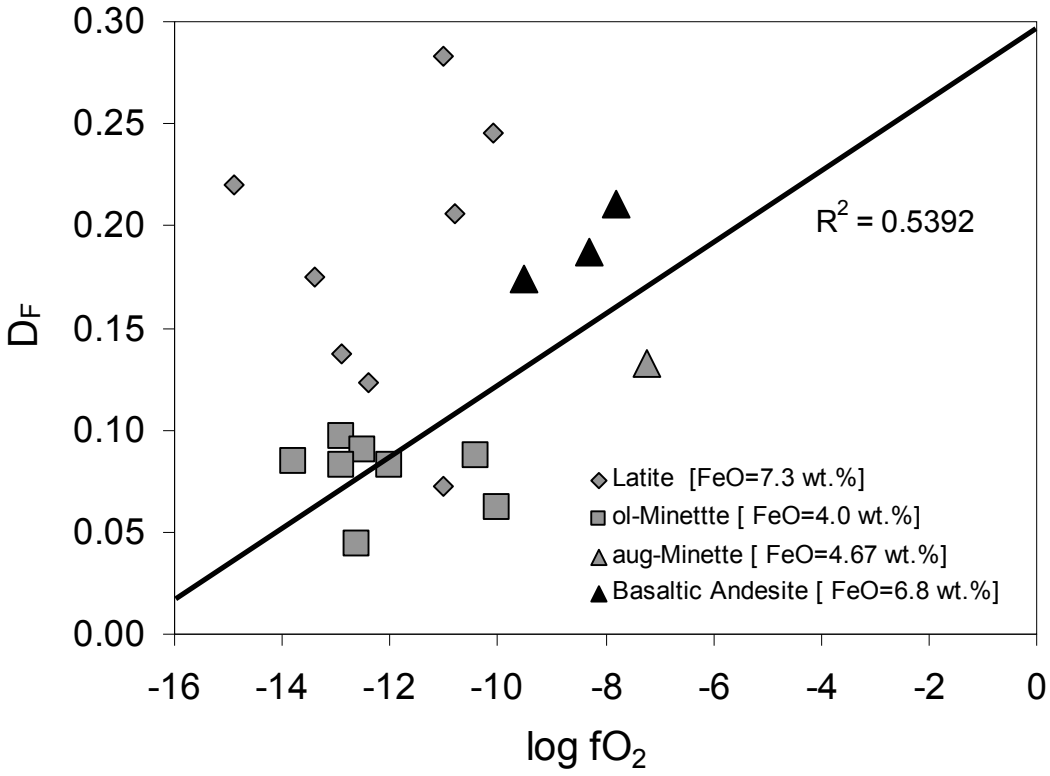
0.30
0.25
0.20
0.15
0.10
0.05
0.00
D_F
-16
-14
-12
-10
-8
-6
-4
-2
0
log fO_2
R^2 = 0.5392
Latite [FeO=7.3 wt.%]
ol-Minettte [FeO=4.0 wt.%]
aug-Minette [FeO=4.67 wt.%]
Basaltic Andesite [FeO=6.8 wt.%]

Figure 5.13 (a)

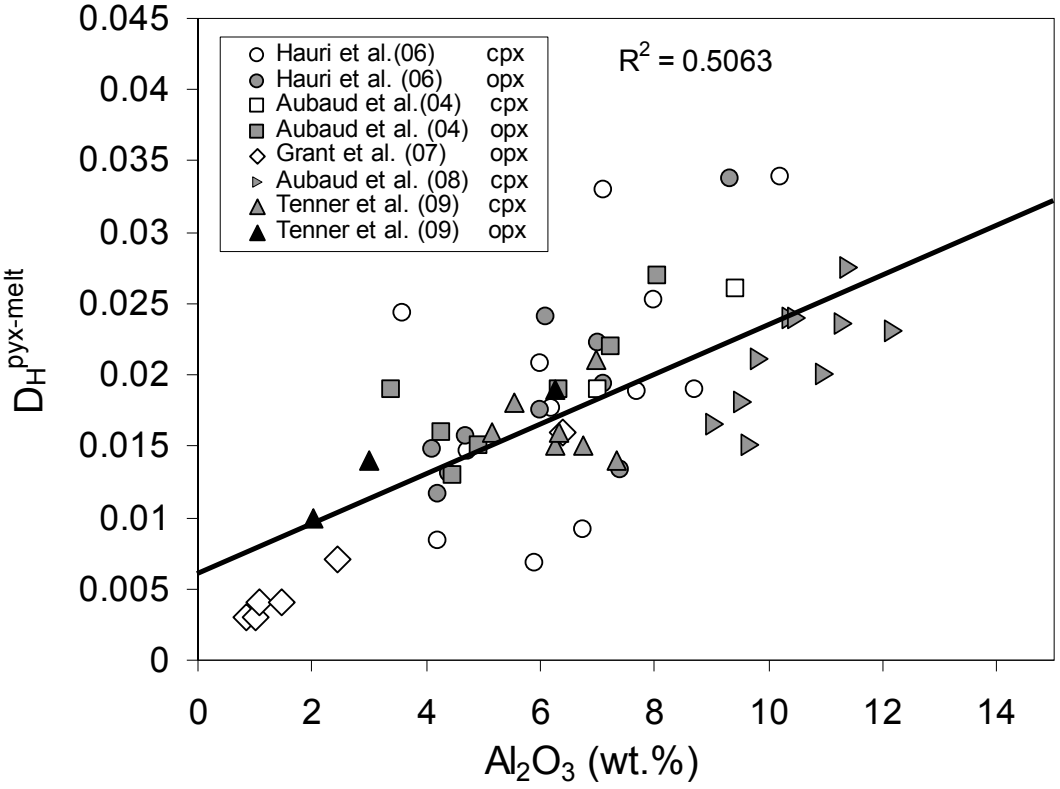
Hauri et al.(06) cpx
Hauri et al. (06) opx
Aubaud et al.(04) cpx
Aubaud et al. (04) opx
Grant et al. (07) opx
Aubaud et al. (08) cpx
Tenner et al. (09) cpx
Tenner et al. (09) opx
R2 = 0.5063
DHpyx-melt
Al2O3 (wt.%)
0.045
0.04
0.035
0.03
0.025
0.02
0.015
0.01
0.005
0
0
2
4
6
8
10
12
14

Figure 5.13 (b)

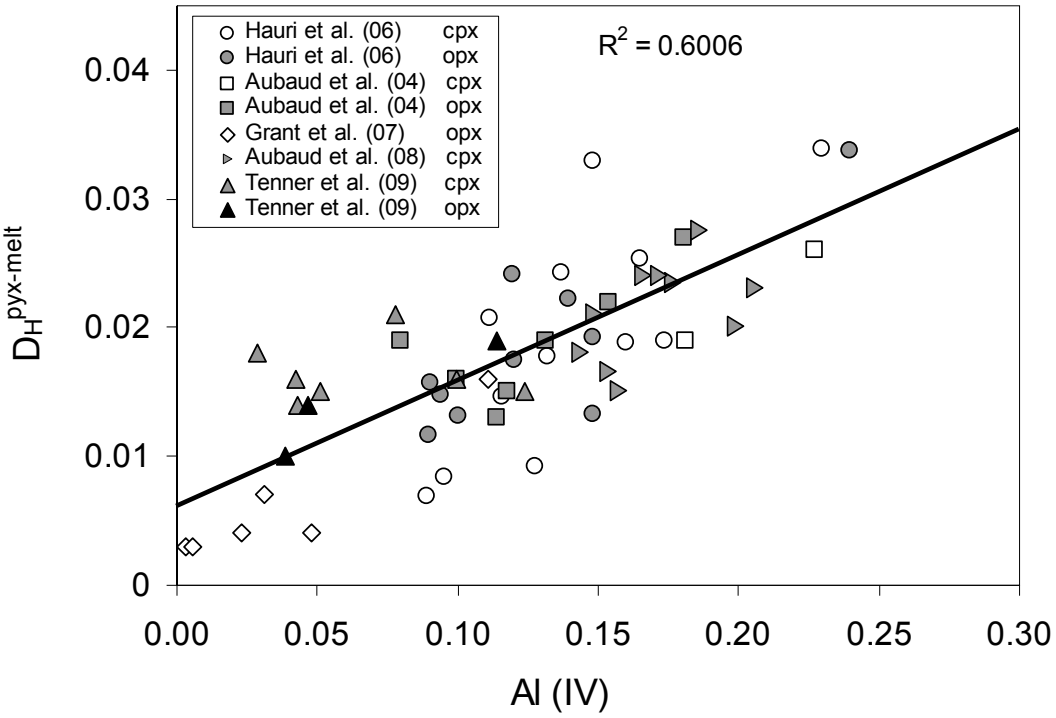
Hauri et al. (06) cpx
Hauri et al. (06) opx
Aubaud et al. (04) cpx
Aubaud et al. (04) opx
Grant et al. (07) opx
Aubaud et al. (08) cpx
Tenner et al. (09) cpx
Tenner et al. (09) opx
R2 = 0.6006
0.04
0.03
0.02
0.01
0
0.00
0.05
0.10
0.15
0.20
0.25
0.30
Al (IV)
DHpyx-melt

Figure 5.14 (a)

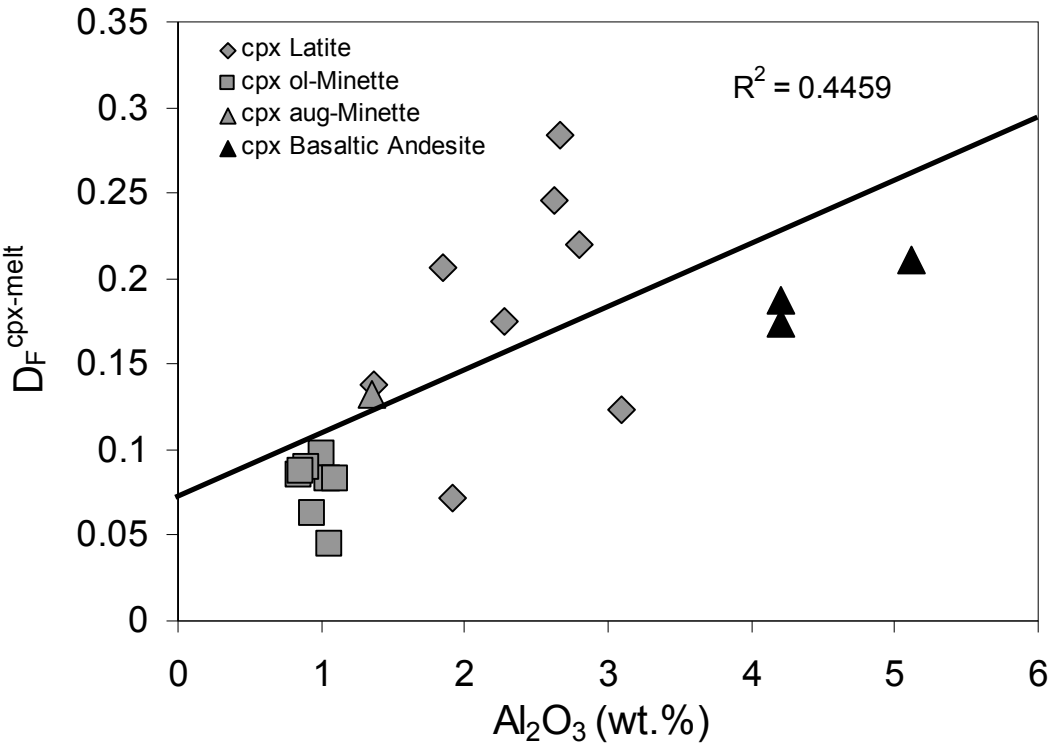
cpx Latite
cpx ol-Minette
cpx aug-Minette
cpx Basaltic Andesite
R2 = 0.4459
DFcpx-melt
Al2O3 (wt.%)
0.35
0.3
0.25
0.2
0.15
0.1
0.05
0
0
1
2
3
4
5
6

Figure 5.14 (b)

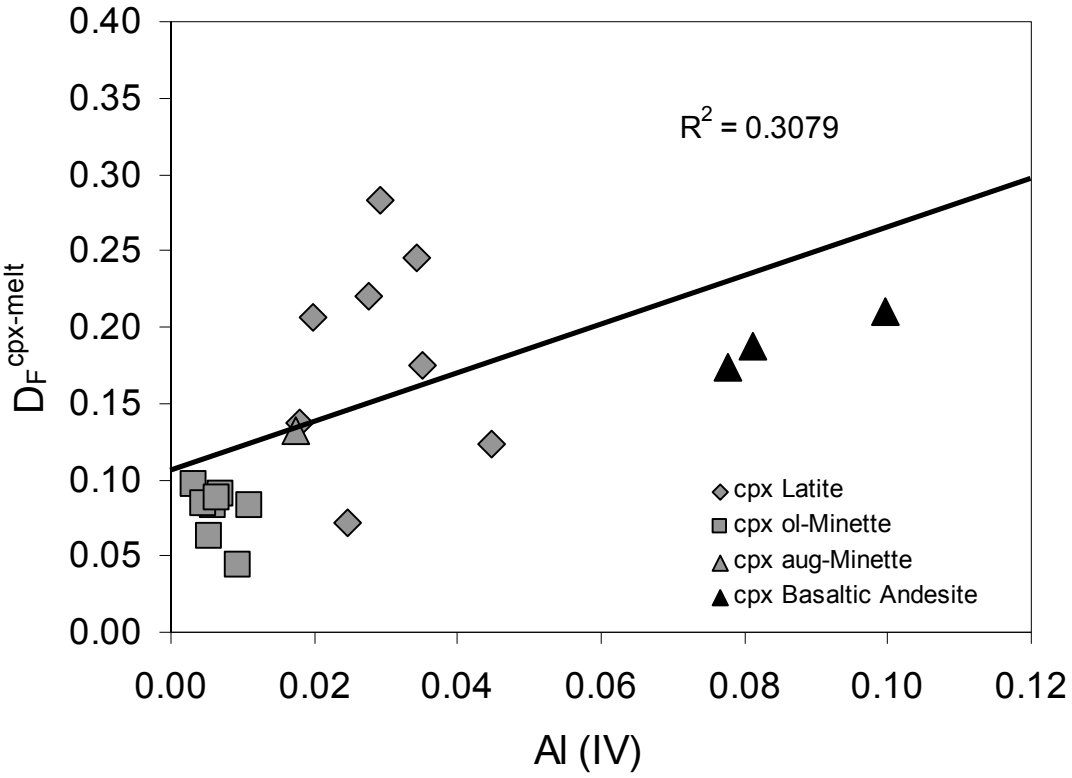
0.40
0.35
0.30
0.25
0.20
0.15
0.10
0.05
0.00
$D_F^{cpx\text{-}melt}$
R^2 = 0.3079
cpx Latite
cpx ol-Minette
cpx aug-Minette
cpx Basaltic Andesite
0.00
0.02
0.04
0.06
0.08
0.10
0.12
Al (IV)

Figure 5.15

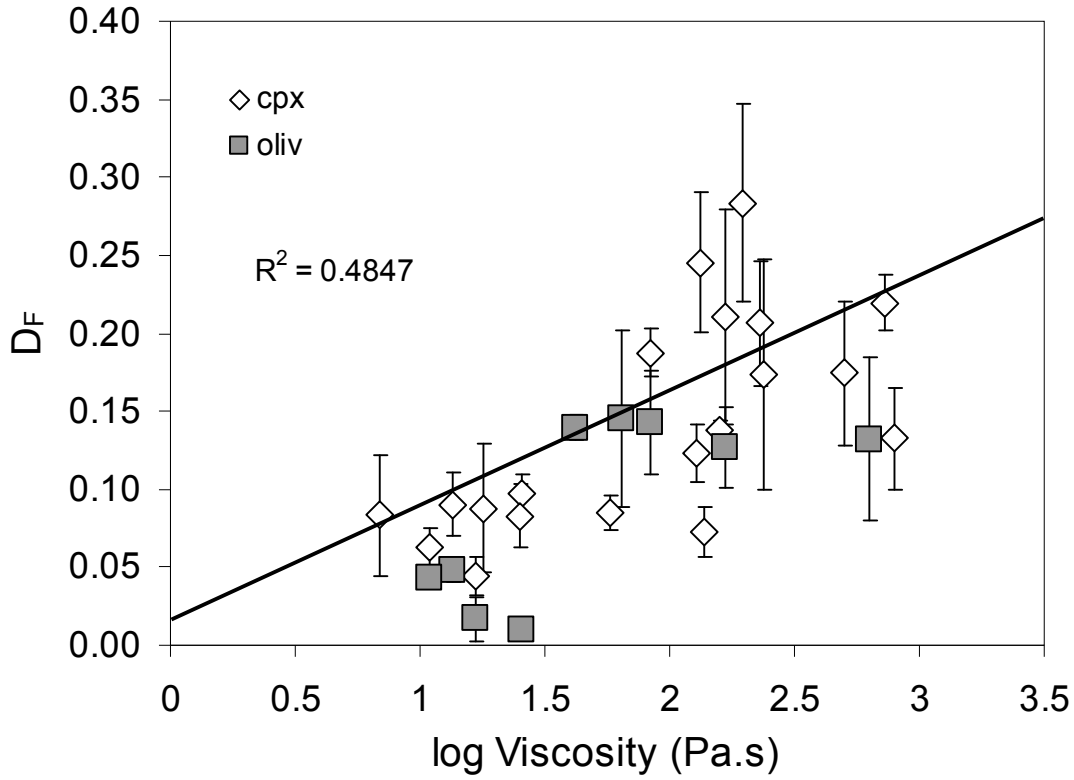
0.40
0.35
0.30
0.25
0.20
0.15
0.10
0.05
0.00
D_F
cpx
oliv
R^2 = 0.4847
0
0.5
1
1.5
2
2.5
3
3.5
log Viscosity (Pa.s)

Figure 5.16 (a)

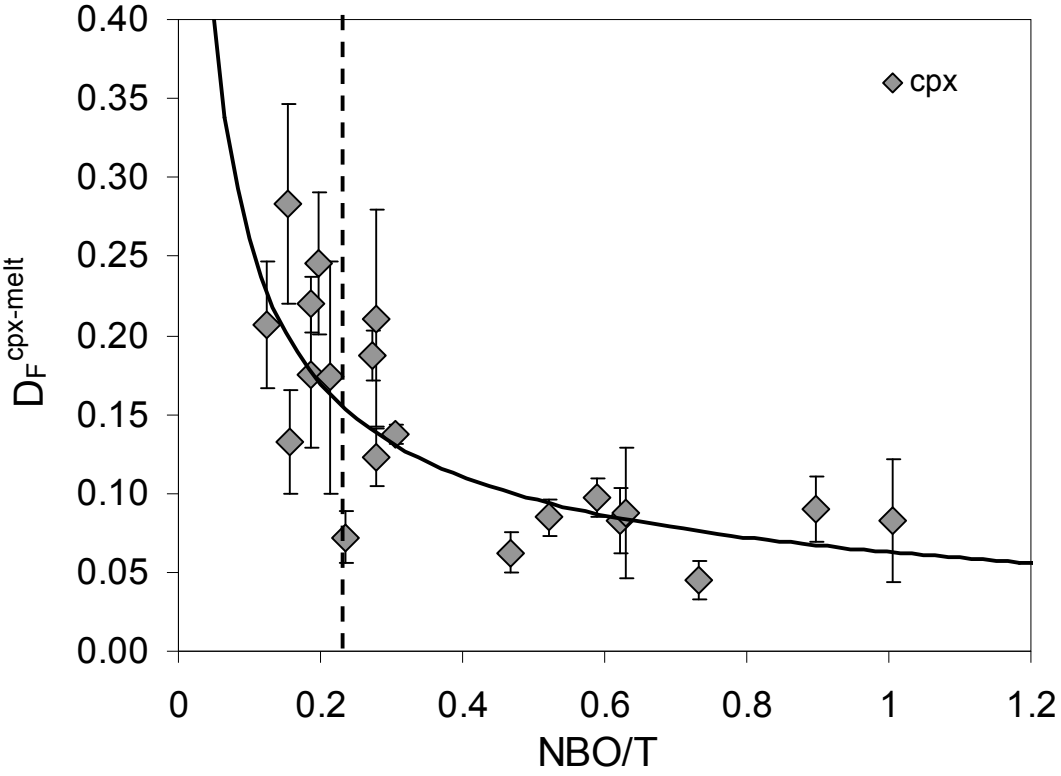
0.40
0.35
0.30
0.25
0.20
0.15
0.10
0.05
0.00
$D_F^{cpx\text{-}melt}$
0
0.2
0.4
0.6
0.8
1
1.2
NBO/T
cpx

Figure 5.17 (b)

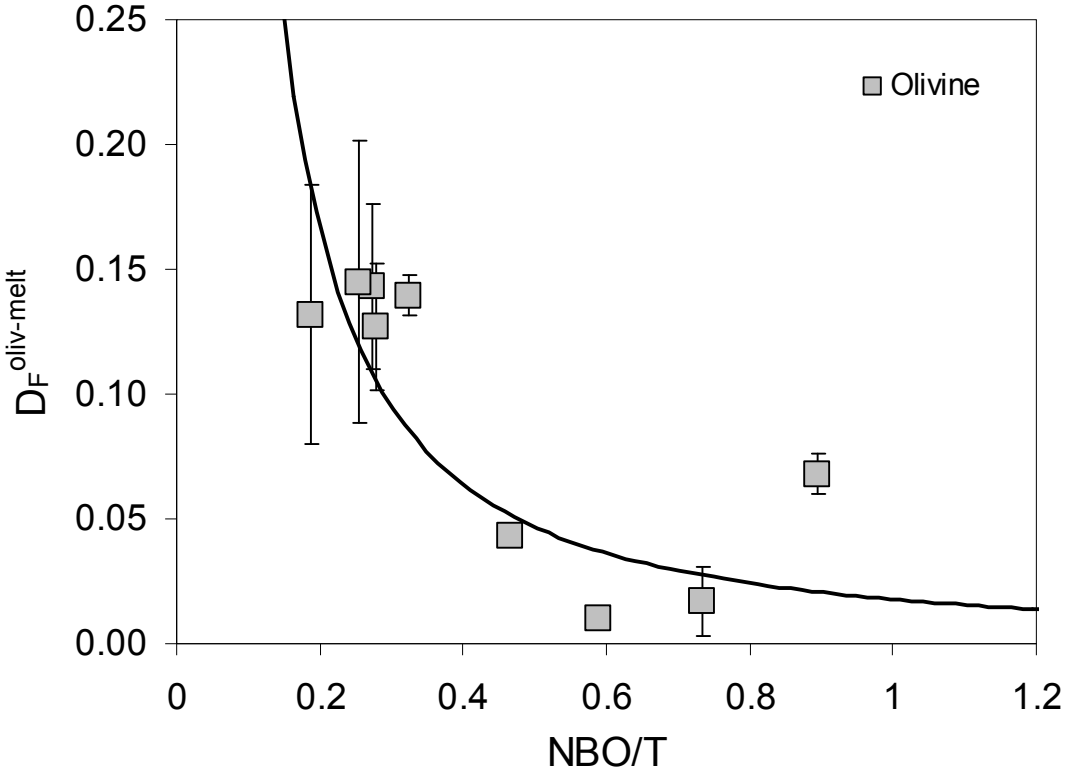
0.25
0.20
0.15
0.10
0.05
0.00
$D_F^{oliv\text{-}melt}$
0
0.2
0.4
0.6
0.8
1
1.2
NBO/T
Olivine

CHAPTER 6

SYNTHESIS

ABSTRACT

The work described in the previous chapters demonstrates the importance and influence of fluorine on igneous systems and the possible role fluorine plays regarding the volatile flux of the mantle. Here, I summarize the major contributions made in the course of my work and speculate on possible research projects that will extend the knowledge of fluorine, and by proxy other volatiles, within the mantle and within a myriad of igneous systems from various source environments.

1. Major Contributions: Basaltic Microanalytical Glass Standards for Fluorine

The measurement of F in low-silica, basaltic systems through the use of microanalytical instruments such as secondary ion mass spectrometry (SIMS), electron probe microanalysis (EPMA), and proton-induced gamma-ray emission (PIGE) spectrometry requires the use of appropriately matrix-matched glass calibration standards. These standards are used to construct calibration curves that convert the instrumental output of counts per second to a concentration value while minimizing the influence of matrix effects. Unfortunately, there is a paucity of well-characterized glass reference materials of basaltic composition. In response to this issue, we utilized two independent methods to measure the F content of some commonly used basaltic glass standards that had not been previously characterized for F.

The first method used was PIGE (See Chapter 2). For this study, we measured the F content of five natural and synthetic basaltic and high-silica geologic reference glasses using a 1.7 MeV Tandetron Cockroft-Walton, gas-insulated, high frequency tandem accelerator. The nuclear reaction measured was the resonant reaction $^{19}F(p,\alpha\gamma)^{16}O$. We calibrated the measurements with two well-established mineral standards (a natural fluor-topaz: 20.3 wt.% F and Durango Apatite: 3.53 wt.% F). After

synthesis of the results, we concluded that the F values obtained using the Durango Apatite calibration standard were the most reliable. The average fluorine concentrations of the standard glasses were calculated to be as follows: BHVO-2G (301±22 ppm), GSE-1G (140±8 ppm), NIST 610 (180±8 ppm), UTR-2 (1048±21 ppm). SIMS analyses were conducted on the above reference glasses in order to ascertain the extent of matrix effects when measuring F on the SIMS. Calibration curves were constructed based on the SIMS output ($^{19}F/^{18}O$) and PIGE fluorine analysis. Two calibration curves were observed that showed the occurrence of SIMS matrix effects of about 52 % between the low-silica and high-silica glasses. We then performed SIMS analyses on eight other commonly used microanalytical glass standards of basaltic and high-silica compositions, and the above SIMS calibration curves were used to calculate their F content: ALV-519-4-1 (76±8 ppm); BCR-2G (319±32 ppm); GSA-1G (7±1 ppm); GSC-1G (9±1 ppm); GSD-1G (18±2 ppm); ML3B-G (47±5 ppm); KL2-G (81±8 ppm); NIST-620 (10±1 ppm) (See Table 6.1).

The second method involved synthesizing five basaltic glasses doped with variable amounts of CaF_2 (see Chapter 3). These glasses (termed collectively as Fba glasses) were analyzed extensively with EPMA and SIMS, and their individual F contents were found to be homogeneously distributed. The F (ppm) contents of the Fba glasses were measured by EPMA and determined to be as follows: Fba-1 (1320±480); Fba-2 (5300±1090); Fba-3 (8650±1040); Fba-4 (14100±1100); Fba-5 (22400±1200) (Table 6.1). We constructed a SIMS calibration curve using the Fba glasses and the mica F standard Biotite-3 (3.53 wt.% F), and we used this calibration curve to determine the F content of nine common microanalytical basaltic glass standards that are in widespread use, but nevertheless have either not been characterized for F or the current data is not reliable. The F (ppm) content of these glasses are as follows: ALV-519-4 (76±4); BCR-2G (320±15); BHVO-2G (295±14); GSA-1G (7±1); GSC-1G (9±1); GSD-1G (18±2); GSE-1G (153±7); ML3B-G (47±2); KL2-G (81±4).

Table 6.1 lists the results of the two independent methods used to determine the F content of the selected glass reference materials (PIGE and SIMS calibration curves from the Fba glasses). Also listed are the F contents from the literature, where applicable, and the F content of the Fba glasses measured directly from EPMA. The two methods show strikingly similar results within error, indicating that the two independent methods are robust and reliable.

2. Major Contributions: Fluorine Partitioning

The study of the partitioning of F between NAMs and silicate melts of various compositions is a relatively new area of research, and the results of our study confirms and adds to the fairly sparse amount of data from literature. Dalou et al. (2011) reports D_F in a basaltic melt for clinopyroxene (0.04 – 0.15; average 0.10±0.04), olivine (0.12±0.07), and plagioclase (0.10±0.04). Within melt compositions similar to that of basalt, our results are in agreement: clinopyroxene (minette: 0.04 – 0.17; basaltic andesite: 0.17 – 0.21; latite: 0.12 – 0.27), olivine (minette: 0.01 – 0.07; basaltic andesite: 0.13 – 0.16), and plagioclase (basaltic andesite: 0.06 – 0.08). We tested a crystal of hornblende from basaltic andesite, and found the D_F to be 3.63±.036, a factor of 2 higher than the D_F value of 1.65±0.14 from an amphibole crystal (LaTourrette et al. 1995),

We found that crystal chemical controls and melt structural controls strongly influence the incorporation of F into clinopyroxene and olivine. Dalou et al. (2011) found no evidence of crystal chemical controls for F in clinopyroxene, but they did find a strong positive correlation between melt viscosity and D_F in clinopyroxene. We likewise found that melt viscosity and degree of melt polymerization has a positive influence on D_F in clinopyroxenes and olivines, and that when NBO/T < 0.3 (cpx) and < 0.35 (oliv), melt polymerization may become a dominant factor in determining D_F in these phases. In this study, we found no crystal chemical controls for D_F in olivines. In clinopyroxenes, F^- substitutes for O^{2-} in the O3 site, which acts to charge balance monovalent cations in the

M2 site and trivalent cations in the tetrahedral site. Accordingly, we found moderately positive correlations between D_F and the jadeite (Na) and Tschermaks (Al) components. However, we found a strong positive correlation between D_F and the ferrrosilite (Fe) component and a strong negative correlation between D_F and the enstatite (Mg) component, indicating that D_F in clinopyroxene increases with increasing Fe content and fractional crystallization.

It has been well-documented that the incorporation of H^+ (as OH^-) in clinopyroxene is heavily influenced by the alumina content of the clinopyroxene and that $D_H^{Cpx-melt}$ increases with total Al_2O_3 and tetrahedral Al^{IV} (Rauch and Keppler 2002, Stalder and Skogby 2002, Stalder 2004, Aubaud et al. 2004, 2008; Hauri et al. 2006; Grant et al. 2007; Tenner et al. 2009. We hypothesized that because F^- and OH^- contain similar charge and ionic radius, then the Al content of the clinopyroxene will influence the incorporation of F as well. Our results show a positive correlation between D_F and Al_2O_3 and tetrahedral ^{IV}Al. However, more work needs to be done on this topic.

3. Future Work

Although the current study proposes crystal chemical controls on the incorporation of F in NAMs, it nevertheless emphasizes that more work needs to be done in testing and quantifying these hypotheses. An avenue of future research is to perform experiments to equilibrate NAMs within melts of variable compositions where volatile content, H_2O content, Na content, trivalent Al, Cr, and Fe content, and fO_2 are controlled. Because of similar ionic radius and charge between F^- and OH^-, experiments where experimental charges are invested with proportioned amounts of F and H_2O to determine if an empirical relationship exists that controls the intake of these anions into NAMs and that minimizes competition for lattice and defect sites.

Research over the past couple of decades has attempted to characterize the abundance and role of OH^- in NAMs, and many studies have shown that NAMs from the

Earth's mantle may constitute the largest reservoir of water on the planet, as well as contributing to magma genesis, magma rheology, and eruption dynamics (Smith 1981, Smith et al. 1981, London et al. 1988, Micheal 1988, Bell and Rossman 1992, Symonds et al. 1994, Carroll and Webster 1994, Johnson et al. 1994, Watson 1994, Hirschmann et al. 2005, Alletti et al. 2007, Chevychelov et al. 2008, Aiuppa et al. 2009). This current study involves the first few steps in characterizing the role of fluorine in NAMs, specifically olivine, clinopyroxene, and plagioclase, and stems from the hypothesis that, because F^- and OH^- share the same charge and similar ionic radius in both 4-fold and 6-fold coordination (Shannon 1976), F^- and OH^- may substitute for each other within NAMs. As a result, there may be an empirical relationship between F^- and OH^- in NAMs such that F^- may serve as a proxy for OH^- within these phases, allowing one to determine the volatile content of the mantle and other igneous systems. The overall goals of this research may take a career's worth of work. However, the initial stages of this study were begun by Hervig et al. (1988), Hervig and Bell (2005), and Guggino et al. (2007). The current study relies on the slow diffusion of fluorine. For F to be a robust and useful proxy for OH, and for the F content of NAMs to reflect the pre-eruptive volatile budget of the mantle and magma systems in general, the diffusion rate of F within NAMs must be orders of magnitude slower than H and not subject to perturbations associated with changing *P*, *T*, and other conditions. While it is well known that H diffuses out rapidly in NAMs, no work has been performed to determine the diffusion rate of F in these phases. There are unpublished data where the diffusion rate of F and O in obsidian was measured (Hervig, unpublished data), and it was found that in obsidian, F diffuses at about the same rate as O. I am hesitant to apply these results to NAMs. An avenue of future study is to conduct diffusion experiments of F within NAMs at various *P*, *T*, and fO_2 conditions.

4. References

Aiuppa, A., Baker, D.R., and Webster, J.D. (2009) Halogens in volcanic systems. Chemical Geology, 263, 1018.

Alletti, M., Baker, D.R., and Freda, C. (2007) Halogen diffusion in basaltic melt. Geochimica et Cosmochimics Acta, 71, 3570-3580.

Aubaud, C., Hirschmann, M.M., Withers, A.C. and Hervig, R.L. (2008) Hydrogen partitioning between melt, clinopyroxene, and garnet at 3 GPa in a hydrous MORB with 6 wt.% H_2O. Contributions to Mineralogy and Petrology, 156, 607-625.

Aubaud, C., Hauri, E.H. and Hirschmann, M.M. (2004) Hydrogen partition coefficients between nominally anhydrous minerals and basaltic melts. Geophysical Research Letters, 31, L20611.

Balcone-Boissard, H., Michel, A. and Villemant, B. (2009) Simultaneous Derermination of Fluorine, Chlorine, Bromine and Iodine in Six Geological Reference Materials Using Pyrohydrolysis, Ion Chromatography and Inductively Coupled Plasma-Mass Spectrometry. Geostandards and Geoanalytical Research, 33, 477-485.

Bell, D.R. and Rossman, G.R. (1992) Water in Earth's mantle: The role of nominally anhydrous minerals. Science, 255, 1391-1397.

Carroll, M.R. and Webster, J.D. (1994) Solubilities of sulfur, noble gases, nitrogen, chlorine, and fluorine in Magmas. In: Carroll, M.R. and Holloway, J.R. (eds), Volatiles in Magmas. Reviews in Mineralogy Volume 30. Mineralogical Society of America (Washington, D.C.), 231-279.

Chevychelov, V.Y., Botcharnokov, R.E., and Holtz, F. (2008) Partitioning of Cl and F between fluid and hydrous phonolitic melt of Mt. Vesuvius at ~850-1000 C and 200 Mpa. Chemical Geology, doi:10.1016/j.chemgeo.2008.06.025.

Dalou, C., Koga, K.T., Shimizu, N., Boulon, J. and Devidal, J.L. (2011) Experimental determination of F and Cl partitioning between lherzolite and basaltic melt Contributions to Mineralogy and Petrology, 1-19.

Grant, K.J., Kohn, S.C. and Brooker, R.A. (2007) The partitioning of water between olivine, orthopyroxene and melt synthesized in the system albite-forsterite-H_2O. Earth and Planetary Science Letters, 260, 227-241.

Guggino, S., Hervig, R. and Bell, D. (2007) Fluorine in olivines from plutonic, extrusive, and hypabyssal suites. American Geophysical Union Fall Meeting Abstract.

Hauri, E.H., Weinreich, T., Saal, A., Rutherford, M.C., and Van Orman, J.A. (2011) High pre-eruptive water contents preserved in lunar melt inclusions. Science, 333, 213-215.

Hauri, E.H., Gaetani, G.A. and Green, T.H. (2006) Partitioning of water during melting of the Earth's upper mantle at H_2O-undersaturated conditions. Earth and Planetary Science Letters, 248, 715-734.

Hervig, R.L. and Bell, D.R. (2005) Fluorine and hydrogen in mantle mega-crysts. American Geophysical Union Fall Meeting Abstract.

Hervig, R.L., Smith, J.V. and Rivers, M.L. (1988) Fluorine content of upper mantle minerals. EOS, Transactions of the American Geophysical Union, 69, 502.

Hirschmann, M.M., Aubaud, C., and Withers, A.C. (2005) Storage capacity of H_2O in nominally anhydrous minerals in the upper mantle. Earth and Planetary Science Letters, 236, 167-181.

Hoskin, P.W.O. (1999) SIMS Determination of μg g^{-1} - level fluorine in geological samples and its concentration in NIST SRM 610. Geostandards Newsletter, 23, 69-76.

Jochum, K.P., Stoll, B., Herwig, K., Willbold, M., Hofmann, A.W., Amini, M., Aarburg, S., Abouchami, W., Hellebrand, E., Mocek, B., Raczek, I., Stracke, A., Alard, O., Bouman, C., Becker, S., Ducking, M., Bratz, H., Klemd, R., de Bruin, D., Canil, D., Cornell, D., de Hoog, C.J., Dalpe, C., Danushevsky, L., Eisenhauer, A., Gao, Y., Snow, J.E., Groschopf, N., Gunther, D., Latkoczy, C., Guillong, M., Hauri, E., Hofer, H.E., Lahaye, Y., Horz, K., Jacob, D.E., Kasemann, S.A., Kent, A.J.R., Ludwig, T., Zack, T., Mason, P.R.D., Meixner, A., Rosner, M., Misawa, K., Nash, B.P., Pfander, J., Premo, W.R., Sun, W.D., Tiepolo, M., Vannucci, R., Vennemann, T., Wayne, D., Woodhead, J.D. (2006) MPI-DING reference glasses for in situ microanalysis: New reference values for element concentrations and isotope ratios. Geochemistry, Geophysics, Geosystems, Technical Brief, 7, 44 p.

Johnson, M.C., Anderson, A.T., and Rutherford, M.J. (1994) Pre-eruptive volatile contents of magmas. In: Carroll, M.R. and Holloway, J.R. (eds), Volatiles in Magmas. Reviews in Mineralogy Volume 30. Mineralogical Society of America (Washington, D.C.), 281-330.

La Tourrette, T., Hervig, R.L., and Holloway, J.R. (1995) Trace element partitioning between amphibole, phlogopite, and basanite melt. Earth and Planetary Science Letters, 135, 13-30.

London, D., Hervig, R.L., and Morgan, G.B. (1988) Melt-vapor solubilities and elemental partitioning in peraluminous granite-pegmatite systems: Experimental results with Macusani glass at 200 MPa. Contributions to Mineralogy and Petrology, 99, 360-373.

Michael, P.J. (1988) The concentration, behavior and storage of H_2O in the suboceanic upper mantle: Implications for mantle metasomatism. Geochimica et Cosmochimica Acta, 52, 555-566.

Michel, A. and Villemant, B. (2003) Determination of halogens (F, Cl, Br, I), sulfur and water in seventeen geological reference materials. Geostandards Newsletter, 27, 163-171.

Rauch, M. and Keppler, H. (2002) Water solubility in orthopyroxene. Contributions to Mineralogy and Petrology, 143, 525-536.

Shannon, R. (1976) Revised effective ionic radii and systematic studies of interatomic distances in halides and chalcogenides. Acta Crystallographica Section A: Crystal Physics, Diffraction, Theoretical and General Crystallography, 32, 751-767.

Smith, J.V. (1981) Halogen and Phosphorous Storage in the Earth. Nature, 289, 762-765

Smith, J., Delaney, J., Hervig, R. and Dawson, J. (1981) Storage of F and Cl in the upper mantle: Geochemical implications. Lithos, 14, 133-147.

Stalder, R. (2004) Influence of Fe, Cr and Al on hydrogen incorporation in orthopyroxene. European Journal of Mineralogy, 16, 703-711.

Stalder, R. and Skogby, H. (2002) Hydrogen incorporation in enstatite. European Journal of Mineralogy, 14, 1139-1144.

Straub, S.M. and Layne, G.D. (2003) The systematics of chlorine, fluorine, and water in Izu arc front volcanic rocks: Implications for volatile recycling in subduction zones. Geochimica et Cosmochimica Acta, 67, 4179-4203.

Symonds, R.B., Rose, W.I., Bluth, G.S.J., and Gerlach, T.M. (1994) Volcanic-gas studies: Methods, results, and applications. In: Carroll, M.R. and Holloway, J.R. (eds), Volatiles in Magmas. Reviews in Mineralogy Volume 30. Mineralogical Society of America (Washington, D.C.), 1-66.

Tenner, T.J., Hirschmann, M.M., Withers, A.C. and Hervig, R.L. (2009) Hydrogen partitioning between nominally anhydrous upper mantle minerals and melt between 3 and 5 GPa and applications to hydrous peridotite partial melting. Chemical Geology, 262, 42-56.

Wang, Q., Makishima, A., Nakamura, E. (2010) Determination of fluorine and chlorine by pyrohydrolysis and ion chromatography: Comparison with alkaline fusion digestion and ion chromatography. Geostandards and Geoanalytical Research, 34, 175-183.

Watson, E.B. (1994) Diffusion in volatile-bearing magmas. In: Carroll, M.R. and Holloway, J.R. (eds), Volatiles in Magmas. Reviews in Mineralogy Volume 30. Mineralogical Society of America (Washington, D.C.), 371-411.

Table 6.1. Comparison of the F content in selected reference glasses based on two methods: PIGE and SIMS Fba glasses calibration curves.

Method →	EPMA		PIGE (Direct & SIMS Calib. Curves)		SIMS (Calib. Curves)		Literature
Sample	F (ppm)	1σ	F (ppm)	1σ	F (ppm)	1σ	F (ppm)
**Fba Basaltic Glasses*							
Fba-1	1320	480	na	na	na	na	na
Fba-2	5300	1090	na	na	na	na	na
Fba-3	8650	1040	na	na	na	na	na
Fba-4	14100	1100	na	na	na	na	na
Fba-5	22400	1200	na	na	na	na	na
Common Basaltic Reference Glasses							
ALV-519-4	na	na	76	8	76	4	90-113[1,2,3]
BHVO-2G	na	na	301†	22	295	14	370-409[4,5,6,7]
BCR-2G	na	na	319	32	320	15	448[8]
GSA-1G	na	na	7	1	7	1	na
GSC-1G	na	na	9	1	9	1	na
GSD-1G	na	na	18	2	18	2	na
GSE-1G	na	na	140†	8	153	7	na
ML3B-G	na	na	47	5	47	2	70
KL2-G	na	na	81	8	81	4	177
High-silica Reference Glasses							
NIST-610	na	na	180†	8	na	na	205-611[9,10,11,12]
NIST-620	na	na	23	2	na	na	na
UTR-2	na	na	1048†	21	na	na	1143[13]

1. Jochum et al. (2006)
2. Hauri et al. (2011)
3. Monteleone, B. (personal communication) WHOI calibration standard
4. As BHVO-2 powder, 370 ppm, USGS Certificate of Analysis (1998)
5. As BHVO-2 powder, 376 ppm, Balcone-Boissaed et al. (2009)
6. As BHVO-2 powder, 402 ppm, Michel and Villemont (2003)
7. As BHVO-2 powder, 409 ppm, Wang et al. (2010)
8. As BCR-2 powder, Michel and Villemont (2003)
9. 205 ppm, Wang et al. (2010)
10. 295 ppm, Hoskin (1999)
11. 413 ppm, Jochum et al. (2006)
12. 611 ppm, Straub and Layne (2003)
13. Stix, J., unpublished data

* All F values for the Fba glasses were determined directly from EPMA

† F values measured directly from PIGE

REFERENCES

Aiuppa, A. (2009) Degassing of halogens from basaltic volcanism: Insights from volcanic gas observations. Chemical Geology, 263, 99-109.

Aiuppa, A., Baker, D.R., and Webster, J.D. (2009) Halogens in volcanic systems. Chemical Geology, 263, 1018.

Allen, R.O. and Clark, P.J. (1977) Fluorine in meteorites. Geochimica et Cosmochimica Acta, 41, 581-585.

Alletti, M., Baker, D.R., and Freda, C. (2007) Halogen diffusion in basaltic melt. Geochimica et Cosmochimics Acta, 71, 3570-3580.

Aubaud, C., Hauri, E.H. and Hirschmann, M.M. (2004) Hydrogen partition coefficients between nominally anhydrous minerals and basaltic melts. Geophysical Research Letters, 31, L20611.

Aubaud, C., Hirschmann, M.M., Withers, A.C. and Hervig, R.L. (2008) Hydrogen partitioning between melt, clinopyroxene, and garnet at 3 GPa in a hydrous MORB with 6 wt.% H_2O. Contributions to Mineralogy and Petrology, 156, 607-625.

Balcone-Boissard, H., Michel, A. and Villemant, B. (2009) Simultaneous Derermination of Fluorine, Chlorine, Bromine and Iodine in Six Geological Reference Materials Using Pyrohydrolysis, Ion Chromatography and Inductively Coupled Plasma-Mass Spectrometry. Geostandards and Geoanalytical Research, 33, 477-485.

Barton, M., Haselton, H., Hemingway, B., Kleppa, O. and Robie, R. (1982) The thermodynamic properties of fluor-topaz. American Mineralogist, 67, 350-355.

Bastin, G.F. and Heijligers, J.M. (1991) Quantitative Electron Probe Microanalysis of Ultra-Light Elements (Boron - Oxygen). In: Heinrich K.F.J. and Newberry, D.E. (eds), Electron Probe Quantitation. Plenum Press (New York), 145-161.

Bell, D.R. and Rossman, G.R. (1992) Water in Earth's mantle: The role of nominally anhydrous minerals. Science, 255, 1391-1397.

Bell D.R., Hervig R.L., Buseck P.R. and Aulbach S. (2009) Lithium isotope analysis of olivine by SIMS: Calibration of a matrix effect and application to magmatic phenocrysts. Chemical Geology, 258, 5-16.

Bewers, J.M. and Flack, F.C. (1969) Determination of fluorine by prompt γ-radiation from proton bombardment. Analyst, 94, 7-14.

Bird, J.R. and Clayton, E. (1983) The PIGME method for fluorine determination. In: Lanford W.A., Tsong I.S.T. and Williams P. (eds), Proceedings of the Sixth International Conference on Ion Beam Analysis, Nuclear Instruments and Methods in Physics Research, Ion Beam Analysis 6, 525-528.

Boyle, D.R. (1981) The analysis of fluorine in geochemical exploration. Journal of Geochemical Exploration, 14, 175-197.

Bromiley, D.W. and Kohn, S.C. (2007) Comparisons between fluoride and hydroxide incorporation in nominally anhydrous and fluorine-free mantle minerals. Goldschmidt conference abstracts.

Bromiley, G.D., Keppler, H., McCammon, C., Bromiley, F.A. and Jacobsen, S.D. (2004) Hydrogen solubility and speciation in natural, gem-quality chromian diopside. American Mineralogist, 89, 941-949.

Brown, G.M. (1956) The layered ultrabasic rocks of Rhum, Inner Hebrides. Philosophical Transactions of the Royal Society of London, 240: 1-54.

Carroll, M.R. and Webster, J.D. (1994) Solubilities of sulfur, noble gases, nitrogen, chlorine, and fluorine in Magmas. In: Carroll, M.R. and Holloway, J.R. (eds), Volatiles in Magmas. Reviews in Mineralogy Volume 30. Mineralogical Society of America (Washington, D.C.), 231-279.

Chevychelov, V.Y., Botcharnokov, R.E., and Holtz, F. (2008) Partitioning of Cl and F between fluid and hydrous phonolitic melt of Mt. Vesuvius at ~850-1000 C and 200 Mpa. Chemical Geology, doi:10.1016/j.chemgeo.2008.06.025.

Clark, P.J., Neal, G.F. and Allen, R.O. (1975) Quantitative multi-element analysis using high energy particle bombardment. Analytical Chemistry, 47, 650-658.

Collins, W., Beams, S., White, A.J.R. and Chappell, B. (1982) Nature and origin of A-type granites with particular reference to southeastern Australia. Contributions to Mineralogy and Petrology, 80, 189-200.

Coote, G. (1992) Ion beam analysis of fluorine: Its principles and applications. Nuclear Instruments and Methods in Physics Research Section B: Beam Interactions with Materials and Atoms, 66, 191-204.

Coote, G., Sparks, R. and Blattner, P. (1982) Nuclear microprobe measurement of fluorine concentration profiles, with application in archaeology and geology. Nuclear Instruments and Methods in Physics Research, 197, 213-221.

Dalou, C., Koga, K.T., Shimizu, N., Boulon, J. and Devidal, J.L. (2011) Experimental determination of F and Cl partitioning between lherzolite and basaltic melt Contributions to Mineralogy and Petrology, 1-19.

Delaney, J., Smith, J., Carswell, D. and Dawson, J. (1980) Chemistry of micas from kimberlites and xenoliths--II. Primary-and secondary-textured micas from peridotite xenoliths. Geochimica et Cosmochimica Acta, 44, 857-872.

Deline, V., Katz, W., Evans, C. and Williams, P. (1978) Mechanism of the SIMS matrix effect. Applied Physics Letters, 33, 832-835.

Dieumegard, D., Maurel, B., Amsel, G. (1980) Microanalysis of fluorine by nuclear reactions 1: $^{19}F(p,\alpha)^{16}O$ and $^{19}F(p,\alpha\gamma)^{16}O$ reactions. Nuclear Instruments and Methods, 168, 93-103.

Dingwell, D.B. (1985) The structures and properties of fluorine-rich magmas: A review of experimental studies. In: Taylor, R.P. and Strong, D.F. (eds), Recent Advances in the Geology of Granite-Related Mineral Deposits. Canadian Institute of Mining and Metallurgy (Montreal), 1-12.

Dingwell, D.B., Scarfe, C.M., and Cronin, D.J. (1985) The effect of fluorine on viscosities in the system Na_2O-Al_2O_3-SiO_2: implications for phonolites, trachytes, and rhyolites. American Mineralogist, 70, 80-87.

Döbeli, M., Gaschen, A.A.M. and Krähenbühl, U. (2006) Fluorine analysis by ion beam techniques for dating applications. Advances in Fluorine Science, 2, 215-252.

Eiler, J.M., Graham, C. and Valley, J.W. (1997) SIMS analysis of oxygen isotopes: Matrix effects in complex minerals and glasses. Chemical Geology, 138, 221-244.

Ekstrom, T.K. (1972) The distribution of fluorine among some coexisting minerals. Contributions to Mineralogy and Petrology, 34, 192-200.

Engi, M. and Lindsley, D.H. (1980) Stability of titanian clinohumite: Experiments and thermodynamic analysis. Contributions to Mineralogy and Petrology, 72, 415-424.

Esperanca, S. (1984) An experimental and geochemical study of the high-K latites and associated nodules from camp Creek, Arizona. PhD Dissertation, Arizona State University, p. 87

Esperança, S. and Holloway, J.R. (1986) The origin of the high-K latites from Camp Creek, Arizona: constraints from experiments with variable fO_2 and aH_2O. Contributions to Mineralogy and Petrology, 93, 504-512.

Esperança, S. and Holloway, J.R. (1987) On the origin of some mica-lamprophyres: experimental evidence from a mafic minette. Contributions to Mineralogy and Petrology, 95, 207-216.

Farver, J.R. (2010) Oxygen and hydrogen diffusion in minerals. In Diffusion in Minerals and Melts. Reviews in Mineralogy and Geochemistry (eds. Y. Zhang and D.J. Cherniak). Mineralogical Society of America. 72, 447-507.

Frei, D., Liebscher, A., Franz, G., Wunder, B., Klemme, S., and Blundy, J.D. (2009) Trace element partitioning between orthopyroxene and anhydrous silicate melt on the lherzolite solidus from 1.1 to 3.2 Gpa and 1,230 to 1,535 C in the model system Na_2O-CaO-MgO-Al_2O_3-SiO_2. Contributions to Mineralogy and Petrology, 157, 473-490.

Gaetani, G.A. (2004) The influence of melt structure on trace element partitioning near the peridotite solidus. Contributions to Mineralogy and Petrology, 147, 511-527.

Gaetani, G.A. and Grove, T.L. (1995) Partitioning of rare earth elements between clinopyroxene and silicate melt: Crystal-chemical controls. Geochimica et Cosmochimica Acta, 59, 1951-1962.

Gasparik, T. (1990) Phase relations in the transition zone. Journal of Geophysical Research, 5, 15751-15769.

Gasparik, T. (1993) The role of volatiles in the transition zone. Journal of Geophysical Research, 98, 4287-4299.

Giordano, D., Russell, J.K. and Dingwell, D.B. (2008) Viscosity of magmatic liquids: A model. Earth and Planetary Science Letters, 271, 123-134.

Grant, K.J., Kohn, S.C. and Brooker, R.A. (2007) The partitioning of water between olivine, orthopyroxene and melt synthesized in the system albite-forsterite-H_2O. Earth and Planetary Science Letters, 260, 227-241.

Guggino, S., Hervig, R. and Bell, D. (2007) Fluorine in olivines from plutonic, extrusive, and hypabyssal suites. American Geophysical Union Fall Meeting Abstract.

Guggino, S.N. and Hervig, R.L. (2010) Determination of fluorine in fourteen microanalytical geologic reference materials using SIMS, EPMA, and proton Induced Gamma Ray Emission (PIGE) Analysis. Abstract, American Geophysical Union Fall Meeting.

Guggino, S.N. and Hervig, R.L. (2011) Synthesis and Characterization of Five New F-bearing Basalt Reference Materials (Fba Glasses): Quantifying the Fluorine Content of the Basaltic Glass Standards BCR-2G, BHVO-2G. GSA-1G, GSC-1G, GSD-1G, GSE-1G, ML3B-G, KL2-G, and ALV-519-4. American Geophysical Union Fall Meeting Abstract.

Hauri, E. (2002) SIMS analysis of volatiles in silicate glasses, 2: Isotopes and abundances in Hawaiian melt inclusions. Chemical Geology, 183, 115-141.

Hauri, E.H., Weinreich, T., Saal, A., Rutherford, M.C., and Van Orman, J.A. (2011) High pre-eruptive water contents preserved in lunar melt inclusions. Science, 333, 213-215.

Hauri, E.H., Gaetani, G.A. and Green, T.H. (2006) Partitioning of water during melting of the Earth's upper mantle at H_2O-undersaturated conditions. Earth and Planetary Science Letters, 248, 715-734.

Hauri, E., Wang, J., Dixon, J.E., King, P.L., Mandeville, C. and Newman, S. (2002) SIMS analysis of volatiles in silicate glasses 1: Calibration, matrix effects and comparisons with FTIR. Chemical Geology, 183, 99-114.

Hazen, R.M., Yang, H., Prewitt, C.T., Gasparik, T. (1997) Crystal chemistry of superfluorous phase B ($Mg_{10}Si_3O_{14}F_4$): Implications for the role of fluorine in the mantle. American Mineralogist, 82, 647-650.

Hermann, J., Fitz Gerald, J.D., Malaspina, N., Berry, A.J. and Scambelluri, M. (2007) OH-bearing planar defects in olivine produced by the breakdown of Ti-rich humite minerals from Dabie Shan (China). Contributions to Mineralogy and Petrology, 153, 417-428.

Hervig, R.L. and Bell, D.R. (2005) Fluorine and hydrogen in mantle mega-crysts. American Geophysical Union Fall Meeting Abstract.

Hervig, R.L., Mazdab, K., Moore, G., McMillan, P.F. (2003) Analysing hydrogen (H_2O) in silicate glass by secondary ion mass spectrometry and relectance Fourier transform infrared spectroscopy. In: De Vivo, B. and Bodnar, R.J. (eds) Melt Inclusions in Volcanic Systems: Methods Applications and Problems. Developments in Volcanology 5. Elsevier, 83-103.

Hervig, R.L., Williams, P., Thomas, R.M., Schauer, S.N. and Steele, I.M. (1992) Microanalysis of oxygen isotopes in insulators by secondary ion mass spectrometry. International Journal of Mass Spectrometry and Ion Processes, 120, 45-63.

Hervig, R.L., Dunbar, N., Westrich, H.R. and Kyle, P.R. (1989) Pre-eruptive water content of rhyolitic magmas as determined by ion microprobe analyses of melt inclusions in phenocrysts. Journal of Volcanology and Geothermal Research, 36, 293-302.

Hervig, R.L., Smith, J.V. and Rivers, M.L. (1988) Fluorine content of upper mantle minerals. EOS, Transactions of the American Geophysical Union, 69, 502.

Hervig, R.L., Kortemeier, W.T. and Burt, D.M. (1987) Ion-microprobe analyses of Li and B in topaz from different environments. American Mineralogist, 72, 392-396.

Hinton, R.W. (1999) NIST SRM 610, 611 and SRM 612, 613 Multi - element glasses: Constraints from element abundance ratios measured by microprobe techniques. Geostandards Newsletter, 23, 197-207.

Hinton, R., Harte, B. and Witt-Eickschen, G. (1995) Ion probe measurements of National Institute of Standards and Technology standard reference material SRM 610 glass, trace elements. Analyst, 120, 1315-1319.

Hirschmann, M.M., Aubaud, C., and Withers, A.C. (2005) Storage capacity of H_2O in nominally anhydrous minerals in the upper mantle. Earth and Planetary Science Letters, 236, 167-181.

Hoskin, P.W.O. (1999) SIMS Determination of μg g^{-1} - level fluorine in geological samples and its concentration in NIST SRM 610. Geostandards Newsletter, 23, 69-76.

Ihinger, P.D., Hervig, R.L., McMillan, P.F. (1994) Analytical methods for volatiles in glasses. In: Carroll, M.R. and Holloway, J.R. (eds), Volatiles in Magmas. Reviews in Mineralogy Volume 30. Mineralogical Society of America (Washington, D.C.), 67-121.

Ingrin, J. and Skogby, H. (2000) Hydrogen in nominally anhydrous upper-mantle minerals: Concentration levels and implications. European Journal of Mineralogy, 12, 543-570

Jochum, K.P., Weis, U., Stoll, B., Kuzmin, D., Yang, Q., Raczek, I., Jacob, D.E., Stracke, A., Birbaum, K. and Frick, D.A. (2011) Determination of reference values for NIST SRM 610–617 glasses following ISO guidelines. Geostandards and Geoanalytical Research.

Jochum, K.P., Stoll, B., Herwig, K., Willbold, M., Hofmann, A.W., Amini, M., Aarburg, S., Abouchami, W., Hellebrand, E., Mocek, B., Raczek, I., Stracke, A., Alard, O., Bouman, C., Becker, S., Ducking, M., Bratz, H., Klemd, R., de Bruin, D., Canil, D., Cornell, D., de Hoog, C.J., Dalpe, C., Danushevsky, L., Eisenhauer, A., Gao, Y., Snow, J.E., Groschopf, N., Gunther, D., Latkoczy, C., Guillong, M., Hauri, E., Hofer, H.E., Lahaye, Y., Horz, K., Jacob, D.E., Kasemann, S.A., Kent, A.J.R., Ludwig, T., Zack, T., Mason, P.R.D., Meixner, A., Rosner, M., Misawa, K., Nash, B.P., Pfander, J., Premo, W.R., Sun, W.D., Tiepolo, M., Vannucci, R., Vennemann, T., Wayne, D., Woodhead, J.D. (2006) MPI-DING reference glasses for in situ microanalysis: New reference values for element concentrations and isotope ratios. Geochemistry, Geophysics, Geosystems, Technical Brief, 7, 44 p.

Jochum, K.P., Willbold, M., Raczek, I., Stoll, B., Herwig, K. (2005) Chemical Characterization of the USGS Reference Glasses GSA-1G, GSC-1G, GSD-1G, GSE-1G, BCR-2G, BHVO-2G and BIR-1G Using EPMA, ID-TIMS, ID-ICP-MS, and LA-ICP-MS. Geostandards and Geoanalytical Research, 29, 285-302.

Jochum, K.P., Dingwell, D.B., Rocholl, A., Brigitte Stoll, B., Hofmann, A.W., Becker, S., Besmehn, A., Bessette, D., Dietze, H.J., Dulski, P., Erzinger, J., Hellebrand, E., Hoppe, P., Horn, I., Janssens, K., Jenner, G.A., Klein, M., McDonough, W.F., Maetz, M., Mezger, K., Münker, C., Nikogosian, I.K., Pickhardt, C., Raczek, I., Rhede, D., Seufert, H.M., Simakin, S.G., Sobolev A.V., Spettel, B., Straub, S., Vincze, L., Wallianos, A., Weckwerth, G., Weyer, S., Wolf, D., Zimmer, M. (2000) The preparation and preliminary characterization of eight geological MPI-DING reference glasses for in-situ microanalysis. Geostandards Newsletter, 24, 87-13.

Johnson, M.C., Anderson, A.T., and Rutherford, M.J. (1994) Pre-eruptive volatile contents of magmas. In: Carroll, M.R. and Holloway, J.R. (eds), Volatiles in Magmas. Reviews in Mineralogy Volume 30. Mineralogical Society of America (Washington, D.C.), 281-330.

Kane, J.S. (2001) The use of reference materials: A tutorial. Geostandards Newsletter, 25, 7-22.

Kane, J.S. and Potts, P.J. (1999) An interpretation of ISO Guidelines for the certification of geological reference materials. Geostandards Newsletter, 23, 209-221.

Katayama, I. and Nakashima, S. (2003) Hydroxyl in clinopyroxene from the deep subducted crust: Evidence for H_2O transport into the mantle. American Mineralogist, 88, 229-234.

Kenny, M. (1981) Thick target gamma yields from fluorine. Australian Journal of Physics, 34, 35-41

Köhler, J., Schönenberger, J., Upton, B., and Markl, G. (2009) Halogen and trace-element chemistry in the Gardar Province, South Greenland: Subduction-related mantle metasomatism and fluid exsolution from alkalic melts. Lithos, 113, 731-747.

Kohlstedt, D.L. and Mackwell, B. (1999) Solubility and diffusion of "water" in silicate minerals. In: Wright K. and Catlow R. (eds), Microscopic Properties and Processes in Minerals. Kluwer (Dordrecht,), 539-559.

Kohn, S., Roome, B., Smith, M. and Howes, A. (2005) Testing a potential mantle geohygrometer; The effect of dissolved water on the intracrystalline partitioning of Al in orthopyroxene. Earth and Planetary Science Letters, 238, 342-350.

Kovalenko, V., Hervig, R.L. and Sheridan, M.F. (1988) Ion-microprobe analyses of trace elements in anorthoclase, hedenbergite, aenigmatite, quartz, apatite, and glass in pantellerite: evidence for high water contents in pantellerite melt. American Mineralogist, 73, 1038-1045.

Kroger, F.A. and Vink, H.J. (1956) Relations between te concentrations of imperfections in crystalline solids. In: Seitz, F. and Turnbull, D. (eds). Solid State Physics, v. 3, pp. 307-435. Academic Press, Inc., New York.

Kushiro, I. and Mysen, B.O. (2002) A possible effect of melt structure on the Mg-Fe^{2+} partitioning between olivine and melt. Geochimica et Cosmochimica Acta, 66, 2267-2272.

La Tourrette, T., Hervig, R.L., and Holloway, J.R. (1995) Trace element partitioning between amphibole, phlogopite, and basanite melt. Earth and Planetary Science Letters, 135, 13-30.

Lange, R.A. (1994) The effect of H_2O, CO_2 and F on the density and viscosity of silicate melts. In: Carroll, M.R. and Holloway, J.R. (eds), Volatiles in Magmas. Reviews in Mineralogy Volume 30. Mineralogical Society of America (Washington, D.C.), 331-369.

London, D., Hervig, R.L., and Morgan, G.B. (1988) Melt-vapor solubilities and elemental partitioning in peraluminous granite-pegmatite systems: Experimental results with Macusani glass at 200 MPa. Contributions to Mineralogy and Petrology, 99, 360-373.

Macdonald, R. and Bailey, D.K. (1973) Chapter N. Chemistry of Igneous Rocks Part 1. The Chemistry of Peralkaline Oversaturated Obsidians. In: Fleischer, M. (eds), Data of Geochemistry 6th Edition. Geological Survey Professional Paper 440-N-1, US Government Printing Office, Washington, 41 p.

MacDonald, G.A. and Katsura, T. (1964) Chemical composition of Hawaiian lavas. Journal of Petrology, 5, 82-133.

Mason, R.A. (1992) Models of order and iron - fluorine avoidance. Canadian Mineralogist, 30, 343-354.

Mateus R., Jesus A., Fonseca M., Luís H. and Ribeiro J. (2007) The sensitivity of the PIGE analytical technique. Nuclear Instruments and Methods in Physics Research Section B: Beam Interactions with Materials and Atoms, 264, 340-344.

Matson, D.W., Muenow, D.W. and Garcia, M.O. (1986) Volatile contents of phlogopite micas from South African kimberlite. Contributions to Mineralogy and Petrology, 93, 399-408.

McCormick, T.C. (1986) Crystal-chemical aspects of nonstoichiometric pyroxenes. American Mineralogist, 71, 1434-1440.

McDonough, W.F. and Sun, S.S. (1995) The composition of the Earth. Chemical Geology, 120, 223-253.

McGee, J.J. and Keil, K. (2001) Application of electron probe microanalysis to the study of geological and planetary materials. Microscopy and Microanalysis, 7, 200-210.

Michael, P.J. (1988) The concentration, behavior and storage of H_2O in the suboceanic upper mantle: Implications for mantle metasomatism. Geochimica et Cosmochimica Acta, 52, 555-566.

Michel, A. and Villemant, B. (2003) Determination of halogens (F, Cl, Br, I), sulfur and water in seventeen geological reference materials. Geostandards Newsletter, 27, 163-171.

Moore, G. and Carmichael, I. (1998) The hydrous phase equilibria (to 3 kbar) of an andesite and basaltic andesite from western Mexico: Constraints on water content and conditions of phenocryst growth. Contributions to Mineralogy and Petrology, 130, 304-319.

Moores, E.M. (1969) The petrology and structure of the Vourinos ophiolitic complex of Northern Greece. Geological Society of America Special Paper 118.

Morse, S.A. (1965) The Kiglapait layered intrusion, Labrador. Geological Society of America Memoir, 112p.

Mosbah, M., Clocchiatti, R., Métrich, N., Piccot, D., Rio, S. and Tirira, J. (1995) The characterization of glass inclusions through nuclear microprobe. Nuclear Instruments and Methods in Physics Research Section B: Beam Interactions with Materials and Atoms, 104, 271-275.

Mosbah, M., Metrich, N. and Massiot, P. (1991) PIGME fluorine determination using a nuclear microprobe with application to glass inclusions. Nuclear Instruments and Methods in Physics Research Section B: Beam Interactions with Materials and Atoms, 58, 227-231.

Moune, S., Sigmarsson, O., Thordarson, T. and Gauthier, P.J. (2007) Recent volatile evolution in the magmatic system of Hekla volcano, Iceland. Earth and Planetary Science Letters, 255, 373-389.

Mysen, B.O., Cody, G.D. and Smith, A. (2004) Solubility mechanisms of fluorine in peralkaline and meta-aluminous silicate glasses and in melts to magmatic temperatures. Geochimica et Cosmochimica Acta, 68, 2745-2769.

Mysen, B.O. (1988) Structure and Properties of Silicate Melts. Developments in Geochemistry 4. Elsevier, New York, 354 p.

Mysen, B.O., Virgo, D. and Seifert, F.A. (1985) Relationships between properties and structure of aluminosilicate melts. American Mineralogist, 70, 88-105.

Nakamura, A. and Schmalzried, H. (1983) On the nonstoichiometry and point defects of olivine. Physics and Chemistry of Minerals, 10, 27-37.

Nicolson, K. (1983) Fluorine determination in geochemistry: errors in the electrode method of analysis. Chemical Geology, 38, 1-22.

Noll ,K., Döbeli, M. and Krähenbühl, U. (1998) Fluorine profiles in Antarctic meteorites by nuclear reaction analysis (NRA). Fresenius' Journal of Analytical Chemistry, 361, 713-715.

Noll, K., Döbeli, M., Krähenbühl, U., Grambole, D., Herrmann, F. and Koeberl, C. (2003) Detection of terrestrial fluorine by proton induced gamma emission (PIGE): A rapid quantification for Antarctic meteorites. Meteoritics & Planetary Science, 38, 759-765.

O'Leary, J.A., Gaetani, G.A., Hauri, E.H. (2010) The effect of tetrahedral Al^{3+} on the partitioning of water between clinopyroxene and silicate melt. Earth and Planetary Science Letters, 297, 111-120

O'Reilly, S.Y. and Griffin, W. (2000) Apatite in the mantle: Implications for metasomatic processes and high heat production in Phanerozoic mantle. Lithos, 53, 217-232.

Ottolini L., Cámara F., Hawthorne F.C. and Stirling J. (2002) SIMS matrix effects in the analysis of light elements in silicate minerals: Comparison with SREF and EMPA data. American Mineralogist, 87, 1477-1485.

Ottolini L., Cámara F. and Bigi S. (2000) An investigation of matrix effects in the analysis of fluorine in humite-group minerals by EMPA, SIMS, and SREF. American Mineralogist, 85, 89-102.

Palais, J.M. and Sigurdsson, H. (1989) Petrologic evidence of volatile emissions from major historic and pre-historic volcanic eruptions. In Berger, A., Dickinson, R.E., Kidson, J.W. (eds), Understanding Climate Change, Geophysical Monograph 52, 31-53.

Pan, Y. and Fleet, M.E. (1996) Rare element mobility during prograde granulite facies metamorphism: significance of fluorine. Contributions to Mineralogy and Petrology, 123, 251-262.

Pivovarov, A.L. and Guryanov, G.M. (2010) F and Cl detection limits in secondary ion mass spectrometry measurements of Si and SiO2 samples. Journal of Vacuum Science and Technology, A, 28, 1181-1186.

Portnyagin, M., Simakin, S. and Sobolev, A. (2002) Fluorine in primitive magmas of the Troodos Ophiolite complex, Cyprus: analytical methods and main results. Geochemistry International, 40, 625-632.

Przybyłowicz, W., Szymczyk, S. and Kajfosz, J. (1986) Fluorine analysis in serpentinite rocks by proton induced gamma-ray emission. Nuclear Instruments and Methods in Physics Research Section B: Beam Interactions with Materials and Atoms, 15, 573-575.

Rauch, M. and Keppler, H. (2002) Water solubility in orthopyroxene. Contributions to Mineralogy and Petrology, 143, 525-536.

Reed, S.J.B. (2005) Electron Microprobe Analysis and Scanning Electron Microscopy in Geology. Cambridge University Press, Cambridge.

Righter, K. and Carmichael, I.S.E. (1996) Phase equilibria of phlogopite lamprophyres from western Mexico: Biotite-liquid equilibria and P-T estimates for biotite-bearing igneous rocks. Contributions to Mineralogy and Petrology, 123, 1-21.

Robert, J.L., Bény, J.M., Della Ventura, G. and Hardy, M. (1993) Fluorine in micas: crystal-chemical control of the OH-F distribution between trioctahedral and dioctahedral sites. European Journal of Mineralogy, 5, 7-18.

Roelandts, I., Robaye, G., Weber, G. and Delbrouck, J.M. (1985) Determination of fluorine in eighty international geochemical reference samples by proton induced gamma ray emission spectrometry (PIGE). Geostandards Newsletter, 9, 191-192.

Roelandts, I., Robaye, G., Weber, G. and Delbrouck-Habaru, J. (1986) The application of proton-induced gamma-ray emission (PIGE) analysis to the rapid determination of fluorine in geological materials. Chemical Geology, 54, 35-42.

Roggensack, K., Hervig, R.L., McKnight, S.B. and Williams, S.N. (1997) Explosive basaltic volcanism from Cerro Negro volcano: Influence of volatiles on eruptive style. Science, 277, 1639-1642.

Rosenberg, P.E. and Foit, F.F. (1976) Fe2+ - F avoidance in silicates. Geochimica et Cosmochimica Acta, 41, 345-346.

Rowe, E. and Schilling, J.G. (1979) Fluorine in Iceland and Reykjanes ridge basalts. Nature, 279, 33-37.

Sahama, T.G. and Hytönen, K. (1958) Calcium-bearing magnesium-iron olivines. American Mineralogist, 43, 862-871.

Sahama, Th.G. (1962) Petrology of Mt. Nyiragongo: A review. Transactions of the Edinburgh Geological Society, 19, 1-28.

Salah, H. and Arab, N. (2007) Application of PIGE to determine fluorine concentration in human teeth: Contribution to fluorosis study. Journal of Nuclear and Radiochemical Sciences, 8, 31-34.

Sawyer, G.M. and Oppenheimer, C. (2006) Volcanic fluorine emissions: Observations by Fourier transform infrared spectroscopy. In: Tressaud, A. (eds), Fluorine and the Environment: Atmospheric Chemistry, Emissions, & Lithosphere. Elsevier (San Francisco), 165-185.

Scaillet, B. and Macdonald, R. (2004) Fluorite stability in silicic magmas. Contributions to Mineralogy and Petrology, 147, 319-329.

Schuhmacher, M., Rasser, B., De Chambost, E., Hillion, F., Mootz, T. and Migeon, H.N. (1999) Recent instrumental developments in magnetic sector SIMS. Fresenius' Journal of Analytical Chemistry, 365, 12-18.

Shannon, R. (1976) Revised effective ionic radii and systematic studies of interatomic distances in halides and chalcogenides. Acta Crystallographica Section A: Crystal Physics, Diffraction, Theoretical and General Crystallography, 32, 751-767.

Sigvaldason, G.E and Oskarsson, N (1986) Fluorine in basalts from Iceland. Contributions to Mineralogy and Petrology, 94, 263-271.

Simkin, T. and Smith, J. (1970) Minor-element distribution in olivine. The Journal of Geology, 304-325.

Simkin, T. (1967) Flow differentiation in the picritic sills of north Skye, in Wyllie, P.J. (eds) Ultramafic and related Rocks: John Wiley and Sons, New York, p. 64-69.

Simkin, T. (1966) Zoned olivines and the cooling history of a picritic sill (abs) Geological Society of America Special Paper, 101, 202-203.

Simonen, A. (1961) Olivine from Rapakivi. Geological Survey of Finland Compte rendus, 33, 371-376.

Smith, J.V. (1981) Halogen and Phosphorous Storage in the Earth. Nature, 289, 762-765

Smith, J., Delaney, J., Hervig, R. and Dawson, J. (1981) Storage of F and Cl in the upper mantle: Geochemical implications. Lithos, 14, 133-147.

Smyth J.R. (1989) Electrostatic characterization of oxygen sites in minerals. Geochimica et Cosmochimica Acta, 53, 1101-1110.

Smyth, J.R. (1987) β-Mg_2SiO_4: A potential host for water in the mantle? American Mineralogist, 72, 1051-1055.

Smyth, J.R. (1980) Cation vacancies and the crystal chemistry of breakdown reactions in kimberlitic omphacites. American Mineralogist, 65, 1185-1191.

Smyth, J.R., Bell, D.R., Rossman, G.R. (1991) Incorporation of hydroxyl in upper mantle clinopyroxenes. Nature, 351, 732-735.

Smyth, J.R., McCormick, T.C., Caporuscio, F.C. (1984) Petrology of a suite of eclogite inclusions from the Bobbejaan kimberlite: 1 Two unique corundum grospydites. In: Kornprobst, J (eds) Kimberlites II: The Mantle and Crust-Mantle Relationships, p. 121-132. Elsevier, New York.

Spilliaert, N., Métrich, N. and Allard, P. (2006) S–Cl–F degassing pattern of water-rich alkali basalt: Modeling and relationship with eruption styles on Mount Etna volcano. Earth and Planetary Science Letters, 248, 772-786.

Stalder, R. (2004) Influence of Fe, Cr and Al on hydrogen incorporation in orthopyroxene. European Journal of Mineralogy, 16, 703-711.

Stalder, R., Klemme, S., Ludwig, T. and Skogby, H. (2005) Hydrogen incorporation in orthopyroxene: Iinteraction of different trivalent cations. Contributions to Mineralogy and Petrology, 150, 473-485

Stalder, R. and Skogby, H. (2002) Hydrogen incorporation in enstatite. European Journal of Mineralogy, 14, 1139-1144.

Stanton, T.R., Holloway, J.R., Hervig, R.L., Stolper, E. (1985) Isotope effect on water diffusivity in silicic melts: an ion microprobe and inrared analysis. EOS, Transactions of the American Geophysical Union, 66, 1131 (abstract).

Stecher, O. (1998) Fluorine geochemistry in volcanic rock series: examples from Iceland and Jan Mayen. Geochimica et Cosmochimica Acta, 62, 3117-3130.

Stern, R.A. (2009) Chapter 1: An introduction to secondary ion mass spectrometry (SIMS) in geology. In: Fayek, M. (eds) Secondary Ion Mass Spectrometry in the Earth Sciences: Gleaning the Big Picture from a Small Spot. Mineralogical Association of Canada Short Course, vol. 41, p. 1-18.

Stix,J. and Layne, G.D. (1996) Gas saturation and evolution of volatile and light lithophile elements in the Bandelier magma chamber between two caldera-forming eruptions. Journal of Geophysical Research, 101, 25181-25196.

Stolper, E. (1982) The speciation of water in silicate melts. Geochimica et Cosmochimica Acta, 46, 2609-2620.

Straub, S.M. and Layne, G.D. (2003) The systematics of chlorine, fluorine, and water in Izu arc front volcanic rocks: Implications for volatile recycling in subduction zones. Geochimica et Cosmochimica Acta, 67, 4179-4203.

Sykes, D., Rossman, G.R., Veblen, D.R., Grew, E.S. (1994) Enhanced H and F incorporation in borian olivine. American Mineralogist, 79, 904-908.

Symonds, R.B., Rose, W.I., Bluth, G.S.J., and Gerlach, T.M. (1994) Volcanic-gas studies: Methods, results, and applications. In: Carroll, M.R. and Holloway, J.R. (eds), Volatiles in Magmas. Reviews in Mineralogy Volume 30. Mineralogical Society of America (Washington, D.C.), 1-66.

Tagirov, B., Schott, J., Harrichourry, and J.C., Salvi, S. (2002) Experimental study of aluminum speciation in fluoride-rich supercritical fluids. Geochimica et Cosmochimica Acta, 66, 2013-2024.

Tenner, T.J., Hirschmann, M.M., Withers, A.C. and Hervig, R.L. (2009) Hydrogen partitioning between nominally anhydrous upper mantle minerals and melt between 3 and 5 GPa and applications to hydrous peridotite partial melting. Chemical Geology, 262, 42-56.

Wang, Q., Makishima, A., Nakamura, E. (2010) Determination of fluorine and chlorine by pyrohydrolysis and ion chromatography: Comparison with alkaline fusion digestion and ion chromatography. Geostandards and Geoanalytical Research, 34, 175-183.

Watson, E.B. (1994) Diffusion in volatile-bearing magmas. In: Carroll, M.R. and Holloway, J.R. (eds), Volatiles in Magmas. Reviews in Mineralogy Volume 30. Mineralogical Society of America (Washington, D.C.), 371-411.

Westrich, H.R. (1990) Materials compatibility studies for the magma energy extraction project. Geothermics, 19, 341-357.

Westrich, H.R. (1987) Determination of water in volcanic glasses by Karl-Fischer titration. Chemical Geology, 63, 335-340.

Wheeler, E.P. (1965) Fayalitic olivine ion northern Newfoundland-Labrador. Canadian Mineralogist, 8, 339-346.

Wilkinson, J. (1958) The petrology of a differentiated teschenite sill near Gunnedah, New South Wales. American Journal of Science, 256, 1-39.

Williams-Jones ,A.E., Samson, I.M. and Olivo, G.R. (2000) The genesis of hydrothermal fluorite-REE deposits in the Gallinas Mountains, New Mexico. Economic Geology, 95, 327-341.

Wilson, R.G., Stevie, F.A., Magee, C.W. (1989) Secondary Ion Mass Spectrometry: A Practical Handbook for Depth Profiling and Bulk Impurity Analysis. John Wiley and Sons. New York.

Witter, J.B. and Kuehner, S.M. (2004) A simple empirical method for high-quality electron microprobe analysis of fluorine at trace levels in Fe-bearing minerals and glasses. American Mineralogist, 89, 57-63.

Wittmaack, K. (2012) Mechanisms responsible for inducing and balancing the presence of Cs adatoms in dynamic Cs based SIMS. International Journal of Mass Spectrometry. 313, 68-72.

Wood, B. and Henderson, C. (1978) Compositions and unit-cell parameters of synthetic non-stoichiometric tschermakitic clinopyroxenes. American Mineralogist, 63, 66-72.

Yagi, K. (1964) Pillow lavas of Keflavik, Iceland and their genetic significance Journal of the Faculty of Science, Hokkaido University. Series 4, Geology and Mineralogy, 12, 171-183.

Yagi, K. (1960) Petrochemistry of the alkalic rocks of the Ponape island, western Pacific Ocean. International Geological Congress, pt. 13, 108-122

Yoder, H.S. and Tilley, C.E. (1962) Origin of basalt magmas: An experimental study of natural and synthetic rock systems. Journal of Petrology, 3, 342-532.

Young, E., Myers, A., Munson, E. and Conklin, N. (1969) Mineralogy and geochemistry of fluorapatite from Cerro de Mercado, Durango, Mexico. US Geological Survey Professional Paper, 650, D84-D93.

Zeigler, J. (2011) http://www.srim.org/.

Zhao, Y.H., Ginsberg, S. and Kohlstedt, D. (2004) Solubility of hydrogen in olivine: Dependence on temperature and iron content. Contributions to Mineralogy and Petrology, 147, 155-161.

Zhao, S., Nee, P., Green, H.W., Dobrzhinetskaya, L.F. (2011) Ca-Eskola component in clinopyroxene: Experimental studies at high pressures and high temperatures in multi-anvil apparatus. Earth and Planetary Science Letters, 307, 517-524.